FINAL REPORT

A HIGH SEASONAL PERFORMANCE FACTOR GAS HEAT PUMP FOR THE NORTH CENTRAL UNITED STATES

APPENDIX VOLUME I

7½ TON TECHNICAL DEMONSTRATION

Prepared By: Mechanical Technology Inc.
Prepared For: Consolidated Natural Gas Service Company Inc.
And The U.S. Department of Energy
Prepared Under: DOE Prime Contract EY-76-C-02-2883

January, 1980

Consolidated Natural Gas Service Company Inc.

Mechanical Technology Inc.

MTI 79TR68

FINAL REPORT

A HIGH SEASONAL PERFORMANCE FACTOR GAS HEAT PUMP FOR THE NORTH CENTRAL UNITED STATES

Appendix Volume I

7 1/2-TON TECHNICAL DEMONSTRATION

Prepared By: Mechanical Technology Incorporated
968 Albany Shaker Road
Latham, New York 12110

Prepared For: Consolidated Natural Gas Service Company Inc.
Research Department
11001 Cedar Avenue
Cleveland, Ohio 44106

And The U.S. Department of Energy
Consumer Products Division
Technology & Consumer Products Branch
20 Massachusetts Avenue
Washington, D.C. 20545

Prepared Under: DOE Prime Contract EY-76-C-02-2883

January, 1980

NOTICE

This report was prepared as an account of work sponsored by the United States Government and Consolidated Natural Gas Service Company Inc. Neither the United States nor the United States Department of Energy, nor Consolidated Natural Gas Service Company Inc., nor any of their employees, nor any of their subcontractors, or their employees, makes any warranty, express or implied, or assumes any legal liability or responsibility for the accuracy, completeness or usefulness of any information, apparatus, product or process disclosed, or represents that its use would not infringe privately-owned rights. Mention of commercial products, their manufacturers, or their suppliers in this publication does not imply or connote approval or disapproval of the product by the U.S. Department of Energy or Consolidated Natural Gas Service Company Inc.

Appendices to Final Report

DEMONSTRATION OF A HIGH SPF GAS HEAT PUMP
FOR THE NORTH CENTRAL UNITED STATES

Table of Contents

Appendix Volume	Title
I*	7-1/2 Ton Technical Demonstration
II	7-1/2 Ton Market Potential Study
III	7-1/2 Ton Comparative Cost of Ownership Study
IV	System Cost Analysis
V	Large Size Model Technical Effort
VI	Large Size Model Market Potential Study
VII	Large Size Model Comparative Cost of Ownership Study
VIII	Business Potential Study

*Contained herein.

APPENDIX - VOLUME I

TABLE OF CONTENTS

Section		Page
	LIST OF FIGURES	iv
1.0	INTRODUCTION	1-1
	1.1 Background	1-1
	1.2 7-1/2-Ton Demonstrator Unit System Capacity and Configuration Selection	1-5
	1.3 Technical Program Overview	1-6
2.0	SYSTEM DESIGN	2-1
	2.1 General Description of the Concept	2-1
	2.2 System Design Approach	2-10
	2.3 Steam and Refrigerant Cycles	2-13
	2.4 Decision Trade-Offs	2-26
	2.5 Rotating Unit Design Summary	2-29
3.0	COMPONENT DESIGN SUMMARIES	3-1
	3.1 Turbine Design Summary	3-1
	3.2 Regenerator	3-8
	3.3 Refrigerant Compressor	3-8
	3.4 Homopolar Alternator	3-18
	3.5 Supporting Design Analyses	3-21
	3.6 Component Test Facility	3-21
4.0	SYSTEM TEST SUMMARY	4-1
5.0	CONCLUSIONS	5-1
ATTACHMENT		
A	TURBINE DESIGN REPORT	A-1
B	DESIGN REPORT - CNG COMPRESSOR	B-1
C	DESIGN REPORT - HOMOPOLAR INDUCTOR ALTERNATOR	C-1
D	FINAL SUMMARY REPORT OF CNG HEAT PUMP ROTOR BEARING DYNAMICS	D-1
E	THERMAL ANALYSIS OF CNG TURBOCOMPRESSOR	E-1
F	7-1/2-TON DEMONSTRATOR HSPF GAS HEAT PUMP SYSTEM TEST	F-1

LIST OF FIGURES

Number		Page
1-1	MTI Design for an Organic Rankine Turbo-Alternator-Pump Unit	1-3
1-2	MTI Design for a Gas-Fired Organic Rankine Heat Pump Layout	1-4
1-3	7-1/2-Ton HSPF Program Tasks	1-7
2-1	Heating Service Schematic	2-3
2-2	Cooling Service Schematic	2-4
2-3	Rotating Unit Schematic	2-6
2-4	Top View of Rooftop Unit Mock-Up	2-7
2-5	Air Flow Paths	2-8
2-6	Elevation View of Rooftop Unit Showing Major Equipment	2-9
2-7	Variation of Speed with Pressure Ratio	2-11
2-8	Steam Rankine Cycle Temperature - Entropy Diagram	2-14
2-9	Simulation Results for Heating Service at 35°F Outdoor Ambient	2-16
2-10	Simulation Results at ARI Nominal Cooling Specified Point (95°F ambient)	2-19
2-11	Heat Flow Versus Ambient Temperature	2-22
2-12	System Performance Versus Ambient Temperature	2-23
2-13	Turbine/Compressor Power	2-24
2-14	Required Component Efficiencies	2-25
2-15	Speed Trade-Offs	2-27
2-16	Rotating Unit Parameters for System Design Trade-Off Analysis	2-28
2-17	Rotating Unit Flow Schematic	2-31
2-18	Rotating Unit Assembly	2-32
3-1	Rotating Unit Components	3-2
3-2	Rotating Unit Component - Turbine	3-3
3-3	Rotating Unit Component - Compressor	3-4
3-4	SES Steam Generator Developed for the Environmental Protection Agency	3-5
3-5	Turbine Wheel Design Detail	3-7
3-6	Simplified Steam Cycle Schematic Showing Reheat Reentry and Regeneration	3-9
3-7	Projected and Experimental Turbine Performance	3-10

LIST OF FIGURES (Cont'd)

Number		Page
3-8	Regenerator Core	3-11
3-9	Final Compressor Design	3-14
3-10	Refrigerant Compressor Performance with Vaned Diffuser	3-16
3-11	Refrigerant Compressor Performance with Vaneless Diffuser	3-17
3-12	Lamination Stack	3-19
3-13	Details of the Lamination	3-20
3-14	Lamination Stacks and Armature Windings	3-22
3-15	Component Test Rig	3-24
3-16	Component Turbomachinery Test Rig Schematic	3-25
4-1	Breadboard Demonstration Unit System Test Facility	4-2
4-2	Compressor Efficiency	4-4
4-3	Turbine Efficiency	4-5
4-4	Heat Pump System Performance-Heating Mode	4-6
4-5	Turbine Wheel After System Test	4-9
4-6	Steam Generator Tube Bundle	4-10

1.0 INTRODUCTION

1.1 Background

The use of a gas-energized Rankine cycle to provide the motive power for an air-conditioning or heat pump system has been under investigation for at least 20 years. Through most of this period, Consolidated Natural Gas (CNG) has supported Rankine-cycle-driven gas heat pump development. CNG favored steam with turbine expanders for these reasons:

- Steam offers a greater potential for good thermodynamic efficiency, even on a relatively small scale, when energized by a high-temperature heat source such as a natural gas burner.
- Steam is better known in terms of its thermodynamic properties and chemical stability, has lower cost, and is not flammable or toxic as compared to alternative fluids.
- Turbine expanders offer superior service life with less maintenance requirement than alternative expanders, especially when used with process-fluid-lubricated bearings.
- Turbine expanders provide superior efficiency in applications where load, and especially, speed variations are limited.
- Turbine expanders are unequalled for minimized noise and vibration.

The historic context of the CNG supported steam turbine gas heat pump efforts prior to the HSPF programs is reviewed in Section 1.0 of the main volume of this report. During this 20-year period, most other Rankine prime mover developers were favoring organic-fluid-based systems for gas heat pump application.

Independently of the prior CNG programs, Mechanical Technology Incorporated (MTI) studied and developed a number of Rankine-cycle prime mover systems

potentially useful for a gas heat pump application. In 1968, MTI developed a single-shaft turbo-alternator (see Figure 1-1) using an organic working fluid, for use with either liquid or gaseous fuels. This system was presented to a number of gas industry representatives and manufacturers of absorption air conditioning. In 1971, MTI began the proprietary development of a unique organic Rankine heat pump based upon DuPont patents. This work is now being advanced by the Gas Research Institute. This design, shown in Figure 1-2, utilized a single-shaft mounting for the compressor, alternator and turbine rotating units. Both MTI designs employed process-fluid-lubricated bearings.

Rankine prime mover-related gas heat pump efforts included a design funded by the American Gas Association (A.G.A.) for a single organic-fluid Rankine heat pump under a cooperate program with Eaton from 1971 through 1974. This design was also a single-shaft design with the compressor and turbine mounted back-to-back. Another related A.G.A. program was an organic Rankine total energy package (1968 through 1976). A.G.A. initiated and the Gas Research Institute is continuing to pursue the development of a Brayton-cycle heat pump (1973 through the present). Both these designs utilized a single-shaft coupling of the turbine with the feed pump or compressor with process-fluid-lubricated bearings. All these concepts utilized dynamic machinery. During the early 1970s, General Electric was evaluating the use of a positive displacement multivane Rankine expander with refrigerants such as R-11 and R-22. The system concept included a directly coupled expander-compressor for heat pump duty and an expander-alternator for power generation with solar or fuel heat sources.

All of the Rankine-power cycle system development programs sought to achieve high-efficiency, low-cost conversion machinery with a high overall cycle efficiency. Steam tended to give high overall cycle efficiency. The organic fluids tended to satisfy the need for high-efficiency, low-cost conversion machinery. However, since promising advances in the performance and cost of small steam turbine expanders were being made, CNG was encouraged to initiate a new effort to design, develop, and demonstrate a steam-Rankine system. Additionally, some advances in overall system design and control suggested that, even with lower than desired conversion machinery efficiency,

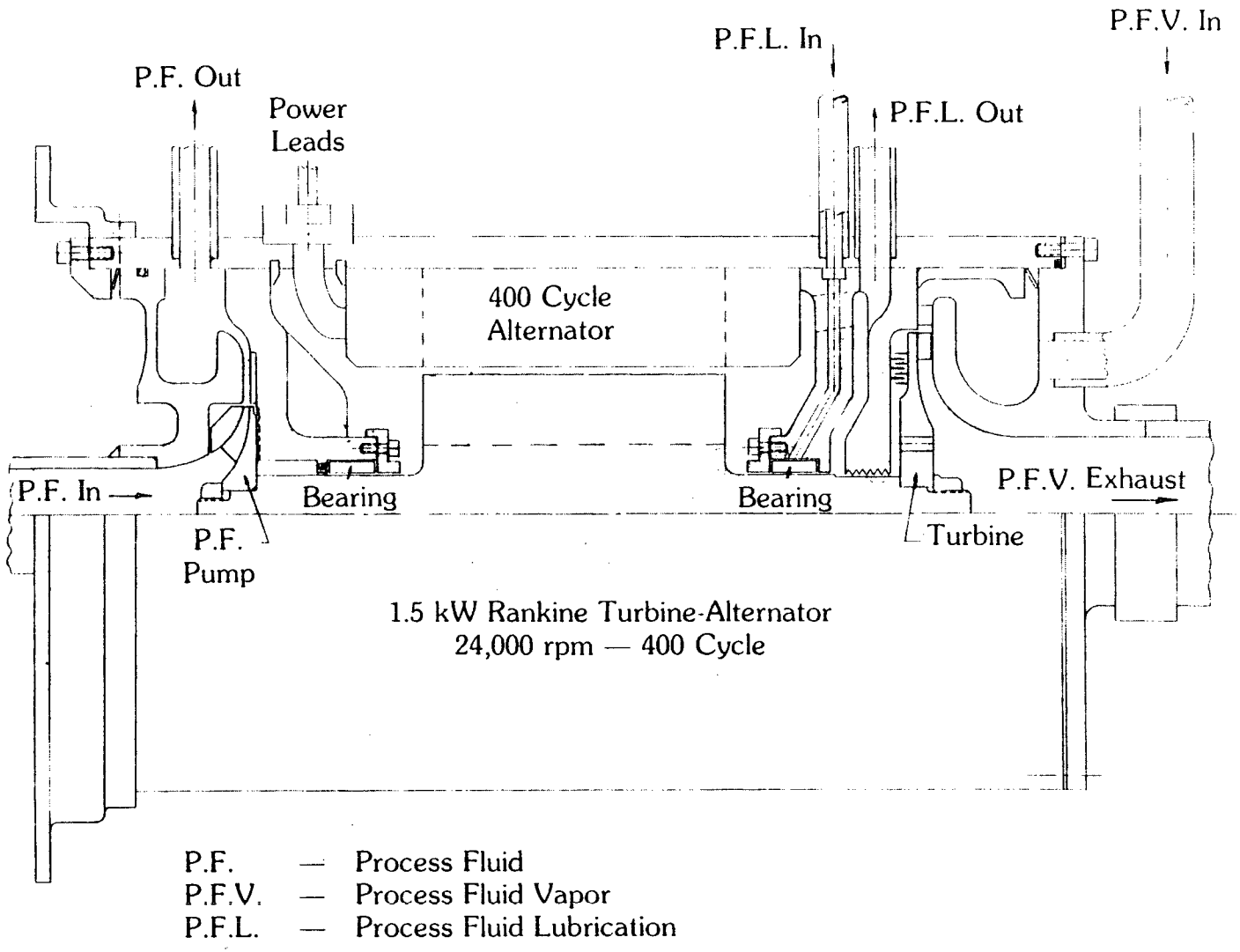

Fig. 1-1 MTI Design for an Organic Rankine Turbo-Alternator-Pump Unit

793622

MECHANICAL TECHNOLOGY INCORPORATED

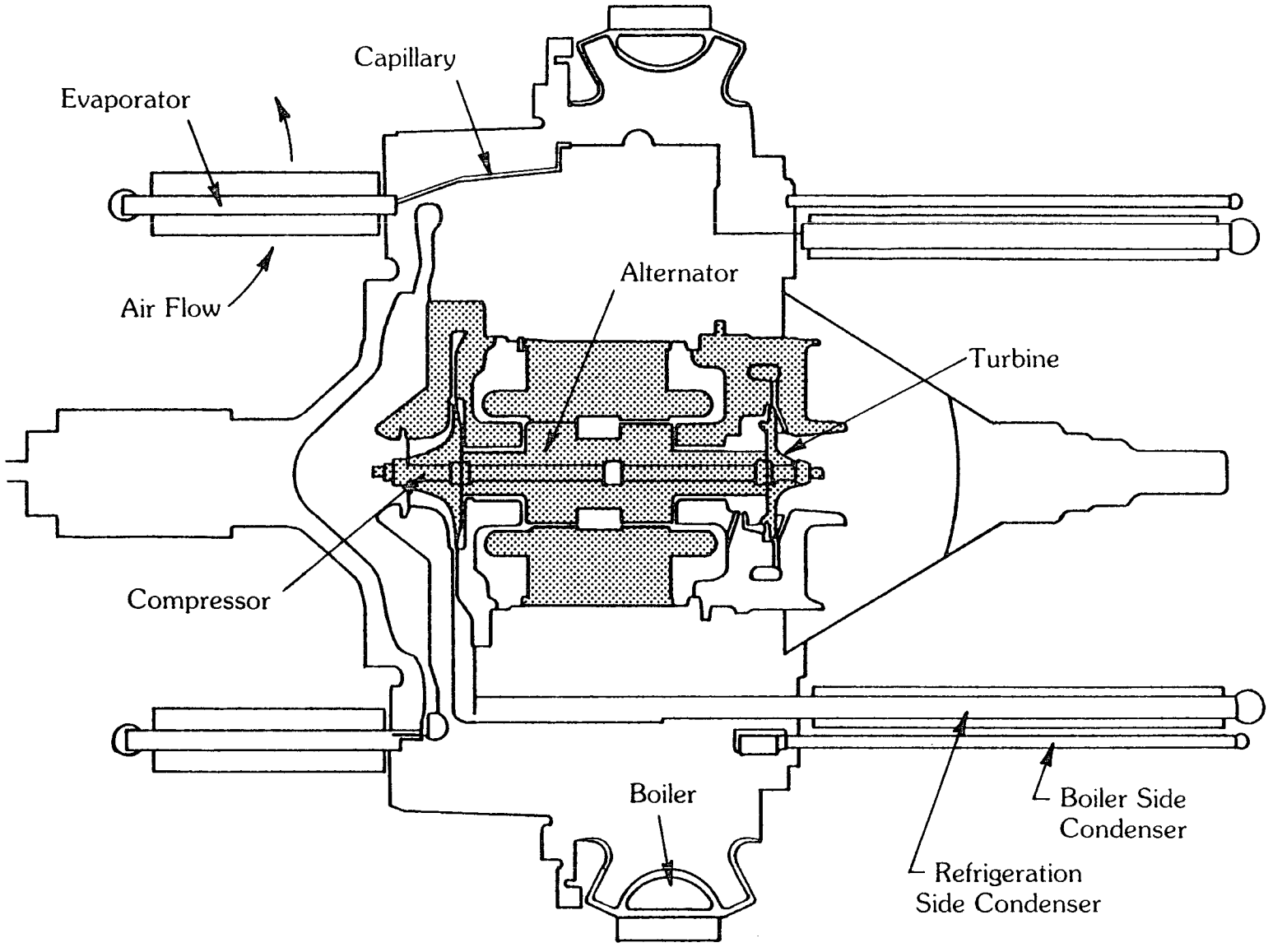

793621

Fig. 1-2 MTI Design for a Gas-Fired Organic Rankine Heat Pump Layout

MECHANICAL TECHNOLOGY INCORPORATED

the overall heat pump performance would be significantly higher than alternative systems. These overall system advantages would be maximized in areas of high heating loads. Furthermore, severe cost and technical restrictions associated with the residential system would be removed when the market segment to be served was shifted from the residential market (characteristically a 3-hp system) to the light commercial market (characteristically a 7- to 50-hp system). Largely as a result of these technical considerations, the concept for the CNG High Seasonal Performance Factor (HSPF) steam turbine-driven pump matured and became the technical focus of the HSPF program.

This report details the technical demonstration effort related to the first HSPF configuration, a 7-1/2-ton rooftop, air-to-air heat pump for the light commercial market. The technical demonstration effort included system design, component design, test and development, and proof-of-concept demonstration unit test. The effort was performed as a part of the ERDA (DOE)-CNG-MTI 7-1/2-ton HSPF program.

The design, development and demonstration of the 7-1/2-ton HSPF system was carried out principally by MTI under contract to CNG and ERDA. As the system integrator, MTI was the principal technical subcontractor and, as such, had primary responsibility for system design, development and demonstration. A number of components were provided by other subcontractors and vendors, who were under direct contract with CNG. In addition, several technical consultants were utilized. The subcontractors, consultants and vendors who contributed to the 7-1/2-ton technical effort are identified in Attachment A of the main volume of this report.

1.2 7-1/2-Ton Demonstrator Unit System Capacity and Configuration Selection

The selection of an appropriate size for the HSPF involved a trade-off among energy conservation potential, total potential market size, technical performance objectives, and system cost goals. These factors were interrelated since the energy conservation potential was a function of total potential market size and technical performance. The actual energy conservation realized was a function of the system cost and performance. The selection of size was driven primarily by qualitative market potential considerations.

At the time of capacity and configuration selection, specific information was not available as to either the sensitivity of system cost to unit size or the market reaction to system cost. Therefore, the 7-1/2-ton demonstrator unit size was selected as the basis for demonstration of the HSPF system. The configuration specified embodied the several important HSPF features defined in Section 2.1. The resulting design heating load was a function of the characteristics of the system, based upon the selection of the 7-1/2-ton cooling capacity rating. The design heating load became 180,000 Btu/hr at 31°F outdoor temperature. For this unit size, the physical size of the turbomachinery approached the lower limit of practical turbomachinery with high performance.

1.3 Technical Program Overview

The 7-1/2-ton HSPF technical demonstration was achieved through a laboratory breadboard configuration. The breadboard unit would incorporate all the design features of the HSPF system concept but not necessarily in a product configuration. Thus, while all the system components would be identical or functionally equivalent to the product concept, their physical locations relative to one another would not be typical of the product configuration.

The overall program plan for the technical effort for the 7-1/2-ton HSPF configuration is shown in Figure 1-3. The effort was carried out through the proof-of-concept test. Due to a determination that the 7-1/2-ton HSPF system manufacturing cost would be unacceptably high, the 7-1/2-ton technical demonstration effort was terminated prior to the system performance demonstration.

The first task was the demonstrator unit's system design. Starting with the specified demonstrator unit capacity and configuration, a system design effort was carried out to optimize the steam power cycle and refrigeration cycle with the turbomachinery components. The system design effort, by necessity, entailed preliminary designing of the basic components of the system. Particular emphasis was placed upon turbine selection and its interaction with the steam-Rankine power cycle, in order to maximize the steam turbine driver system's overall performance.

MECHANICAL TECHNOLOGY INCORPORATED

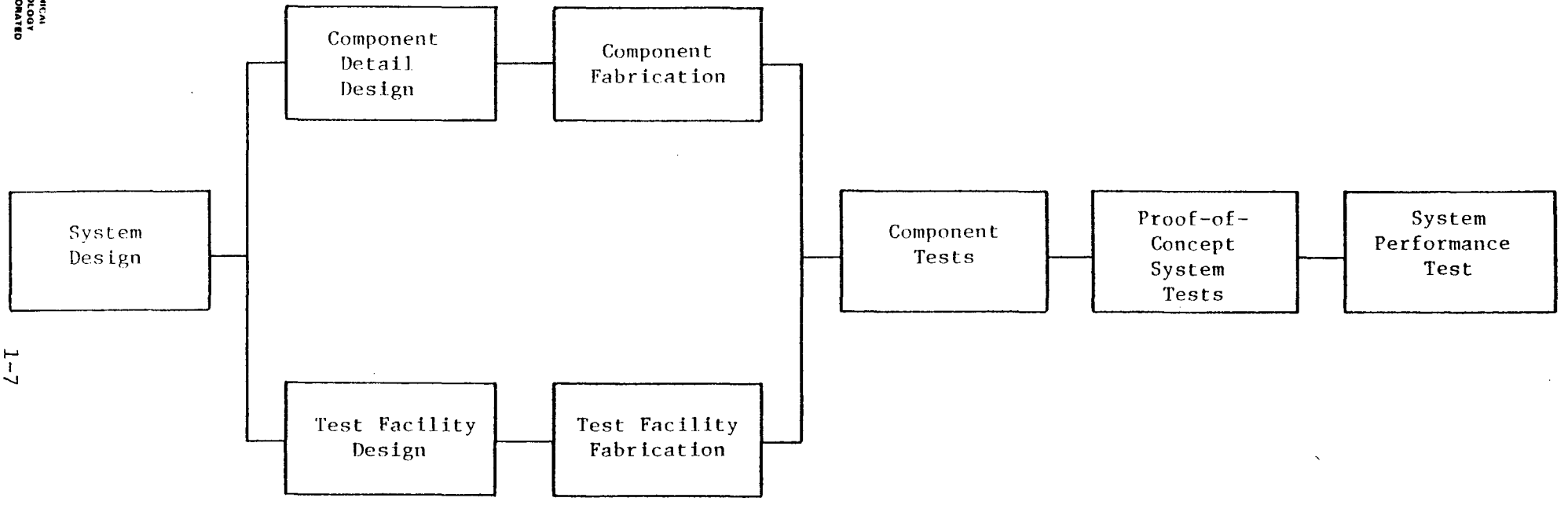

Fig. 1-3 7-1/2-Ton HSPF Program Tasks

793713

After the selection of the basic system design details, two parallel activities were initiated. The first activity dealt with the detail design and fabrication of the unique components of the system, including the steam components and the turbomachinery package. The second activity dealt with the design and fabrication of a laboratory facility to test the basic components and the full system.

Each of the principal components was tested independently. The steam generator was designed, fabricated and tested by Scientific Energy Systems. The turbomachinery package components of the compressor, alternator and turbine were designed, fabricated and tested by MTI.

The technology proof-of-concept system test was performed by MTI. In this test, the demonstrator unit system was totally assembled and operated as a system. However, some critical clearances were not set at design specifications. The clearances of most concern are those related to the steam turbine nozzle ring and the recovery scoop. This portion of the package was subjected to the highest mechanical and thermal loads. While these loads were analyzed in detail, the interactions of all the components of a complex system were not amenable to extremely precise analysis. Therefore, a conservative test program called for a preliminary proof-of-concept or mechanical verification of the analytical design parameters before a definitive attempt for design performance was made.

As noted previously, the final performance demonstration test procedure was not conducted.

2.0 SYSTEM DESIGN

2.1 General Description of the Concept

The HSPF system concept was defined as a gas-fueled, steam-Rankine driven, unitary air-to-air heat pump. The 7-1/2-ton technical effort incorporated technically advanced component features including a compact, high-efficiency steam generator and a single-shaft, gas-bearing turbomachine incorporating the steam turbine, alternator, and refrigerant compressor. In addition to advanced components, the HSPF system concept included the following novel operational and design features:

1) Phased cooling of system condensers. During cooling operation heat being rejected to the surroundings from the heat pump (air conditioning) circuit was given first access to cooling air. The outdoor air first accepted rejected heat from the refrigeration circuit and second, from the steam turbine's exhaust, thus significantly reducing the head pressure requirement of the heat pump compressor. Second-law considerations showed that reducing the work per unit heat being pumped was a favorable trade-off for the resulting elevation in the turbine's back pressure.

2) Phased heating of the conditioned air. First, the pumped heat was transferred to the return conditioned air, and second, the steam turbine's exhaust was used to heat the air. This process significantly reduced the head pressure requirement of the heat pump compressor. Second-law considerations showed that reducing the work per unit heat being pumped was a favorable trade-off for the resulting elevation in the turbine's back pressure.

3) Direct heating of conditioned air with steam, bypassing the turbine at very low temperatures. The bypassed steam augmented the turbine's exhaust, both of which then heated the conditioned air after it was heated by pumped heat. By this method, useful heat pumping could coexist with heating by means of bypassed steam. This technique,

coupled with the technique of item 2 above, led to useful heat pumping, down to about 7°F with single-stage centrifugal compression.

4) Fully modulated steam cycle operation. Full utilization of this technique could only accomplished when both the heat pump compressor and the air-moving fans were speed-coupled to the prime mover. An advantage inherent in this approach was that at low capacity operation, air-moving power requirements did not destroy the basic energy-saving advantages of modulation. Control inputs were to the burner and to the turbine throttle.

5) Self-powered auxiliaries. The use of the steam-Rankine prime mover to provide electricity for the auxiliaries such as the air handling fans and the feed pump removed the need for utility electric service for these functions. This use of the high-quality energy in the steam to first provide electricity for the auxiliaries and then for heating service was an example of energy cascading and improved the overall fuel efficiency of the system.

Figures 2-1 and 2-2 are schematics of the HSPF heat pump system operating in the heating and cooling modes, respectively. These schematics illustrate the phased heating of air in both the indoor and outdoor heat exchanger assemblies, the direct use of steam for supplemental heating, and the self-powering of the auxiliaries. Phase heating indoors and phased cooling outdoors required the four heat exchanger system configuration shown in Figures 2-1 and 2-2. This configuration is the "trademark" of the HSPF system.

The operation of the steam-Rankine driver can be best described as follows. Driver operation began at the feed pump and the steam generator. The feed pump supplied condensate water to the steam generator at a pressure somewhat above 300 psia. The steam generator then produced 300 psia, 1100°F steam. This steam passed through a steam turbine to produce shaft power. The steam system also provided for reheat and regeneration, as will be discussed later.

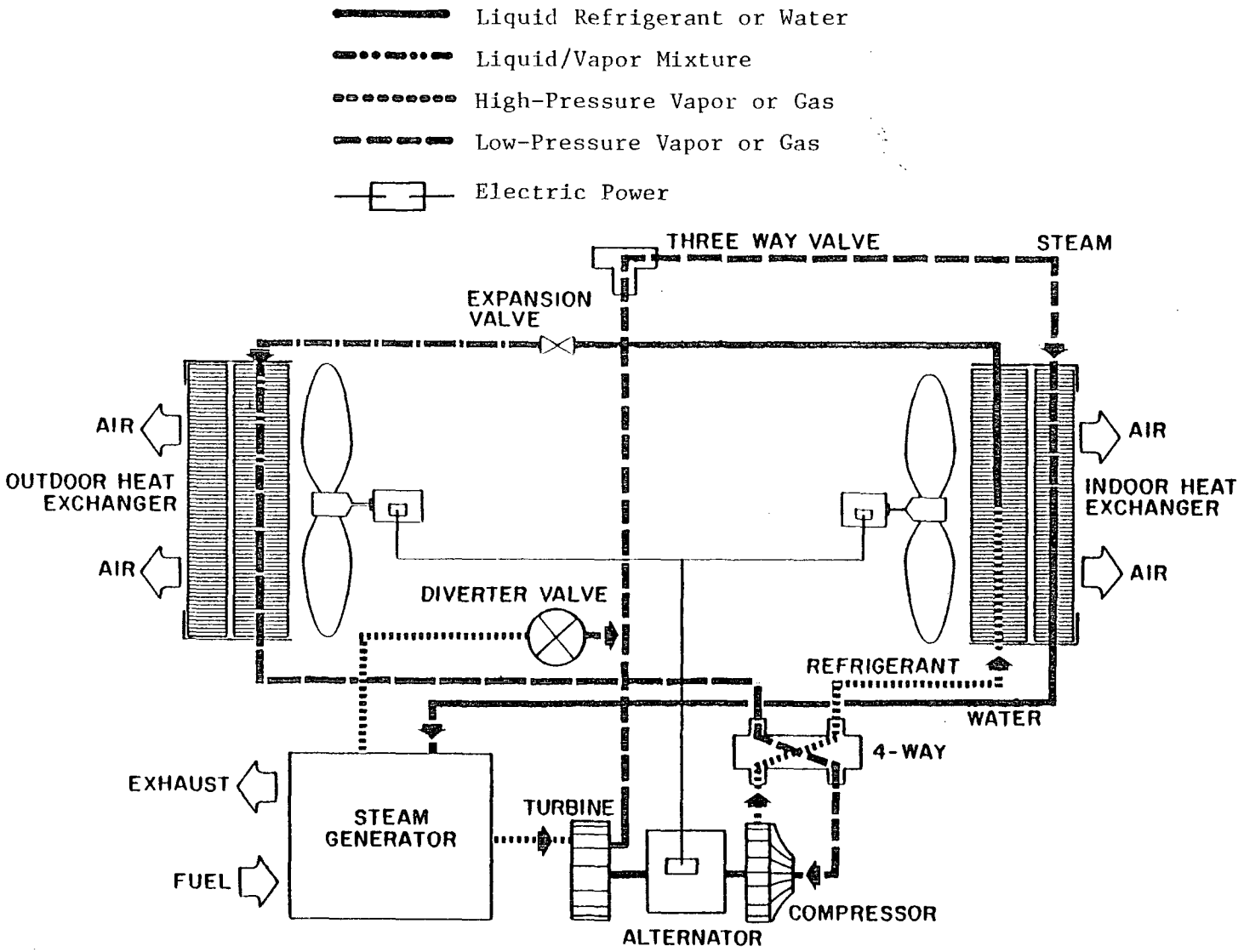

Fig. 2-1 Heating Service Schematic

MECHANICAL TECHNOLOGY INCORPORATED

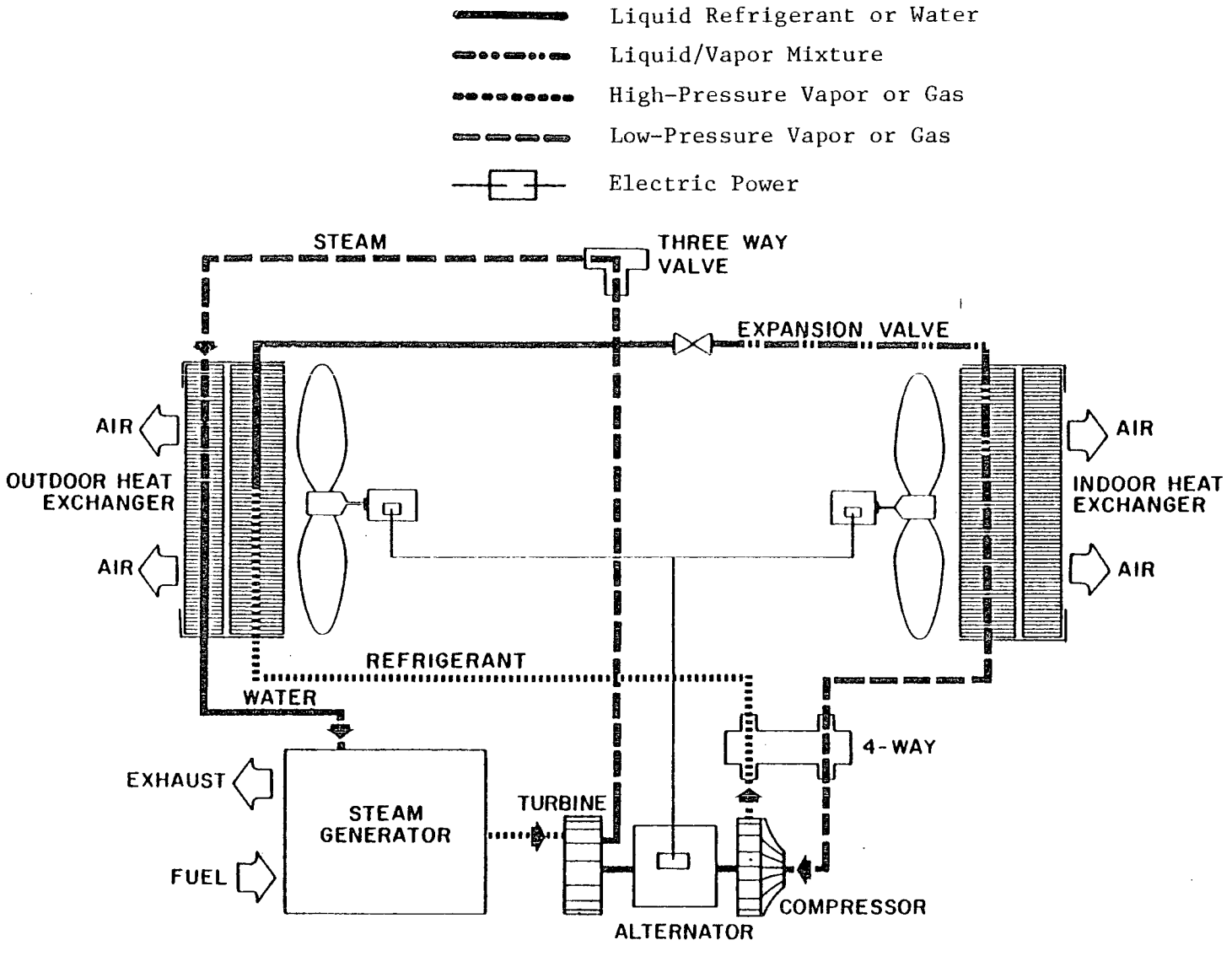

792944

Fig. 2-2 Cooling Service Schematic

MECHANICAL TECHNOLOGY INCORPORATED

However, these details are not necessary to understand the basic principles of operation of the HSPF system. The steam exiting from the steam turbine was condensed in either the outdoor steam heat exchanger (for cooling) or the indoor steam heat exchanger (for heating). The power from the steam turbine drove an alternator and a refrigerant compressor. The alternator provided power for the auxiliaries. The refrigerant compressor compressed the heat pump refrigerant in a standard heat pump refrigeration circuit.

The rotating machinery package is shown in Figure 2-3 in simplified form. The turbomachinery package design consisted of the axial-flow steam turbine, the alternator rotor, and the refrigerant compressor which were mounted on a single shaft. The shaft was supported by refrigerant-lubricated gas bearings. The shaft seal between the steam and refrigerant systems was at the steam turbine. Thus, the alternator and bearings operated in an environment of superheated refrigerant. The system was designed for use with refrigerant 11.

The major auxiliary devices were driven by electric motors which were powered by the high-frequency alternator. The breadboard demonstrator employed a rectifier and direct-current drive motors. The product concept favored synchronous high-frequency ac transmission and drive motors. Either way, the major auxiliary devices were speed-locked to the prime mover.

A mock-up of the HSPF in a rooftop product configuration was fabricated to illustrate the features noted above and the packaging of the novel components. This mock-up is shown in Figure 2-4. Figure 2-5 shows the air path through the refrigerant and steam heat exchangers and illustrates the novel combination of phased heat exchangers noted above. Figure 2-6 shows the general arrangement of the mechanical components. These components represented the principal difference between the HSPF heat pump and the conventional units utilizing electric motor driven compressors. Thus, a principal program technical goal was to match the individual components to achieve superior overall system performance.

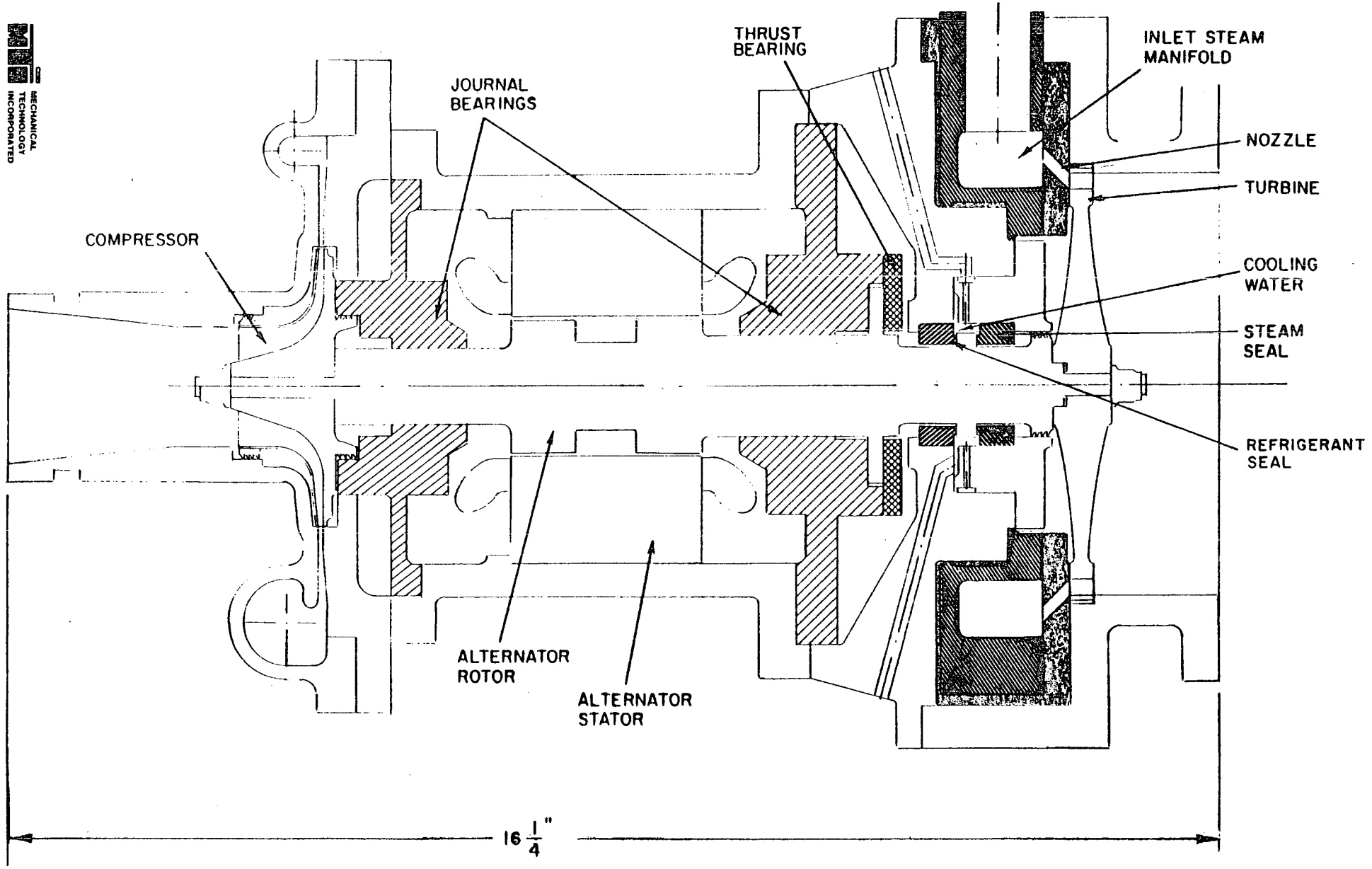

Fig. 2-3 Rotating Unit Schematic

792912

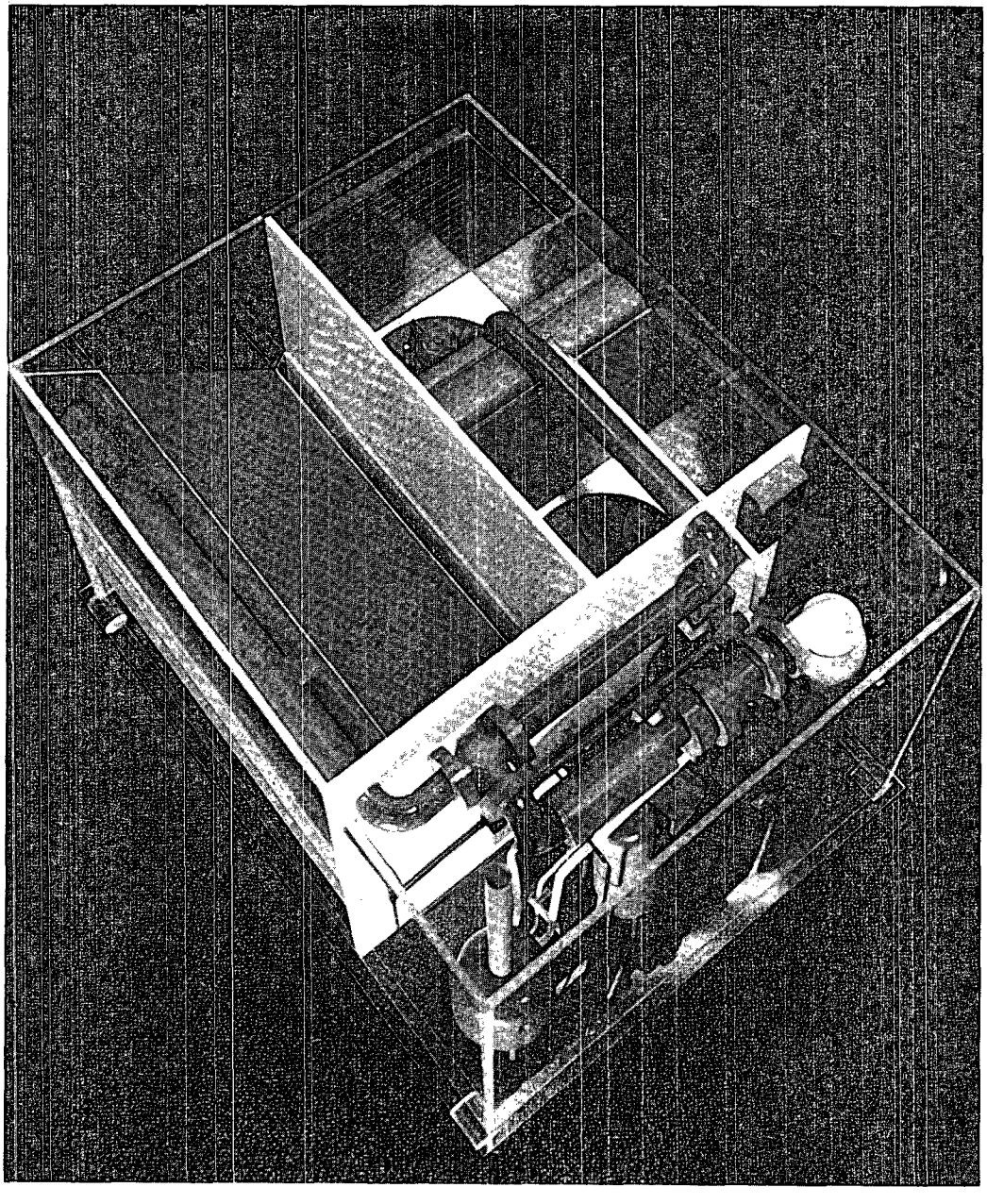

Fig. 2-4 Top View of Rooftop Unit Mock-up

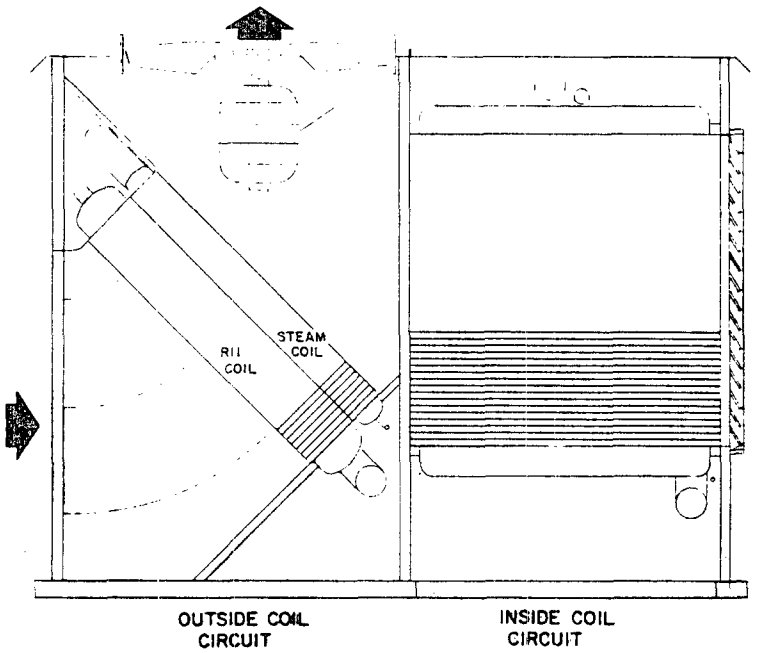

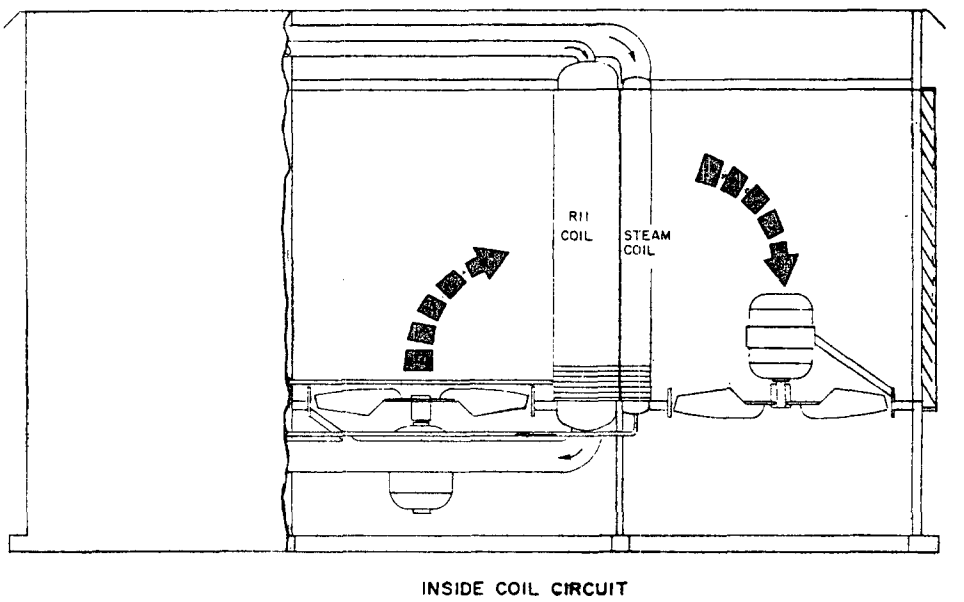

Fig. 2-5 Air Flow Paths

792941

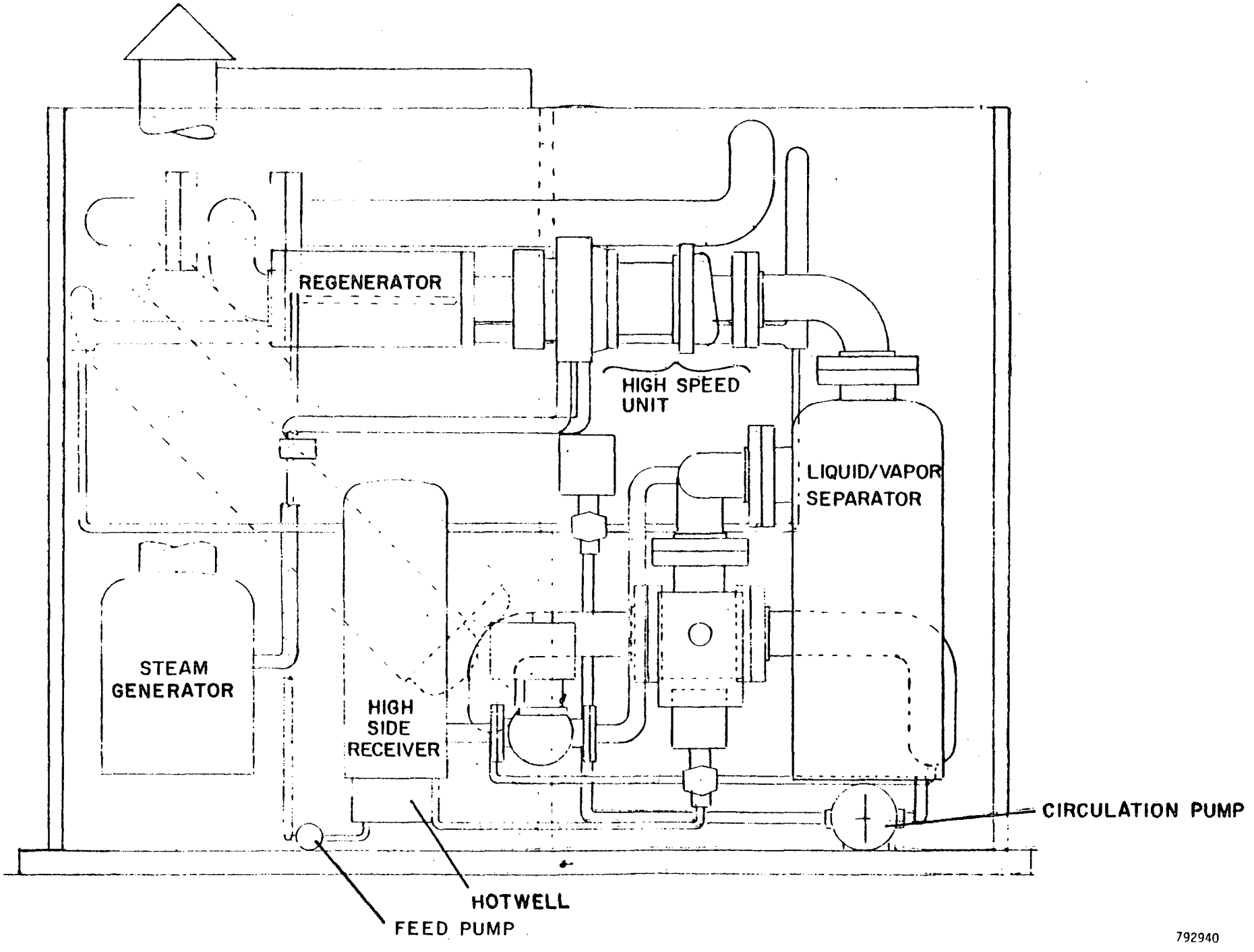

Fig. 2-6 Elevation View of Rooftop Unit Showing Major Equipment

MECHANICAL TECHNOLOGY INCORPORATED

The overall program plan for the technical effort as implemented is shown in Figure 2-7. The program effort on the 7-1/2-ton HSPF unit was terminated at the end of proof-of-concept testing of the 7-1/2-ton breadboard demonstrator in July, 1978.

2.2 System Design Approach

The system design started with a specification of a design point cooling requirement of 7-1/2-tons at 95°F dry bulb (DB) and 80°F wet bulb (WB). This design point, combined with the general characteristics of the HSPF, produced the design point heating load of 180,000 Btu/hr at 31°F DB, outdoor ambient. The system design objective, then, was to achieve the design point heating and cooling loads with optimized system performance. The overall goals were to achieve seasonal performance factors of 1.3 for heating service and 0.6 for cooling service for application in Cleveland, Ohio. These levels of performance would have provided superior energy conservation capability relative to contemporary HVAC concepts. The optimization of the system performance required a matching of and trade-off among the various components. Table 2-1 lists the major components in the system. The differences between the components used in the breadboard demonstrator and those expected to be used in the eventual product are noted.

Of the major components listed in Table 2-1, MTI was responsible for the design of those components in the high-speed rotating package including the turbine, alternator, seal, bearings and compressor. The steam generator was designed and fabricated by Scientific Energy Systems under contract to CNG. The heat exchangers and drive motors were selected from commercially available equipment. MTI was responsible for specifying and purchasing these components. The feed pump was designed and fabricated by Phillips Engineering Company, St. Joseph, Michigan. The design of the turbomachinery components required that each component be matched to the other components in the assembly and that the overall performance of the system be optimized. Such a design process required numerous iterations starting with a basic design of each component.

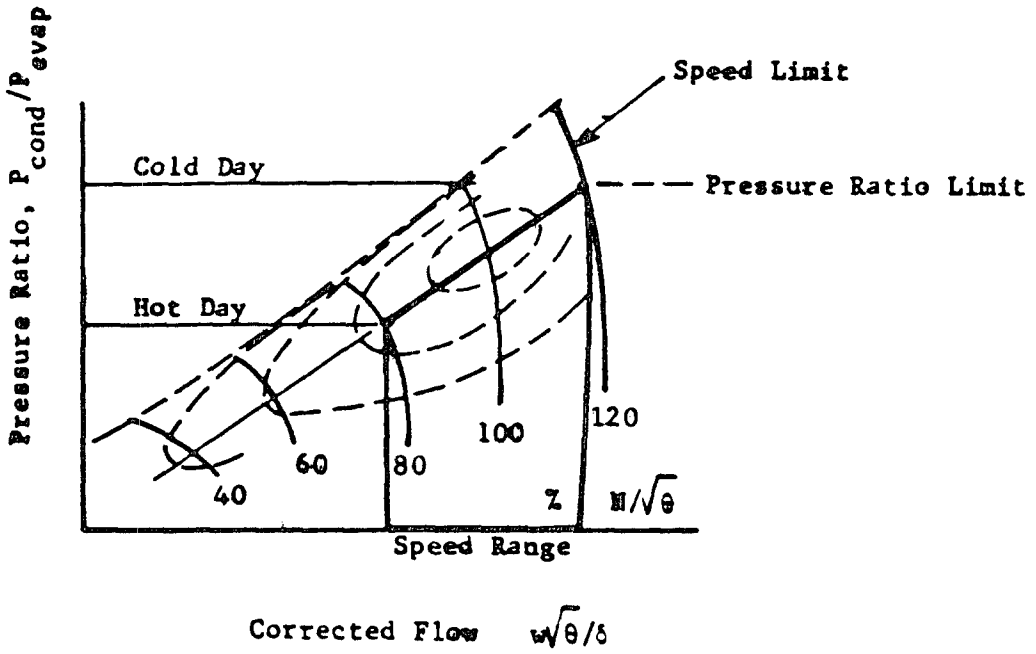

Fig. 2-7 Variation of Speed with Pressure Ratio

792942

TABLE 2-1

MAJOR SYSTEM COMPONENTS

Steam Generator	Monotube, power burner, with integrated superheater, reheater and combustion air preheater.
Turbine	Single stage, axial flow with reentry.
Alternator	3-Phase inductor homopolar.
Bearings	Refrigerant-gas-lubricated.
Breadboard	Pivoted shoe.
Product	Hydresil® foil type.
Shaft Seal	
Breadboard	Combination floating labyrinth and carbon-ring face seal.
Product	Hermetic.
Compressor	Single-stage centrifugal, fixed geometry.
Air/Steam and Air/Refrigerant Heat Exchangers	Flat tube and plate-fin, all parallel circuits. Series air-flow
Feed Pump	Hermetic diaphragm-type with gear-type booster.
Drive Motors	
Breadboard	dc
Product	ac squirrel-cage.

® Mechanical Technology Incorporated

The primary design/optimization tool developed during the program was a computer model which integrated both the steam and refrigerant systems. The simulation was configured as an "analysis" rather than a "design" program. That is, the computer program determined the match of components as ambient conditions were varied about the design point rather than generating the performance of a number of "infinitely variable" designs.

The need for the former type of analysis was apparent by examination of Figure 2-7. Figure 2-7 shows a generalized compressor map: pressure ratio as a function of corrected flow and corrected speed. With centrifugal compression, the location of the compressor operating point varied considerably as the condenser and evaporator pressures varied with local ambient conditons. Relative positions are shown for "hot" and "cold" day operation. The complete range of heat pump/air conditioning operation, in fact, required variable operating speed by the turbomachinery. For heat pump operation, the operating speed was basically a linear schedule passing through 60,000 rpm at 7°F and 40,000 rpm at 68°F. Utilization of this control strategy constrained the compressor to operation parallel to the surge line. The compressor characteristics dominated system performance; all other components had to accommodate the operating characteristics needed by the compressor.

2.3 Steam and Refrigerant Cycles

The idealized steam-Rankine cycle selected is shown in Figure 2-8. This cycle provided for reheat and regeneration to maximize potential thermodynamic efficiency. The state points for the first stage expansion were a maximum of 300 psia and 1100°F. After the first expansion, the steam was reheated to 1100°F at state point 3. The pressure ratio across both stages of expansion was 10 to 1. The steam exiting the second stage of expansion had considerable superheat. This superheated steam was cooled in a regenerator from state points 4 to 5 by heating the feedwater from state points 8 to 9. Even with the low aerodynamic expansion efficiencies characteristic of small-scale turbomachinery operating with high energy fluids, the overall thermal efficiency of this Rankine cycle would be comparatively high.

State Point 1	300 psia	1100°F
State Point 3	30 psia	1100°F

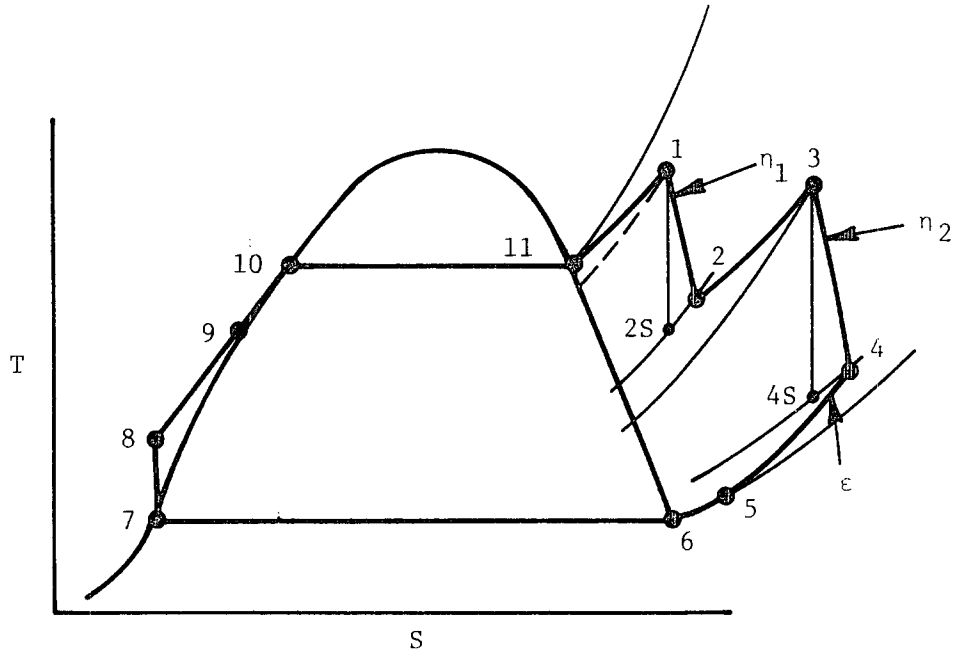

792667

Fig. 2-8 Steam Rankine Cycle Temperature - Entropy Diagram

The selection of the peak temperature was made on the basis of state-of-the-art for water chemistry and material compatibility. The selection of turbine inlet pressure was made on the basis of optimizing turbine and steam generator efficiency. The condensing pressure was determined by the requirements of the heat exchangers and the use of air as the heat sink.

Based on the surge avoidance control strategy previously described and the thermal cycle presented above, the computer simulation was used to generate a family of operating characteristics as a function of ambient temperature. Figure 2-9 shows simulation results for heating service at 35°F outdoor ambient air temperature (representative of the mean weather profile in the Cleveland/Pittsburgh area). Figure 2-10 summarizes the same parameters at the ARI nominal cooling specification point (95°F ambient). Based on fixed heat exchanger surface areas, compressor, turbine and alternator maps, and air flows specified for the refrigerant condenser and evaporator, the computer simulation executed the necessary components match and calculated system performance. A large number of simulation runs were carried out to aid in specifying wide range component performance required (in particular, the compressor/turbine combination) and to generate system performance data for the cost of ownership studies. Figures 2-11 through 2-14 show representative summary data generated by the simulation. Figure 2-11 shows the heating capacity of the system as supplied by the combination of the refrigerant system (as a heat pump) and the steam condenser. At the 35°F design point, pumped heat and Rankine-cycle rejected heat were about equal in magnitude. The upper portion of the figure shows the turbine speed established by the controller as a function of ambient temperature to satisfy the surge avoidance criteria.

Figure 2-12 presents the overall heating COP for the system (ratio of heat delivered to the dwelling to heating value of gas consumed). Integrating that performance against weather profiles typical of Pittsburgh or Cleveland, a seasonal performance factor of about 1.21 was predicted for the breadboard unit. Figures 2-13 and 2-14 scope the turbine and compressor power requirements as well as minimum component efficiencies to achieve the COP levels shown in Figure 2-12.

COMBINED SYSTEM - HEATING

POWER

COMPRESSOR SHAFT,HP... 4.799E+00
PARASITICS,HP..... 3.290E+00
TURBINE,HP..... 8.089E+00

SYSTEM CONFIGURATIONS..... 1

PERFORMANCE

HEAT ADDITION TO STEAM GENERATOR,BTU/HR... 8.026E+04
HEATING EFFECT,BTU/HR..... 1.234E+05
STEAM GENERATOR * BURNER EFFICIENCY..... 8.000E-01
TOTAL SYSTEM ENERGY INPUT..... 1.003E+05
OVERALL HEATING COP..... 1.230E+00
STEAM CYCLE THERMAL EFFICIENCY..... 2.565E-01

50 000 RPM
HEATING

Fig. 2-9 Simulation Results for Heating Service at 35°F Outdoor Ambient

MECHANICAL TECHNOLOGY INCORPORATED

REFRIGERANT SYSTEM (R-11)

	1 COMPRESSOR SUCTION	2 COMPRESSOR DISCHARGE+ CONDENSOR INLET	4 CONDENSOR DISCHARGE	5 EVAPORATOR INLET	7 EVAPORATOR DISCHARGE
TEMPERATURE,DEG.F	4.401E+01	1.516E+02	9.165E+01	2.601E+01	2.601E+01
PRESSURE,PSIA	5.044E+00	2.019E+01	2.019E+01	5.044E+00	5.044E+00
ENTHALPY,BTU/LB	9.747E+01	1.118E+02	2.701E+01	2.701E+01	9.508E+01

FLOW RATES

EVAPORATOR DISCHARGE,PPH...	7.541E+02
SEAL COOLANT,PPH.....	1.000E+02
COMPRESSOR SUCTION,PPH.....	8.541E+02

COMPRESSOR PARAMETERS

SPEED,RPM.....	5.000E+04
SPECIFIC SPEED.....	7.757E+01
CORRECTED SPEED,RPM.....	4.930E+04
CORRECTED FLOW,PPH.....	7.471E+02
PRESSURE RATIO.....	4.003E+00
ADIABATIC HEAD,FT.....	8.378E+03
ISENTROPIC EFFICIENCY.....	7.530E-01
Z.....	7.923E-01
SHAFT POWER,HP.....	4.799E+00
COOLANT FLOW HEAT ADDITION,BTU/HR....	9.730E+02
COOLANT DISCHARGE TEMPERATURE,DEG.F..	1.801E+02
COMPRESSOR MAP NUMBER.....	6

EVAPORATOR PARAMETERS

TOTAL SURFACE AREA,SQ.FT.....	2.235E+03
BOILING SURFACE AREA,SQ.FT.....	2.235E+03
OVERALL HEAT TRANSFER COEFFICIENT,BTU/HR.SQFT.DEG.F.	4.500E+00
EFFECTIVENESS.....	7.537E-01
AIR FLOW RATE,PPH.....	2.978E+04
AIR FLOW RATE,CFM.....	6.618E+03
AIR INLET TEMP,DEG.F.....	3.550E+01
AIR DISCHARGE TEMP,DEG.F.....	2.835E+01
TOTAL HEAT TRANSFERRED,BTU/HR.....	5.133E+04

CONDENSOR PARAMETERS

TOTAL SURFACE AREA,SQ.FT.....	1.118E+03
OVERALL HEAT TRANSFER COEFFICIENT,BTU/HR.SQFT.DEG.F.	4.500E+00
EFFECTIVENESS.....	7.539E-01
AIR FLOW RATE,PPH.....	1.489E+04
AIR FLOW RATE,SCFM.....	3.309E+03
AIR INLET TEMP,DEG.F.....	6.800E+01
AIR DISCHARGE TEMP,DEG.F.....	8.583E+01
TOTAL HEAT TRANSFERRED,BTU/HR.....	6.398E+04

Fig. 2-9 Cont'd

STEAM SYSTEM

TURBINE STATE POINTS

	1 FIRST STG INLET	2 FIRST STG. DISCHARGE + REHEATER INLET	3 SECOND STG. INLET + REHEATER DISCHG	4* SECOND STG DISCHG	4 REGENERATOR INLET
TEMPERATURE,DEG.F	1.100E+03	7.313E+02	1.100E+03	6.958E+02	6.981E+02
PRESSURE,PSIA	2.134E+02	2.102E+01	2.005E+01	2.052E+00	2.052E+00
ENTHALPY,BTU/LB	1.584E+03	1.402E+03	1.584E+03	1.385E+03	1.386E+03

SYSTEM STATE POINTS

	5 STEAM SIDE REGENERATOR DISCHARGE	7 CONDENSOR DISCHARGE	9 LIQ.SIDE REGENERATOR DISCHARGE
TEMPERATURE,DEG.F	2.253E+02	1.215E+02	3.538E+02
PRESSURE,PSIA	1.765E+00	1.765E+00	-----
ENTHALPY,BTU/LB	1.165E+03	8.950E+01	3.218E+02

FLOW RATES

FIRST STG INLET,PPH.....	5.605E+01
INTER STG LEAKAGE,PPH.....	3.566E+00
SECOND STG INLET,PPH.....	5.266E+01
STEAM SIDE REGEN INLET,PPH.	5.605E+01
DIRECT STEAM INJECTION,PPH.	.0
CONDENSOR DISCHARGE,PPH....	5.605E+01

TURBINE PARAMETERS

	FIRST STAGE	SECOND STAGE
SPEED,RPM.....	5.000E+04	5.000E+04
SPECIFIC SPEED.....	3.299E+00	1.018E+01
CORRECTED SPEED,RPM...	5.000E+04	5.000E+04
FLOW,PPH.....	5.605E+01	5.266E+01
PRESSURE RATIO.....	1.015E+01	9.768E+00
ISENTROPIC EFFICIENCY.	5.807E-01	6.439E-01
SHAFT POWER,HP.....	3.992E+00	4.110E+00
TURBINE MAP NUMBER....	.0	.0

REGENERATOR PARAMETERS

TOTAL SURFACE AREA,SQFT.....	8.400E+00
OVERALL HEAT TRANSFER COEFFICIENT,BTU/HR.SQFT.DEG.F.	8.000E+00
EFFECTIVENESS.....	8.200E-01
HEAT TRANSFERRED,BTU/HR.....	1.302E+04

CONDENSOR PARAMETERS

TOTAL SURFACE AREA,SQ.FT.....	4.977E+02
OVERALL HEAT TRANSFER COEFFICIENTS,BTU/HR.SQFT.DEG.F	4.500E+00
EFFECTIVENESS.....	4.643E-01
AIR FLOW RATE,PPH.....	1.489E+04
AIR FLOW RATE,SCFM.....	3.309E+03
AIR INLET TEMP,DEG.F.....	8.583E+01
AIR DISCHARGE TEMP,DEG.F.....	1.024E+02
STEAM HEAT TRANSFERRED,BTU/HR.....	5.945E+04

Fig. 2-9 Cont'd

MECHANICAL TECHNOLOGY INCORPORATED

COMBINED SYSTEM - COOLING

POWER

COMPRESSOR SHAFT,HP... 8.219E+00
PARASITICS,HP..... 3.460E+00
TURBINE,HP.....1.168E+01

SYSTEM CONFIGURATIONS..... 2

PERFORMANCE

HEAT ADDITION TO STEAM GENERATOR,BTU/HR... 1.155E+05
COOLING EFFECT,BTU/HR..... 9.003E+04
STEAM GENERATOR * BURNER EFFICIENCY..... 8.000E-01
TOTAL SYSTEM ENERGY INPUT..... 1.444E+05
OVERALL COOLING COP..... 6.234E-01
STEAM CYCLE THERMAL EFFICIENCY.....2.573E-01

Fig. 2-10 Simulation Results at ARI Nominal Cooling Specified Point (95°F ambient)

MECHANICAL TECHNOLOGY INCORPORATED

STEAM SYSTEM

TURBINE STATE POINTS

	1 FIRST STG INLET	2 FIRST STG. DISCHARGE + REHEATER INLET	3 SECOND STG. INLET + REHEATER DISCHG	4* SECOND STG DISCHG	4 REGENERATOR INLET
TEMPERATURE,DEG.F	1.100E+03	7.288E+02	1.100E+03	6.833E+02	6.862E+02
PRESSURE,PSIA	3.021E+02	2.995E+01	2.837E+01	2.747E+00	2.747E+00
ENTHALPY,BTU/LB	1.554E+03	1.401E+03	1.584E+03	1.379E+03	1.380E+03

SYSTEM STATE POINTS

	5 STEAM SIDE REGENERATOR DISCHARGE	7 CONDENSOR DISCHARGE	9 LIQ.SIDE REGENERATOR DISCHARGE
TEMPERATURE,DEG.F	2.805E+02	1.313E+02	3.307E+02
PRESSURE,PSIA	2.302E+00	2.302E+00	-----
ENTHALPY,BTU/LB	1.191E+03	9.931E+01	2.987E+02

FLOW RATES

FIRST STG INLET,PPH..... 7.935E+01
INTER STG LEAKAGE,PPH..... 5.085E+00
SECOND STG INLET,PPH..... 7.452E+01

STEAM SIDE REGEN INLET,PPH. 7.935E+01
DIRECT STEAM INJECTION,PPH. .0
CONDENSOR DISCHARGE,PPH.... 7.935E+01

TURBINE PARAMETERS

	FIRST STAGE	SECOND STAGE
SPEED,RPM.....	5.100E+04	5.100E+04
SPECIFIC SPEED.....	3.350E+00	1.048E+01
CORRECTED SPEED,RPM...	5.100E+04	5.100E+04
FLOW,PPH.....	7.935E+01	7.452E+01
PRESSURE RATIO.....	1.009E+01	1.033E+01
ISENTROPIC EFFICIENCY.	5.858E-01	6.518E-01
SHAFT POWER,HP.....	5.689E+00	5.997E+00
TURBINE MAP NUMBER....	.0	.0

REGENERATOR PARAMETERS

TOTAL SURFACE AREA,SQFT..... 8.400E+00
OVERALL HEAT TRANSFER COEFFICIENT,BTU/HR.SQFT.DEG.F 8.000E+00
EFFECTIVENESS..... 7.311E-01
HEAT TRANSFERRED,BTU/HR..... 1.582E+04

CONDENSOR PARAMETERS

TOTAL SURFACE AREA,SQ.FT..... 1.329E+03
OVERALL HEAT TRANSFER COEFFICIENT,BTU/HR.SQFT.DEG.F 4.540E+00
EFFECTIVENESS..... 5.615E-01
AIR FLOW RATE,PPH..... 3.037E+04
AIR FLOW RATE,SCFM..... 6.750E+03
AIR INLET TEMP,DEG.F..... 1.103E+02
AIR DISCHARGE TEMP,DEG.F..... 1.221E+02
STEAM HEAT TRANSFERRED,BTU/HR..... 8.631E+04

Fig. 2-10 Cont'd

MECHANICAL TECHNOLOGY INCORPORATED

REFRIGERANT SYSTEM (R-11)

	1 COMPRESSOR SUCTION	2 COMPRESSOR DISCHARGE + CONDENSOR INLET	4 CONDENSOR DISCHARGE	5 EVAPORATOR INLET	7 EVAPORATOR DISCHARGE
TEMPERATURE,DEG.F	5.789E+01	1.663E+02	1.154E+02	4.720E+01	4.720E+01
PRESSURE,PSIA	8.259E+00	3.054E+01	3.054E+01	8.259E+00	8.259E+00
ENTHALPY,BTU/LB	9.503E+01	1.133E+02	3.189E+01	3.189E+01	9.762E+01

FLOW RATES

EVAPORATOR DISCHARGE,PPH... 1.370E+03
SEAL COOLANT,PPH..... 1.000E+02
COMPRESSOR SUCTION,PPH..... 1.470E+03

COMPRESSOR PARAMETERS

SPEED,RPM..... 5.100E+04
SPECIFIC SPEED..... 8.551E+01
CORRECTED SPEED,RPM..... 4.961E+04
CORRECTED FLOW,PPH..... 7.959E+02
PRESSURE RATIO..... 3.698E+00
ADIABATIC HEAD,FT..... 7.950E+03
ISENTROPIC EFFICIENCY..... 7.180E-01
Z..... 3.451E-01
SHAFT POWER,HP..... 8.219E+00
COOLANT FLOW HEAT ADDITION,BTU/HR.... 1.017E+03
COOLANT DISCHARGE TEMPERATURE,DEG.F.. 2.049E+02
COMPRESSOR MAP NUMBER..... 6

EVAPORATOR PARAMETERS

TOTAL SURFACE AREA,SQ.FT..... 1.118E+03
BOILING SURFACE AREA,SQ.FT..... 1.118E+03
OVERALL HEAT TRANSFER COEFFICIENT,BTU/HR.SQFT.DEG.F. 4.540E+00
EFFECTIVENESS..... 7.501E-01
AIR FLOW RATE,PPH..... 1.519E+04
AIR FLOW RATE,CFM..... 3.375E+03
AIR INLET TEMP,DEG.F..... 8.000E+01
AIR DISCHARGE TEMP,DEG.F..... 5.540E+01
TOTAL HEAT TRANSFERRED,BTU/HR..... 9.003E+04

CONDENSOR PARAMETERS

TOTAL SURFACE AREA,SQ.FT..... 2.235E+03
OVERALL HEAT TRANSFER COEFFICIENT,BTU/HR.SQFT.DEG.F. 4.540E+00
EFFECTIVENESS..... 7.500E-01
AIR FLOW RATE,PPH..... 3.037E+04
AIR FLOW RATE,SCFM..... 6.750E+03
AIR INLET TEMP,DEG.F..... 9.500E+01
AIR DISCHARGE TEMP,DEG.F..... 1.103E+02
TOTAL HEAT TRANSFERRED,BTU/HR..... 1.121E+05

Fig. 2-10 Cont'd

MECHANICAL TECHNOLOGY INCORPORATED

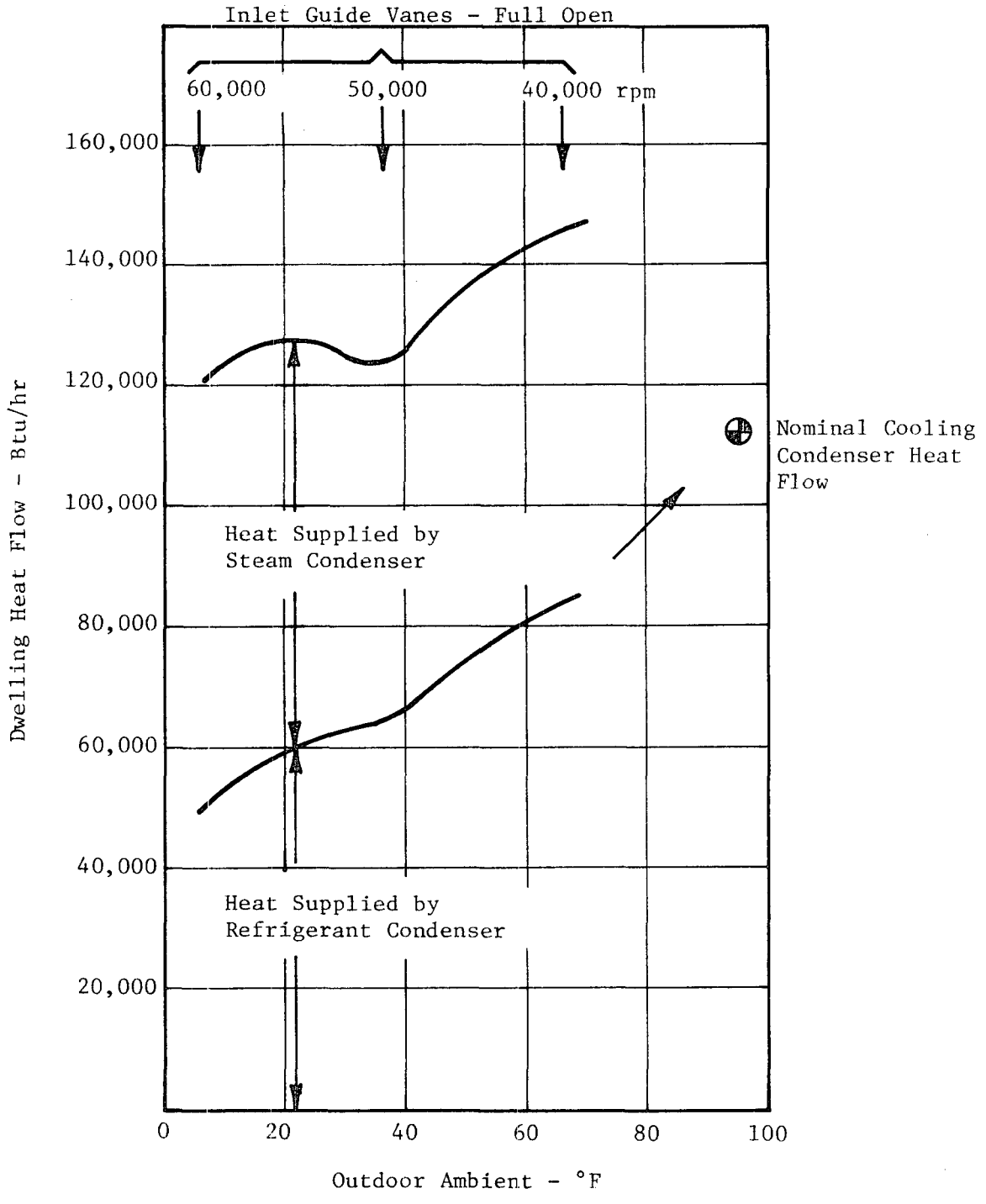

792668

Fig. 2-11 Heat Flow Versus Ambient Temperature

MECHANICAL TECHNOLOGY INCORPORATED

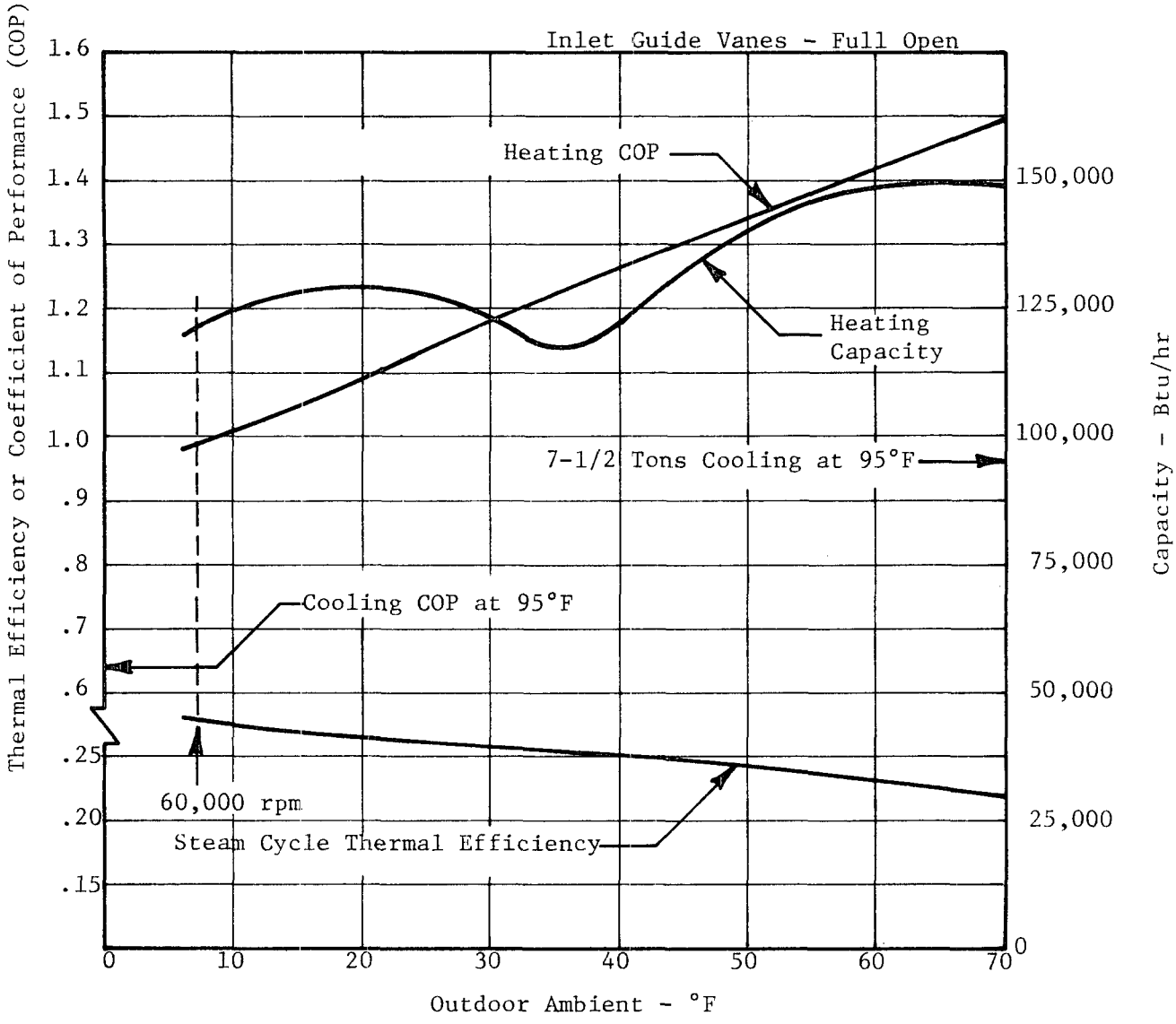

Fig. 2-12 System Performance versus Ambient Temperature

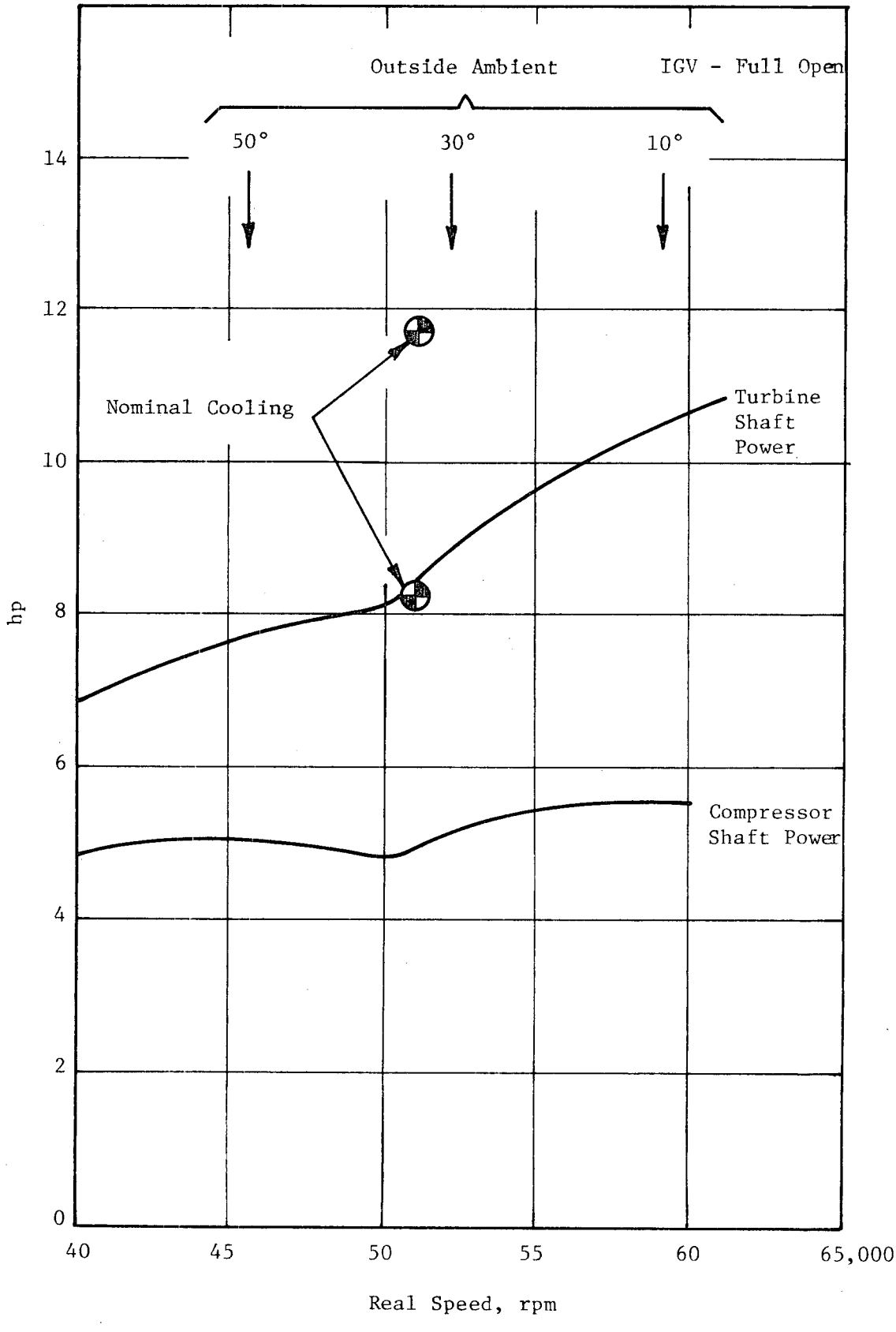

Fig. 2-13 Turbine/Compressor Power

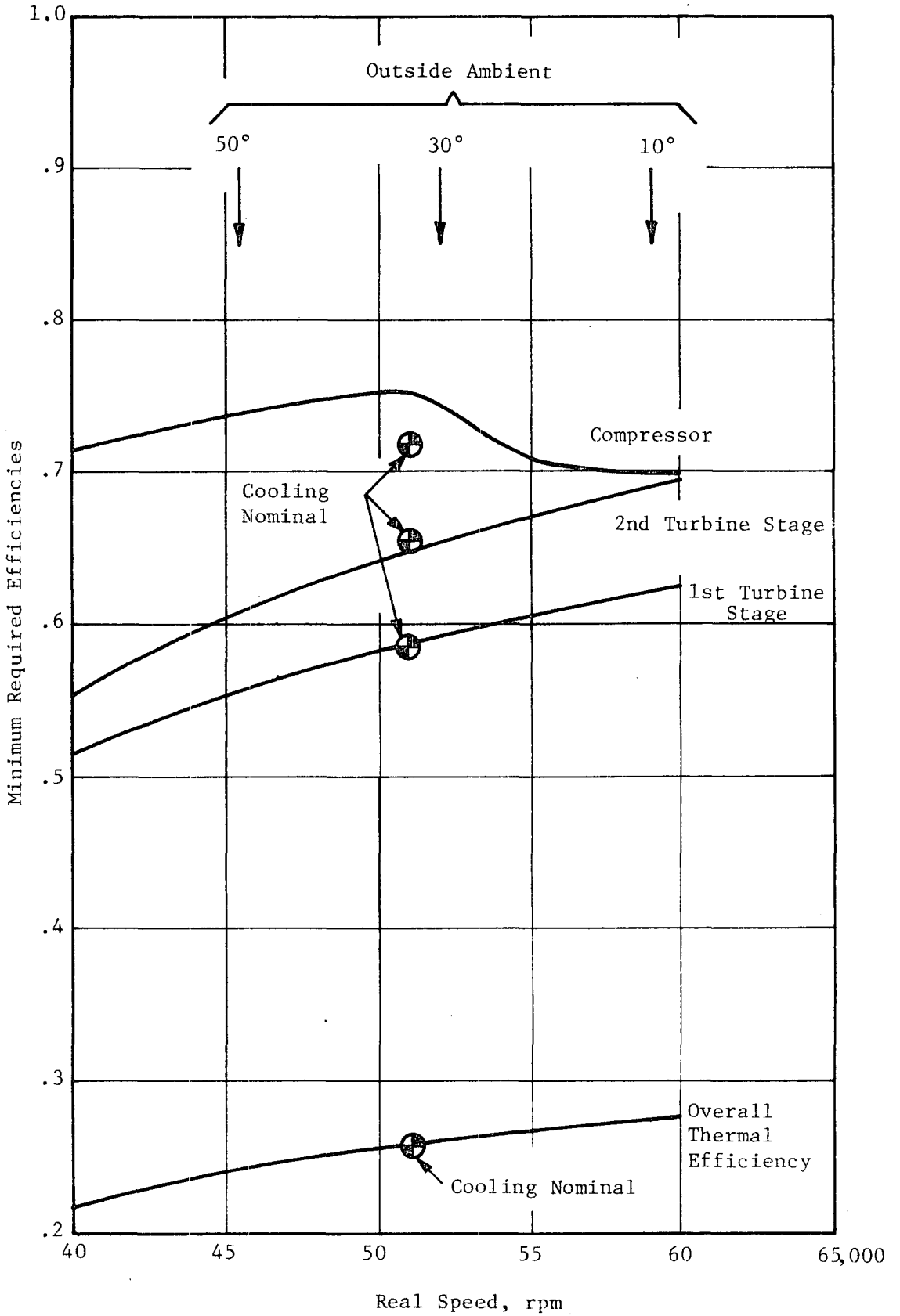

Fig. 2-14 Required Component Efficiencies

2.4 Decision Trade-Offs

Two major optimizations were carried out concurrently with the system analysis efforts. These optimizations concerned air flow quantities through the outdoor refrigerant and steam condenser cores, and selection of operating speed for the rotating unit. The air flow optimization was a relatively straightforward trade-off between air-moving power and refrigerant compressor power (as effected by refrigerant evaporator and condensing temperatures). The rotating unit speed optimization considered compressor and turbine efficiencies, parasitic losses, seal losses, and the proximity of operating speed to the third critical speed of the unit. The rotating unit was parameterized by 10 key dimensions describing geometry changes as affected by speed.

Figure 2-15 shows the general relationship of the above mentioned variables to design speed. The combined efficiency of the turbine and compressor, system parasitic losses (primarily bearings and windage) and minimization of bearing loads all favored high-speed operation. However, mechanical limitations were encountered in the mechanical face seal as rubbing velocities increased with operating speed. Additionally, to insure rotor stability the maximum operating speed was constrained to not exceed 80% of the third (bending) critical speed. The latter two constraints established a nominal speed of 50,000 rpm as the best design compromise with minimum and maximum speeds of 40,000 and 60,000 rpm for hot and cold day operation. With respect to Figure 2-15, the selected operating speed range approximately straddled the peak compressor efficiency point.

Figure 2-16 shows key dimensional variations as design point speed of the unit varies as used in the trade-off analysis. These parameters indicated the starting point for the detailed component design. For example, the parameters in Figure 2-16 show that the compressor specific speed (N_s) was 90 at the selected nominal 50,000 rpm and the compressor/diffuser relative Mach number (M_2) was about 0.88. These parameters are reasonable parameters for a compressor. The actual parameters resulting from the detailed design were not very different.

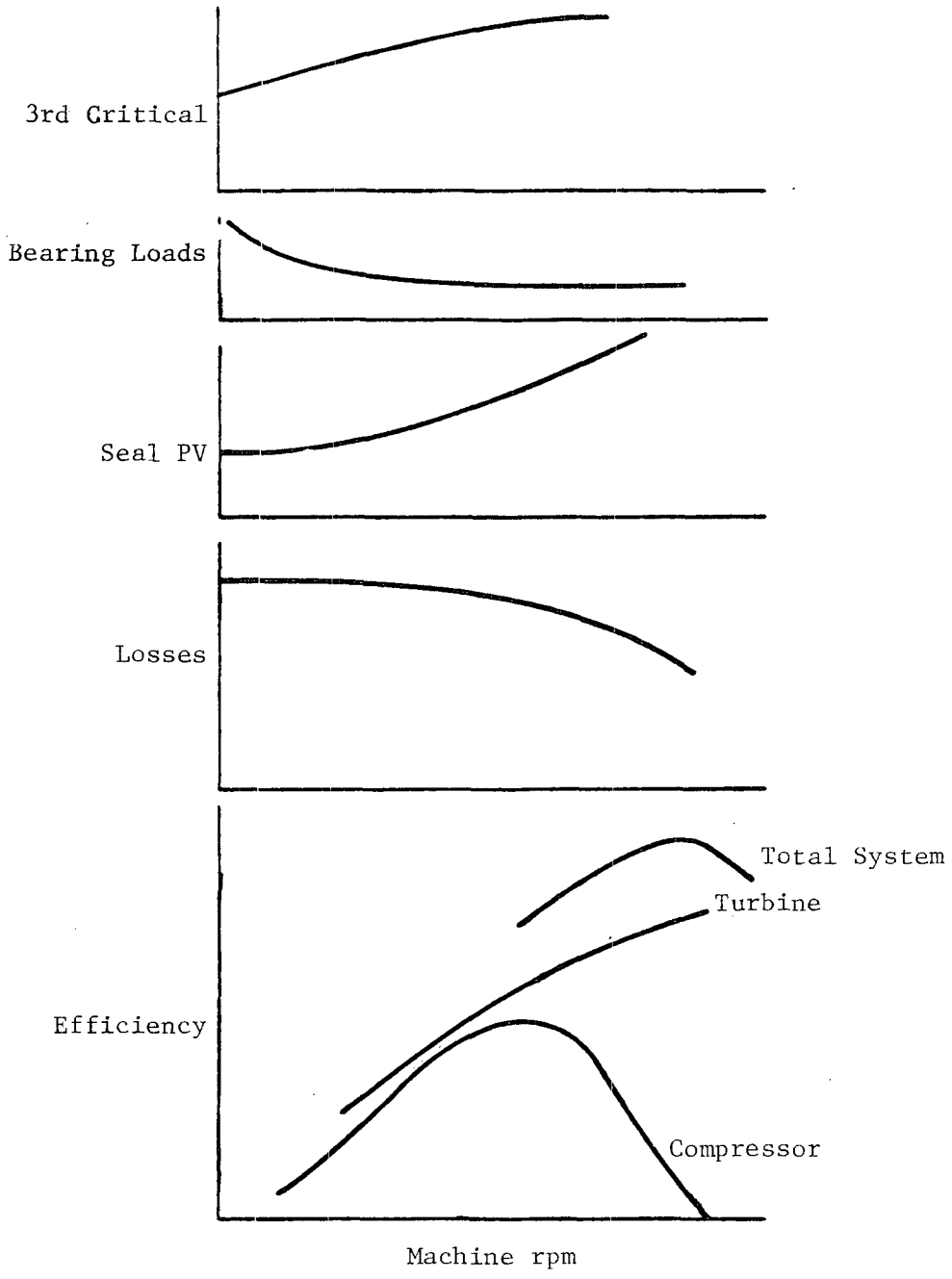

792943

Fig. 2-15 Speed Trade-Offs

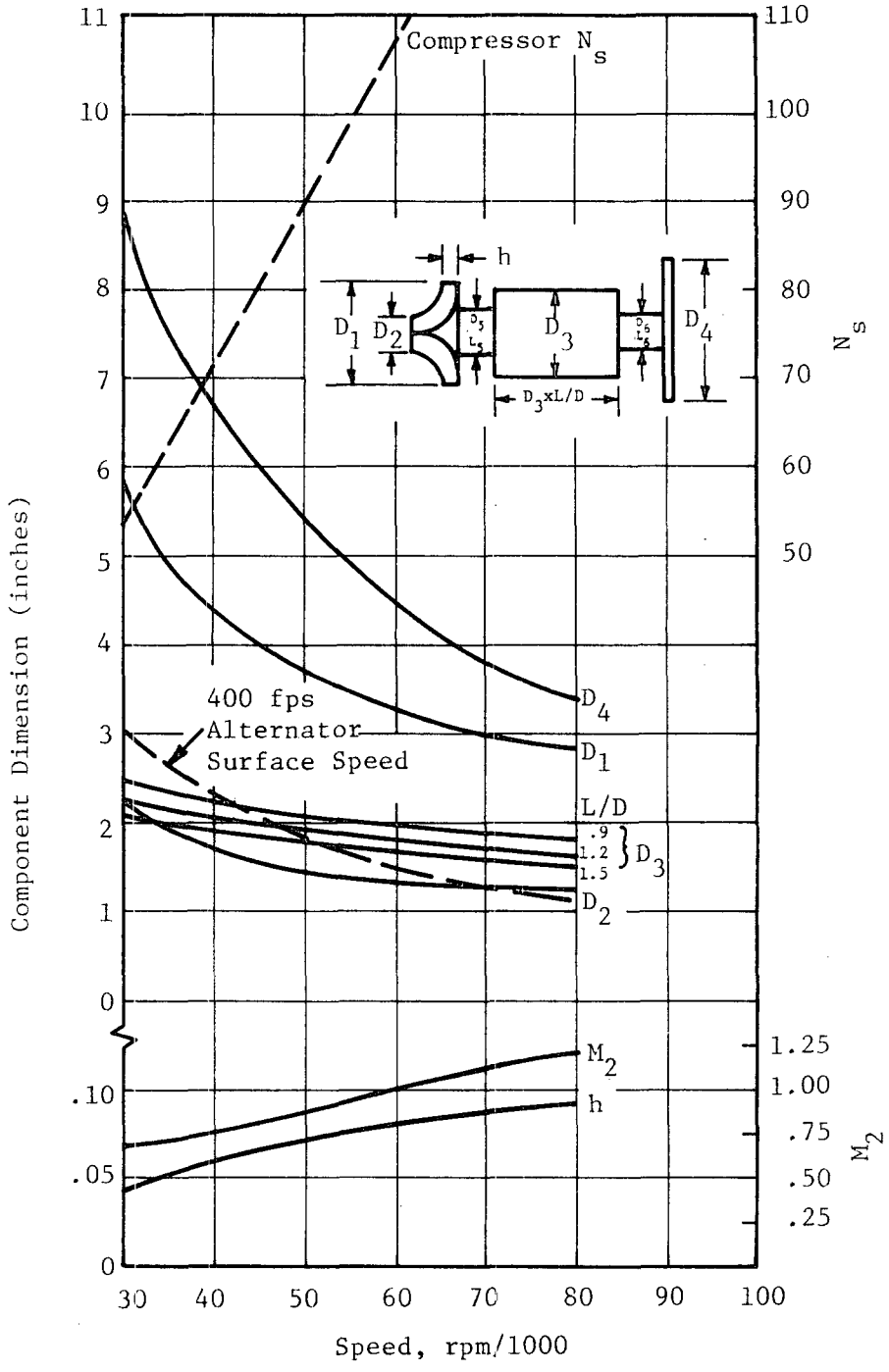

Fig. 2-16 Rotating Unit Parameters for System Design Trade-Off Analysis

792946

MECHANICAL TECHNOLOGY INCORPORATED

Considering the mechanical attachment contemplated for the alternator rotor filler pieces (dimension D_3), previous experience indicated that a maximum alternator surface speed of 400 fps should not be exceeded. This constraint fixed the alternator rotor L/D in the range of 1.2 to 1.5 - which is a reasonable value from the standpoint of electrical losses.

The dimensions of Figure 2-16 were also employed in determination of the rotating group weights and stiffnesses for the parametric critical speed calculations. As component design progressed, the rotor dynamics were continuously reevaluated. Material selection and bearing characteristics were altered as necessary.

2.5 Rotating Unit Design Summary

The principal components comprising the rotating unit were the turbine, compressor, alternator, bearings and seal. The turbine was an axial flow reentry expander. Superheated steam was provided at both the first and second entry at 1100°F at nominal flow rates of about 80 pph at design cooling service operation. Each stage of expansion operated at a 10/1 pressure ratio; therefore, identical velocity diagrams existed for each expansion. Maximum turbine (and rotating unit) speed was 60,000 rpm, occurring for both maximum design heating and cooling operation. The peak total to static turbine stage efficiency (for the low pressure expansion) was about 70% at maximum design speed. The refrigerant compressor was a single-stage shrouded centrifugal with fixed geometry. The refrigerant employed was R-11 and the design point flow rate at 50,000 rpm was 1450 pph at 47°F evaporator temperature. The compressor pressure ratio varies from 2 to 7 over the range of operating conditions for which the unit is expected to function. Over the range, compressor design efficiency is approximately at 72%.

The alternator was an inductor-homopolar machine with a maximum design output of 3170 watts at 60,000 rpm. The air-moving and fluid-pumping requirements of the design heating service consumed almost all of this power. The alternator bench test results indicated a net design efficiency of 93%, slightly above design specifications.

Figure 2-17 shows a schematic of the major components of the rotating unit and the flow of coolant and cycle fluids within the rotating unit. Bearing and alternator rotor losses were dissipated by about 100 pph of Freon bleed flow which was recirculated to and slightly superheated the compressor suction gas. The primary steam/Freon face seal lubrication and cooling was provided by recirculated feed water. Figure 2-18 presents an assembly drawing of the rotating unit.

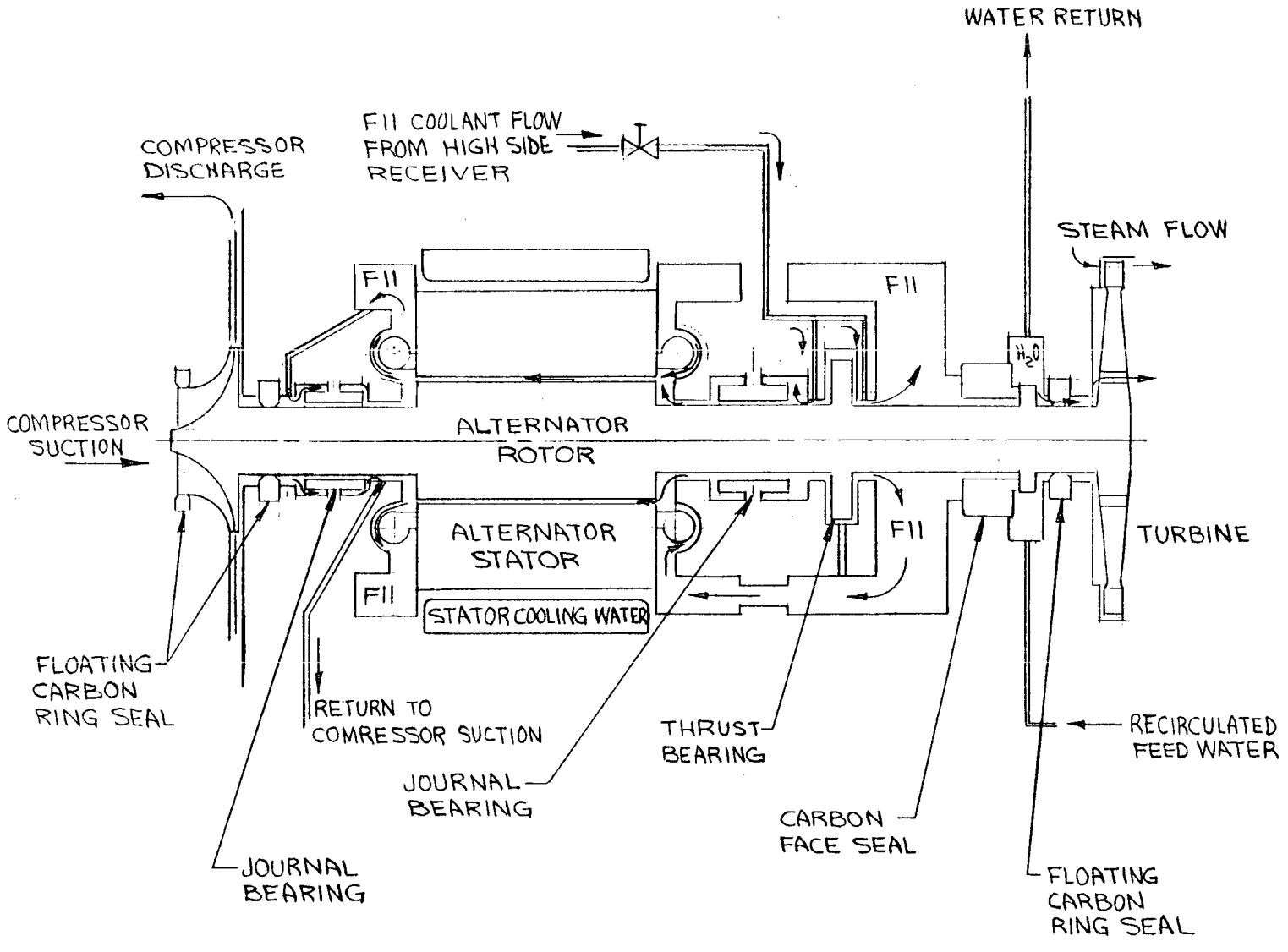

Fig. 2-17 Rotating Unit Flow Schematic

792672

MECHANICAL TECHNOLOGY INCORPORATED

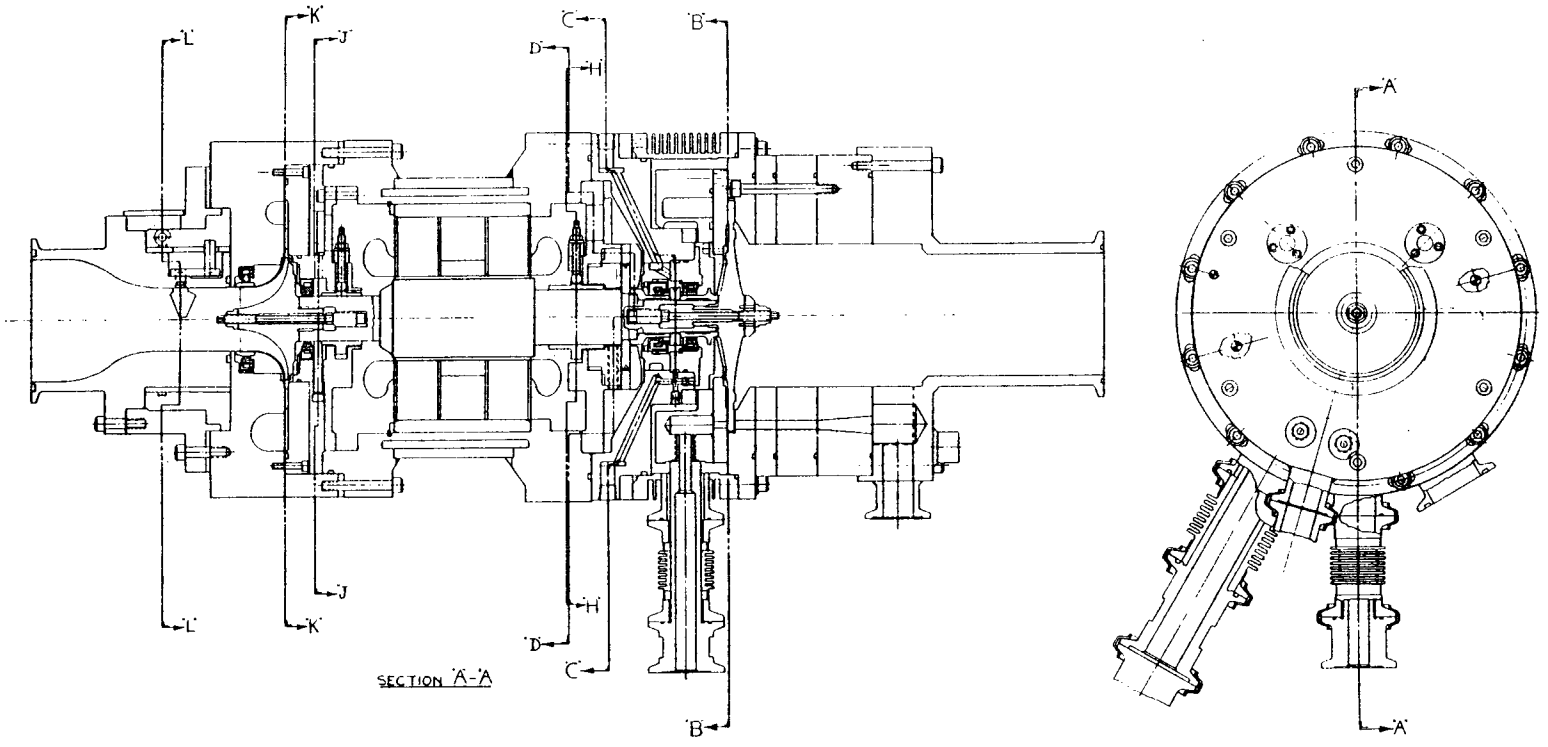

Fig. 2-18 Rotating Unit Assembly

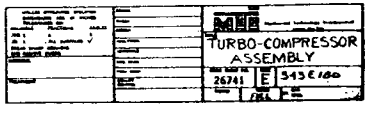

3.0 COMPONENT DESIGN SUMMARIES

A major portion of the technical effort consisted of the design, fabrication, and testing of the components of the HSPF heat pump. The major system components for which MTI was responsible were the high-speed rotating components listed in Table 2-1, on page 2-12, and shown in Figures 3-1 through 3-3.

The steam generator was designed, fabricated and tested by Scientific Energy Systems (SES). The SES design was based upon a compact Rankine system evaporator developed by SES for the government's automotive Rankine program. The specifications for the generator in terms of temperature, pressure, and flow rates were provided by MTI. The SES steam generator is shown in Figure 3-4. A summary of the MTI design effort for each component is presented here. Additional information is available in Attachments A through E.

3.1 Turbine Design Summary

The concept initially preferred for the turbine was a radial-outflow, single-rotation, Ljungstrom type turbine of six or seven stages. While this design seemed to give promise of good efficiency, some severe mechanical design and stress problems appeared and the potential cost was judged to be prohibitive. Further, the only potentially qualified subcontractor for a radial-outflow turbine, Energy Technology, Inc. (ETI), declined to participate in the HSPF program. ETI was the only potential source for this particular turbine. For these and other reasons as discussed further, consideration of use of a multiple-stage, radial-outflow turbine was abandoned.

With the steam conditions required for good cycle efficiency, the specific speed and diameter range were not suitable for a simple, single-stage, radial-inflow turbine. Therefore, only axial-flow turbines were finally considered. For cost reasons, the choice was narrowed to either a Curtis-type wheel or some form of reentry turbine. The reentry turbine can be an axial-flow turbine, a "Terry" type turbine, or a "drag turbine". The latter is the equivalent of the so-called regenerative type pump. The latter two did not promise a sufficiently high level of efficiency, and so were not considered further.

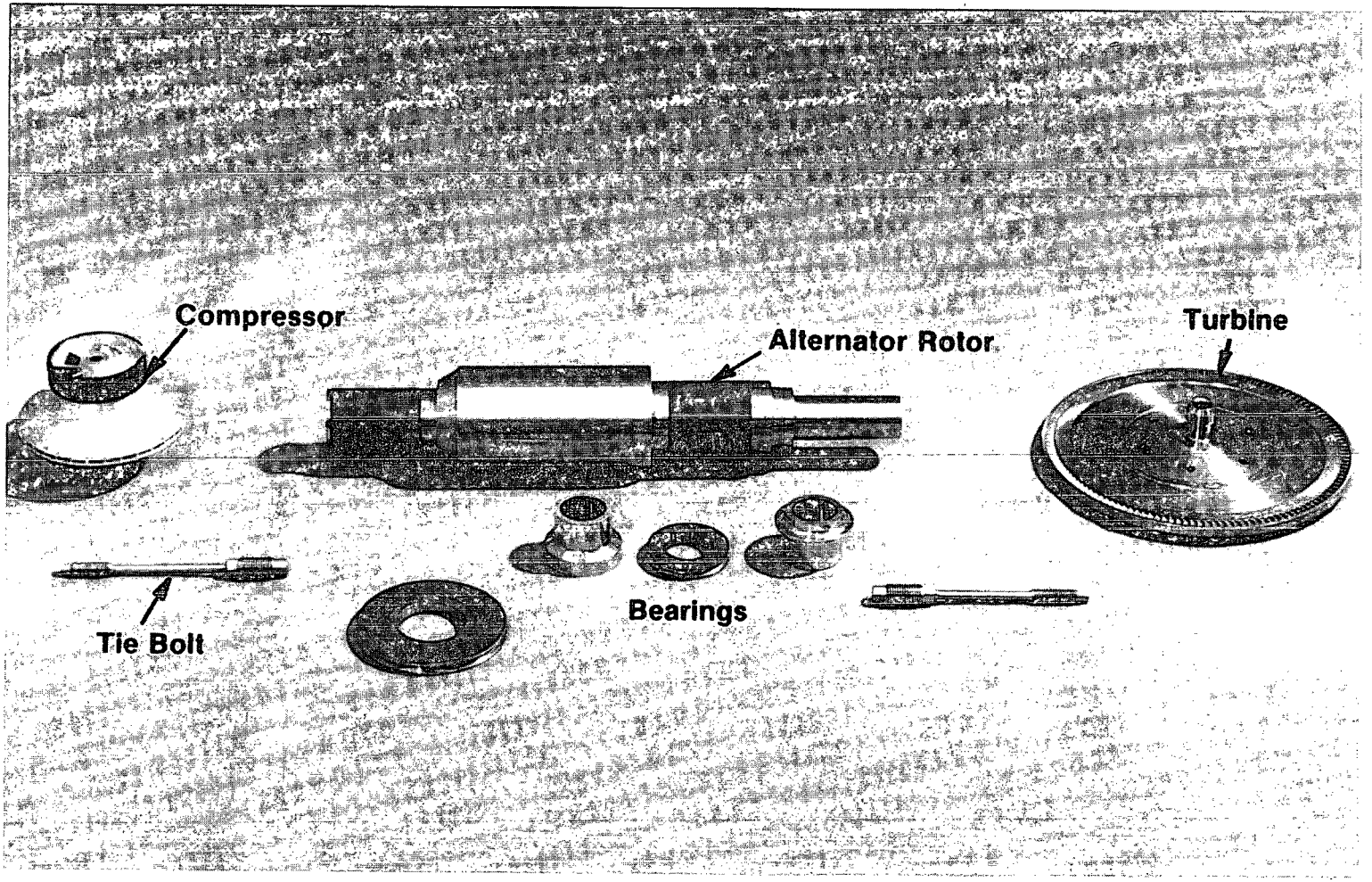

Fig. 3-1 Rotating Unit Components

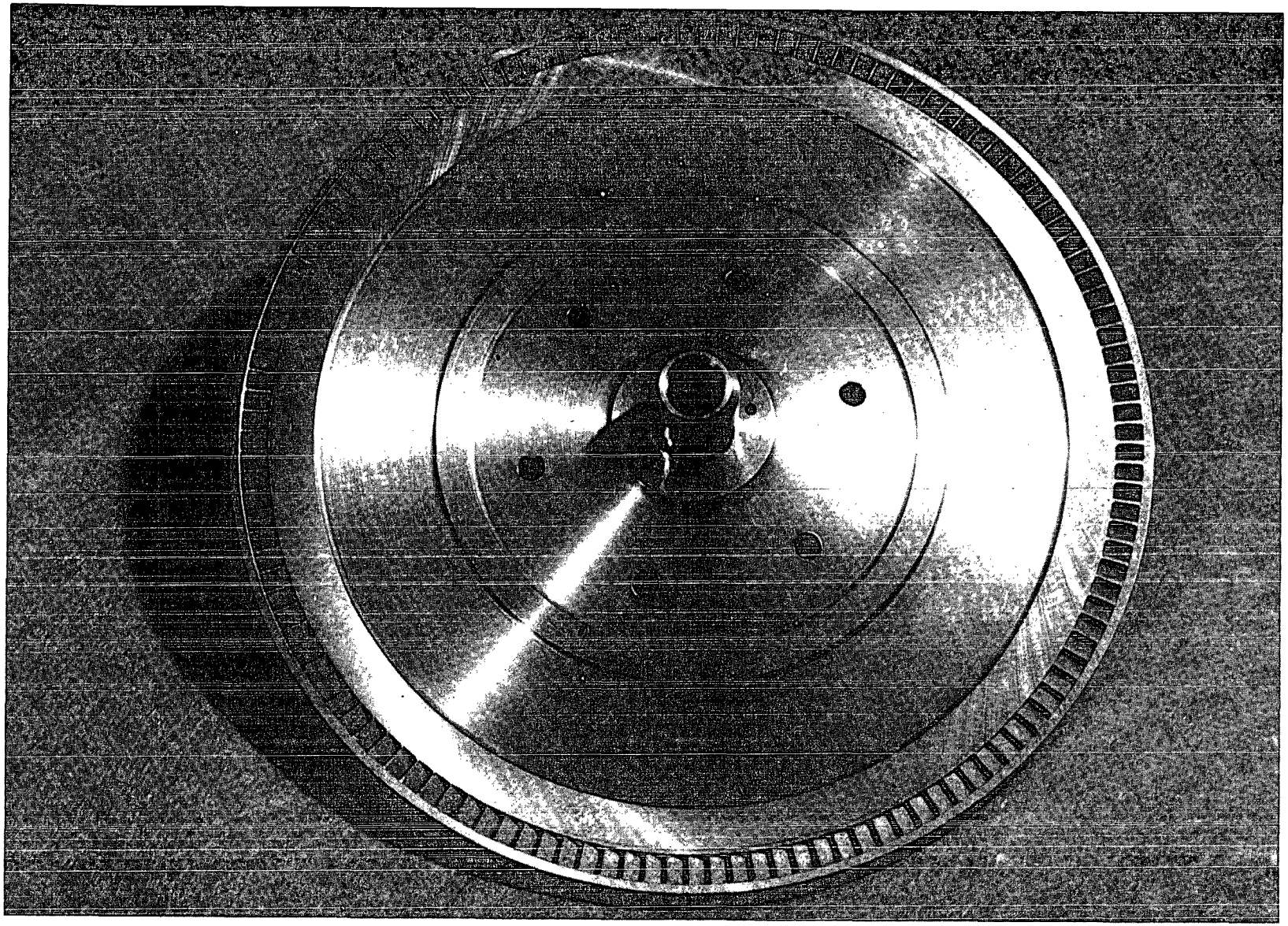

Fig. 3-2 Rotating Unit Component - Turbine

MTI-17863

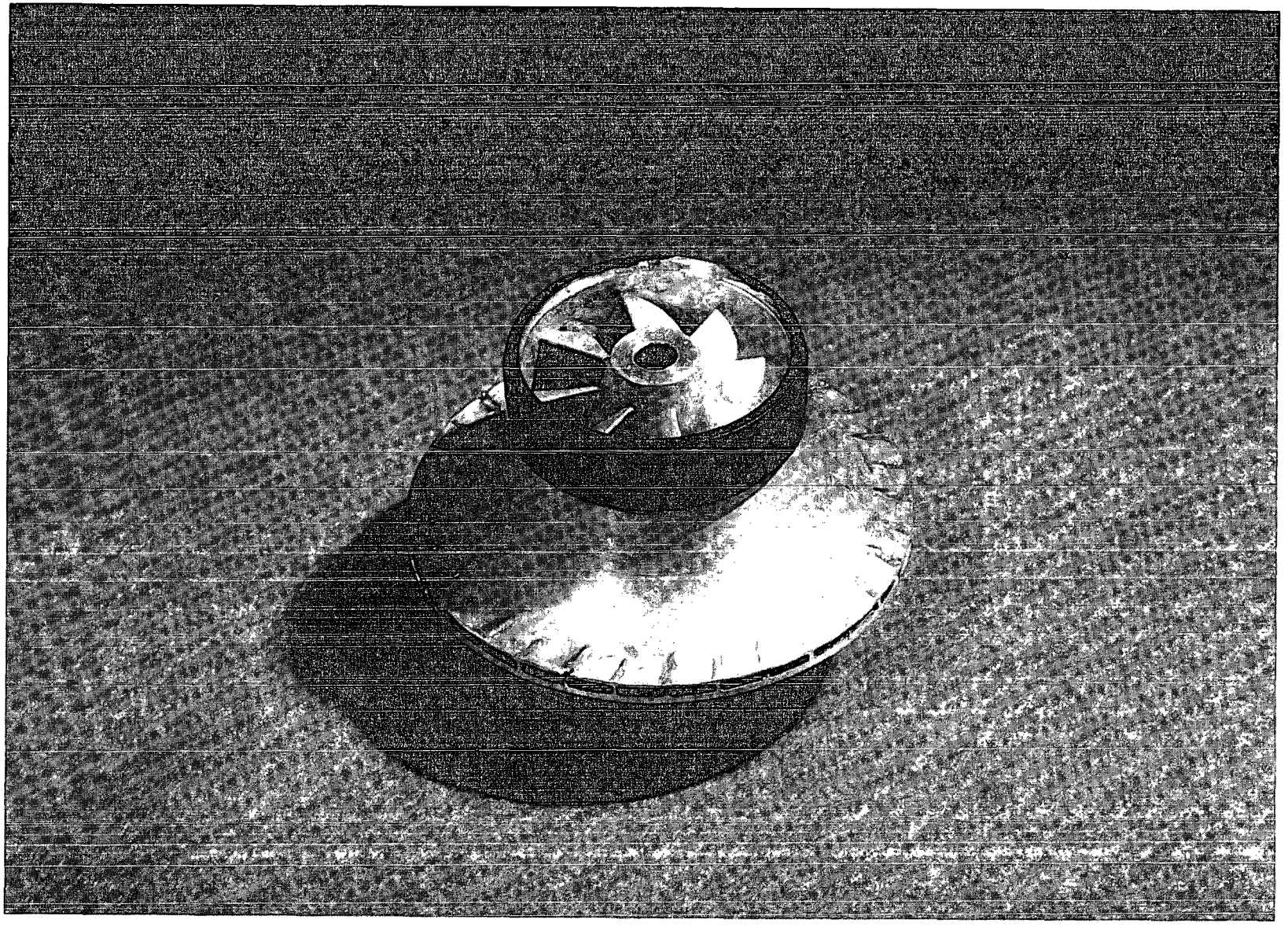

Fig. 3-3 Rotating Unit Component - Compressor

-18445

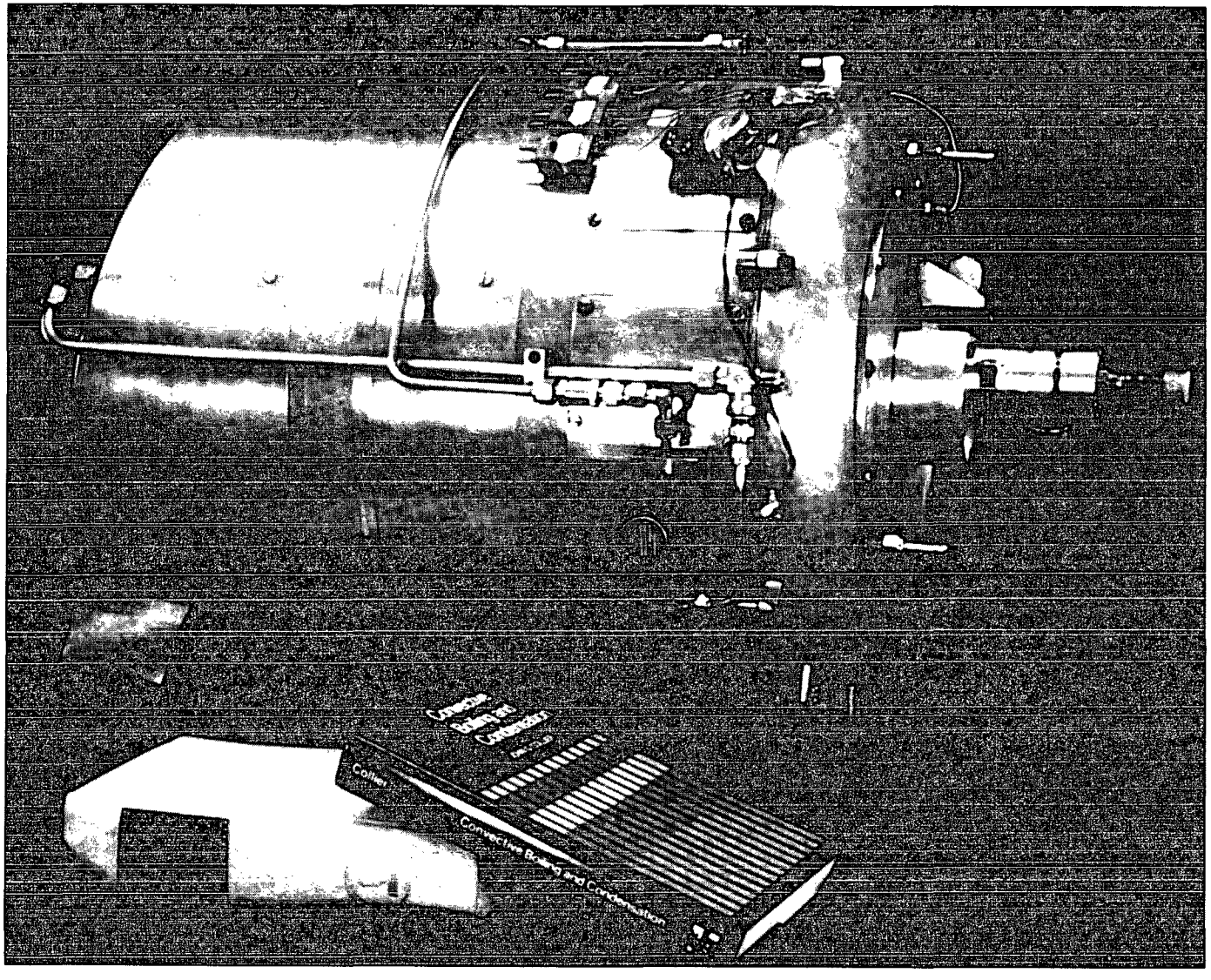

Fig. 3-4 SES Steam Generator Developed for the Environmental Protection Agency

A two-row Curtis stage would probably have given an acceptable level of performance. However, consideration of the simpler single-row rotor of the reentry turbine, coupled with the concept of using reheat between the expansions of the reentry design, led to the decision to concentrate on the axial-flow, reentry design. This decision was based on the fact that with reheat and reentry, a 10 to 15% improvement in overall cycle efficiency could be obtained. This overall cycle efficiency improvement, combined with a simpler and less costly turbine design, was an attractive alternative.

The reentry design was studied in configurations with and without reheat using the methods presented by Hans D. Lenhardt and David H. Silvery in their paper "Analysis of Partial Admission Axial Impulse Turbines". These methods and data enabled the steam conditions, including the reheat pressure, and the speed, diameter, and bucket configuration of the turbine to be selected for optimum performance.

The design was then reviewed by Mr. Andre Stromquist, a consultant to CNG, who suggested some detail changes that were incorporated into the design. Mr. Stromquist also calculated the efficiencies of the two expansions, using his own methods, which confirmed the values predicted by MTI's design process.

Final detail design was based on rectangular nozzle passages, and a bucket section which provided a slightly diverging passage to accommodate the supersonic flow conditions.

For component test purposes, the exhaust passage from the first expansion and the diffuser from the second expansion were designed with a flexible geometry in order to enable the optimum configuration to be determined by test. The optimum geometry would then be incorporated in the final turbine configuration.

The final turbine wheel design is shown in Figure 3-2. The design details are shown in Figure 3-5. As noted, this turbine wheel is of a single-row design. The initial expansion was designed to be from 3000 psia and 1100°F

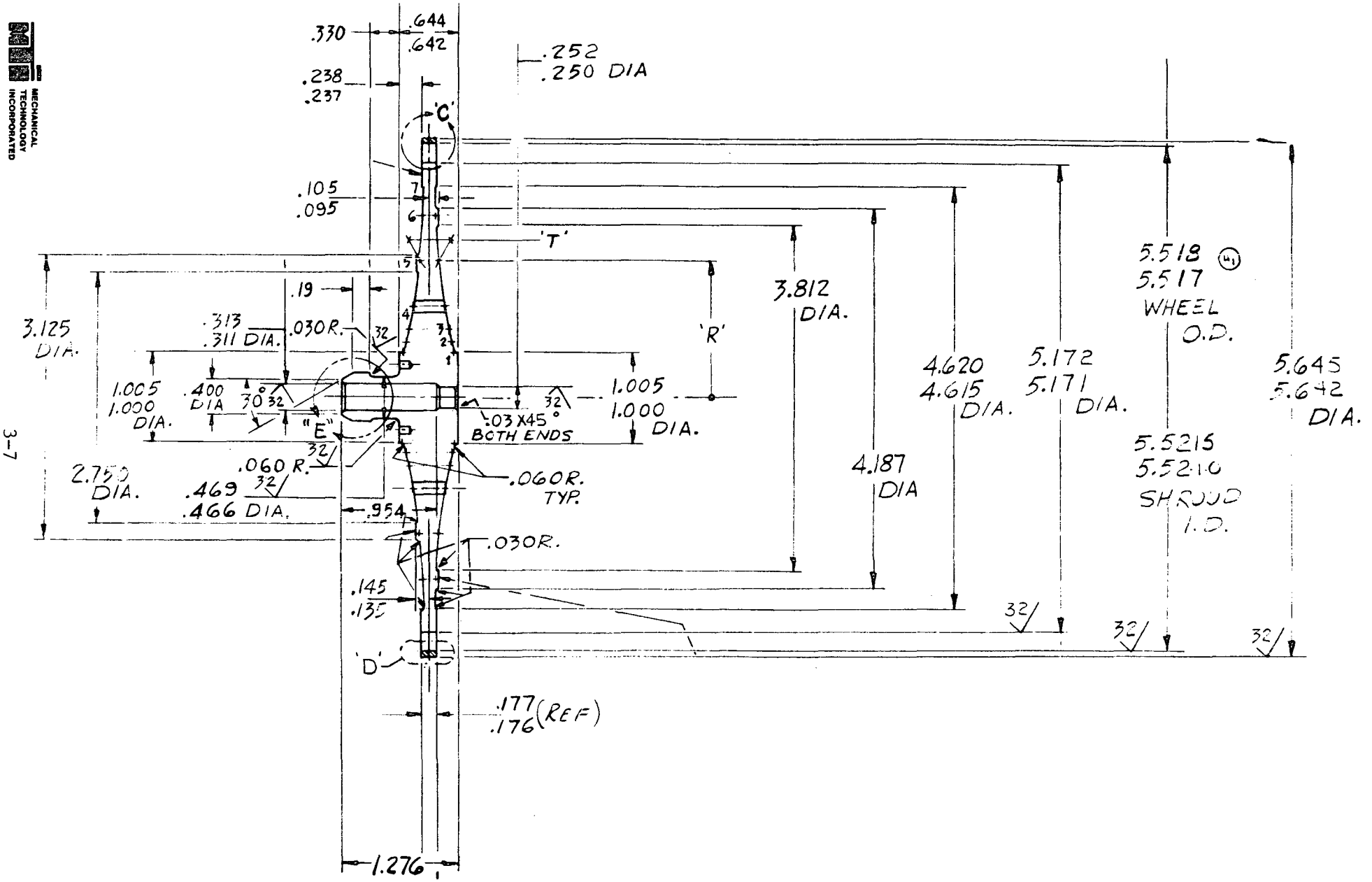

Fig. 3-5 Turbine Wheel Design Detail

MECHANICAL TECHNOLOGY INCORPORATED

793120

to 30 psia and requiring a partial entry, using about 8 degrees arc of the turbine wheel. The exhaust from this expansion is collected and returned to the generator to be reheated. The second expansion was designed to be from 30 psia and 1100°F to 3 psia and requiring about 80 degrees arc of the turbine wheel. The exhaust of this expansion is collected and passed through a regenerator. This steam cycle is illustrated in Figure 3-6.

After the design and fabrication of the steam turbine, the turbine was tested to determine its performance. The experimental results were in very good agreement with the computed performance. Figure 3-7 presents the design projections and some actual data points.

The clearances between the fixed nozzles and the turbine wheel and the first stage collector were important to the overall performance of the turbines. Setting the clearances at other than design conditions resulted in leakage losses beyond those allowed for in the design. As noted earlier, the initial proof-of-concept system tests were conducted with the fixed portions of the turbine assembly located at larger than design clearances until the thermal and mechanical deflection estimates were verified.

The design report for the steam turbine is presented in Attachment A.

3.2 Regenerator

The regenerator in a steam-Rankine prime mover handled a small portion of the thermal energy budget. In this system between 8 and 13% of the heat input to the steam evaporator was handled by the regenerator. However, this energy transfer had a significant impact upon the efficiency of the cycle. The regenerator should have transferred the energy from the turbine exhaust to the evaporator feedwater with a high effectiveness and with a low pressure drop. The MTI designed regenerator shown in Figure 3-8 accomplished these functions.

3.3 Refrigerant Compressor

A centrifugal compressor was designed to provide 7-1/2 tons of cooling capacity at the standard rating conditions with R-11. The basic design provided for a shrouded wheel as shown in Figure 3-3.

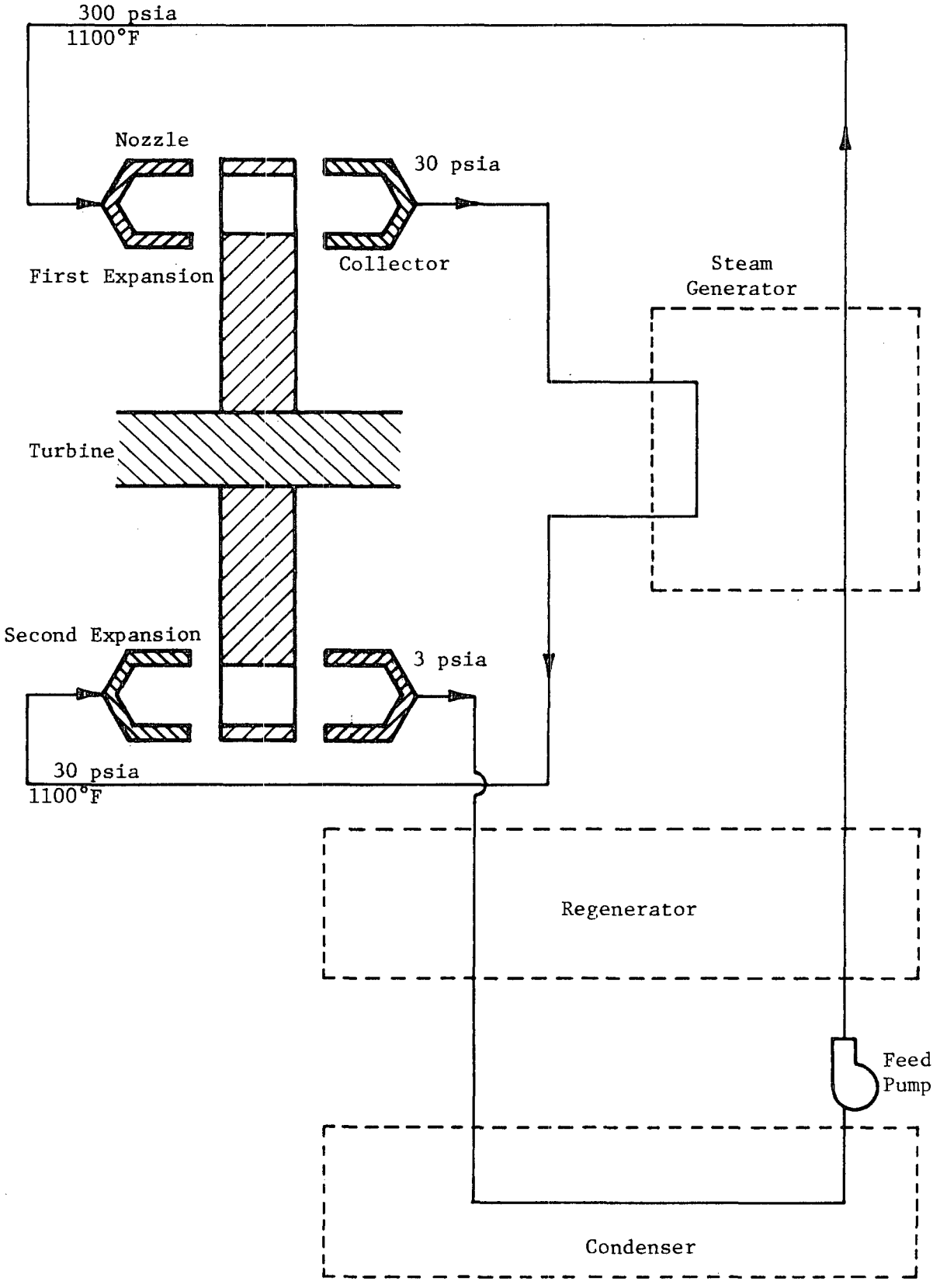

Fig. 3-6 Simplified Steam Cycle Schematic Showing Reheat Reentry and Regeneration

793445

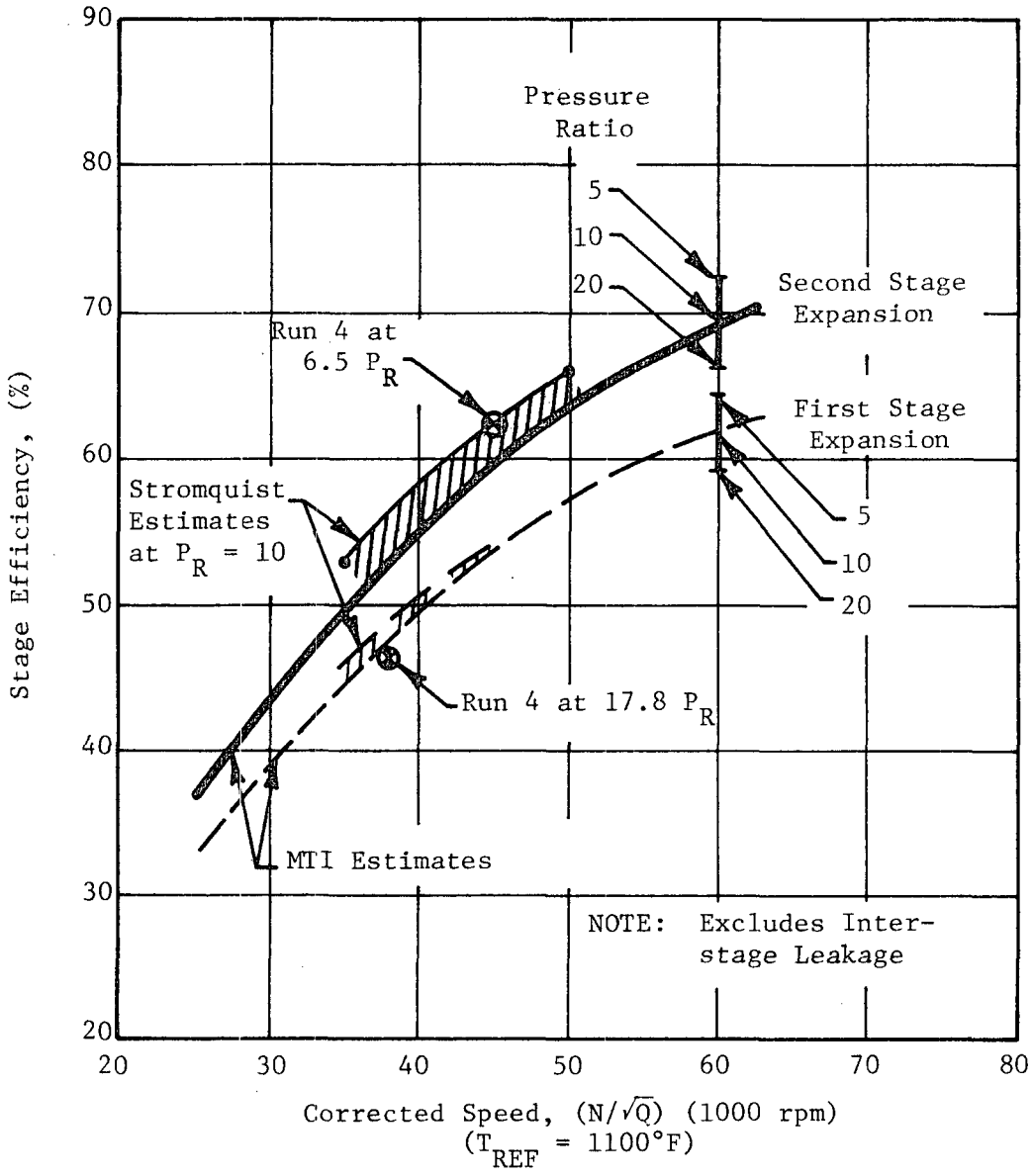

Fig. 3-7 Projected and Experimental Turbine Performance

793442

MECHANICAL TECHNOLOGY INCORPORATED

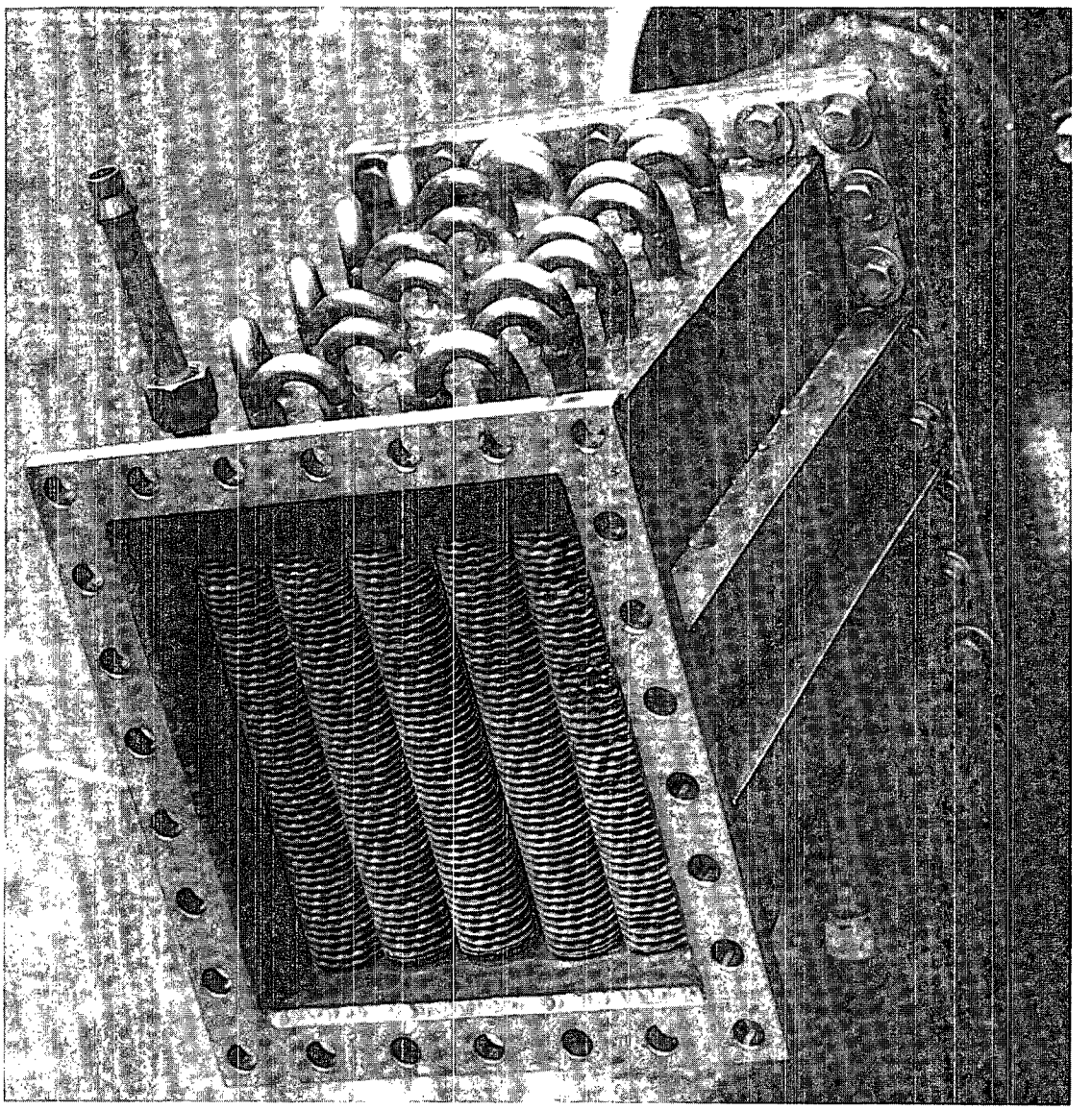

Fig. 3-8 Regenerator Core

The design process started with the capacity design specifications along with a speed range. A preliminary sizing and efficiency estimate was made using the similarity techniques of Balje. The detail blading, passage, and shroud design was made with detail aerodynamic computer design programs available to MTI.

The compressor stage was designed for three operating points: a baseline performance point of 50,000 rpm and two off-design conditions at 40,000 and 60,000 rpm (see Table 3-1). A target efficiency of 75% was selected at the baseline with a total pressure ratio of 3.92:1. At design conditions, a specific speed (N_s) of 78 was selected. With this favorable specific speed, the efficiency goal was considered achievable.

The compressor design was performed to a level of detail which included a flow analysis of the impeller. In that analysis, impeller loading characteristics dictated the use of splitters. Therefore, the design provided for eight full blades and 16 splitters. The impeller blade design incorporated a backward curve to maximize pressure rise at maximum efficiencies. The impeller design analysis indicated that 0.025 inch thin blades were required at the inducer inlet tip to allow passage of the design gas flow. The stage design was completed with a vaned diffuser and scroll specification. The final design of the compressor is shown in Figure 3-9.

As noted in the design report (see Attachment B), fine tuning of the compressor stage components was anticipated to achieve the stage performance goals. The level of eyeseal leakage at the impeller inlet, and the diffuser performance were of particular concern. The test program illustrated that the concerns regarding the diffuser design were well founded. The basic test findings at design point as compared to projected performance are presented in Table 3-2. The results showed that the compressor achieved its flow capacity but that efficiency was about 6% low and the head rise (pressure ratio) was about 15% low.

The projected and test data performance map is presented in Figure 3-10 for the vaned diffuser configuration. The projected performance map for the vaned diffuser configuration and the test data performance map for a vaneless configuration is shown in Figure 3-11.

TABLE 3-1

COMPRESSOR DESIGN SPECIFICATIONS

P_1 ref. = 4.35 psia ; T_1 ref. = 490°R

Actual Speed, rpm	40,000	50,000	60,000
Inlet Temperature, °F (°R)	63(523)	44(504)	35(495)
Inlet Stag. pressure, psia	9.30	5.10	2.65
Minimum Efficiency, %	71.5	75	70
Flow lbs/hr (lbs/sec)	1150 (0.320)	850(0.236)	650(0.180)
$N/\sqrt{\theta}$	38725	49300	59700
$\omega/\sqrt{\theta}/\delta$	555.6	735.8	1072.7
Outlet Pressure, psia	25.5	20.0	17.6
Total Pressure Ratio	2.74	3.92	6.64
$\omega\sqrt{\theta}/\delta$ Surge (%)[a]	515(92.7)	690(93.8)	980(91.4)
Choke (%)	580(104.4)	780(106.0)	1125(104.9)

Derived Values

Inlet Vol. flow Q_1 des. cfm	82.2	106.8	156.6
(Stagnation) Surge[a]	76.2	100.2	143.1
Choke	85.8	113.2	164.3
Available head, ft.lbs/lb	6075	8144	11610
Temperature rise ΔT °F	79	105	161
Horsepower	4.94	4.70	5.43
Specific Speed	68	78	87
Optimum Rotor Diameter, Inches[b]	3.18	3.03	2.99

NOTE:

a) "Surge" and "choke" are not stability limits but minimum and maximum flow operating points.

b) Optimum rotor diameter from specific speed - efficiency diagram.

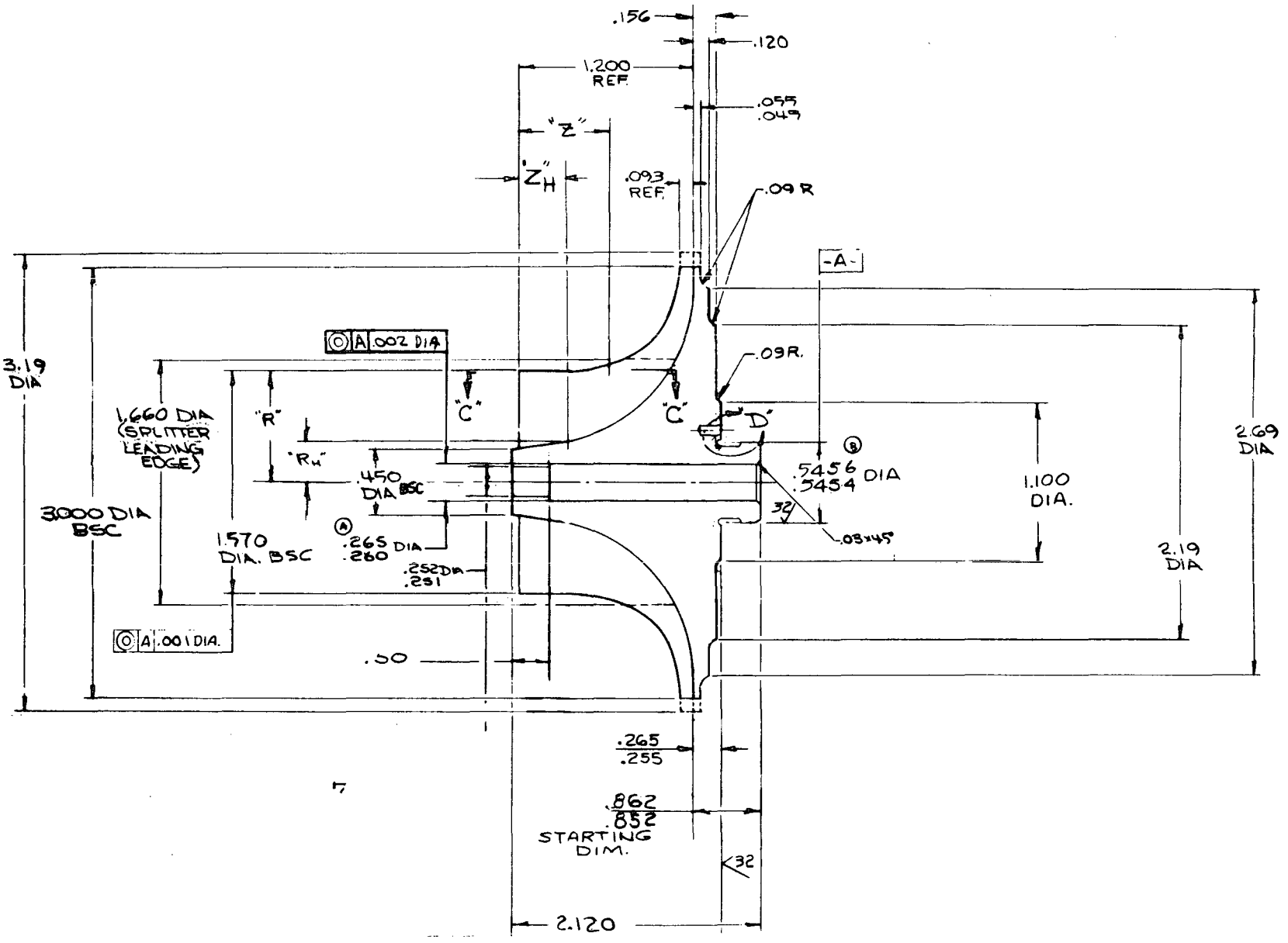

Fig. 3-9 Final Compressor Design

MECHANICAL TECHNOLOGY INCORPORATED

793122

TABLE 3-2

REFRIGERANT COMPRESSOR DESIGN POINT COMPARISION

Case	Design	Vaned Diffuser Test (D.P. 28)
Speed*	50,000	50,000 rpm
Flow**	0.204	0.203 lb/sec
Pressure Ratio	3.92	3.32
Efficiency	75%	70.5%
Percent of Design Flow		
At Surge	94	74
At Choke	106	108

* Corrected to reference temperature = 490°R

**Corrected to reference temperature and reference pressure = 4.35 psia

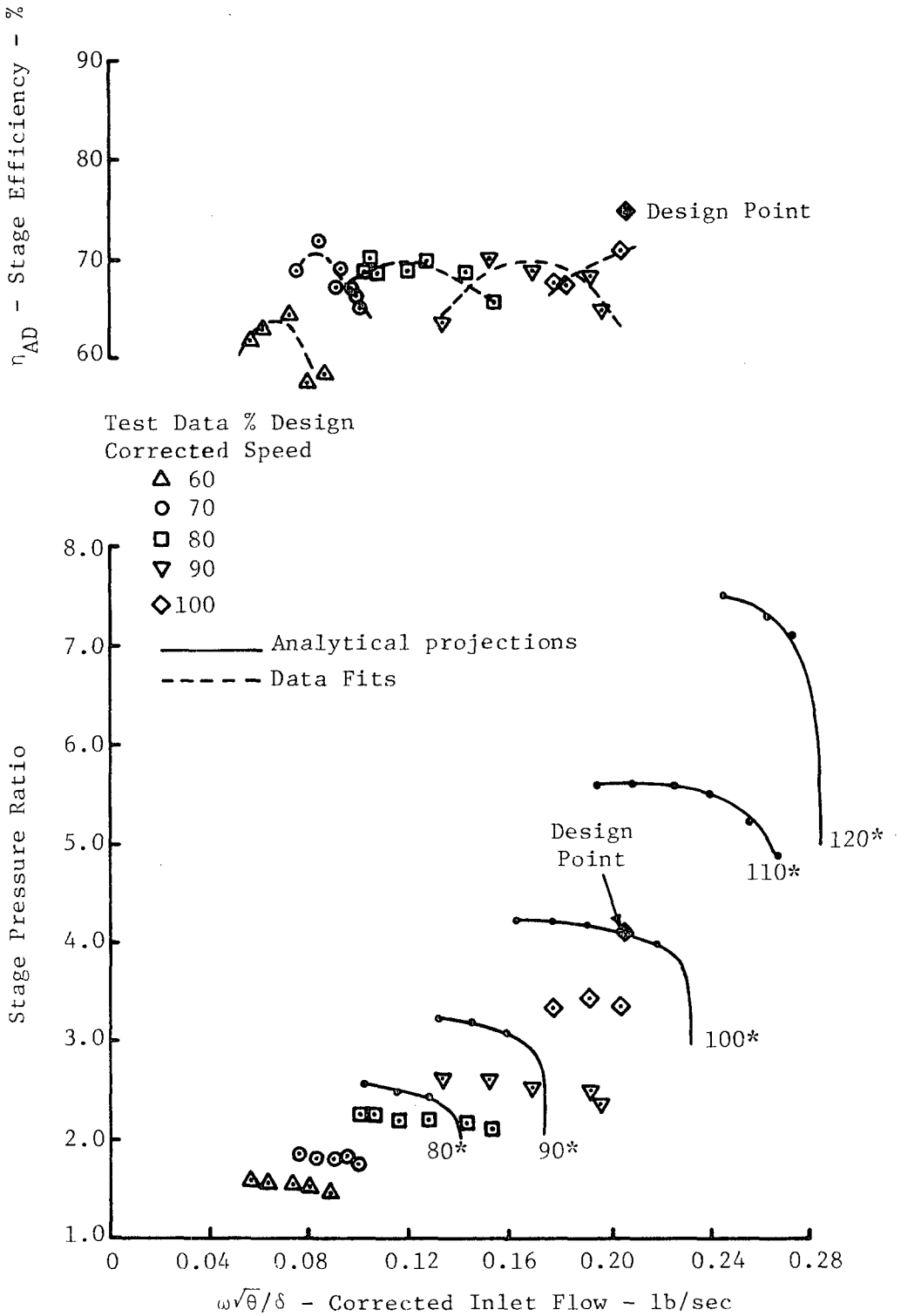

*Percent of Design Corrected Speed
Design Corrected Speed = $(N/\sqrt{\theta})$ = 49,300

Fig. 3-10 Refrigerant Compressor Performance with Vaned Diffuser

793441

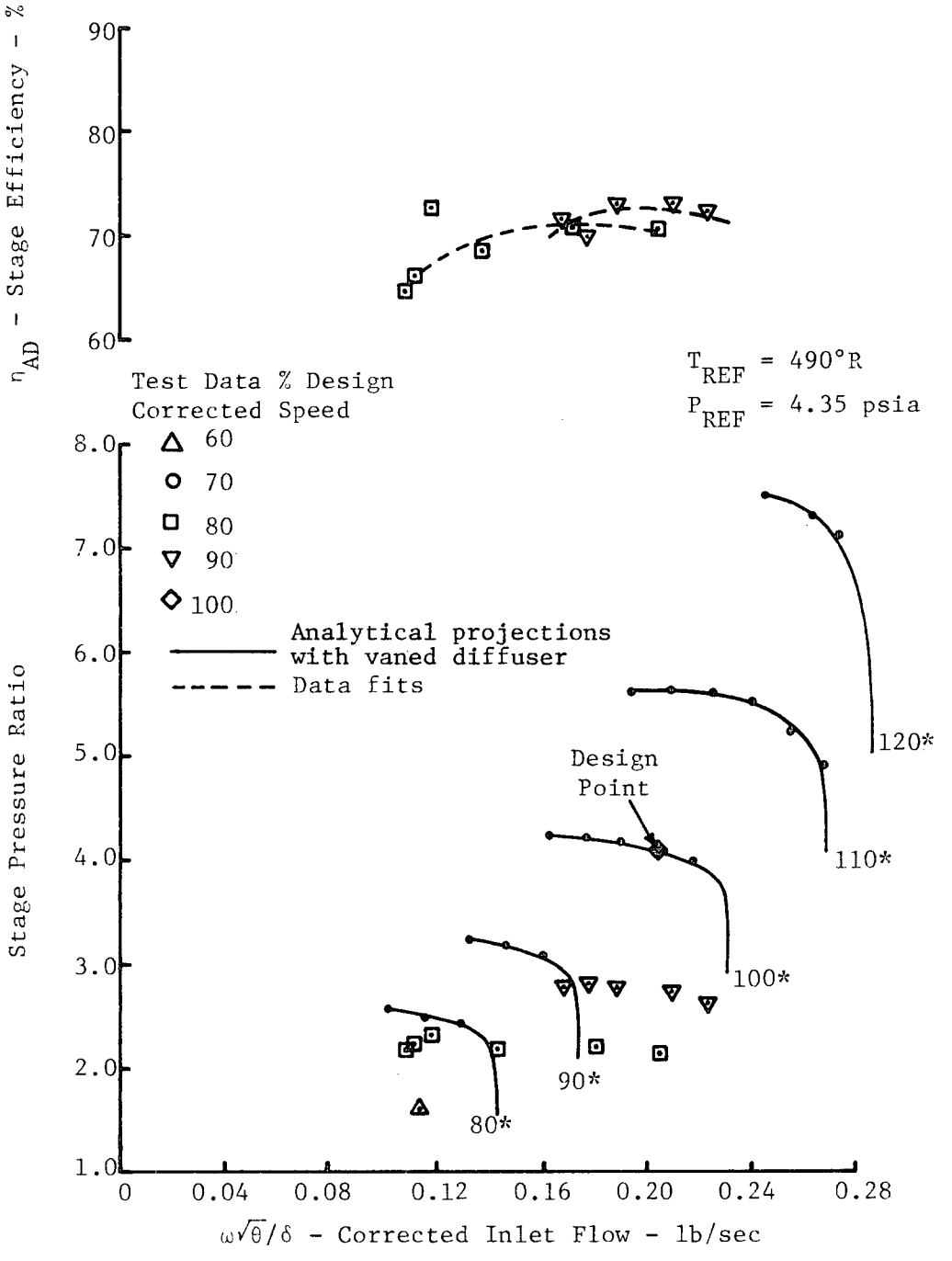

*Percent of Design Corrected Speed
Design Corrected Speed = $(N/\sqrt{\theta})$ = 49,300

Fig. 3-11 Refrigerant Compressor Performance with Vaneless Diffuser

793443

A comparison of the test data for the vaned and vaneless diffuser configurations showed an interesting anomaly: an example is given here. At a flow rate of 0.18 lb/sec at 90% of corrected speed, the vaneless configuration showed about a 10% higher pressure ratio and a 5% higher efficiency than the vaned diffuser configuration. This result was exactly opposite of what would be expected and implied that the diffuser design was not correct. A correct diffuser design should have achieved a higher performance, in terms of pressure ratio and efficiency, than shown in the experimental data for the vaneless diffuser. Thus, the test conclusions were that the basic compressor wheel design fully achieved its performance goals and, that an empirical diffuser design effort would result in overall compressor performance that would match or exceed design point requirements. The optimization of the diffuser design was not made.

3.4 Homopolar Alternator

An important feature of the HSPF concept was the ability to provide power for parasitics such as air handlers and blowers. This power would be generated by an alternator driven by the steam turbine. The turbine-alternator-compressor configuration schematic is shown in Figure 2-3 on page 2-5, and the finished components are shown in Figure 3-1. As noted previously, the design speed of the rotating package was 50,000 rpm with an operational range of 40,000 rpm to 60,000 rpm. The alternator rotor had to have a high degree of mechanical stability. In order to achieve this stability, the rotor was fabricated of high-strength steel with no electrical windings.

The design used was a "Homopolar Inductor" alternator. Only one dc field winding was used on the stationary part, supplying flux in only one direction, but this flux was switched between the stator winding coils by salient poles on both ends of the rotor. Nonmagnetic filler pieces made of Rene' 41 were placed around the rotor, filling the spaces between the salient poles, thus producing a smooth rotor surface to reduce windage. These pieces were electron-beam-welded to the rotor body. A lamination stack faced the salient poles on each end of the rotor. The lamination stack is shown in Figure 3-12 and the details of the lamination are shown in Figure 3-13. The armature windings passed through slots in both lamination stacks in a manner

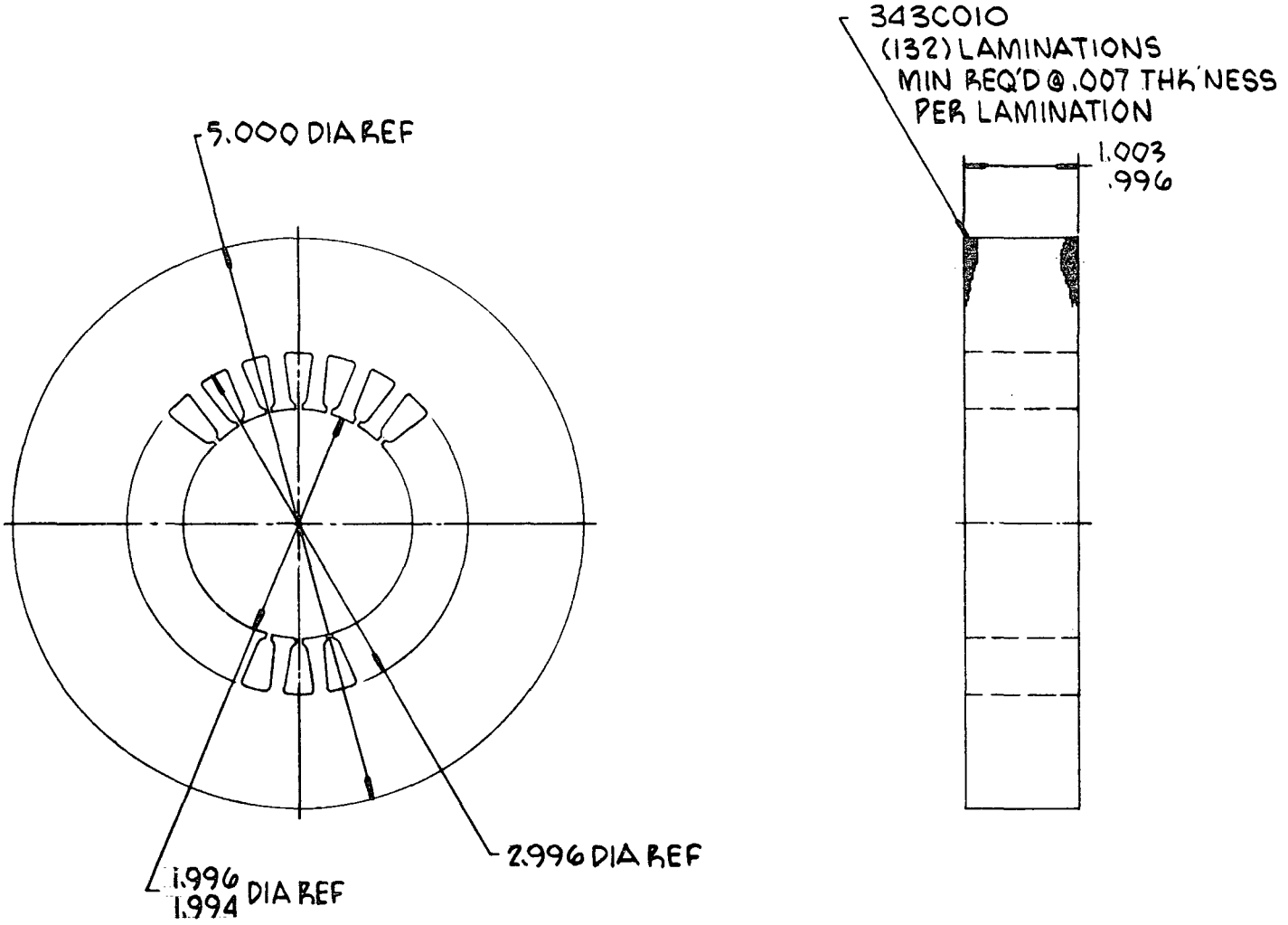

Fig. 3-12 Lamination Stack

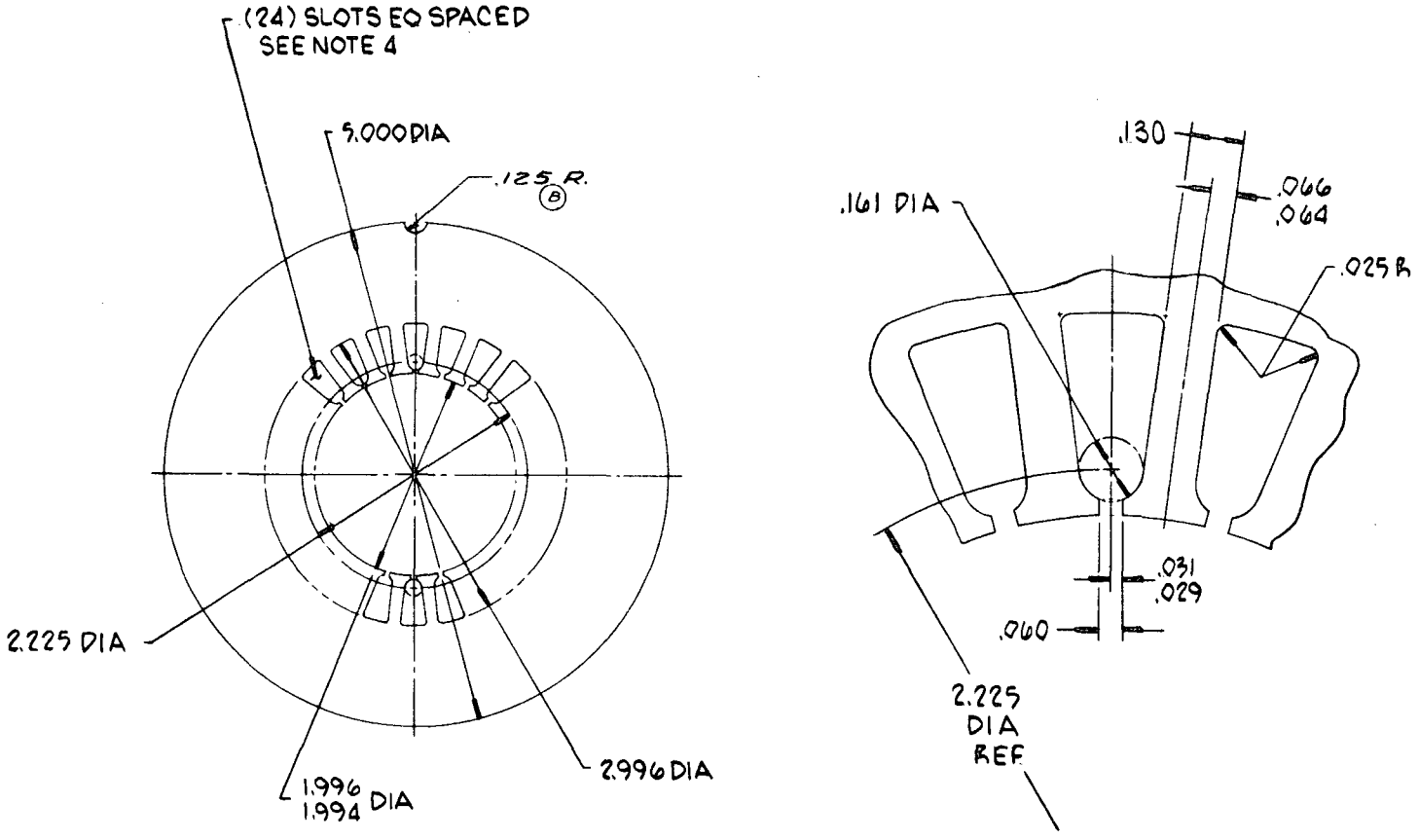

Fig. 3-13 Details of the Lamination

similar to a standard three-phase induction motor. The lamination stacks and armature windings are shown in Figure 3-14. The dc field coil was pre-wound and placed between the lamination stacks around the outside of the space for the armature winding which was inserted later. A steel sleeve was then placed around the lamination stacks which supported them and also served as the return flux path.

As with all the rotating components designed by MTI, a component test was performed on the alternator. The test results indicated that the alternator met all design goals. Table 3-3 presents the design goals and test results. A complete description of the alternator design and test results are presented in Attachment C.

3.5 Supporting Design Analyses

The rotating unit components and assembly required high performance at high thermal and mechanical stress levels and at a high rotational speed. The high rotational speed and variable operating range required close attention to the rotor bearing dynamics. A number of analyses of rotor dynamics were conducted to define the critical speed, unbalance response, and stability. These analyses impacted the design, selection and location of the bearings, and the design of the shaft. Also, these analyses impacted the selection of materials for the compressor and turbine wheels, and the method of attachment of the wheels to the shaft. A summary of the results and methods used for the rotational dynamic analysis is presented in Attachment D.

Thermal and mechanical stress analyses were also conducted for each of the components. Attachment E presents the thermal analysis of the turbocompressor assembly.

3.6 Component Test Facility

To accomplish the component testing, a special turbomachinery assembly was fabricated and a test facility built. An overall view of the component test facility area is shown in Figure 3-15. The turbomachinery test rig is shown schematically in Figure 3-16.

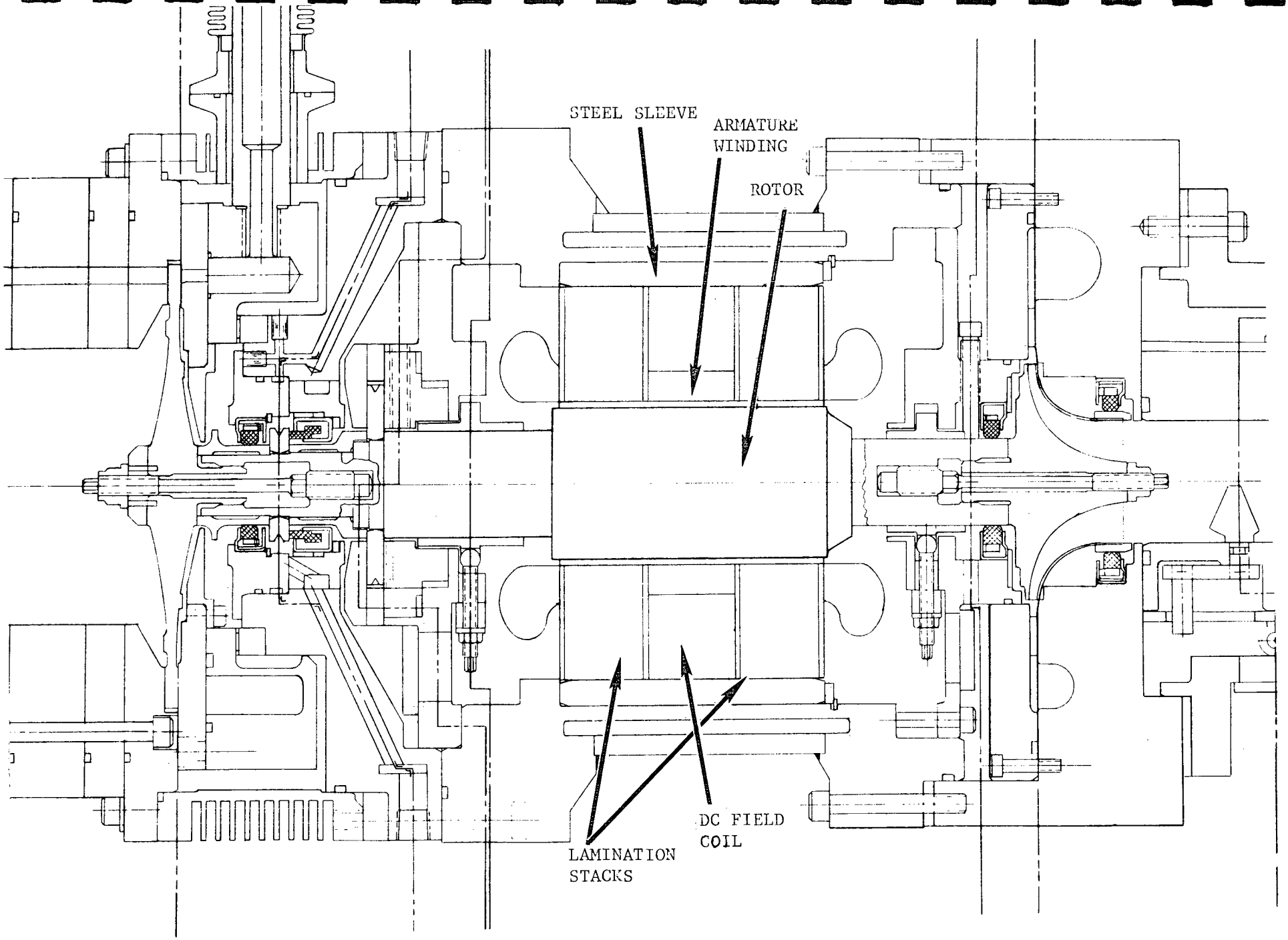

Fig. 3-14 Lamination Stacks and Armature Windings

793732

MECHANICAL TECHNOLOGY INCORPORATED

TABLE 3-3

ALTERNATOR DESIGN PERFORMANCE

	Design	Test
Power Output	3.17 kW at 60,000 rpm	3.17 kW at 60,000 rpm
Voltage	240 Vdc	240 Vdc
Efficiency	>90%	95.6%

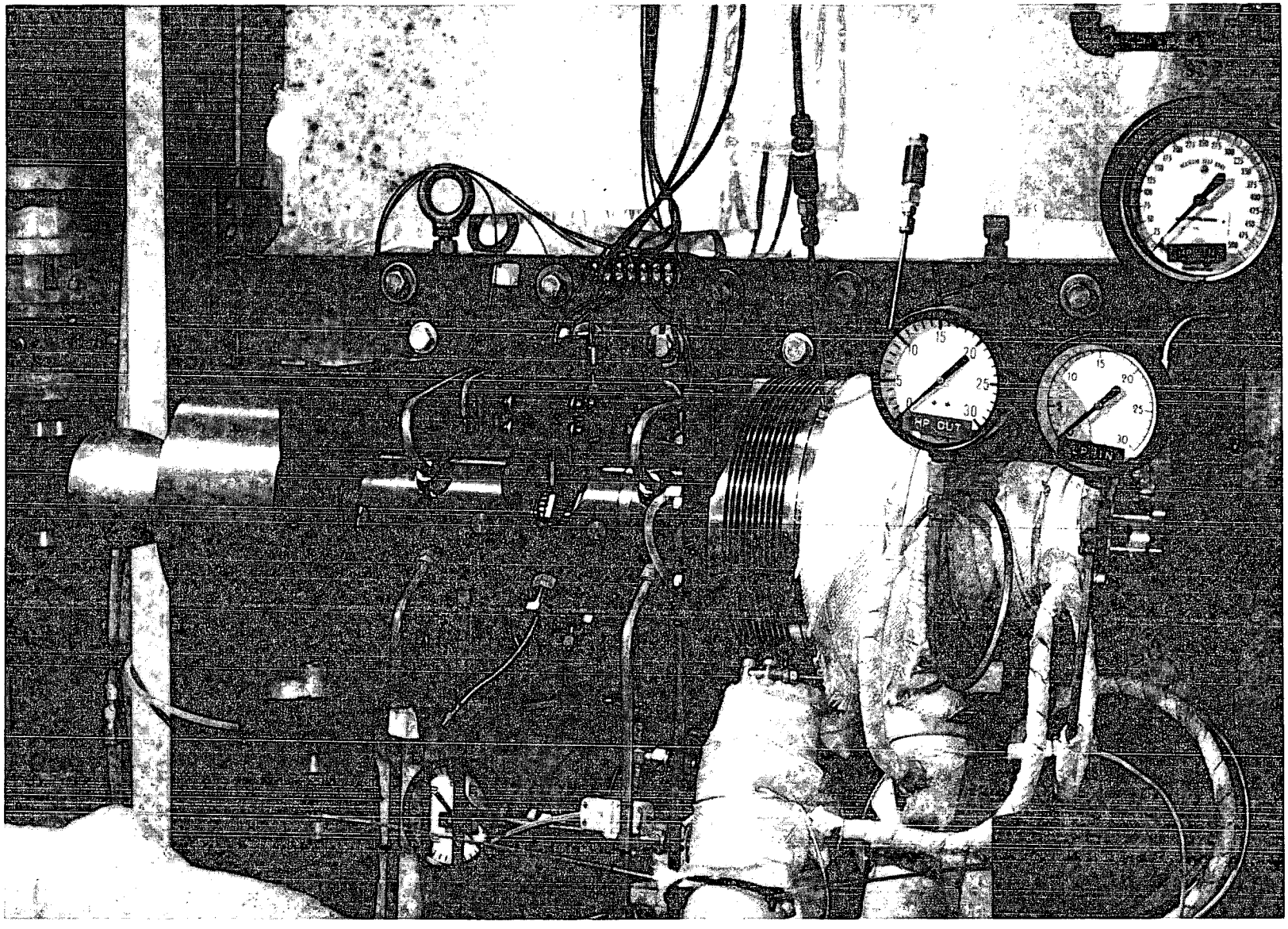

Fig. 3-15 Component Test Rig

MECHANICAL TECHNOLOGY INCORPORATED

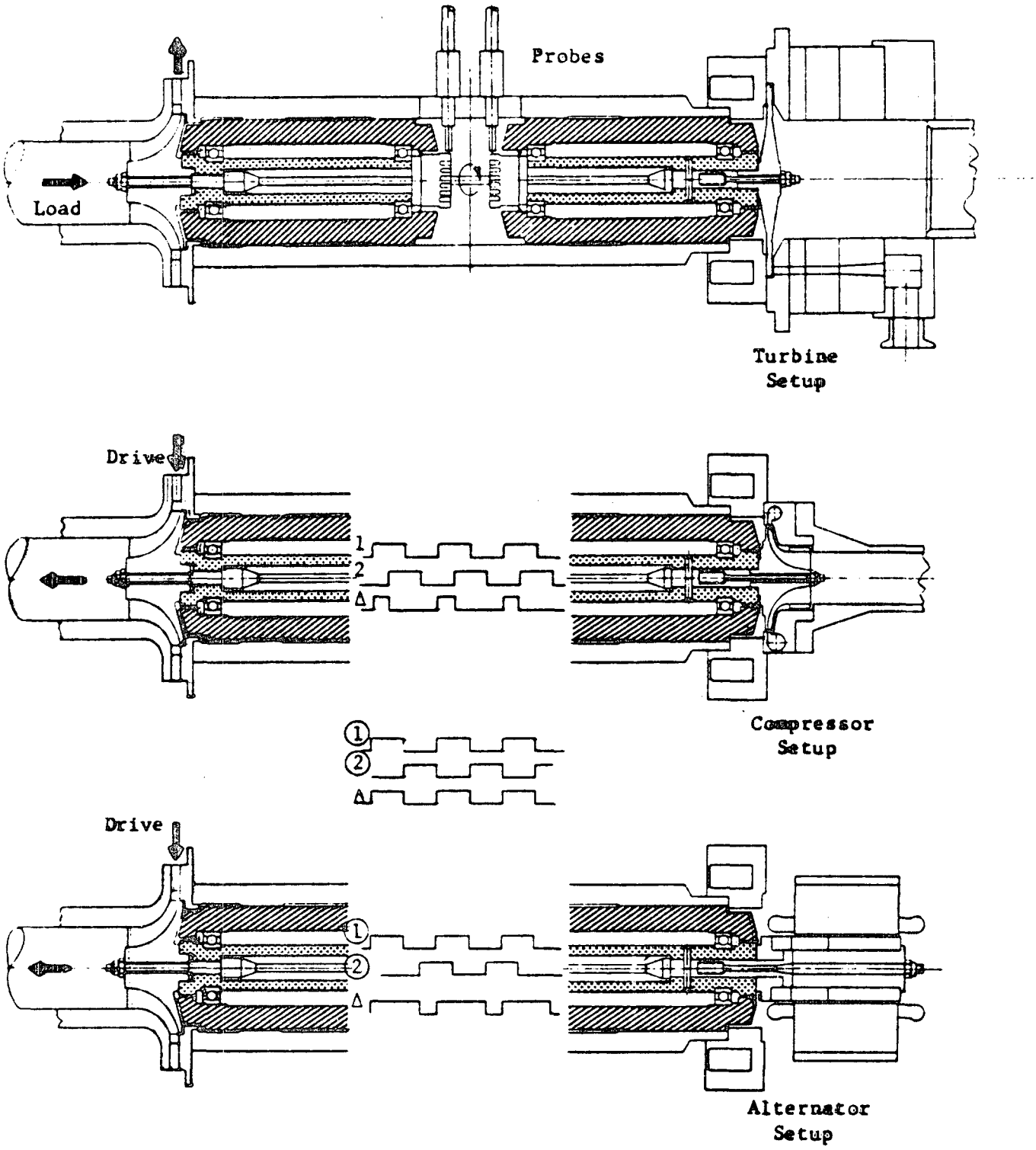

Fig. 3-16 Component Turbomachinery Test Rig Schematic

The wheel on the left of the assembly was either the load for the turbine test or the driver for the compressor or alternator test. This particular wheel was common to all component tests. The component to be tested was mounted on the right side of the assembly. The wheel on the left was connected to the test component on the right by a quill shaft which allowed for a degree of torsional deflection between the right and left components. The torsional deflection is proportional to the load. The deflection was sensed by two photonic sensors (see Figure 3-16) which produced a signal. The phase shift between the signal was related to the torsional deflection which is related to the load.

Flow meters, pressure and temperature measurements were made to provide an evaluation of the performance of the compressor and turbine. Electrical quantities were measured to evaluate the performance of the alternator.

The component testing helped in verifying design procedures and in determining empirically the optimum placement of some components such as the first-stage turbine expansion collector. Some design problems were identified for the compressor, as noted above, but were not corrected. The use of the component test procedure provided a better understanding of the total system test results and indicated how the desired performance levels could be attained.

4.0 SYSTEM TEST SUMMARY

The system test program was designed to be conducted in two phases. The first phase was to be a proof-of-concept test wherein all the system components would be tested as a system for the first time. During the proof-of-concept test a number of precautions were taken to avoid a catastrophic failure due to minor discrepancies between predicted and actual performances. These possible failures were of particular concern in the high-speed rotating group where combined mechanical and thermal loading may have resulted in larger than anticipated deflections of the rotating parts. Therefore, clearances were set larger than design specifications in the area of the turbine assembly, thus affecting the overall efficiency of the turbine. Because of the changed clearances, minor adjustments would be made after proof-of-concept tests and a series of tests would be conducted to verify maximum performance. This latter test procedure was not conducted.

The system test was designed to be conducted in a breadboard configuration. All major components were tested in their ultimate configuration, except as noted for the proof-of-concept tests. Further, the air handling and distribution system was designed to allow the test unit itself to provide for the test's environmental conditions in terms of wet bulb and dry bulb temperatures. The overall system test facility is shown in Figure 4-1.

This section presents a summary of the system test results reported in Attachment F. The basic test approach involved operating the fully assembled rotating unit/steam generator combination in conjunction with a closed-loop facility heat exchange system to provide the refrigerant evaporator and condenser. Data were taken during the system test program which, together with previously generated component test results, allowed a separate determination of both turbine interstage leakage and system parasitics. Using the calculation procedure described in Attachment F, the system data was then corrected to other operating conditions sufficient to permit an integrated value of seasonal performance to be predicted.

The system tests for the proof-of-concept were very successful. The equipment operated at speed, and repeated starts and stops did not seem to affect

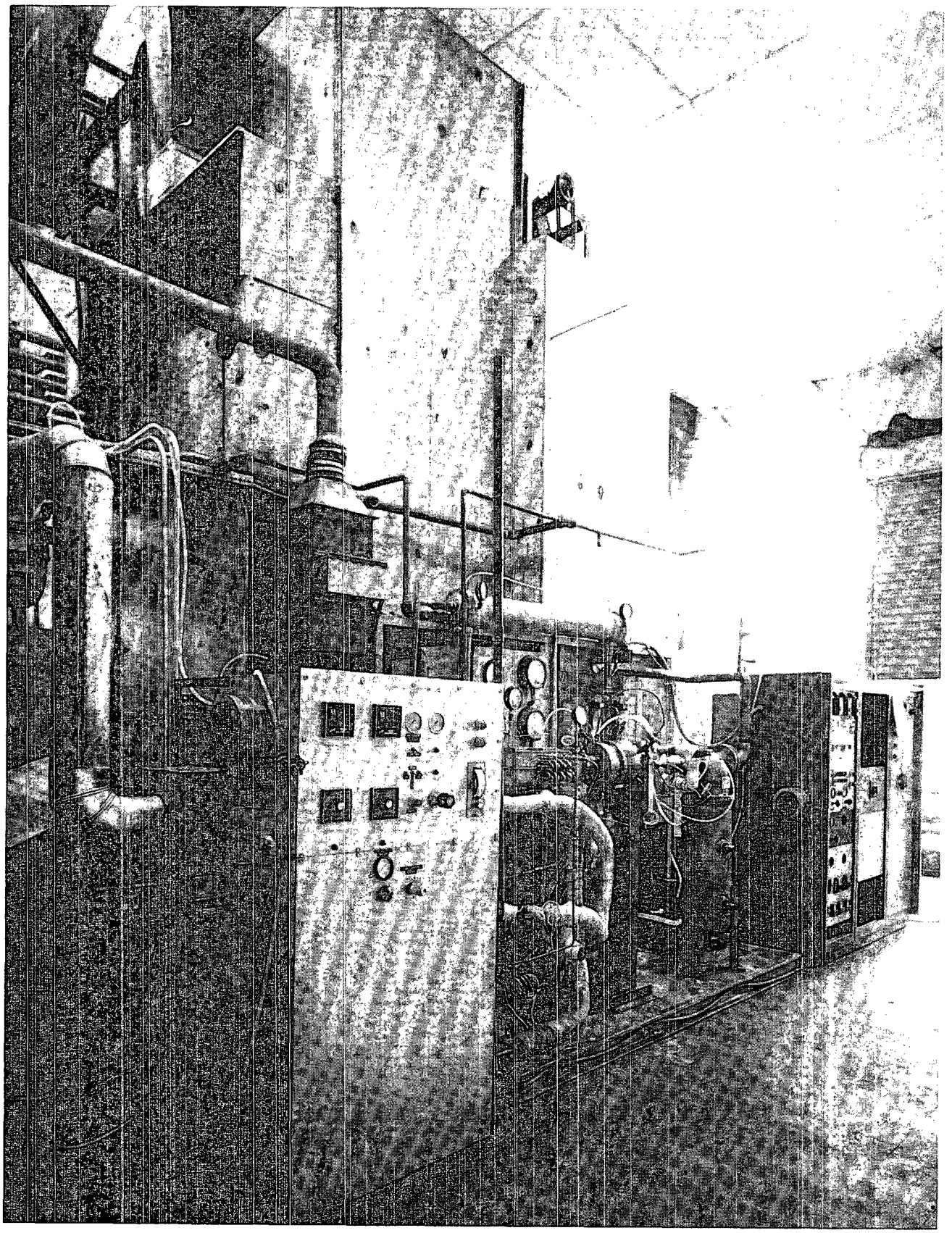

Fig. 4-1 Breadboard Demonstration Unit System Test Facility

the equipment. The performance was less than predicted, as expected. The differences were due to the larger clearances used, the below-design performance of the compressor (as was determined during the component tests) and larger-than-expected parasitic losses. Figures 4-2 and 4-3 show the refrigerant compressor and drive turbine efficiency as a function of corrected speed. Figure 4-4 shows the heating mode system COP as a function of outside ambient temperature. Three cases have been shown on both the compressor efficiency and system COP curves.

The test results are presented in Table 4-1 in terms of the simulated seasonal performance of the demonstrator with heating and cooling loads corresponding to Cleveland, Ohio. The results are expressed as heating and cooling seasonal performance factors (SPFs). The test result SPFs were computed directly from coefficient of performance data generated by the demonstrator during proof-of-concept testing at MTI. Also shown in Table 4-1, for reference purposes, are four sets of analytically derived performance data. The analytically derived data and the test results are listed together in Table 4-1 in the chronological order of their dates of origin, as follows:

1) The original design performance predictions, made 7-76, at the time the 7½-ton unit design was first completed

2) Performance data generated in early 1977 by the Comparative Cost of Ownership Study (CCOS) run for Cleveland weather, the Retail Store. The performance specification input for the CCOS was from the same analysis that supported the original design performance predictions. The small differences between the design performance and CCOS results (+8%, heating; -2% cooling) are due to the much finer-scale simulation provided by the CCOS. The CCOS data should be most definitive.

3) The proof-of-concept test results generated at MTI in the summer of 1978

4) Performance believed to be achievable had the demonstrator been modified to meet original design specifications. These modifications would have incorporated system clearances set

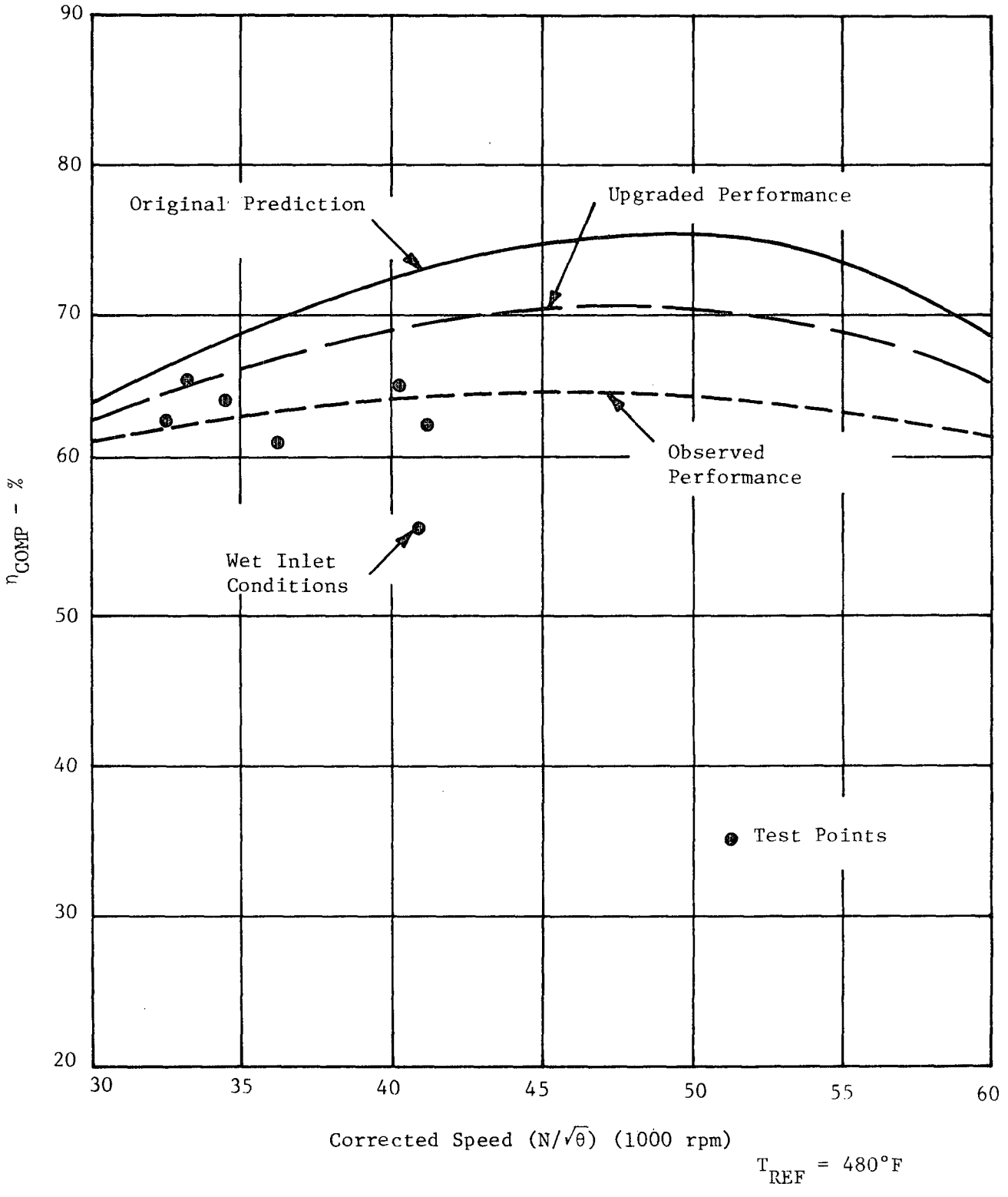

Fig. 4-2 Compressor Efficiency

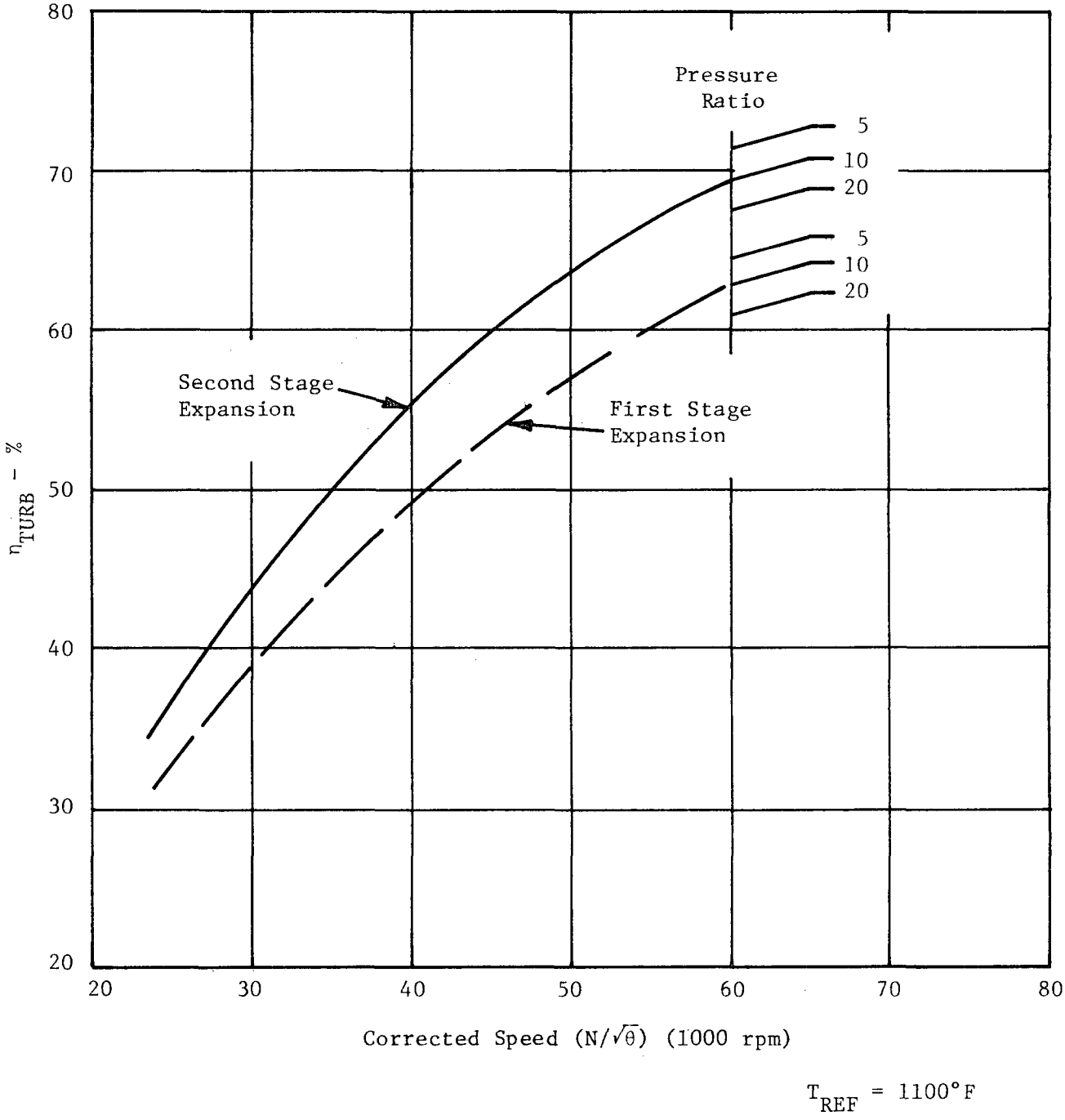

Fig. 4-3 Turbine Efficiency

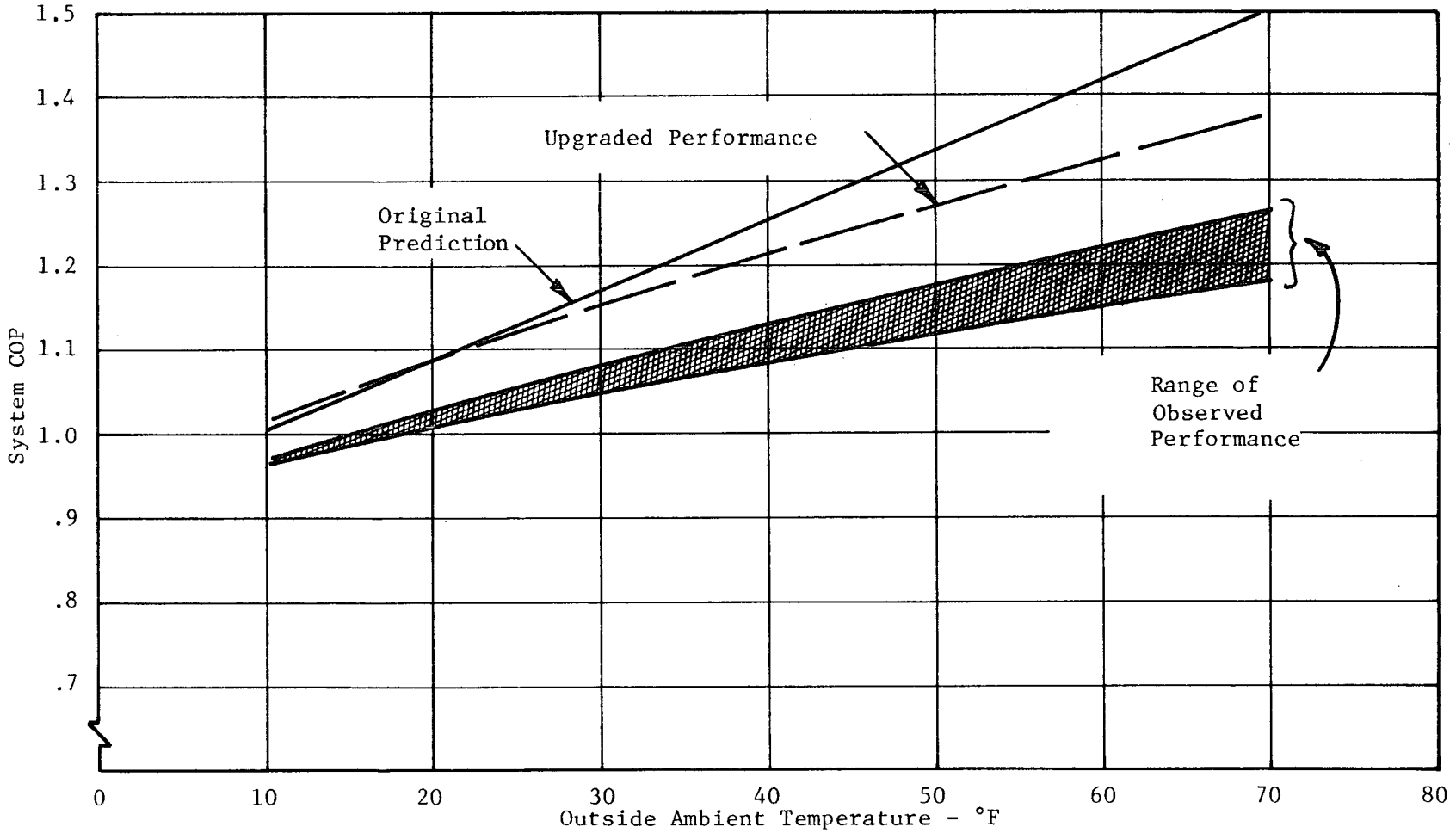

NOTES: 1. Data shown includes allowance for energy used for self-propelled auxiliaries.

2. Based on Higher Heating Value, natural gas.

792949

Fig. 4-4 Heat Pump System Performance-Heating Mode

TABLE 4-1

7-1/2-TON HSPF SYSTEM PERFORMANCE

	Seasonal Performance Factor[1] (Cleveland Weather)	
	Heating	Cooling
Original Design Performance Prediction (7-76)	1.21	.93
Generated by Comparative Cost of Ownership Study, Retail Store, Cleveland	1.31	.91
Derived from Observed Proof-of-Concept Test Data, 7-1/2-Ton Breadboard Demonstrator	1.08	.705
Predicted for Performance Demonstration	1.18	.90
Expected Product Performance		
a) Noncondensing Steam Generator	1.24	.91
b) Condensing Steam Generator	1.31	.96

NOTE: (1) Includes allowance for energy to drive self-powered auxiliary components, and based on higher heating value for natural gas.

at design points, modifications to the compressor wheel, and reduction of system thermal and mechanical parasitics.

5) Performance to be expected from a refined product. These data are expressed in terms of both noncondensing and condensing-type steam generators. The data under 1 through 4 (above) corresponds to a noncondensing steam generator. A condensing-type steam generator would require either additional heat transfer surface, or incorporation of pulse combustion or jet impingement technology.

The turbocompressor operated satisfactorily throughout the system test program. The maximum speed obtained was 43,000 rpm. The design maximum speed of 60,000 rpm could not be obtained due to the large turbine wheel clearance set during initial assembly as a precaution. The turbocompressor was operational at the program conclusion. A teardown inspection showed no unusual items that would have limited future operation of the turbocompressor. Figure 4-5 shows the turbine wheel still installed in the machine during disassembly.

A teardown inspection was also performed on the package steam generator. Figure 4-6 shows the steam tube bundle. Sections of the tube bundle were removed to allow the interior of the tubes to be examined. While significant corrosion was observed on the exterior of the tubes, there was no indication of scale buildup in the tubes. Steam generator corrosion was shown, by chemical analysis performed by CNG's Research Department Laboratory, to be due to the high concentrations of halogenated hydrocarbons (e.g.; R-11) present in the test area.

The system performance testing with the identified modifications was not conducted. The actual demonstration of performance was meaningless because proof-of-concept and potential attainment of design performance had already been demonstrated. Since the cost-of-ownership study showed that the 7-1/2-ton HSPF was uneconomical, the program had, by this point, had been redirected to consider the large scale model design.

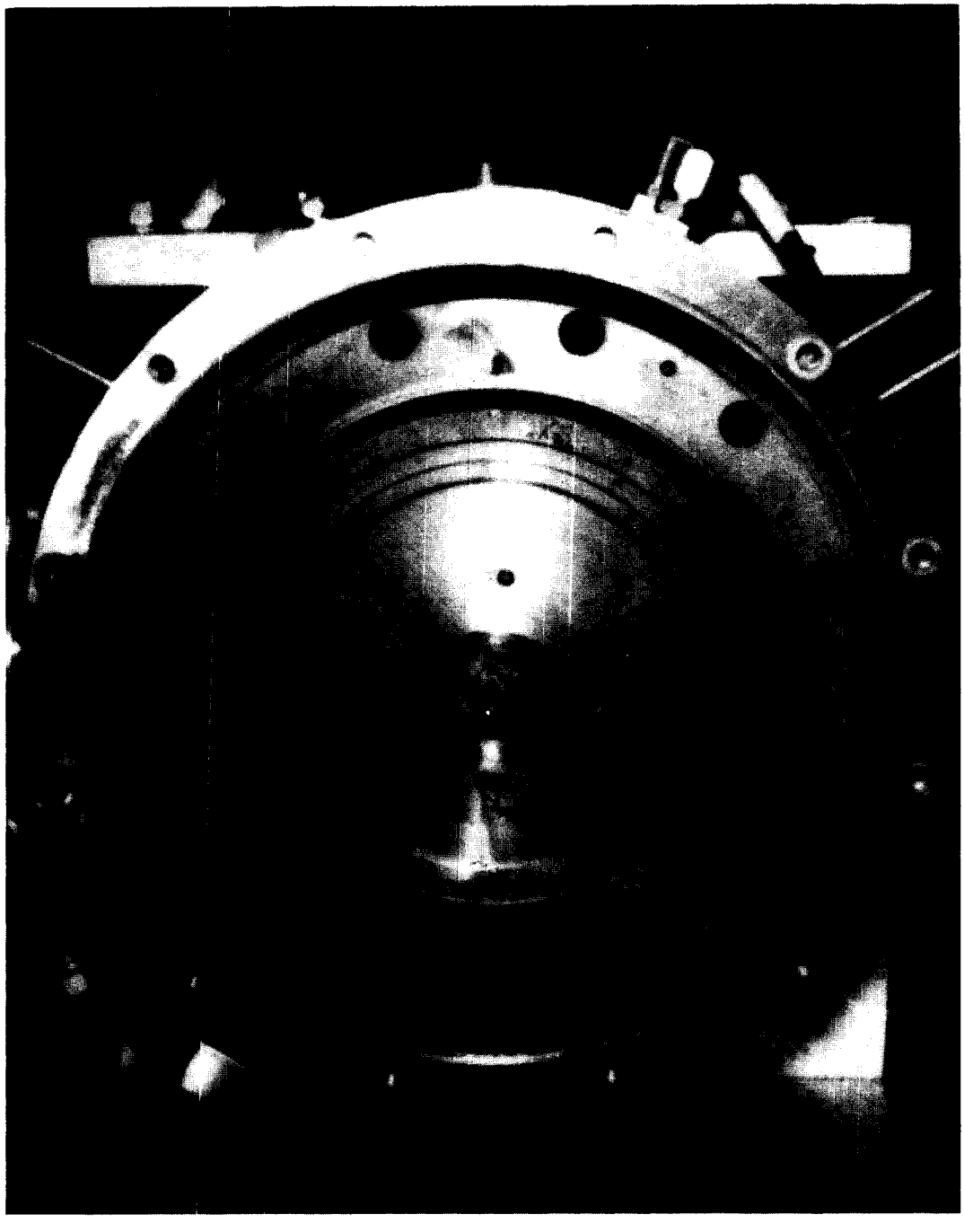

Fig. 4-5 Turbine Wheel After System Test

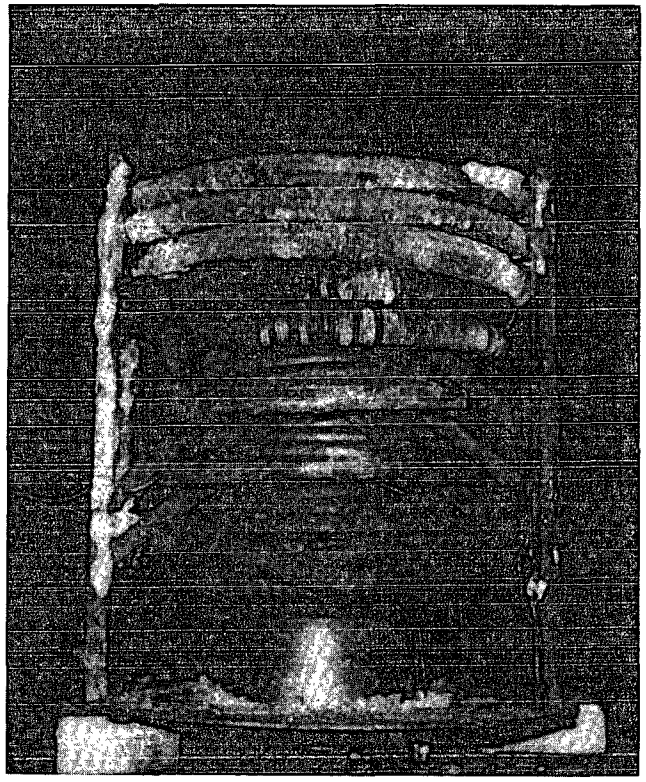

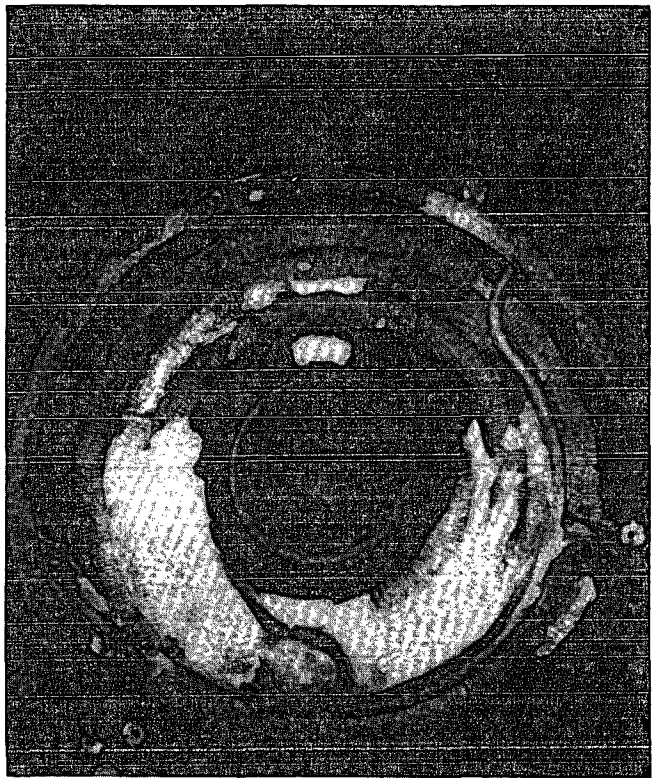

Fig. 4-6 Steam Generator Tube Bundle

5.0 CONCLUSIONS

The 7½-ton HSPF technical effort demonstrated that a steam-Rankine driven gas heat pump could be built that would obtain the performance levels required of a product of this type. The basic design tools, design methodology, and fabrication techniques were shown to be adequate to achieve the technical design objectives. Although technically feasible, the system concept failed to fulfill the product commercialization requirements. The principal shortfall was a prohibitively high estimate for manufacturing cost.

ATTACHMENT A

TURBINE DESIGN REPORT

TURBINE DESIGN REPORT

BY

Al White

Prepared For:

CONSOLIDATED NATURAL GAS COMPANY, INC.
Cleveland, Ohio

Prepared by:

MECHANICAL TECHNOLOGY INCORPORATED

October 1976

CNG/ERDA

TURBINE DESIGN REPORT

		Page
I	Introduction	1
II	Sources & Use of Information	3
III	Preliminary Investigation	5
	a) Non Reheat Turbine	
	b) Reheat Turbine	
	1. Optimum Pressure	
	2. Optimum Energy Dist (XO Press)	
	3. Optimum Diameters	
	4. Optimum Energy at Optimum Diameter	
IV	Turbine Characteristics (for System Study)	15
	a) First Stage	
	b) 2nd Stage	
V	Application of Linhardt & Silvern's Equations	18
VI	Design Layout Calculations	22
	a) Design Conditions	
	b) Preliminary Proportions	
	c) Nozzle Calculations	
	d) Optimum Bucket Height	
	e) Velocity Diagrams & Exit Conditions	
	f) Diagram Efficiencies	
	g) Losses	
VII	Exhaust Diffusers & Connections	26
VIII	Supersonic Design Considerations	27
IX	Bucket Geometry	28
X	Bucket Stresses	30
XI	Shrouding & Leakage Losses	33

CNG/ERDA

TURBINE DESIGN REPORT

I. INTRODUCTION

The basic concept of the Gas Fired Heat Pump uses a high-temperature, moderate pressure steam turbine to drive the centrifugal refrigeration compressor. For good cycle efficiency and corresponding COP over the operating range, the turbine should have as high an efficiency as possible.

The original concept for the turbine was a radial outflow, single rotation Ljungstrom type turbine of six or seven stages. While this gave promise of good efficiency, for various reasons, including some severe mechanical design problems, this concept was discarded.

The specific speed and specific diameter range for the turbine is not suitable for a simple radial inflow turbine, so the choice was narrowed to axial flow machines, either of the Curtis type or some form of re-entry turbine. The re-entry type can be either axial flow, or a "Terry" type turbine or a "drag turbine", the latter being equivalent to the so-called "regenerative" type pump. The latter two did not promise a sufficiently high efficiency level for the operating conditions of interest, and so were not considered further.

A 2-row Curtis stage was investigated by Sapozhniko, Shchlekoldin and Usanovich (Ref. 1) and this information was used to calculate the performance of a turbine suitable for this application, i.e. 15 HP at 40000 rpm, over a range of initial pressures. The corresponding Flow vs. Initial Pressure is shown on Fig. 1.

The performance shown, when corrected to the approximately 11 HP required by the preliminary design, would probably have been acceptable. However, the simpler rotor construction of the axial flow re-entry turbine, coupled with the possibility of using reheat between the stages of an axial re-entry turbine, led to the decision to concentrate on the axial flow, re-entry design.

Cycle studies also indicated a distinct advantage in using reheat, so the final design is based on an axial re-entry turbine, with reheat between the two "stages".

K+E 10 TO INCH 7 X 10 INCHES
KEUFFEL & ESSER CO. MADE IN U.S.A.
46 1322

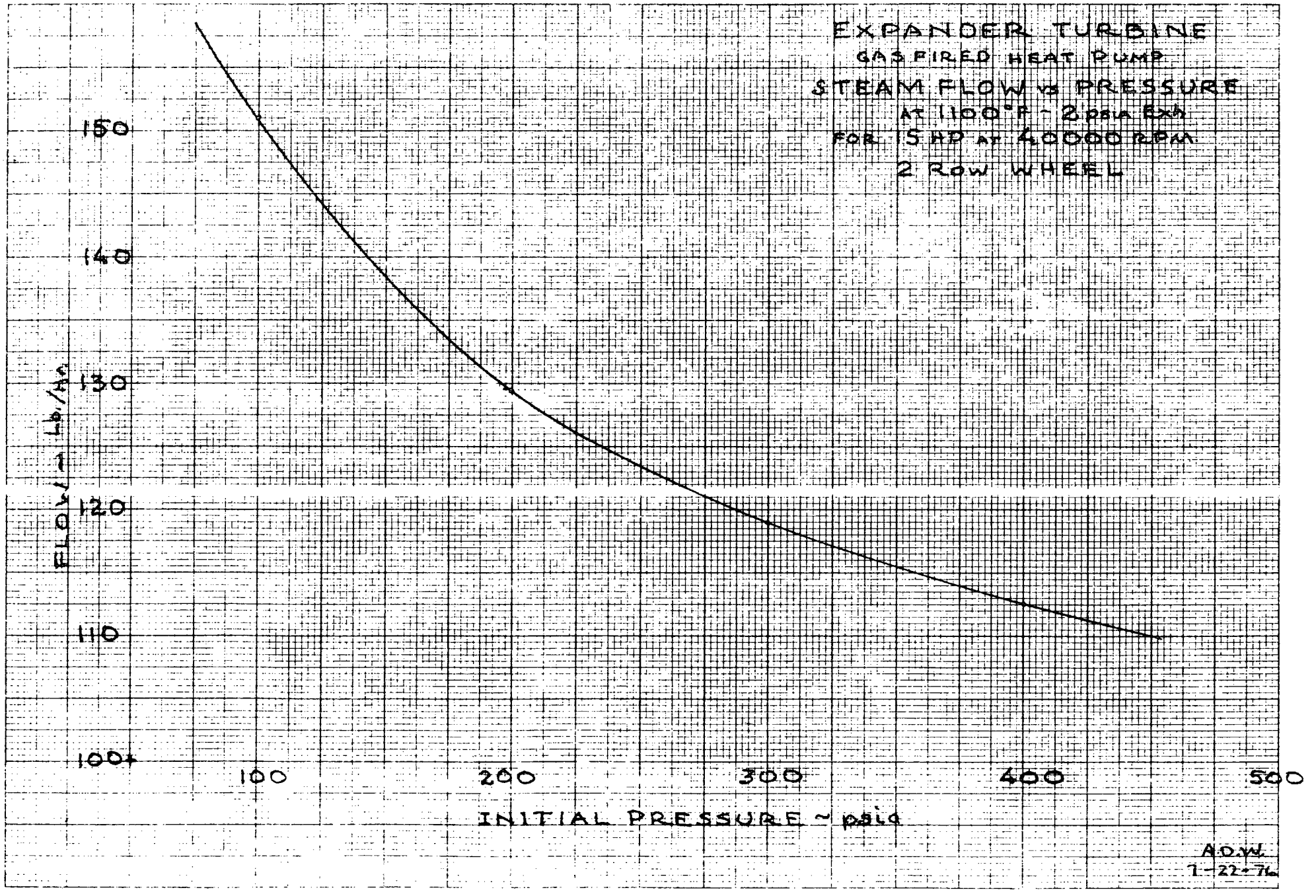

FIG. 1.

II. SOURCES AND USE OF INFORMATION

The state-of-the-art for small turbine design, such as is required for this application is not as well developed as for large steam turbines and gas turbines. There is, however, some rather fundamental information in the way of analytical studies and test results, as reported in the literature, that is available and, when coupled with basic turbine design experience, could be used for the design.

The specialized references that were reviewed and used in the design are as follows:

1. Investigation of the Operation of a Supersonic Velocity Stage by V.N. Sapozhnikov, A.V. Shchekolidin and L. Yu. Usanovich, from TEPLOENERGETIKA, 1970 17(S)29-32

2. Drag Turbine Performance, by O.E. Baljé, Transactions ASME, 1956 pgs. 1291-1304 (ASME Paper No. 56-AV-6)

3. Design of Turbines for High-Energy-Fuel, Low-Power-Output Applications, by Alan H. Stenning, Massachusetts Institute of Technology, Dynamic Analysis and Control Laboratory, Report No. 79, 1953.

4. A Study of High Energy Level, Low Power Output Turbines by O.E. Baljé, AMF/TD No. 1196 (1958) Department of the Navy, ONR, prepared by Sundstrand Turbo, A Division of Sundstrand Machine Tool Co.

5. Study of Turbine and Turbopump Design Parameters, Vol. I - A Study of High Pressure Ratio Re-entry Turbines by Hans D. Linhardt S/TD 1735. Department of the Navy, ONR, prepared by Sundstrand Turbo, a Division of Sundstrand Corp. - 1 Feb. 1958 thru 30 Jan. 1960.

6. Analysis of Partial Admission Axial Impulse Turbines by Hans D. Linhardt and David H. Silvern, ARS Journal, presented at ARS Semi-Annual Meeting, Los Angeles, Ca., May 9-12, 1960.

7. The Radial Flow Turbine in Comparison to the Axial Flow Turbine by Eugen Knoernschild, Technical Report No. F-TR-1198-IA, GS-USAF-Wright Pat. No. 160, published by Air Material Command, Wright-Patterson Air Force Base.

8. Determining Fluid Friction or Windage of Rotating Disks by H.W. Hamm, Allis-Chalmers Electrical Review, Fourth Quarter, 1962.

The analytical methods and data contained in these reports is particularly well summarized in Ref. 6. The equations, relations, turbine characteristic plots, etc. provided in this paper were used as the primary basis in evaluating the turbine proportions, determing efficiency levels and characteristics, and specifying the nozzle and bucket designs. Basic turbine design practices and other standard references, such as STODDLA, were also used where applicable.

A more detailed description of the application of the equations and data is given in the following Sections.

III. PRELIMINARY INVESTIGATIONS

Prior to the decision to employ a reheat cycle, a preliminary study was made on both non-reheat and reheat units, using the data and methods of Linhardt and Silvern's paper (Ref. 6). It had been decided that the cycle and corresponding turbine design would be based on a turbine inlet temperature of 1100 F, but the best turbine inlet pressure was not known. The turbine exhaust pressure was assumed as 2 psia for preliminary calculations.

As a first step the required turbine output was assumed to be 11 HP at 40000 rpm (corresponding to about 15 tons refrigeration). Specific speeds were then calculated for initial pressures from 100 to 400 psi, based on approximate efficiencies, as follows:

Initial Press.	100	200	300	400
AE-Btu/lb.	446.9	490.9	515.5	532.0
Assumed Eff.-%	62	60	59.5	59
Approx. Flow-lb/hr.	101	95.5	91.5	89.1
Exhaust Sp. Vol.	295	284	275	268
Q_3	2.875	2.795	2.645	2.58
$H^{3/4}$	14330	15400	15950	16300
N_s	8.025	7.26	6.63	6.33

From Fig. 15 of Ref. 6, the optimum Specific Diameters corresponding to these specific speeds, and the actual turbine diameters that can be calculated from these are as follows:

Initial Press.	100	200	300	400
D_s	6	6.1	6.7	6.9
$H^{1/4}$	24.1	24.7	25.2	25.3
D in feet	.715	.689	.705	.705
D' in inches	8.58	8.25	8.45	8.45

These calculations then give a basis for calculating the turbine efficiencies at the various pressures, using the methods given in Ref. 6. For purposes of the calculation it was assumed there would be equal pressure ratio on each stage.

The turbine efficiency, as calculated, is made up of a hydraulic efficiency, η_h and the parasitic losses, and can be expressed as

$$\eta_T = \eta_h (1 - L_t) - \Sigma L$$

where

η_h = hydraulic efficiency

L_t = total leakage as percentage of total mass flow

ΣL = sum of scavenging loss and disk friction and pumping loss (as a percent of available power)

Using an average nozzle energy coefficient of .96 and a bucket loss coefficient calculated in accordance with Eq. 13 of Ref. 6, the corresponding efficiencies and flows were calculated as follows:

Initial Press.	100	200	300	400
Pr. Ratio	50	100	150	200
Pr. Ratio/Stg.	7.06	10.0	12.2	14.3
$N_s D_s$	68.83	59.89	56.02	53.49
1st Stg. AE	274.25	310.85	329.45	341.0
2nd Stg. AE	216.0	231.0	243.0	248.5
Overall AE	446.9	490.9	515.5	532.0
η_h	.7849	.8184	.8446	.8413
L_T	.1265	.1695	.2158	.2512
ΣL	.2326	.1686	.1812	.1806
η_T-%	45.30	51.11	48.11	44.93
UE_T	202.5	250.9	248.0	239.0
Flow @ 11 HP-lb/hr	138.2	111.6	112.9	117.1

K X 10 INCH 10 INC
KEUFFEL & ESSER CO. MADE IN U.S.A.
46-1322

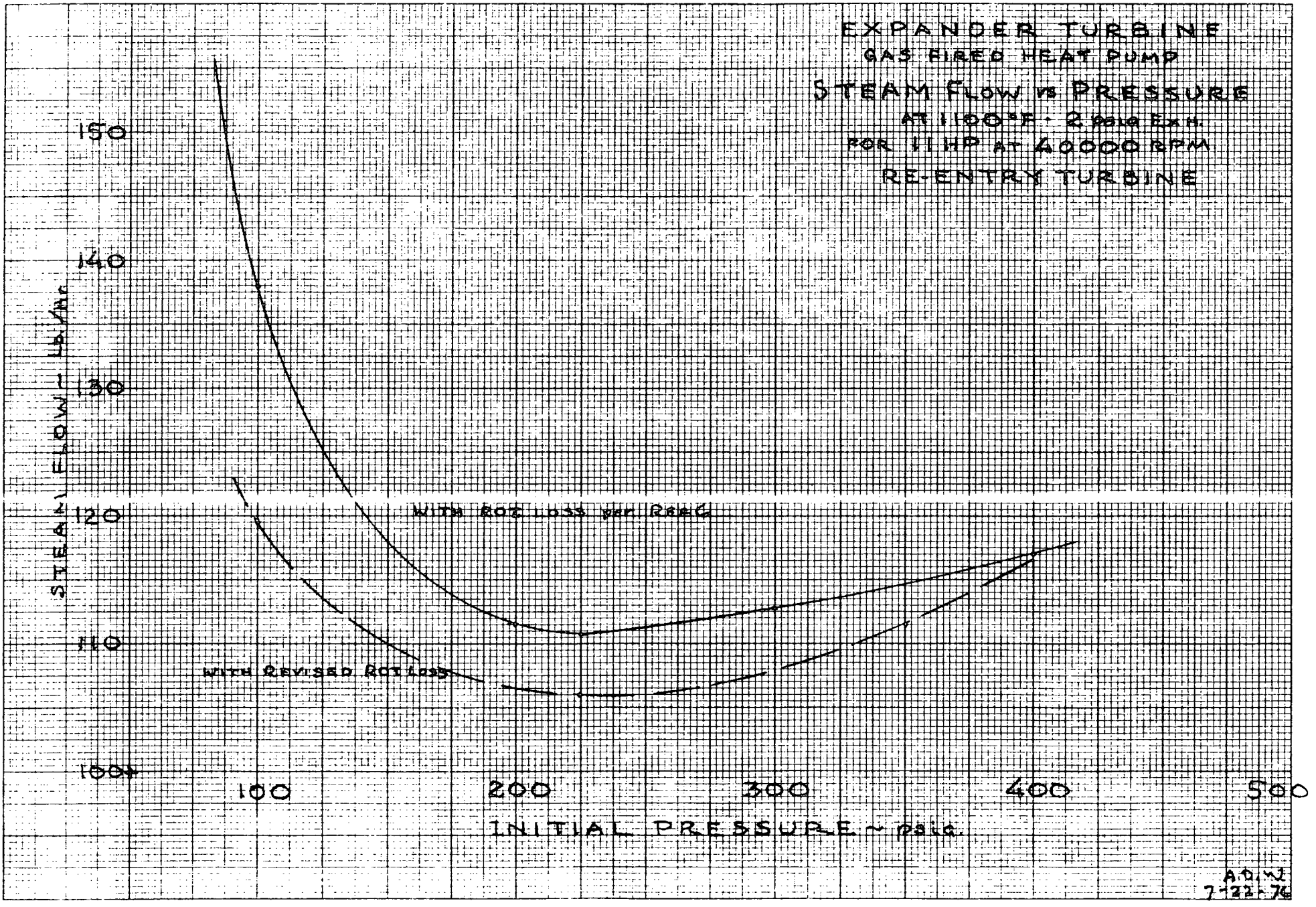

FIG. 2

The disk rotation loss as calculated by Eq. 7 in Ref. 6 did not seem to agree with values based on steam turbine practice, so the loss was recalculated using the formula

$$Kws = .03 \times \frac{D^2}{\rho} \left(\frac{\omega}{100}\right)^3$$

where D is in feet
ρ is in lb/ft^3
ω is rim velocity fps.

On this basis the efficiencies and corresponding flows are calculated as follows:

Initial Press.	100	200	300	400
Disk Loss - %	16.35	14.06	17.16	18.23
η_T - %	52.3	53.9	49.1	44.9
Flow - lb/hr.	119.5	106.0	111.5	117.0

These flows are plotted on Fig. 2 vs. initial pressure.

Reheat Turbine

Since cycle studies had shown an advantage to using reheat, which could be readily employed with an axial flow, re-entry type turbine, the next step was to consider the effect of reheat on the turbine design.

Equal pressure ratio per stage, with reheat to the initial temperature, i.e. 1100 F, gives approximately equal energy distribution over the pressure range of interest as shown below.

Initial Pressure	100	200	300	400
1st Stg. - AE	274.3	310.9	324.5	341.0
2nd Stg. - AE	272.8	310.2	329.1	344.0
Total AE = ΣAE's	547.1	621.1	653.6	685.0

Using an estimated efficiency and corresponding flow, the Specific Speed and Specific Diameter of an 11 HP - 40000 rpm turbine are as follows:

Initial Pressure	100	200	300	400
N_s	7.64	6.34	6.12	6.19
D_s - optimum	6.0	6.8	7.0	7.0
D_{tip} - ft.	.746	.747	.768	.791
inches	8.95	8.96	9.22	9.49

In order to estimate the corresponding turbine efficiencies, the generalized plot of axial turbine efficiencies from Fig. 4 of Ref. 6 were used, based on individual Specific Speeds and Specific Diameters, which were calculated using the flows, energy distribution and specific volumes for equal pressure ratios. These values are as follows, at 40000 rpm:

Initial Pressure	100	200	300	400
1st Stage N_s	4.78	3.40	2.90	2.74
D_s	13.37	18.1	20.7	22.3
2nd Stage N_s	12.7	10.8	10.2	10.4
D_s	5.03	5.72	5.88	5.90

The corresponding efficiencies from the Ref. 6 plot were less than 15% on the first stage and 50 to 51% on the second stage. From this it was obvious that the optimum diameter chosen from an overall specific speed was not optimum for a reheat machine, and a different approach would have to be used to select the turbine diameter to get good overall efficiency.

Accordingly, the generalized plot from Ref. 6 was used to estimate the optimum Specific Diameter for each stage individually based on its corresponding specific speed. This gave values as follows:

Initial Pressure	100	200	300	400
1st Stage - N_s	4.78	3.40	2.90	2.74
D_s-opt.	8.4	10.7	12.0	12.5
D - ft.	.469	.442	.446	.451
2nd Stage N_s	12.7	10.8	10.2	10.4
D_s-opt.	4.2	4.9	5.0	4.95
D-ft.	.624	.643	.654	.677
Mean Dia. - ft.	.547	.543	.550	.564
inches	6.56	6.50	6.60	6.65

Converting these mean diameters to equivalent specific diameters for the first and second stage conditions, and using the generalized turbine plot of Ref. 6 to determine the obtainable efficiencies, gives values as follows:

Initial Pressure	100	200	300	400
1st Stage - D's	9.8	13.15	14.78	15.95
η	42%	35%	33%	32%
2nd Stage D"s	3.68	4.14	4.20	4.21
η	60.5%	58%	58%	58%

The investigation thus far had been based on equal pressure ratios on the two stages, which may well not be the optimum split for these specific conditions. Accordingly, a check was made on the optimum reheat pressure, the initial pressure being selected as 300 psia from overall system considerations.

The same method of calculation was used as before, based on the turbine characteristics given in Ref. 6, with stage diameters of .45, .50 and .55 feet and reheat pressures of 24.6, 30 and 35 psia. The corresponding specific diameters, specific speeds and efficiencies from Fig. 4 of Ref. 6 are given below.

Reheat Press.	24.6	30	35
<u>.45 Ft. Diameter</u>			
1st Stage - N_s	3.05	2.87	2.74
D_s	11.65	12.55	13.35
η-%	38.5	37.5	36
2nd Stage-N_s	10.05	9.55	9.21
D_s	3.53	3.63	3.68
η-%	52.5	52.0	51.5
Σ UE	299.6	298.0	302.7
Flow at 11 HP - lb/hr	93.5	93.9	92.5

Reheat Pressure	24.6	30	35
.50 Ft. Diameter			
1st Stage - N_s	3.05	2.87	2.74
D_s	12.92	13.97	14.85
η-%	38.0	36.0	34.0
2nd Stage - N_s	10.05	9.55	9.21
D_s	3.92	4.02	4.09
η-%	55.0	54.0	53.0
ΣUE	306.0	300.0	292.0
Flow at 11 HP-lb/hr	91.45	93.28	95.83
.55 Ft. Diameter			
1st Stage - N_s	3.05	2.87	2.74
D_s	14.22	15.36	16.33
η-%	33.0	32.0	31.0
2nd Stage - N_s	10.05	9.55	9.21
D_s	4.32	4.42	4.50
η-%	57.0	57.5	56.0
ΣUE	296.3	300.2	294.3
Flow at 11 HP-lb/hr	94.38	93.24	95.09

The required flows and corresponding enthalpy to reheater (1st Stage exhaust) are plotted vz. the cross-over (XO) pressure, i.e. reheat pressure in Fig. 3. From the curves the optimum reheat pressure is between 20 and 25 psia with an optimum rotor diameter of .50 ft. at 40000 rpm.

Because this optimization was based on a generalized plot, which could not be read with any great accuracy, a revised calculation was then made for the .50 ft diameter (6" dia.) turbine calculating the actual diagram efficiencies and parasitic losses, using the relations and corresponding coefficients given in Ref. 6. The expression for the hydraulic (diagram) efficiency is

$$\eta_h = 4 \times \left(\frac{\omega}{V_o}\right)\left\{1 + \psi_R\left[1 - \frac{t}{4a_I}\left(1 + \frac{a_I}{a_{II}}\right)\right]\right\}\left\{\psi_N \cos\alpha - \frac{\omega}{V_o}\right\}$$

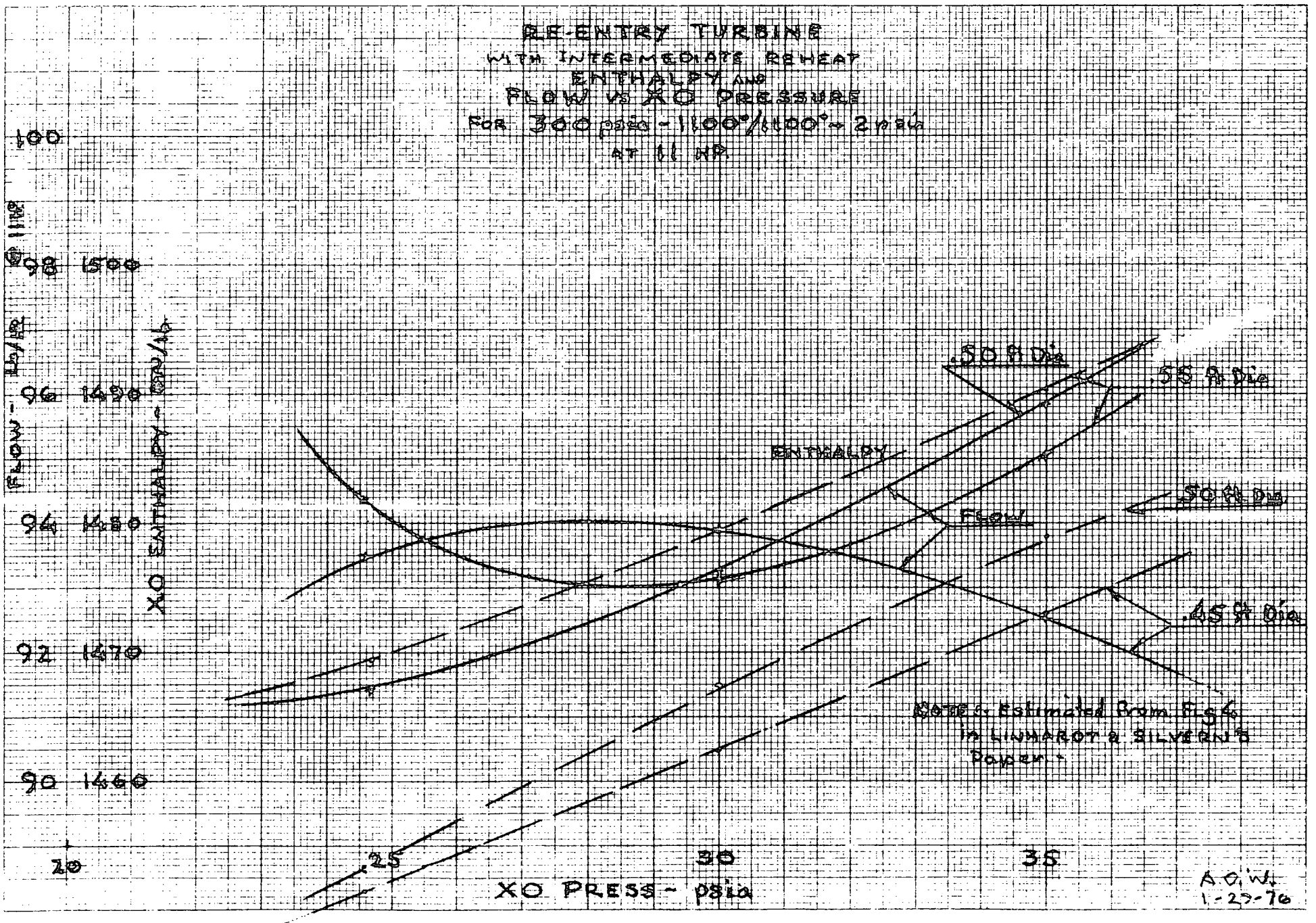
RE-ENTRY TURBINE
WITH INTERMEDIATE REHEAT
ENTHALPY AND
FLOW VS XO PRESSURE
FOR 300 psia - 1100°/1100° - 2 psia
AT 11 HP.
100
98 1500
96 1490
94 1480
92 1470
90 1460
FLOW - LB/HR @ 11 HP
XO ENTHALPY - BTU/LB
.50 ft Dia
.55 ft Dia
ENTHALPY
FLOW
.50 ft Dia
.45 ft Dia
NOTE: Estimated from Fig 6 in LINHAROT & SILVERNS Paper.
20
25
30
35
XO PRESS - psia
A.O.W.
1-27-76

FIG. 3.

where ω = wheel speed in fps

V_o = theoretical spouting velocity corresponding to the available energy - fps

ψ_R = bucket coefficient calculated from the relationship

$$\psi_R = [1 - .228(1 - \frac{\beta^\circ}{90})^3] \times$$

$$[1 - .05\ (M_w - 1)^2]\ [1 - .06\ \frac{c}{h}]$$

in which - c = bucket chord

h = bucket height

M_w = relative Mach. No.

β = bucket angles

ψ_N = nozzle coefficient

a_I = 1st Stage arc of admission

a_{II} = 2nd Stage arc of admission

t = blade spacing - inches

α = nozzle angle, in degrees

Disk losses, bucket losses and leakage losses are accounted for by the methods of Ref. 6. The resulting overall efficiencies and corresponding flow to develop 11 HP are plotted in Fig. 4. This plot shows clearly that at 300 psia - 1100/1100 - 2 psia exhaust pressure, the reheat pressure should be about 20 psia. for highest efficiency and minimum steam flow.

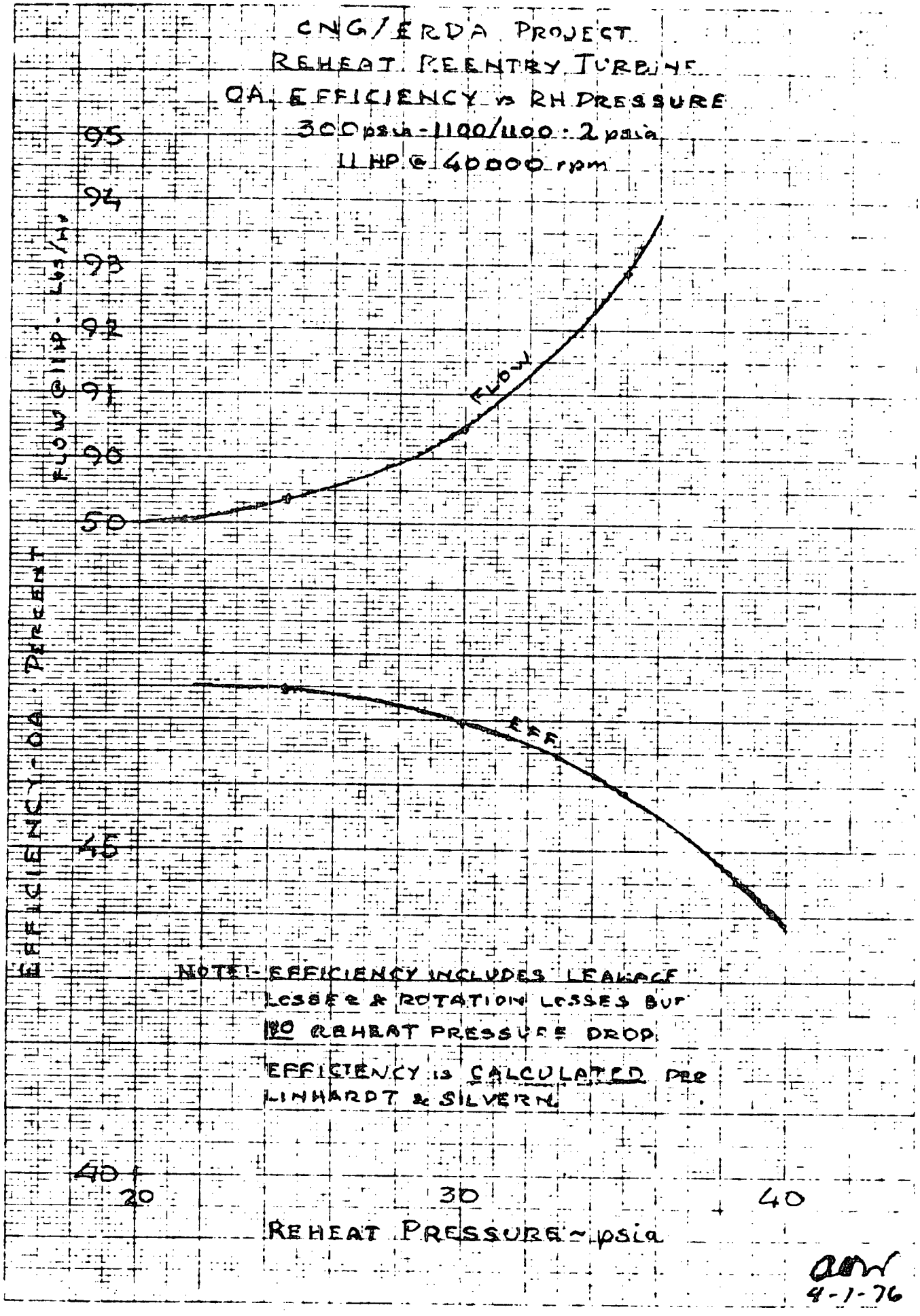
CNG/ERDA PROJECT
REHEAT REENTRY TURBINE
OA EFFICIENCY vs RH PRESSURE
300 psia - 1100/1100 : 2 psia
11 HP @ 40000 rpm
FLOW @ 11 HP - LBS/HR
95
94
93
92
91
90
50
FLOW
EFF
45
40
EFFICIENCY OA - PERCENT
NOTE:- EFFICIENCY INCLUDES LEAKAGE LOSSES & ROTATION LOSSES BUT NO REHEAT PRESSURE DROP
EFFICIENCY IS CALCULATED PER LINHARDT & SILVERN
20
30
40
REHEAT PRESSURE ~ psia

4-1-76

FIG 4

IV. TURBINE CHARACTERISTICS

With the basic features and general characteristics of the turbine delineated from the preliminary surveys, the next step was to define the turbine operating characteristics so that they could be used in a more comprehensive system study.

Assuming a design point of 89.37 lb/hr. flow at 300 psia - 1100/1100 F - 2 psia exh. press. and 40000 rpm the first and second stage efficiencies were calculated separately for a range of operating speed from 16000 to 56000 rpm, with a reheat pressure of 24.6 psia.

Again, the equations from Linhardt & Silvern (Ref. 6) were used, with the bucket coefficients calculated for the corresponding relative Mach. Numbers at each speed. The first stage was assumed to operate at constant pressure ratio (corresponding to constant reheat temperature) and the second stage was calculated for pressure ratios corresponding to 150 psia and 600 psia initial pressure to cover a wide range of operating conditions. The disk rotation loss, and the bucket pumping loss was assumed to be divided equally between the two stages. It was also assumed that leakage losses would be accounted for by a separate leakage calculation between the stages.

The results of these calculations are shown in Figs. 5 and 6 for the first and second stages, respectively. These curves, with a corresponding plot of the compressor characteristics, were then used in the overall system calculations to determine the system, and the turbine operating conditions over a range of operating parameters.

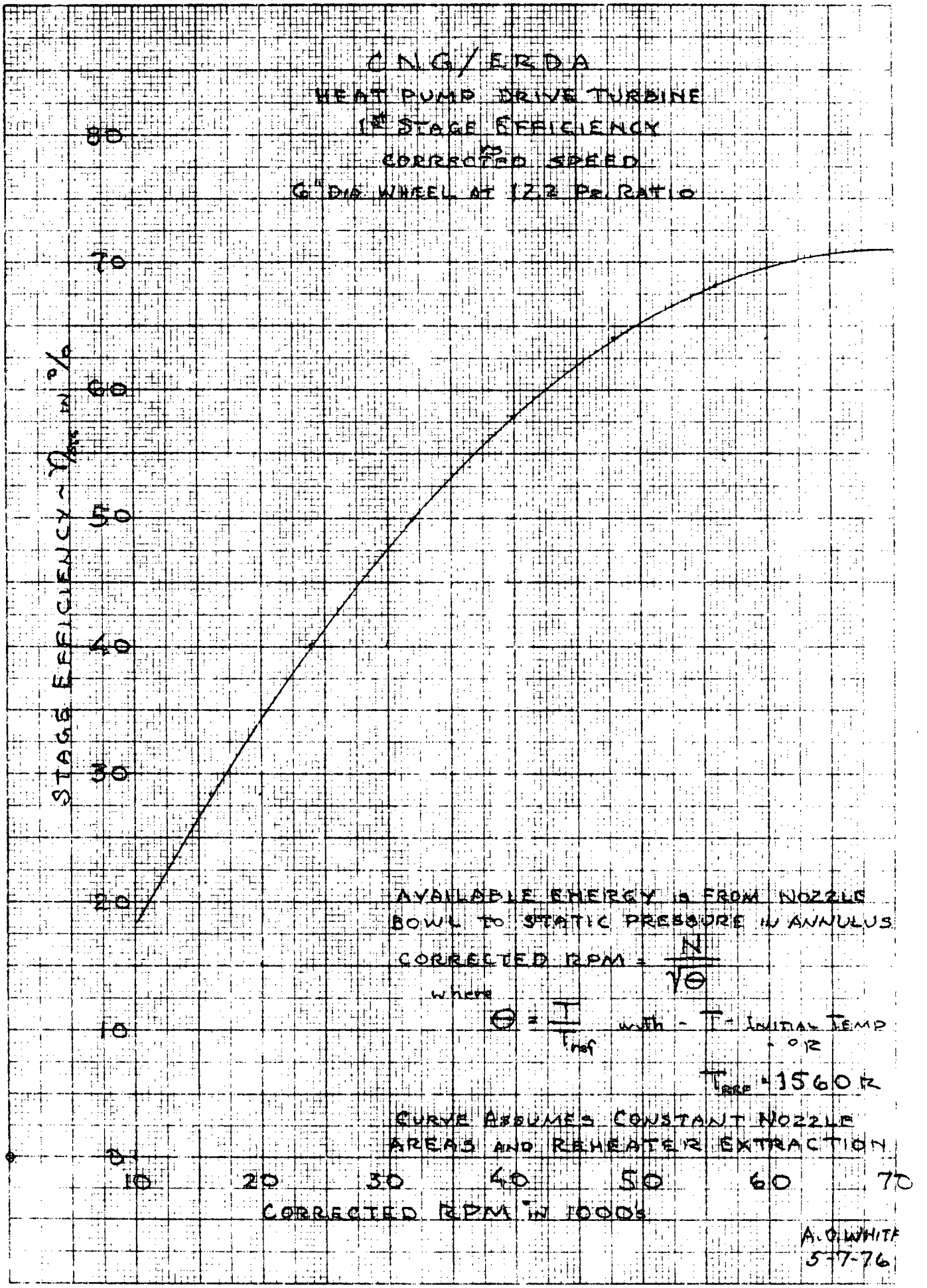
CNG/ERDA
HEAT PUMP DRIVE TURBINE
1st STAGE EFFICIENCY
CORRECTED SPEED
6" DIA WHEEL AT 1.22 PR. RATIO
STAGE EFFICIENCY ~ η_{ADIA} IN %
80
70
60
50
40
30
20
10
0
10
20
30
40
50
60
70
CORRECTED RPM IN 1000's
AVAILABLE ENERGY IS FROM NOZZLE BOWL TO STATIC PRESSURE IN ANNULUS
CORRECTED RPM = $\frac{N}{\sqrt{\Theta}}$
where
$\Theta = \frac{T}{T_{ref}}$ with - T - INITIAL TEMP - °R
T_{REF} = 1560 R
CURVE ASSUMES CONSTANT NOZZLE AREAS AND REHEATER EXTRACTION
A.O. WHITE
5-7-76

FIG 5

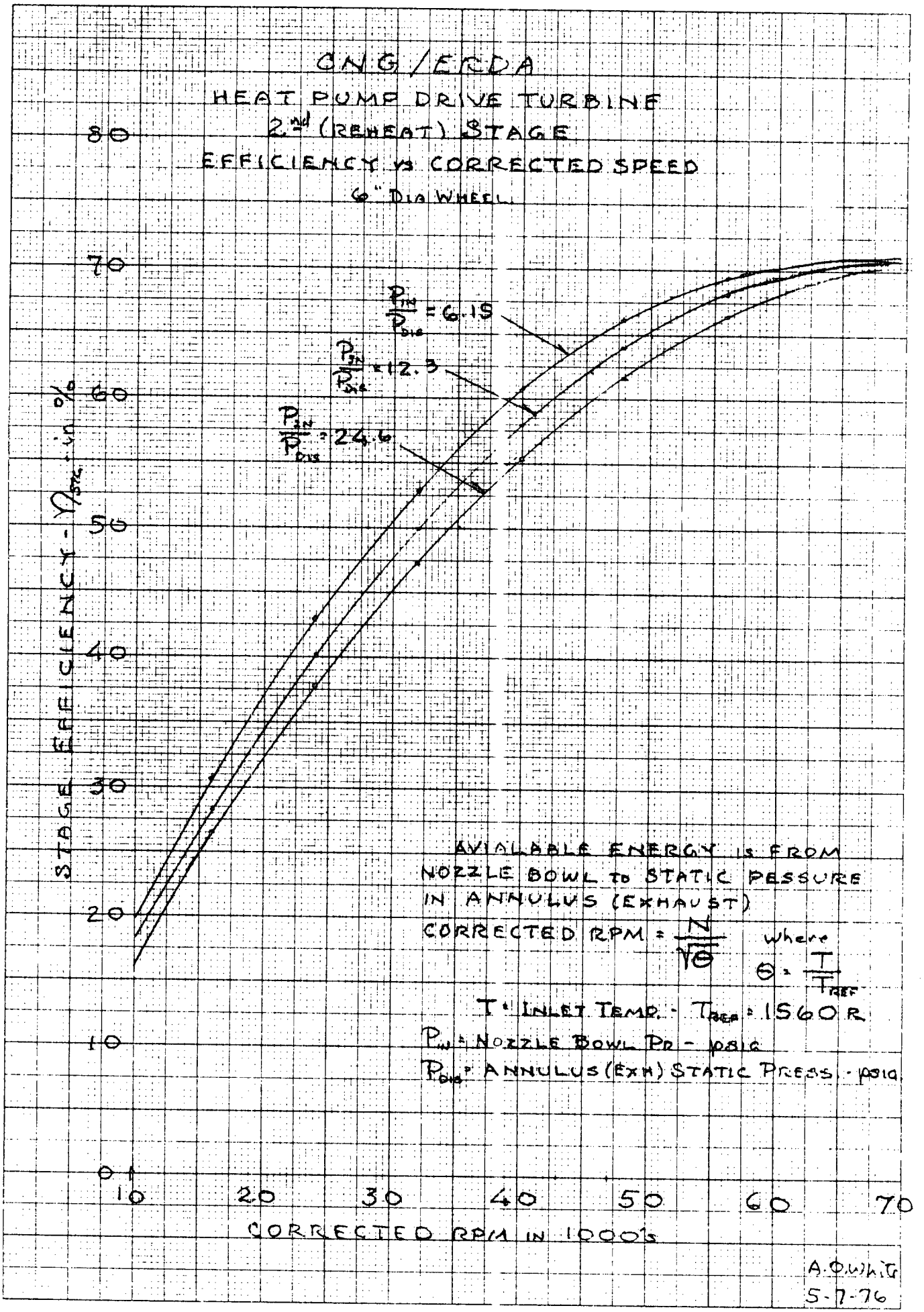
CNG/ERDA
HEAT PUMP DRIVE TURBINE
2nd (REHEAT) STAGE
EFFICIENCY vs CORRECTED SPEED
6" DIA WHEEL
P_{IN}/P_{DIS} = 6.15
P_{IN}/P_{DIS} = 12.3
P_{IN}/P_{DIS} = 24.6
STAGE EFFICIENCY - η_{STG} - in %
80
70
60
50
40
30
20
10
0
10
20
30
40
50
60
70
CORRECTED RPM in 1000's
AVIALABLE ENERGY IS FROM NOZZLE BOWL TO STATIC PESSURE IN ANNULUS (EXHAUST)
CORRECTED RPM = $\frac{N}{\sqrt{\theta}}$ where $\theta = \frac{T}{T_{REF}}$
T = INLET TEMP. - T_{REF} = 1560 R
P_{IN} = NOZZLE BOWL PR - psia
P_{DIS} = ANNULUS (EXH) STATIC PRESS. - psia
A.O.White
5-7-76

Fig 6

V. APPLICATION OF LINHARDT & SILVERN'S EQUATIONS

Linhardt and Silvern (Ref. 6) give generalized equations for the calculation of a re-entry turbine efficiency without reheat. These are given in Fig. 8 of their paper and take the form:

$$\eta_T = \eta_h (1 - L_t) - L_b - L_d$$

where

$$\eta_h = \left(\frac{4}{154}\right) N_s D_s \left\{1 + \bar{\psi}_R \left[1 - \frac{t}{4a_I}\left(1 + \frac{a_I}{a_{II}}\right)\right]\right\} \times \left(\bar{\psi}_N \cos\alpha - \frac{N_s D_s}{154}\right)$$

while these relations do not apply directly to a reheat, re-entry turbine, it was thought worthwhile to use the equations, with the corresponding coefficients as given in the paper, to work out the turbine efficiency for a non-reheat unit, for a range of initial pressures at the specific speeds and optimum diameters as given in Section III for the original assumptions.

The corresponding inputs to the calculation are given in Table I. The resulting efficiencies are plotted versus Initial Pressure in Fig. 7, which gives a picture of the overall efficiencies that can be realized in small re-entry turbine suitable for this specific application, at an operating speed of 40000 rpm. Higher speeds will improve the efficiency as can be observed from Figs. 5 and 6.

TABLE I

GAS FIRED HEAT PUMP

Turbine Study

Data for Re-Entry Turbine Calc. - NRH

Fig. 8 of Linhardt & Silvern's Paper

Initial Pr. psia	100	200	300	400
N_s	8.025	7.26	6.63	6.33
D_s	6	6.1	6.7	6.9
k	1.3	1.3	1.3	1.3
$\overline{\psi}_R$		Equation 3B		
K_1		Equation 5B		
K_2		Equation 6B		
$\overline{\psi}_H$	Use Equation [18]-pg. 301-i.e. $1/2\left[\psi_{N_1}\frac{C_{a_I}}{C_o} + \psi_{N_2}\frac{C_{o_{II}}}{C_o}\right]$			
α	16°	16°	16°	16°
$\left\{\frac{1+\frac{K_1}{K_2}}{4xZ}\left(1+\frac{K_2}{K_1}\right)\right\}$ -substitute- $\frac{t}{4a_1}\left(1+\frac{a_I}{a_{II}}\right)$				
t	.276	.210	.179	.159
No. of buckets	92	117	142	160
a_I - inches	.835	.635	.540	.471
a_{II} - inches	5.28	5.53	5.69	5.73
a_I/a_{II}	.158	.1145	.0950	.082
$\psi_{R_I} = \psi_{R_{II}} = [1 - 0.228\,(1 - \frac{\beta°}{90°})^2]\,[1 - .05\,(M_w - 1)^2]\,[1 - .06\,(\frac{C}{h})]$				
C - inches	.435	.330	.282	.250
h - inches	.290	.220	.188	.167
β	27°	26°	26°	26°
M_{w_I}	1.175	1.34	1.41	1.43
$M_{w_{II}}$	1.082	1.25	1.30	1.34
$\psi_{N_I} = \psi_{N_{II}}$	.96	.95	.94	.93
C_{o_I}	3700	3940	4060	4125
$C_{o_{II}}$	3280	3400	3490	3530
C_o	4730	4950	5070	5160
K_3		Equation 7B		

Table I - continued

Data for Re-Entry Turbine Calc. - NRH

Pr_{tot}	50	100	150	200
g	32.2			32.2
η_{tot}	.52	.54	.49	.45
δ_{tot}	.02	.01	.0066	.005
C_F	2/3	2/3	2/3	2/3
C*-inches	.005	.005	.005	.005
D-inches (tip)	8.58	8.25	8.45	8.45
Initial Pr	100	200	300	400
$\delta_I = \delta_{II}$	.1413	.1000	.0820	.0705
η_I	.78	.81	.84	.84
C^*_T - inches				
C_D	.35	.35	.35	.35
$Pr_I = Pr_{II}$	7.06	10.0	12.2	14.13
C_{F_T}	2/3	2/3	2/3	2/3
M_{i_2}	1.95	2.16	2.28	2.37
K_D	.0002568			
K_B	1.5×10^{-3}			
$\varepsilon = \left(\frac{a_1 + a_2}{D}\right)$	.227	.238	.234	.233

KEUFFEL & ESSER CO. 46 1320

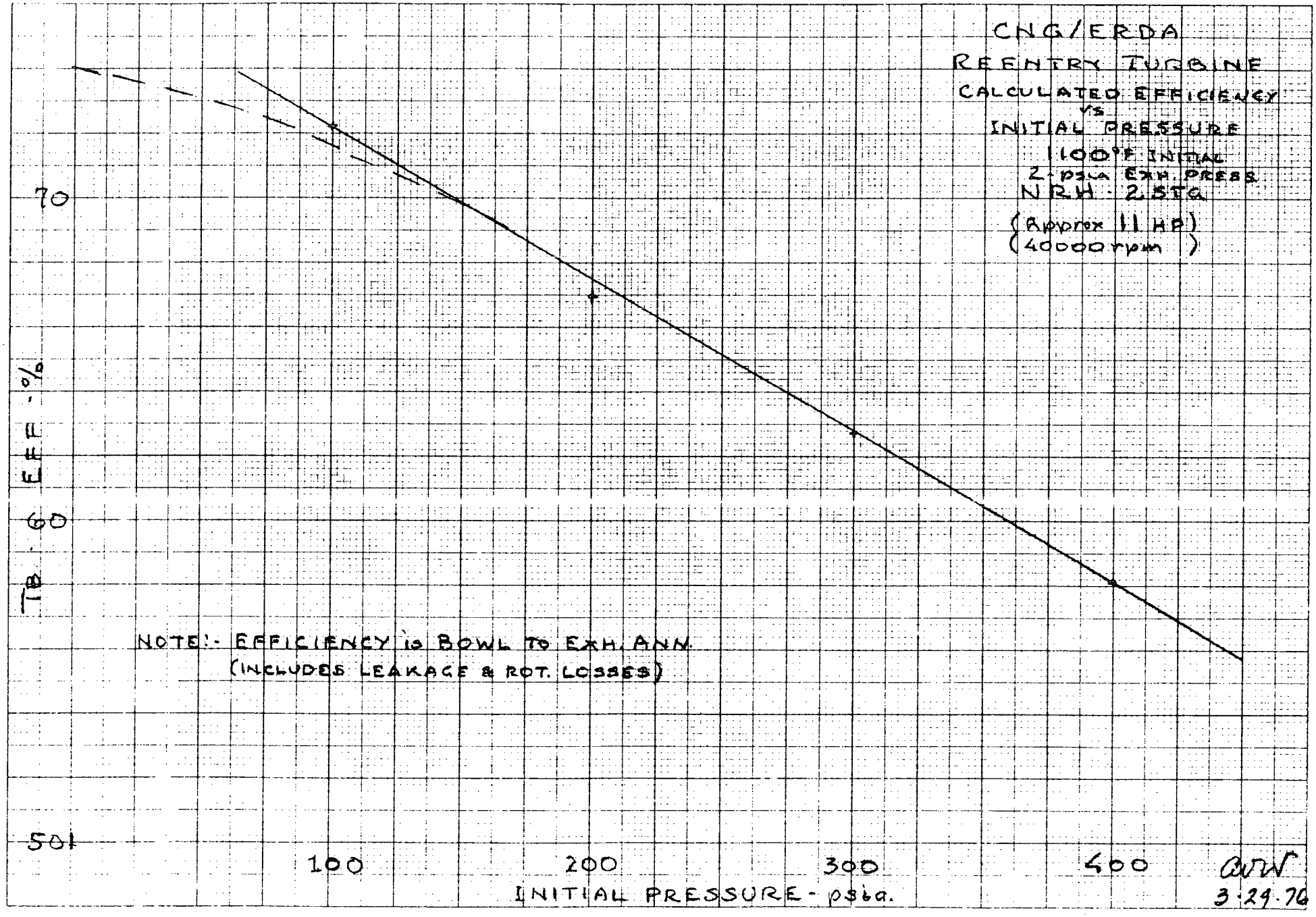

FIG 7

VI. DESIGN LAYOUT CALCULATIONS

The system studies provided the operating conditions for the turbine over a range of operating parameters. From these a "Design Point" was selected for the detail layout of the turbine. The "Design Point" conditions are:

50000 rpm - 56.5 lb/hr - flow
Inlet - 213 psia - 1100 F
1st Stage Exh. D_R = 20.88 psia
2nd Stg. Inlet - 20.3 psia - 1100 F
Exhaust - 2.082 psia

Preliminary layouts had established a nozzle configuration using reamed nozzles set at 15° on an exit diameter of 5.347". The corresponding nozzle dimensions are:

	1st Stg.	2nd Stg.
Flow	56.5 lb/hr	53.5 lb/hr
Throat Area	.00733 in^2	.0723 in^2
Throat Diameter	.0966 in	.0960 in.
A_{exit}/A_{throat}	2.35	2.38
Exit Diameter	.1481 in.	.1481 in.
No. of Nozzles	1	10

Ref. 6 derives an equation for the optimum blade height over diameter ratio, h/D as follows:

$$\left(\frac{h}{D}\right)_{opt} = \sqrt{\frac{\sin 2\beta}{4D_s^2 \sin \alpha \sqrt{2g}}}$$

for the design conditions, α = 15° and β = 21°-40' for the first stage and 21°-50' for the second stage.

The corresponding (h/D) opt. are .0189 for the first stage and .0601 for the second stage. Assuming a tip diameter of 5.75", the corresponding heights, h are .1086" for the first stage and .345" for the second. However, since the same bucket is used for both stages, both dimensions can't be satisfied. The average would be .2268".

Based on a nozzle mouth height (exit diameter) of .1481", a bucket height of .2268" would seem to give excessive overlaps. A check of the stage dimensions given by the Russian data in Ref. 1 would indicate the bucket height should be .1763", giving reasonable overlaps.

The bucket exit throat area, and corresponding bucket heights can also be calculated from the corresponding velocity diagrams. Assuming a bucket coefficient of .87 (on the high side) and an exit stream angle of 22° ($\sin \beta = .3746$) the calculated heights for a 5.347" P.D. are:

1st Stg. = .0957" 2nd Stg. = .0987"

Since both these are less than the nozzle diameter they obviously cannot be used.

A bucket height of .175" was finally chosen, which assuming an exit $S/t = \sin 22°$ or thereabouts, means the bucket will not be filled, i.e., it has approximately 100% excess area, with the reamed nozzles. Even assuming a bucket energy coefficient $\psi_R = .75$ (as originally calculated) the buckets will still have nearly 100% excess area.

Subsequent to the completion of the preliminary design, discussions were held with Mr. André Stromquist, culminating in a meeting in Cleveland at which the design was reviewed in some detail. While in agreement with the general philosophy and proportions of the turbine design, Mr. Stromquist strongly recommended that rectangular supersonic nozzles be used, in place of the reamed nozzles, particularly for the second expansion.

While Mr. Stromquist's estimate of the efficiency improvement that could be realized by using a rectangular nozzle were rather more than we would have predicted, the high importance of any significant improvement in performance led to a decision to make the necessary design changes and go to a rectangular nozzle design.

This required a minor modification to the bucket vane section to give the required inlet and exit area (and area ratios) and provide a slightly diverging bucket passage to accommodate the supersonic flow conditions. The bucket

height was maintained at .175" and a nozzle mouth height (NMH) of .160" adopted. This gave a reasonable overlap considering the calculated expansions and movements of the nozzle box and wheel.

The corresponding supersonic nozzles were laid out to give a .00733 sq. in. throat area, with a throat to exit area ratio of 2.14 to give an exit area of .01568 sq. in. The nozzle nominal angle as defined by its S/t ratio was reduced to 14°, an S/t = .24192. With the NMH of .160", this gives a passage exit width of .0980" and a pitch of .4051".

The throat height was set at .140" with a corresponding width of .0524". One nozzle passage is used for the first expansion and ten (10) nozzle passages for the second expansion. It was agreed in the discussions with Mr. Stromquist that the first expansion nozzle should be ahead of the second expansion nozzles, in the direction of rotation, which also agrees with the desired arrangement of the steam inlet passages to keep the nozzle box at as uniform a temperature as possible. Final layouts of the turbine are being made on this basis.

The velocity diagrams for the first and second expansions give an absolute leaving velocity of 1602 and 1487 fps (based on a bucket coefficient of .87) at an angle of 39°-20' and 40°-40' respectively.

As a check on the efficiencies used in the system calculations, the stage efficiencies were calculated using the equations of Ref. 6, except that the rotation loss of the disk was based on the equation and coefficients of Ref. 8. The efficiencies so calculated were 66.49% for the First Stage and 65.25% for the Second Stage: a very good agreement with Figs. 5 and 6. These calculations incorporated the corrections to the nozzle coefficients and bucket coefficients found by Linhardt and Silvern to be required to make a calculated efficiency agree with their test results, so there is a reasonable expectation that the efficiencies used in the system calculations can be attained.

As a further check, Mr. Stromquist has independently calculated the efficiency and output of the turbine, assuming rectangular nozzles, for several operating conditions, as tabulated below:

	Rectangular Nozzles					Conical Nozzles
	50,000 rpm 100:1 P_r	50,000 rpm 50:1 P_r	50,000 rpm 200:1 P_r	50,000 rpm 100:1 P_r	50,000 rpm 50:1 P_r	50,000 rpm 100:1 P_r
1st Stage-HP/7	3.87/.57	1.94/.57	7.74/.57	3.18/.46	1.59/.46	3.72/.54
2nd Stage-HP/7	3.25/.66	1.18/.65	6.98/.59	2.78/.53	1.14/.58	2.36/.61
Flow 1st/2nd	56.5/40.7	28.2/20.4	113/80.5	56.5/43.6	28.2/21.8	56.5/32.3

VII. EXHAUST DIFFUSERS AND CONNECTIONS

It is hoped that some improvement in overall efficiency of the turbine and the cycle can be obtained by the proper design and orientation of the exhaust passages from both the first and second stages, to obtain some diffusion and recovery of a significant portion of the leaving energy.

However, high velocity at the bucket exit, and the partial arc conditions will make it difficult to make good diffusers even when matched up to the stream angle. In addition, the angular location and required arc for the exhaust opening cannot be determined analytically.

The exhaust passage from the first stage is therefore being designed with considerable geometric flexibility. The passage immediately following the bucket is being designed with turning vanes to turn the stream from the absolute leaving angle to an axial direction. The length of arc, and corresponding number of passages can be made 1x, 1-1/2x and 2x the nozzle arc, and the angular location with respect to the nozzle can be varied on the test turbine. The length of the cylindrical passage between the turning vanes and a conical diffuser section can also be varied on the test turbine. The optimum combination will be determined on test and incorporated in the final design.

The discharge from the end of the collector (diffuser) space will be via a pipe connection, not less than .677" dia., which will keep the pipe velocity below 12000 fpm at design flow. The velocity was chosen on the high side to keep passage and pipe sizes low, since losses at this point are partially recoverable in the following expansion (less heat added in reheater).

For the second stage, the same situation holds, although the gain due to pressure recovery is somewhat less. Therefore, the inner and outer walls will be the same as for the first stage exhaust, but with a corresponding increase in arc to match up with the 10 second stage nozzles. At the end of the passage, the flow will dump radially inward into the circular exhaust connection which is co-axial with the turbine axis. The exhaust velocity to the condenser will be limited to about 9000 fpm, which will require a 2.5" ID connection.

VIII. SUPERSONIC DESIGN CONSIDERATIONS

At the pressures and temperatures involved, velocities in the steam path are generally supersonic. Theoretically there should be some gain in efficiency by designing both the nozzle and bucket passages with supersonic contours. However, due to the very small size of the passages, the deviation of a true supersonic contour from the simpler straight taper that will be used in the nozzle, and essentially uniformly increasing width passage that will be used for the bucket will be measured in thousandths of an inch.

The corresponding accuracy required in machining is probably practically not realizable, and since the relative Mach Numbers are low, where the difference between a simple blade passage and the so-called "supersonic blade passage" is small as indicated by Fig. 14 of Ref. 6, the design will be based on non-supersonic shapes.

IX. BUCKET GEOMETRY

As indicated above in discussing supersonic considerations, the bucket section design will be based on simple geometry to give an increasing width passage.

The calculation of the bucket entrance and exit requirements from the velocity diagram gives the necessary S/t ratios at the entrance and exit, which are to be provided by the geometry.

Balje (Ref. 4) recommends that the pitch/chord ratio for the buckets be between .5 and .8. Ref. 6 also notes that the basic equation for the blade coefficient is based on the assumption that the ratio of the trailing edge thickness to the spacing (in circumferential direction) is smaller than 0.02.

A preliminary rough check of the bucket bending stresses indicated that an acceptable stress level could be reached with a bucket chord (width) as small as .170". For a t/c = .75 the pitch (at the pitch line) for 132 buckets is .12725". The corresponding edge thickness at .02 ratio would be only .00245" which is considered too thin for practical service.

Therefore, an edge thickness of .0065" was chosen, somewhat arbitrarily as representing a practical lower limit, and the vane section laid out on that basis. Fig. 8 shows the bucket section as presently laid out.

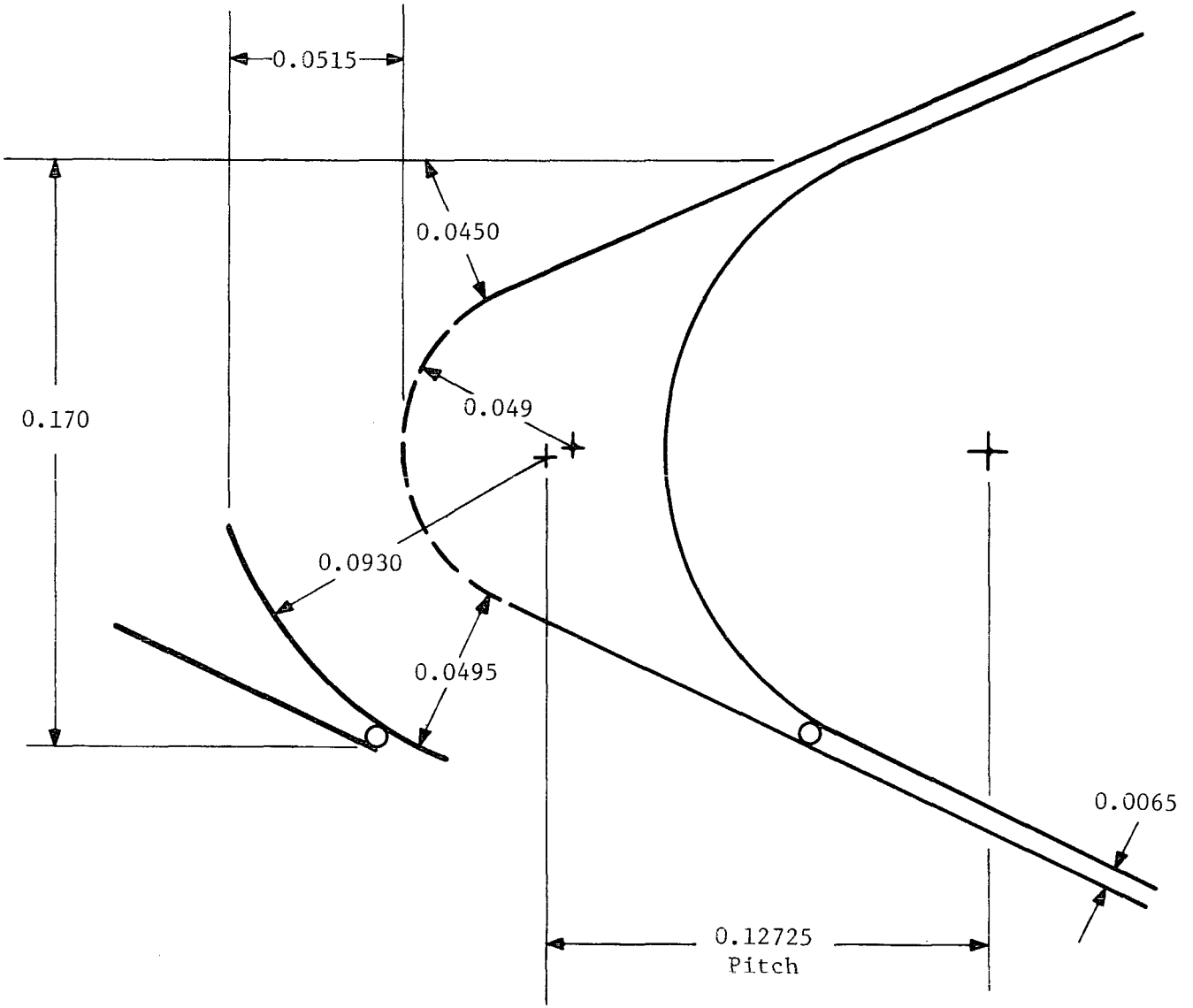

801887

Fig. 8

X. BUCKET STRESSES

Bucket tensile stress and Manson Disk hub stress calculations have been made for the CNG turbine design, taken from M.T.I. drawing number 343D014. The results show that when operating at an overspeed condition of 70,000 rpm for the titanium alloy specified, the stresses are at acceptable levels with the bucket tensile stresses at 19,400 psi, and the maximum radial and average tangential stresses in the hub equal to 42,900 and 37,800 psi respectively.

The bucket tensile stress calculation considers the centrifugal blade and shroud load carried by the blade root area as follows:

1) $\frac{\text{Shroud wt.}}{\text{Blade}} = \frac{\rho \pi L\ (Ro^2 - Ri^2)}{N}$ $\qquad \frac{\text{lbs}}{\text{in}^3}\ (\text{in})\ (\text{in}^2)$

$$= \frac{.16\ \pi\ (.17)(2.836^2 - 2.7735^2)}{132}$$

$$= 2.27 \times 10^{-4} \text{ lbs.}$$

2) $\underline{\text{Blade wt.}} = \rho h\ A$ $\qquad \frac{\text{lbs}}{\text{in}^3}\ (\text{in})\ (\text{in}^2)$

$$= .16(.2)(.0102)$$

$$= 3.264 \times 10^{-4} \text{ lbs.}$$

3) $F = \frac{Wa}{g}$ $\qquad \frac{W}{g} = \frac{2.27 \times 10^{-4} + 3.264 \times 10^{-4}}{386}$

$$= 1.434 \times 10^{-6}$$

$$a = rW^2$$

$$= 2.5735\ \left(\frac{70000\ \pi}{30}\right)^2$$

$$= 1.383 \times 10^8$$

4) $\sigma = F/A$ $\quad F = 1.434 \times 10^{-6}/1.383 \times 10^{8} = 198.3$ lbs.

$A = .0102 \text{ in}^2$

$\therefore \sigma = 19{,}400$ psi

The calculation method used for the turbine wheel hub stresses is the Manson Disk Stress Analysis Computer Program (PN065), which assumes a symmetrical disk with no bending or stress concentrating geometry factors. A density of 0.16 lbs/in^3 and Poisson's ratio of 0.3 were used to represent the titanium alloy, with a thermal coefficient of expansion and temperature rise, of 5.8×10^{-6} in/in/°F and 800°F respectively, used for the thermal growths.

The attached figure shows the radial and tangential stresses and radial growth versus radius for the turbine disk. A radial bucket loading of 9700 psi was placed at the 2.58 in. radius location. The average tangential stress is 42.9 Kpsi with the maximum radial stress equal to 37.8Kpsi. The maximum tangential stress at the bore is approximately 68.1Kpsi. The maximum radial growth is approximately 15.7 mils at the 2.58 in radius location

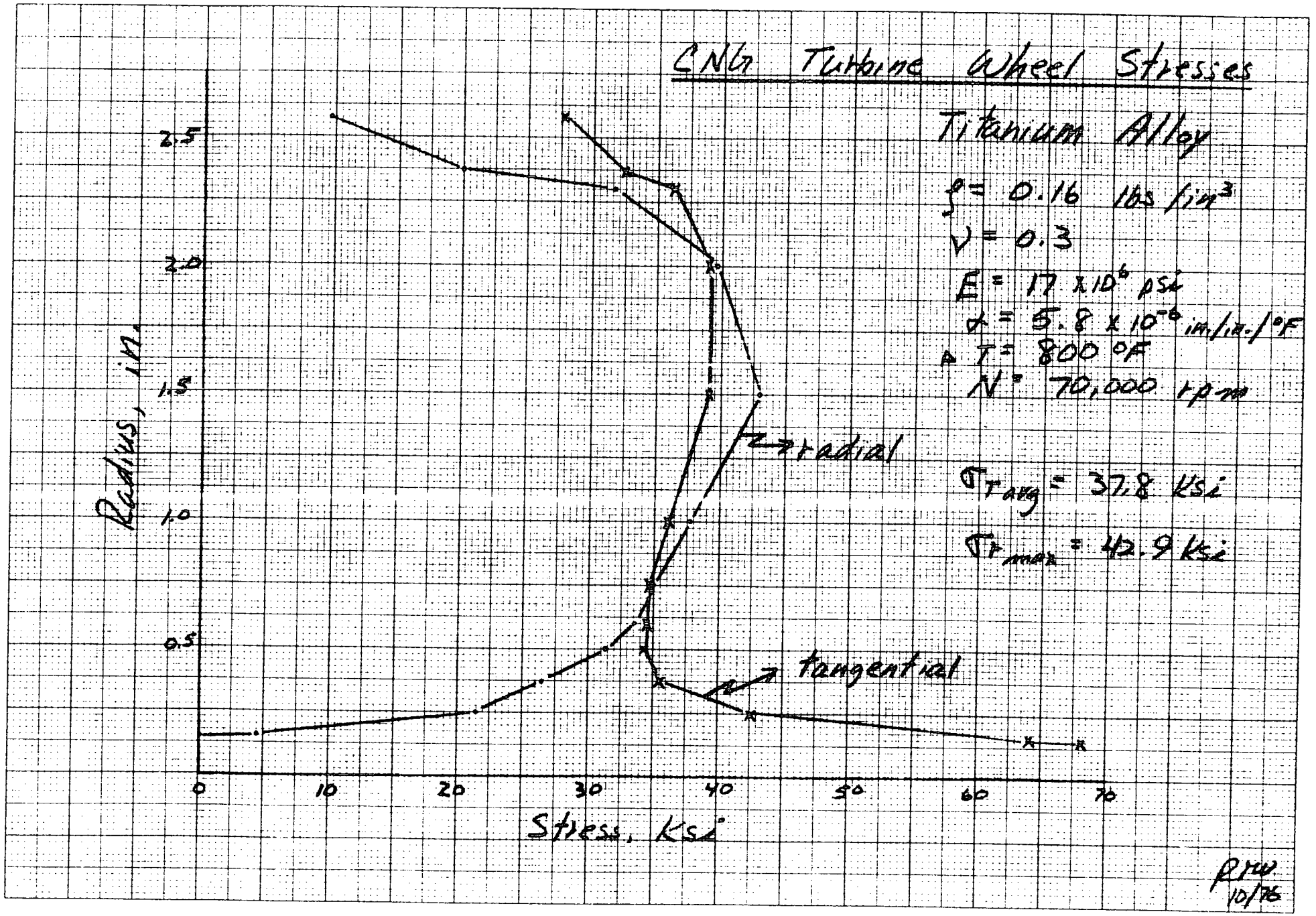
CNG Turbine Wheel Stresses
Titanium Alloy
ρ = 0.16 lbs/in³
ν = 0.3
E = 17 x 10⁶ psi
α = 5.8 x 10⁻⁶ in./in./°F
ΔT = 800 °F
N = 70,000 rpm
σr avg = 37.8 ksi
σr max = 42.9 ksi
radial
tangential
Radius, in.
Stress, ksi
0
10
20
30
40
50
60
70
0.5
1.0
1.5
2.0
2.5
RTW
10/76

XI. SHROUDING & LEAKAGE LOSSES

The use of shrouding (or covers) on the buckets involves both stress and leakage conditions. A continuous cover, electron beam welded to the buckets will effect some reduction in leakage, and definitely reduce the root bending stresses, at the expense of a considerable increase in the bucket root centrifugal stresses.

Steam turbines using rotor and diaphragm construction (impulse type) normally use bucket covers, while gas turbines normally do not. Experience indicates that for stages with low reaction (impulse) at the tip, the cover has little effect on efficiency, while for stages with high reaction, it offers a definite improvement.

However, since this turbine is of the partial arc, re-entry type, there would seem to be some gain in reduced tangential tip leakage by using bucket covers (or a shroud). It should be noted that Ref. 6 in Fig. 17 also neglects the radial (tip) clearance leakage and losses when both nozzles are on the same side of the wheel, as in this reheat turbine design.

Accordingly, the use of a cover for the buckets was adopted, since bucket stress considerations allowed it and there was a potential gain in efficiency.

In addition to the tangential or circumferential leakages discussed in Linhardt and Silvern's paper,Ref. 6, Mr. Stromquist has pointed out that there is an additional leakage, or more properly a carry-over loss that is not analyzed, or apparently properly accounted for by Linhardt and Silvern.

This loss consists of the steam that is trapped in the bucket passages as they leave the first expansion exhaust port and is carried over directly into the turbine exhaust, without doing any further work in the bucket. Calculated purely as a carry-over loss, this amounts to about 24% on the second expansion.

Since the data of Linhardt and Silvern do not indicate a loss of any such magnitude (see Fig. 13 of Ref. 6), we will attempt to measure the magnitude of this loss by testing the turbine, on air, and measuring the turbine inlet

flow, the flow from the first expansion discharge passage, and the flow from the exhaust when the exhaust is maintained under vacuum, with no air flow to the second expansion nozzles. This should give a measure of the leakage and carry-over flows and corresponding losses.

The straight leakage losses will be kept to a minimum by running as close a clearance between the nozzle and bucket, and between the bucket and downstream casing wall, and between the bucket cover and the casing walls, as is mechanically feasible.

ATTACHMENT B

DESIGN REPORT - CNG COMPRESSOR

DESIGN REPORT

CNG COMPRESSOR

By

Val Smith

Prepared For:

CONSOLIDATED NATURAL GAS COMPANY, INC.
Cleveland, Ohio

Prepared by:

MECHANICAL TECHNOLOGY INCORPORATED

October 8, 1976

DESIGN REPORT – CNG COMPRESSOR

1.0 INTRODUCTION

This report gives details of the design of the CNG compressor. The unit is to operate on Freon 11 gas at moderate specific speed and at conditions corresponding to relative Mach numbers in the region of unity at the inducer and at the impeller tip. Efficiency is to be maintained as high as possible at large overspeed and under-speed from the design point. The volume flow is small and manufacturing considerations have considerable influence.

The principal design tools used are the in-house computer programs, for performance predictions and internal analysis, but checks have been made to ensure that the results are in-line with previous experience on similar machines.

The input data is first established, followed by fundamental decisions on the design features. Basic sizes and proportions are determined, and followed by computer checks of performance on an overall basis. The design layout details were then found and modified as appropriate according to the indications of the internal analysis program.

The principal conclusions are then given with suggestions of the probable steps required in development.

2.0 BASIC SPECIFICATIONS

The machine is to operate on Freon 11 (See Section 3.0) and have a best design point at 50,000 rpm without seriously compromising the performance at two secondary design points at 40,000 and 60,000 rpm (speeds are approximate). A desired positive and negative flow variation at each speed is also given.

The details of the three design points, together with desired values, are given in Table 1 and shown in Figure 1.

A further requirement is that the machine is to have inlet guide vanes and operate at a near-shut-off condition. This has not been allowed to influence the design, and the inlet vane setting and corresponding performance to meet this large off-design specification will be determined experimentally to optimize the whole system performance.

3.0 GAS PROPERTIES

Freon 11 is not a perfect gas and consideration is to be given to the variation of the gas properties through the process. However, in general, the change in pressure and temperature through the machine is small enough that constant values can be assumed for initial design purposes.

Figure 2 shows the change in gas properties with temperature and pressure. The table below shows the constant values assumed and derived values.

TABLE 1

DESIGN SPECIFICATIONS

P_1 ref. = 4.35 psia ; T_1 ref. = 490°R

Actual Speed, rpm	40,000	50,000	60,000
Inlet Temperature, °F (°R)	63(523)	44(504)	35(495)
Inlet Stag. pressure, psia	9.30	5.10	2.65
Minimum Efficiency, %	71.5	75	70
Flow lbs/hr (lbs/sec)	1150 (0.320)	850(0.236)	650(0.180)
$N/\sqrt{\theta}$	38725	49300	59700
$\omega\sqrt{\theta}/\delta$	555.6	735.8	1072.7
Outlet Pressure, psia	25.5	20.0	17.6
Total Pressure Ratio	2.74	3.92	6.64
$\omega\sqrt{\theta}/\delta$ Surge (%)	515(92.7)	690(93.8)	980(91.4)
Choke (%)	580(104.4)	780(106.0)	1125(104.9)

Derived Values

Inlet Vol. flow Q_1 des. cfm	82.2	106.8	156.6
(Stagnation) Surge	76.2	100.2	143.1
Choke	85.8	113.2	164.3
Available head, ft.lbs/lb	6075	8144	11610
Temperature rise ΔT °F	79	105	161
Horsepower	4.94	4.70	5.43
Specific Speed	68	78	87
Optimum Rotor Diameter, Inches	3.18	3.03	2.99

NOTE:

a) "Surge" and "choke" are not stability limits but minimum and maximum flow operating points.

b) Optimum rotor diameter from N_s-η_s diagram.

COMPRESSOR PERFORMANCE

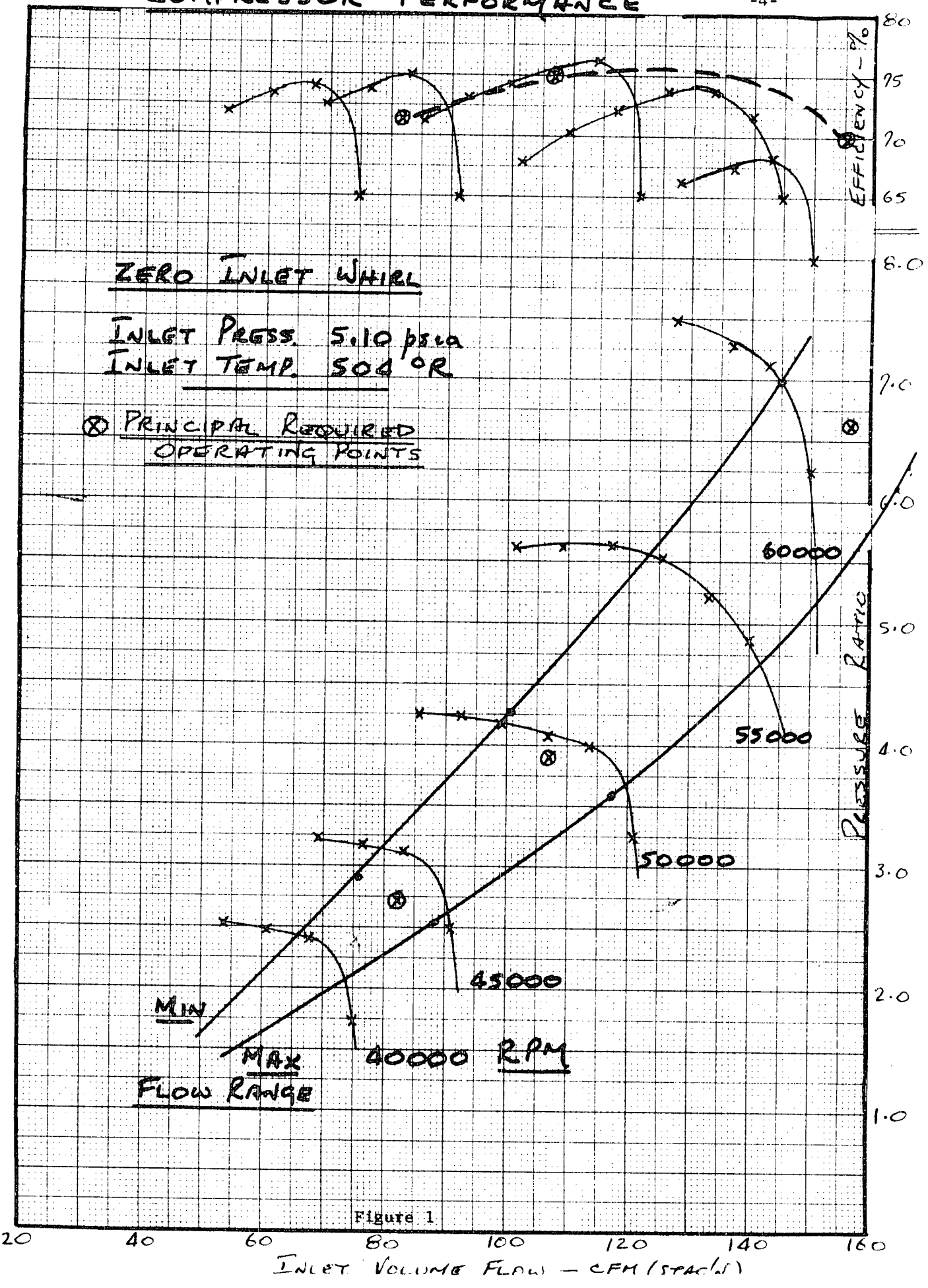

Figure 1

46 1320
K+E 10 X 10 TO ½ INCH 7 X 10 INCHES KEUFFEL & ESSER CO. MADE IN U.S.A.

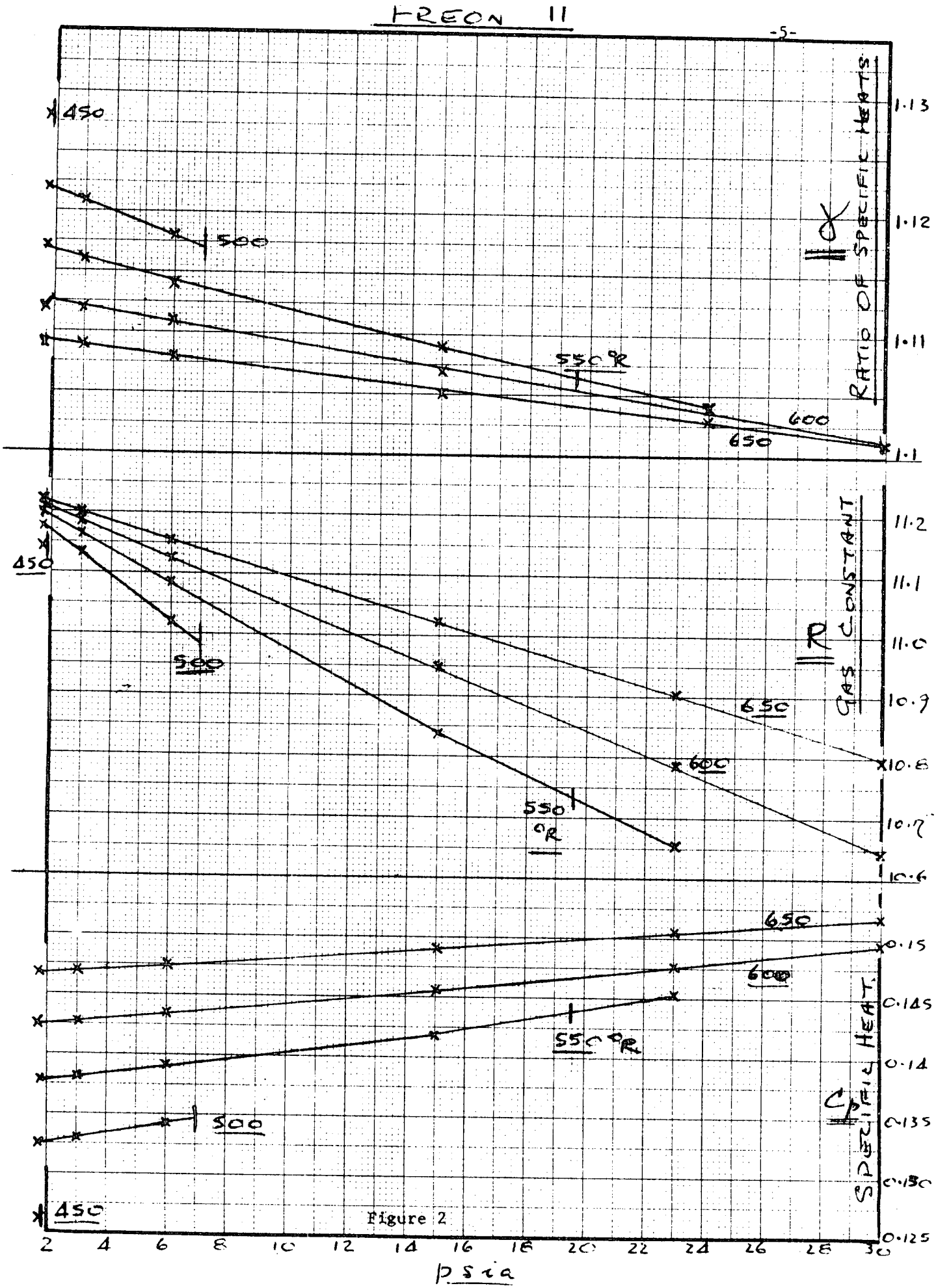

Figure 2

46 1320
K+E 10 X 10 TO ½ INCH 7 X 10 INCHES KEUFFEL & ESSER CO. MADE IN U.S.A.

Speed, RPM	40,000	50,000	60,000
Specific heat, Btu/lb^{o}F	0.138	0.134	0.1325
Gas constant "R", ft-lbs/lb^{o}F	10.945	11.00	11.17
Ratio of specific heats	1.1135	1.1180	1.1215
Viscosity μ, lbs/ft.sec x 10^6	7.03	7.00	6.99
*Inlet density, lbs/ft^3	0.234	0.1325	0.069
*Inlet acoustic velocity, ft/sec	453	447	447

Compressibility factor = 0.954

Temperature exponent of viscosity = 1.243

*Stagnation values.

4.0 PREDETERMINED DESIGN FEATURES

The basic specification is such as to indicate that certain design details will prove advantageous, as shown by previous experience, and can be included from the beginning.

4.1 Inducer Eye Diameters

The relative velocity on to the inducer tip will approach Mach Number unity at design speed of 50,000 rpm, and possibly exceed 1.0 at maximum overspeed 60,000 rpm. These eye diameters are, therefore, to be proportioned to give the minimum relative Mach Number at the tip in the usual way, but because of the small eye and relatively thick inducer blades (minimum thickness limited by manufacturing considerations), the optimization must take account of inducer blockage. The inducer blade leading edge is to be as thin as practical, and the curvature to the throat is to be as low as possible to minimize losses from any shock system.

4.2 Number of Impeller Blades

The normal minimum for machines of this rating is about 16 blades; maximum for reduced friction drag and exit wake losses is about 24. However, in this range, it would be difficult to avoid inducer choking without considerable incidence and turning loss. Splitter vanes are therefore required, and the

number of full blades will be 8 to 12 (one splitter per pitch) or 8 blades (two splitters per pitch).

To favor the eye, it was decided to have 8 full blades (with, however, a correspondingly long inducer required for minimum solidity) and 8 splitter vanes.

4.3 Shrouded Wheel

To minimize leakage, it was decided to take advantage of the potential improvement of a fully shrouded wheel. This presupposes that satisfactory sealing between the shroud and the outer casing can be achieved.

4.4 Impeller Blade Profile (Sweepback)

The impeller tip speed will be low and liberties can be taken with the blade design from the point of view of acceptable stress limits.

Sweepback is desirable to emphasize the loading in to the more efficient impeller rather than the diffuser, and to reduce the Mach Number into the diffuser. It is to be noted, however, that increasing sweepback increases impeller loading, increases impeller diameter (more friction drag losses), and reduces tip width (increased diffusion losses).

For unshrouded wheels, the optimum is in the range 20-25° at the specific speed of this design, and about 30°-35° for shrouded wheels. Because the actual physical size is small so that manufacturing tolerances are significant in affecting flow areas, it was decided to choose 30° (shrouded wheel) for maximum impeller tip and diffuser width.

4.5 Diffuser System

The high tip Mach Number will require a vaned diffuser to prevent recirculation losses from the high radial pressure gradient and to reduce the overall diameter. The vanes will be thin with only small relative turning.

However, some vaneless space between the impeller tip and the diffuser vanes will be required in order to stabilize the flow and to reduce the incident Mach Number into the vanes.

4.6 Outlet

The outlet is to be a standard single-exit scroll with an exit conical diffuser.

5.0 INITIAL DESIGN

The initial design was performed for purposes of first entering into the computer program for performance prediction, subsequent modifications to be performed in the program.

5.1 Impeller Sizing

Calculations were based on a "fundamental" efficiency of the compressor of 82% (75% specification). This assumes 2% leakage loss front and rear each, and 3% disk windage drag (total front and rear by approximate calculation) all of which lower the net observed efficiency but do not affect the basic blading design except for flow area. These losses change local temperatures and Mach Numbers to only a negligible degree.

The basic results were:

Impeller diameter	3.00 inches
Sweepback angle	30°
Number of blades at tip	16

and hence:

Impeller tip speed	655 ft/sec
Absolute tip gas angle	20°
Impeller tip width	0.080 inches
Absolute tip Mach Number	1.210
Machine Mach Number	1.465
Machine Reynolds Number	3.10×10^{6}

This was considered satisfactory for a first insertion into the computer. In

particular it is noted that the Reynolds Number is satisfactorily high.

5.2 Inducer Proportions

For inducer sizing a hub/tip ratio of 0.316 was assumed (annulus area = 90% of eye area). This is the minimum practical value for acceptable blade design at the hub.

Without consideration of vane blockage the minimum relative Mach Number at the inducer tip is achieved at an eye diameter of 1.42 inches. However, assuming 8 blades of average thickness 0.050 inches, the required eye diameter is 1.53 inches. This was used for first insertion into the computer program.

5.3 Diffuser System

The first trial values for the vaneless and vaned space diameter ratios were 1.20 and 1.25. From experience, it was known that the vaned space ratio would be close to optimum, but it was expected (and later confirmed) that a smaller vaneless space would be required.

6.0 RESULTS OF PERFORMANCE COMPUTATIONS

The first computer run revealed, as expected, problems of premature choking in the inducer and diffuser, and excessive loss in the vaneless space. The underspeed and overspeed curves were displaced relative to their design points as shown earlier. However, it was shown that the target efficiency should be achievable.

In successive runs supported by hand calculations, the design was adjusted until it was considered satisfactory. The principal changes involved were:

a) Reduction of inducer throat choking by a small increase in eye diameter, by calling for positive incidence at the design point, and by thinning of the blades to the practical minimum.

b) Balancing of the vaneless/vaned diffuser losses by reduction of the vaneless space and by widening of the passage.

c) Increase of vaned diffuser choke capacity by thinning of the vanes and by positive incidence setting at design.

The predicted performance is shown in Figure 1 and design details are in Tables 2 and 3.

6.1 Comments on Performance Map

Figure 1 shows the predicted performance, finally adjusted for parasitic losses, and the three specification points.

The curves have adequate flow range for the system operation and the efficiency is satisfactorily high up to 55,000 rpm. The two lower specification points are well covered but the highest point is not achieved in efficiency.

At 55,000 and 60,000 rpm, the maximum flow is limited by inducer choke. If correction is attempted by increase in the eye area, the increase in incidence (aready 5°) at lower speeds will certainly deteriorate the performance, and similarly if the inducer angle is increased.

However, subsequent to this computation, it was decided that the inducer leading edge can be made thinner than assumed (presently 0.030 ins. average), sufficient to increase the inducer throat area about 5%. The top specification point would then be at 60,000 rpm at an efficiency of 65%, (5% deficient), but if this point can be moved to a lower flow (with higher pressure ratio) an efficiency of 68% is available (2% deficient).

At these extreme requirements, the performance is very dependent on fine tuning of the components, particularly the match between the impeller and diffuser characteristics. This can be done properly only through experiment, which, in this case, requires small-scale changes in impeller diameter and diffuser width. Given careful adjustment to the design there is every possibility that the required efficiency can be achieved, although probably at a slightly lower flow and higher pressure ratio.

Finally, it is to be remembered that the predicted efficiency is based on the assumption of 4% gas leakage from the impeller tip at 50,000 rpm, and prorated at other speeds. At 60,000 rpm, the leakage is 6.4%. Any reduction in this amount by efficient sealing will be directly reflected in a corresponding increase in compressor efficiency.

TABLE 2

DESIGN DETAILS

Eye Hub Diameter	0.45 inches
Eye Diameter	1.55 inches
Impeller Diameter	3.00 inches
Impeller Tip Width	0.090 inches
Impeller Tip Blade Angle	30°
Impeller Tip Blade Thickness	0.040 inches
Number of Blades	8 + 8 Splitters
Splitter Leading Edge Diameter	1.70 inches
Inducer Tip Angle	33°
Average Inducer L.E. Thickness	0.030 inches
Total Inducer Throat Area	1.046 sq. inches
Vaned Diffuser Inlet Diameter	3.45 inches
Vaned Diffuser Outlet Diameter	4.35 inches
Vaned Diffuser Inlet Angle	16°
Vaned Diffuser Vane Number	15
Vaned Diffuser Total Throat Area	0.277 sq. inches
Vaned Diffuser Blade Thickness	0.037 inches

NOTE:

Certain details above relating to the detailed inducer and diffuser design were obtained later, but are included here for convenience.

TABLE 3

DESIGN POINT OPERATING CONDITIONS

Inlet Mass Flow - 0.236 lbs/sec
Inlet Volume Flow - 106.8 cfm
Total Pressure Ratio - 4.094
Total Temperature Rise - 97.8°F
Total Efficiency - 82.58%
(Not including leakage and Windage Losses)

	Hub	Eye	Diff. In	Diff. Out	Exit
Total Pressure, psia	5.10	5.10	23.20	21.73	20.88
Total Temperature °R	504.0	504.0	601.8	601.8	601.8
Density, lbs/ft^3	0.122	0.122	0.355	0.439	0.454
Static Pressure, psia	4.66	4.66	15.59	20.02	20.88
Merid. Velocity, ft/sec	178	179	101	63	0
Merid. Mach Number	0.402	0.404	0.211	0.130	0
Relative Velocity, ft/sec	204	383	407	186	0
Relative Mach Number	0.457	0.864	0.852	0.383	0
Relative Flow Angle	61.2	28.0	14.4	19.8	0

Impeller Tip

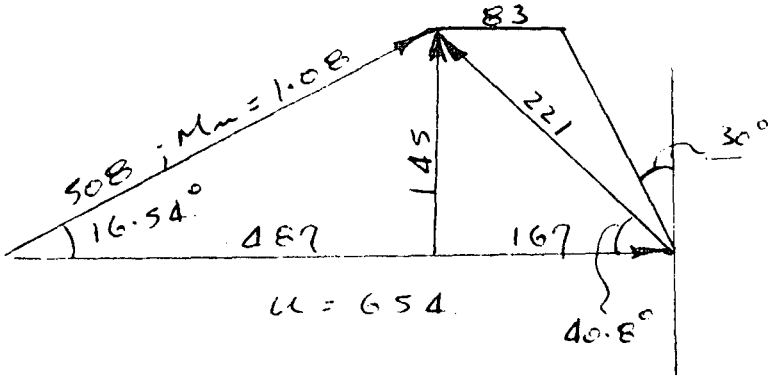

P = 24.95 psia
T = 601.8 °R
ρ = 0.311 lb/ft^3
p = 13.30 psia
R = 4.89
η = 94.2%

Vane Blockage = 7.85%
Aero Blockage = 3.22%
Total = 11.07%

Computer Output Case 9; 50,000 Rpm

7.0 BLADING DESIGN

7.1 Inducer Design

The inducer blade profile will be a parabolic arc on the unwrapped cylindrical coordinates, specified at the tip and with inner sections defined by radial ruling.

The first design attempt was to obtain a solidity of 2.0 and a tangential displacement of the trailing edge of 1.20 x circular pitch. It was not found possible to obtain the minimum required throat area with practical thickness blading.

The final profiles for tip and hub sections (at constant diameter) are shown in Figure 3. The leading edge thickness at the tip is 0.025 inches and at the hub 0.035 inches, and the required throat area is obtained. The solidity is 1.67, tangential displacement equal to circular pitch, and the tip suction surface angle is 33° (incidence - 5.0° at design). The average trailing edge thickness is 0.050 inches (actual tip and hub thicknesses determined by shroud profiles).

The tip suction surface coordinates are:

x = axial distance from leading edge

f = circular tangential displacement

x	0	0.1	0.2	0.3	0.4	0.5	0.6	0.7	0.8
f	0	0.144	0.269	0.375	0.461	0.528	0.576	0.604	0.613

The small number of blades combined with the need for high solidity leads to a relatively long inducer, but the shroud outward bend can start before the inducer trailing edge is reached. NOTE: As mentioned previously, the inducer leading edge is to be thinned down to the minimum manufacturing dimension to increase flow area to the maximum.

7.2 Impeller Blade Design

The impeller blade in the radial portion is to begin at 0° and curve to 30° backsweep at the tip. The profile in the radial plane will be a circular arc.

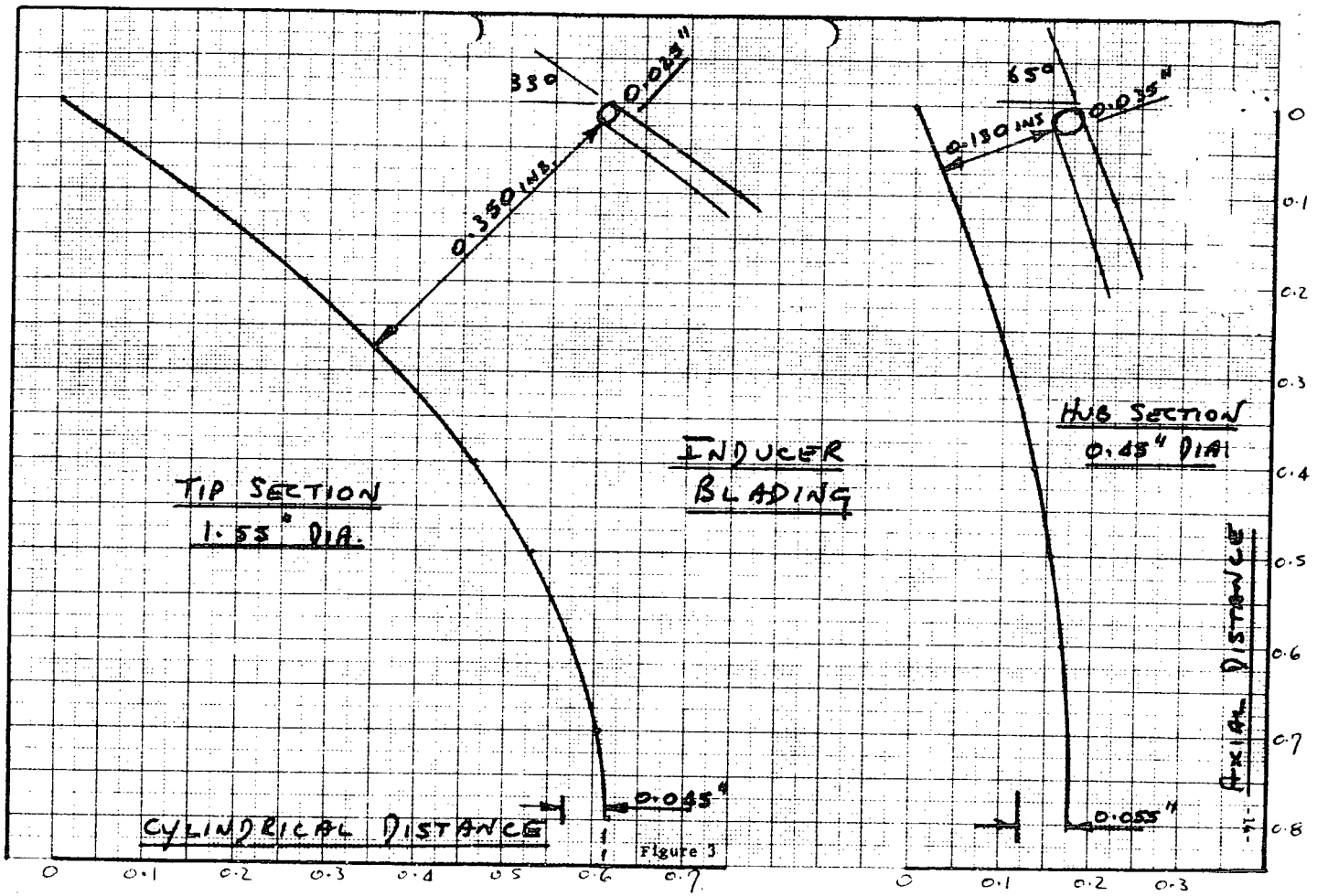
TIP SECTION
1.55" DIA.
INDUCER
BLADING
HUB SECTION
0.45" DIA.
33°
0.025"
0.350 INS.
65°
0.035"
0.130 INS
0.045"
0.055"
CYLINDRICAL DISTANCE
AXIAL DISTANCE
0
0.1
0.2
0.3
0.4
0.5
0.6
0.7
0.8

Figure 3

It was decided to start the blade curvature as soon as practical in the impeller bend at a diameter of 1.70 inches. This is also the first choice for the leading edge of the splitter vane or vanes, but if excessive blockage occurs, particularly if two splitters are required, the leading edge can be moved out to a layer diameter without appreciable effect.

The main blading tapers down from the inducer exit to a tip thickness of 0.040 inches (also the splitters), and the splitters leading edge thickness is 0.030 inches.

The choice of one or two splitters was decided by blade loading results in the computer program. It was found that 2 splitters are required, making 24 vanes in the radial portion of the wheel.

8.0 SHROUD PROFILES

The inner and outer profiles of the wheel are determined essentially by the computer program for blade loading analysis. However, an approximate profile is first required.

8.1 Inducer Exit

At the design point, the velocity in the inducer throat (RMS) is calculated to be 340 ft/sec and the wheel leaving relative velocity is 220 ft/sec (ratio 1.545).

It was decided to apportion the velocity diffusion to a ratio of 1.30 in the inducer (exit velocity of 260 ft/sec) leaving a velocity diffusion ratio of 1.182 in the radial part.

Calculations then gave an inducer hub diameter of 0.900 inches at exit (constant tip diameter 1.55 inches).

8.2 Radial Section

The flow areas required in the radial portion of the wheel were calculated

assuming reasonable distributions of efficiency, slip and radial velocity, as below:

Diameter	1.70	2.05	2.40	2.72	3.00
Slip Factor	0.97	0.945	0.915	0.89	0.87
Sweepback	0	9.1	17.05	24.25	30.0
Radial Velocity	260	228	197	169	144
Total Blockage %	14.0	12.6	11.6	11.1	11.2
Channel Width	0.187	0.146	0.114	0.103	0.090

The radial velocity at inlet to this section, 260 ft.sec, has been made equal to the inducer exit velocity, providing for constant velocity around the bend.

8.3 Impeller Bend

The bend forming the inducer and the radial section is initially designers choice from appearance and experience, modified by results of blade loading analysis. It is desirable to have large radii to limit velocity acceleration on the outer shroud, and the bend can overlap the inducer. NOTE: Flow areas presented herein do not include allowance for recirculated leakage. This adjustment is, however, made on the final released drawings.

8.4 Final Impeller Design

The final profile is shown in Figure 4 and the shroud coordinates are listed in Table 4.

The blade loading analysis program showed that two splitters are required to limit the accelerations and decelerations on the blade surfaces. To reduce blockage the splitter leading edge is then reduced in thickness to 0.20 inches.

The results of the internal analysis which led to this conclusion are shown in Figure 5. This shows the computed gas velocities along the RMS stream tube at the trailing and driving faces of the blade, and also the mid-channel velocity.

It should be pointed out that the computed velocities are very sensitive to small dimensional changes, and do not take account of the "self-correcting" feature of gas flow. Velocity variations are therefore exaggerated, but

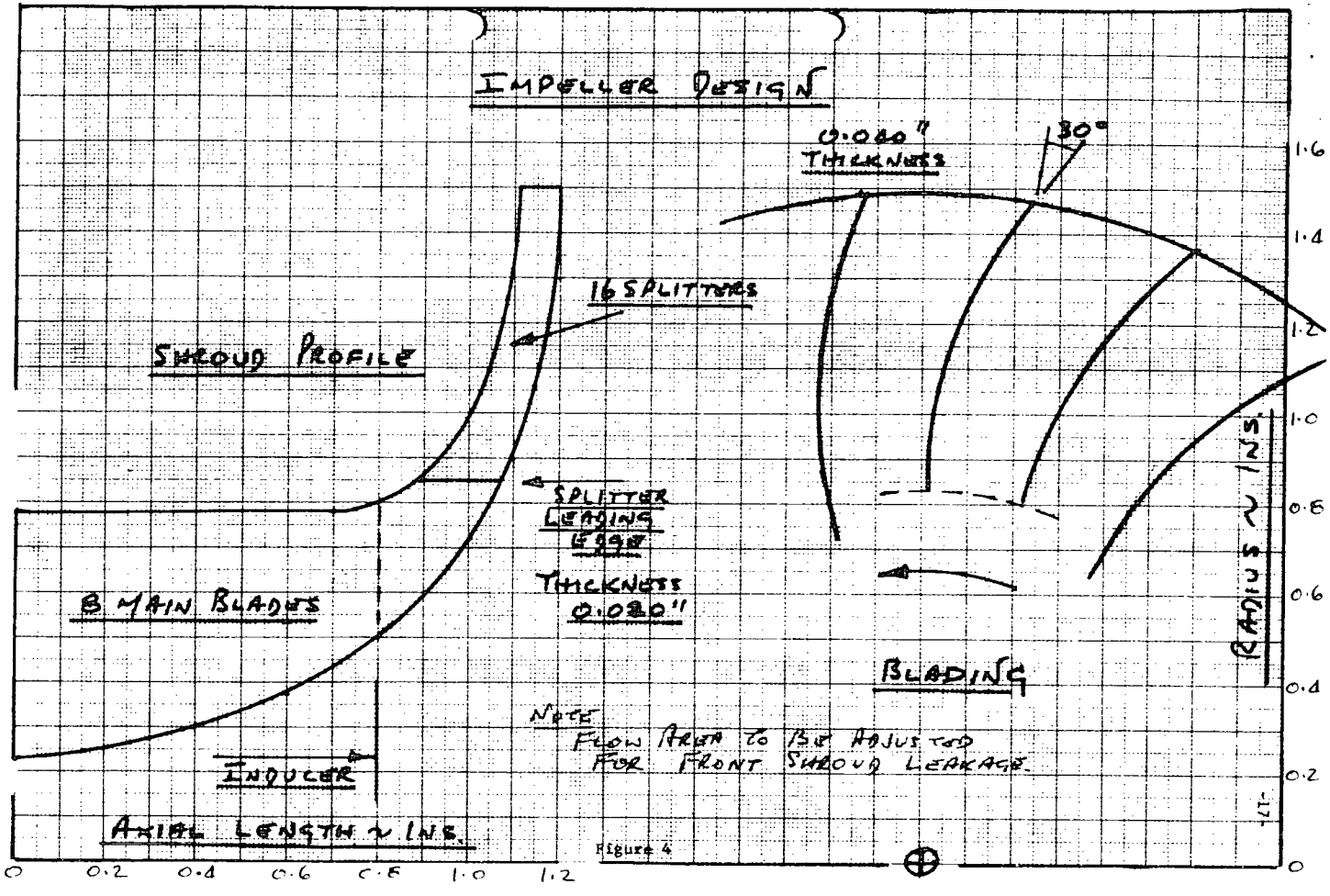
IMPELLER DESIGN
0.080" THICKNESS
30°
16 SPLITTERS
SHROUD PROFILE
SPLITTER LEADING EDGE
THICKNESS 0.080"
8 MAIN BLADES
BLADING
NOTE
FLOW AREA TO BE ADJUSTED FOR FRONT SHROUD LEAKAGE.
INDUCER
AXIAL LENGTH ~ INS.
RADIUS ~ INS.
0
0.2
0.4
0.6
0.8
1.0
1.2
1.4
1.6

Figure 4

TABLE 4

SHROUD AND BLADE PROFILES

Referenced from a radial line through the inducer leading edge.

z = axial distance

r_o = Outer shroud radius

r_i = Inner shroud radius

θ = Angular displacement of blade (suction surface)

z	r_o	r_i	θ
0	0.775	0.225	0
0.1	0.775	0.230	10.65
0.2	0.775	0.250	19.90
0.3	0.775	0.275	27.72
0.4	0.775	0.305	34.08
0.5	0.775	0.335	39.04
0.6	0.775		42.59
0.65		0.403	43.62
0.7	0.780		44.66
0.78		0.490	45.00
0.8	0.800		45.32
0.9		0.600	45.32
0.85	0.830		45.32
0.96		0.670	45.32
0.895	0.865		45.35
1.040		0.780	45.32
0.975	0.965		45.80
1.115		0.925	45.60
1.040	1.100		46.95
1.165		1.080	46.70
1.080	1.250		49.07
1.190		1.250	49.07
1.090	1.350		50.90
1.200		1.350	50.90
1.100	1.430		52.60
1.200		1.430	52.60
1.110	1.500		54.30
1.200		1.500	54.30

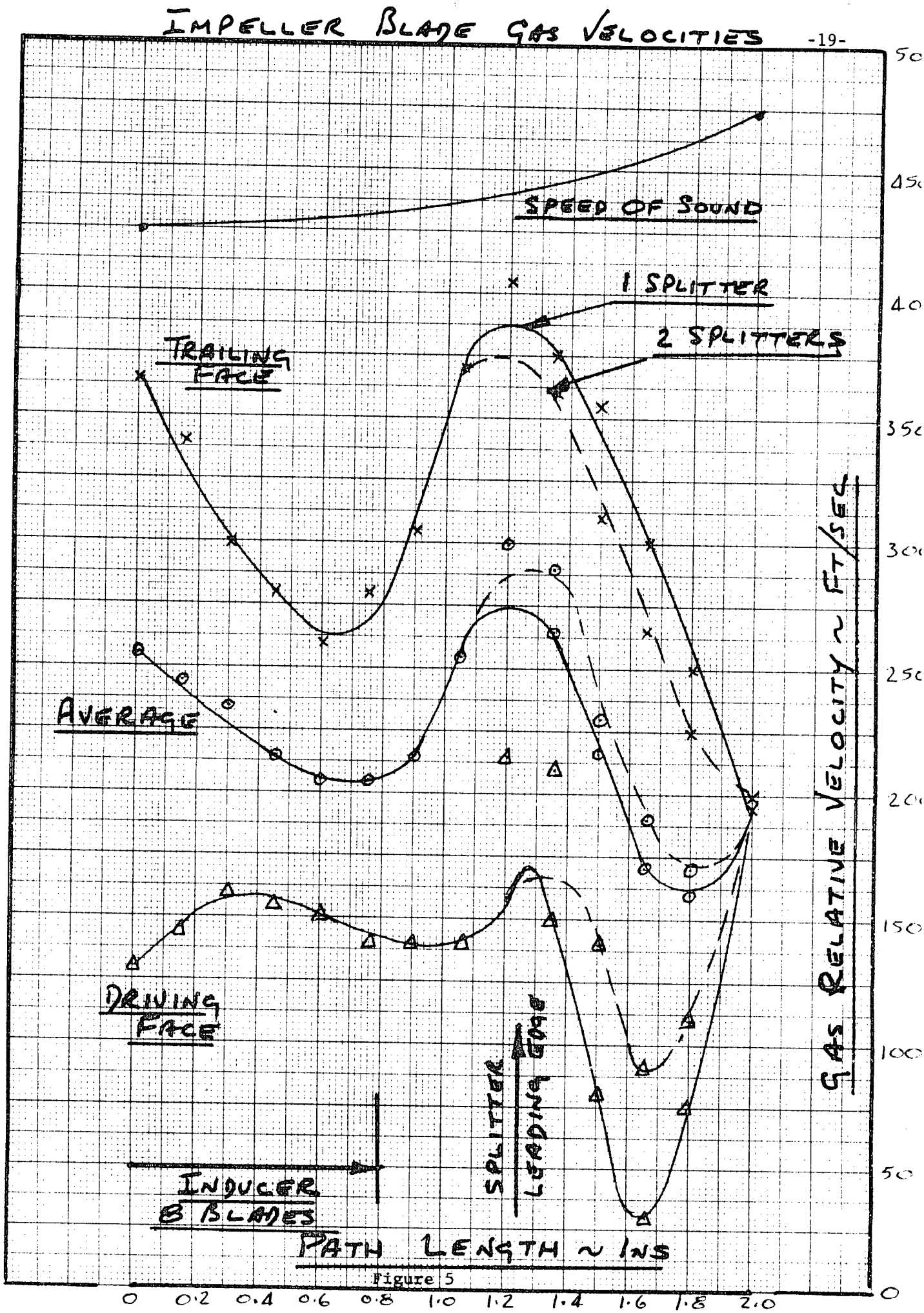

Figure 5

46 1320
KEUFFEL & ESSER CO. MADE IN U.S.A.

trends are significant and also relative values.

The only variables available to affect the shape of the curves are the flow area, local radius of curvature; and number of blades. The curves show the results with the first two items at the limit of influence, but with alternatively one or two splitters in eight main vanes.

The object is to keep the velocity as uniform as possible, and particularly the rate of velocity change to the minimum.

The velocity variance along the inducer must be accepted since this is by its nature a diffusing cascade. On average, the diffusion is moderate. The increase in velocity around the bend has been minimized as above, and the effect is over-stated in the computation. Further, it is unlikely that the three locations will terminate at the same velocity. The critical issue is the minimum velocity on the driving face. Here the effect of using 2 splitters in place of one is quite evident in reducing the internal diffusion, and avoiding separation of the flow as the velocity approaches zero. Two splitters was, therefore, decided upon.

9.0 DIFFUSER DESIGN

The very small size of the unit dictates that the diffuser vane design should be basically simple. Although the Mach Number at inlet is not excessive at design, the requirements for satisfactory operation at high overspeed limit the amount of achievable gas deflection.

The design requirements are:

Inlet Diameter	3.45 inches
Outlet Diameter	4.35 inches
Number of Vanes	15
Exit Throat Area Ratio	1.50
Total Throat Area	0.277 sq. inches
Throat Diameter	0.205 inches
Vane inlet anlge	16°
Mean gas outlet angle	22.2^{o}
Inlet Mach Number	0.852
Incidence at Design	1.6^{o}

The blades were first laid out in the transformed axial cascade plane, which shows the blades relative to undisturbed streamlines. Because of the over-speed high Mach Number requirement, it was hoped to have blades of zero camber up to the throat, but the required throat area could not be achieved.

Consequently, it was decided to make the vanes a true circular arc (in the transformed plane) to have the maximum radius of curvature up to the throat. To obtain the required throat area, the deflection up to the throat is 5.5°. Continuing the curvature to the vane exit radius, the total camber is 9.6°, blade outlet angle 25.6°, and solidity 1.68.

The calculated deviation using Carter's rule for this cascade is 2.92°, giving a gas outlet angle of 22.68°. The computer program gives an angle of 22.15° so that agreement is good.

The cascade was then transformed at Mach Number 0.85 into the circular flow plane to provide the true vane suction surface. The coordinates are given in Table 5.

On layout, the correct throat diameter is obtained at a blade leading edge thickness of 0.037 inches. This is slightly thicker than intended, but allows for minus tolerance in manufacture and development adjustment of the throat diameter if found to be necessary.

The required exit throat area ratio is 1.50. In vane layout it was found that that this is obtained if the vane thickness is very nearly constant, and this was decided upon. Over the channel section this gives a diffuser divergence angle of 4.8° and an area ratio of 1.258, both quite moderate figures.

10.0 OUTLET SCROLL AND DIFFUSER

The gas leaving the diffuser vanes is to be collected in a scroll, passed through a conical diffuser, and discharged into the system.

TABLE 5

DIFFUSER VANE COORDINATES

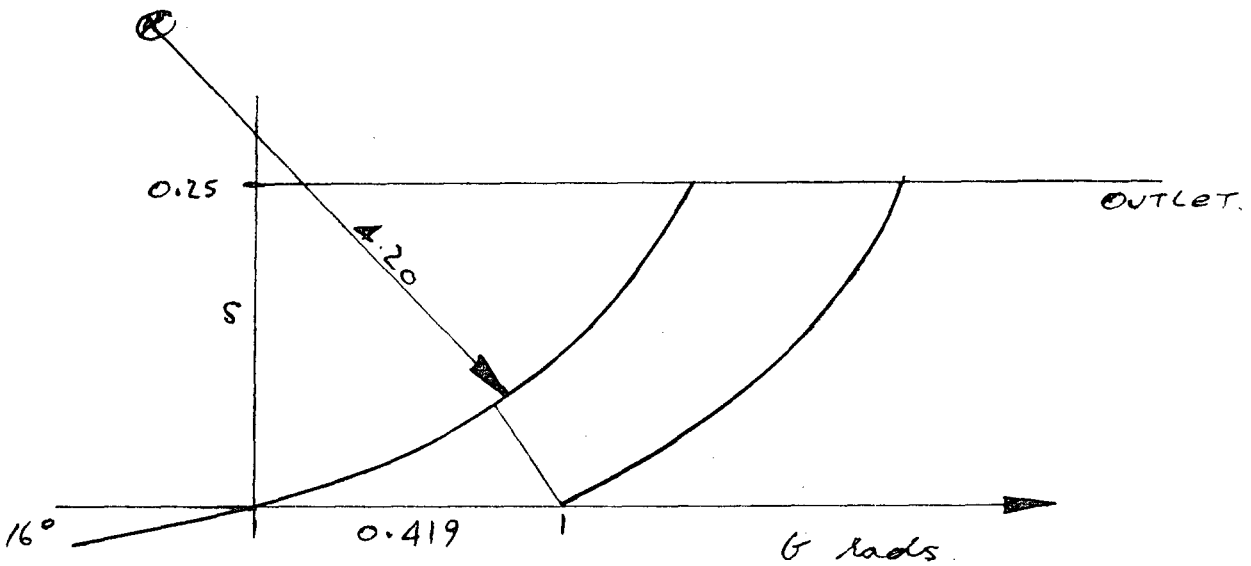

Axial Cascade Plane

Circular Coordinates

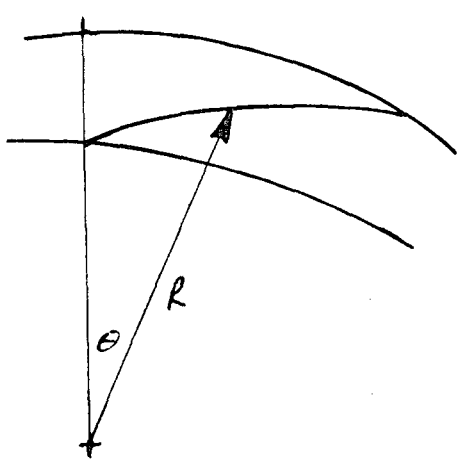

Suction Side Values

θ^o	R_{sine}
0	1.725
4.03	1.762
8.03	1.802
12.02	1.844
15.98	1.888
19.91	1.934
23.82	1.982
27.70	2.032
31.55	2.084
35.37	2.139
37.65	2.175

The diffuser vane exit conditions are shown in Table 3. It was assumed that the final discharge velocity will be 37 ft/sec, Mach Number 0.075.

The assumed loss in the computation was 50% of the diffuser vane exit head. This requires an overall diffusion efficiency of 54.5% with an area ratio of 4.03. By optimization of the losses, it was decided to:

a) Let the diffuser exit velocity by 60 ft/sec, with a final dump loss to 37 ft/sec.

b) Equalize the head loss in the scroll and in the exit diffuser.

Consequently:

i) Scroll exit area = 0.642 square inches
Diameter = 0.903 inches

ii) Exit diffuser exit area = 1.23 square inches, diameter - 1.250 inches length - 1.645 inches at an included cone angle of 12°.

11.0 PERFORMANCE WITH IGV CLOSURE

The specification points with full closure of the inlet guide vanes are:

RPM Nominal	40,000	50,000	60,000
Inlet Temperature ^{o}F (^{o}R)	65(535)	56(516)	55(515)
Inlet Pressure, psia	8.7	5.5	3.2
Pressure Ratio	2.15	3.10	5.00
Minimum Efficiency %	64.0	67.5	63.5
Flow pph (lbs/sec)	630(0.175)	550(0.153)	455(0.126)
$N/\sqrt{\theta}$	38650	48750	58480
$\omega\sqrt{\theta}/\delta$	326.3	446.3	634.6
Surge (%)	300.0(92.0)	420.0(94.1)	570.0(69.9)
Choke (%)	350.0(107.4)	470.0(105.3)	660.0(104.0)
Inlet Volume Flow, cfm	48.4	65.7	93.2
Surge	44.5	61.8	83.9
Choke	52.0	69.2	97.0

These points are shown in Figure 6 together with the computed performance at inlet whirl angles of 15°, 30° and 45°. The performance does not take account of pressure loss across the IGV's but it is clear that combinations

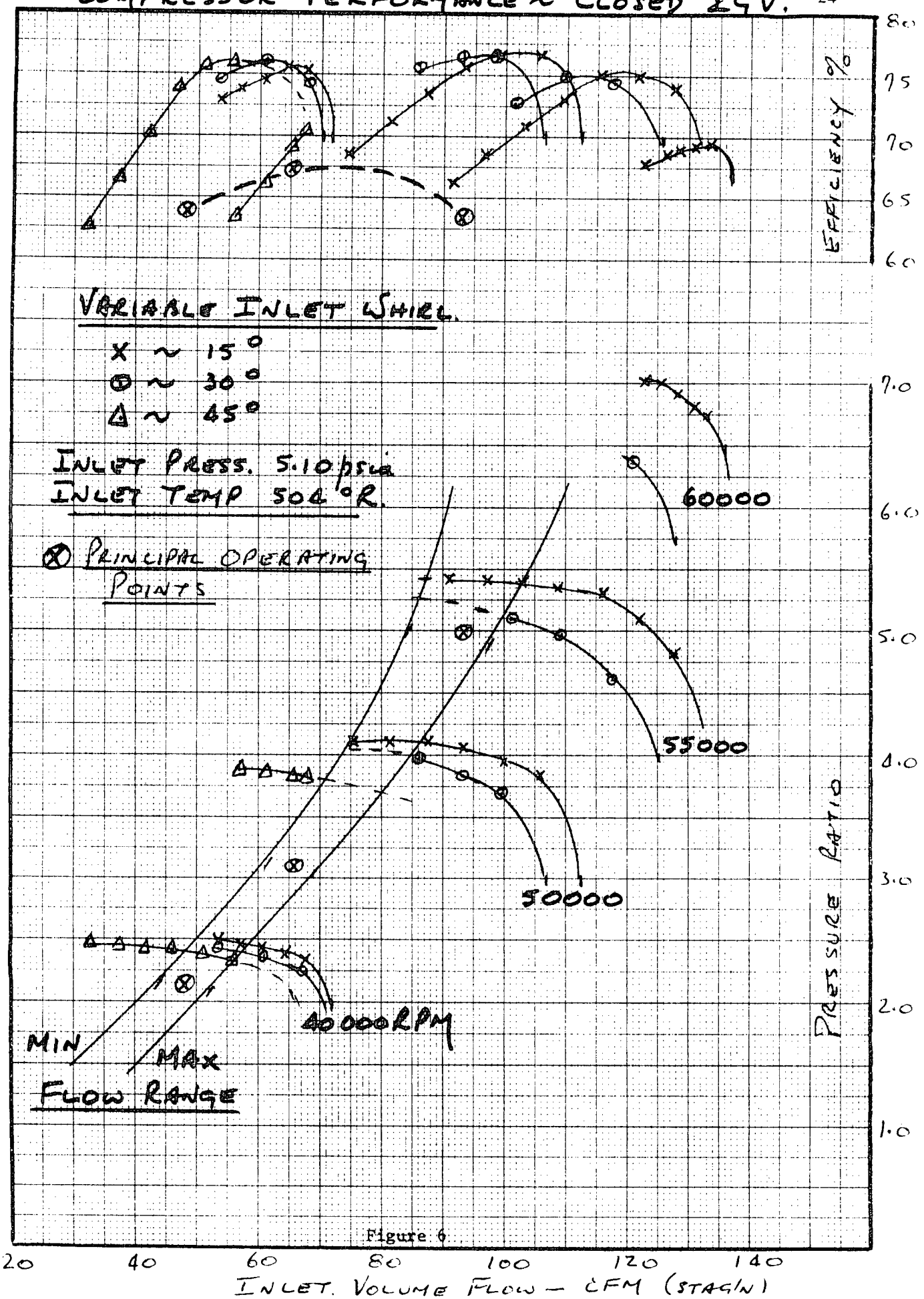

Figure 6

46 1320
K+E 10 X 10 TO ½ INCH 7 X 10 INCHES KEUFFEL & ESSER CO. MADE IN U.S.A.

of speed and IGV closure can be selected which will meet the specifications.

12.0 CONCLUSIONS

1. The compressor design shown in the report meets or exceeds the specification at the nominal speeds of 40,000 and 50,000 rpm at full load, and all points closed IGV's.

2. The design is deficient at 60,000 rpm nominal at full load in flow (about 5.5% low) and efficiency (about 2 points low) due to inducer choking. However, with the minimum practical thickness of the inducer blading at the leading edge, allied with a modification of the specification, the overall system performance should not suffer. At the 60,000 rpm specification point, the performance will be dependent on careful experimental development. The major variables are rotor diameter and diffuser width.

3. The overall performance at all conditions is highly influenced by the containment of gas leakage to the minimum by efficient seals.

ATTACHMENT C

DESIGN REPORT - HOMOPOLAR INDUCTOR ALTERNATOR

MTI 77TR56

DESIGN REPORT
HOMOPOLAR INDUCTOR ALTERNATOR
3.17 KW 60,000 RPM

by

H.L. Clark

Prepared For:

Consolidated Natural Gas Company
Incorporated

MECHANICAL TECHNOLOGY INCORPORATED
968 Albany-Shaker Road
Latham, New York 12110

NO. MTI 77TR56

DATE: July 1977

TECHNICAL REPORT

DESIGN REPORT

HOMOPOLAR INDUCTOR ALTERNATOR

3.17 KW 60,000 RPM

Author (s) H. Clark

Approved R. Hohenberg

Approved C. Boyajian

Prepared for

Consolidated Natural Gas Company Incorporated

Cleveland, Ohio

Prepared under

MECHANICAL TECHNOLOGY INCORPORATED

968 ALBANY - SHAKER ROAD — LATHAM, NEW YORK — PHONE 785-0922

TABLE OF CONTENTS

Section		Page
1.0	INTRODUCTION	1
2.0	DESIGN SPECIFICATIONS	6
	2.1 Output	6
	2.2 Load	6
	2.3 Efficiency Goal	6
3.0	SIZING EQUATIONS	7
	3.1 Introduction	7
	3.2 Output Constant	7
	3.3 Calculation of D^2L	9
	3.4 Choice of D and L	9
4.0	MAGNETIC CIRCUIT ANALYSIS	12
	4.1 Waveform of Induced Voltage for One-Turn Coil	12
	4.2 Generated Voltage	14
	4.3 Required Line-to-Line Voltage	16
	4.4 Load Current	17
	4.5 Lamination Layout	18
	4.6 Leakage Reactance Calculation	18
	4.7 A-C Winding Resistance Calculation	21
	4.8 A-C Coil Turns Calculation	21
	4.9 D-C Magnetic Circuit	22
5.0	LOSS ANALYSIS	31
	5.1 Stator I^2R Loss	31
	5.2 Stator Iron Loss	31
	5.3 Pole Face Loss	33
	5.4 Field Loss	38
	5.5 Stray Loss	38
6.0	PERFORMANCE SUMMARY	39
7.0	TEST RESULTS	40
	7.1 D-C Saturation Curve	40
	7.2 Resistance Measurements Tests	40
	7.3 Open Circuit Generated Voltage Test	42
	7.4 Short Circuit Test	45
	7.5 Load Test	45
8.0	CONCLUSIONS	49

1.0 INTRODUCTION

An alternator driven by a turbine is to produce power to operate a d-c motor driving a fan and several other d-c loads. Since the turbine speed is 60,000 rpm, the rotor of the alternator must have a high degree of mechanical stability. In order to accomplish this, the rotor is fabricated of high strength steel with no electrical windings.

The design used is a "Homopolar Inductor" alternator. Only one d-c field winding is used on the stationary part, supplying flux in only one direction, but this flux is switched between the stator winding coils by salient poles on both ends of the rotor. The construction of the rotor is shown in Figure 1-1. Non-magnetic filler pieces made of Rene' 41 are placed around the rotor, filling the spaces between the salient poles, thus producing a smooth rotor surface to reduce windage. These pieces are electron-beam-welded to the rotor body. A lamination stack faces the salient poles on each end of the rotor. The lamination stack is shown in Figure 1-2 and the details of the lamination are shown in Figure 1-3. The armature windings pass through slots in both lamination stacks in a manner similar to a standard three-phase induction motor. The lamination stacks and armature windings are shown in Figure 1-4. The d-c field coil is pre-wound and placed between the lamination stacks around the outside of the space for the armature winding which is inserted later. A steel sleeve is then placed around the lamination stacks which supports them and also serves as the return flux path.

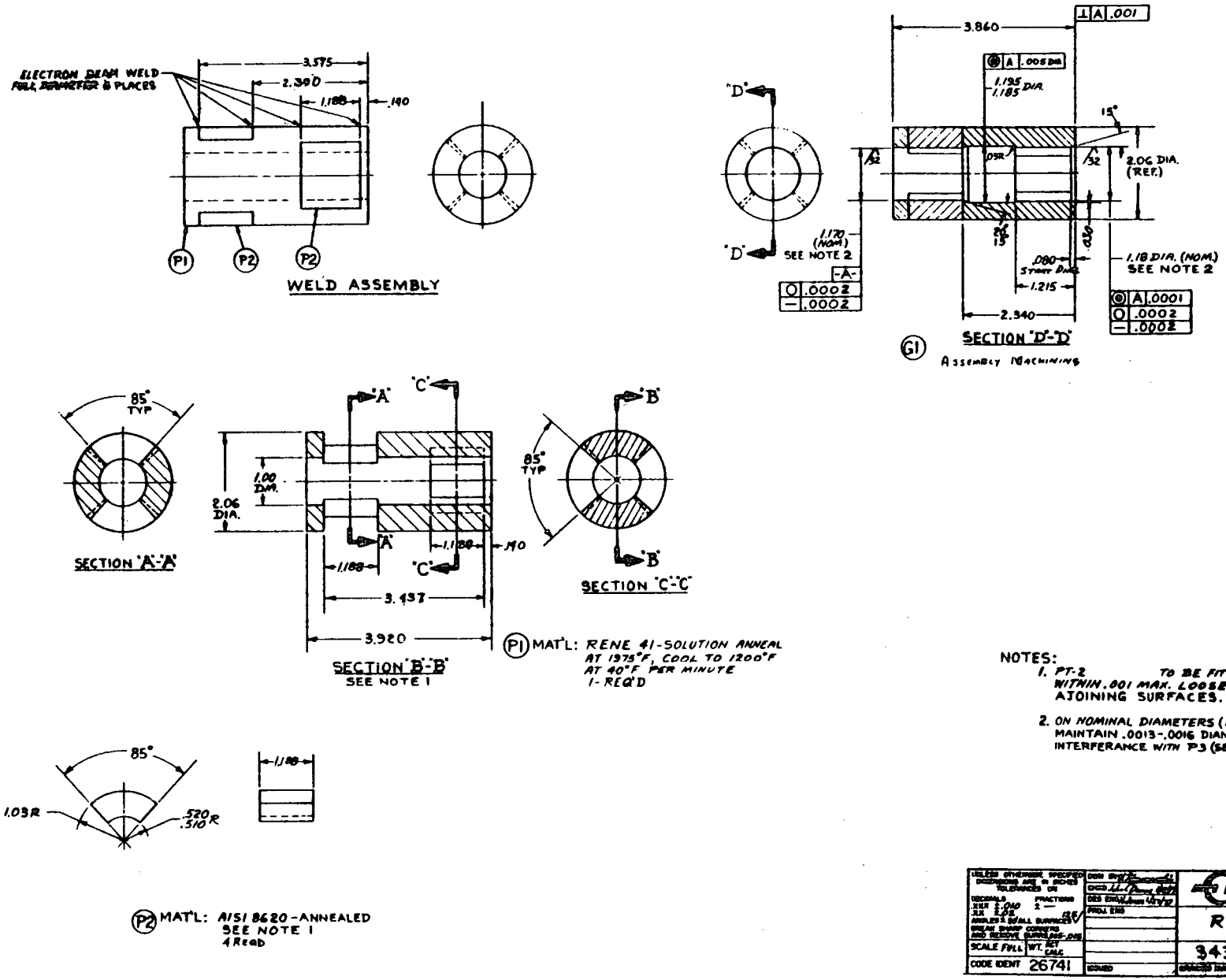

Figure 1-1. Rotor Construction

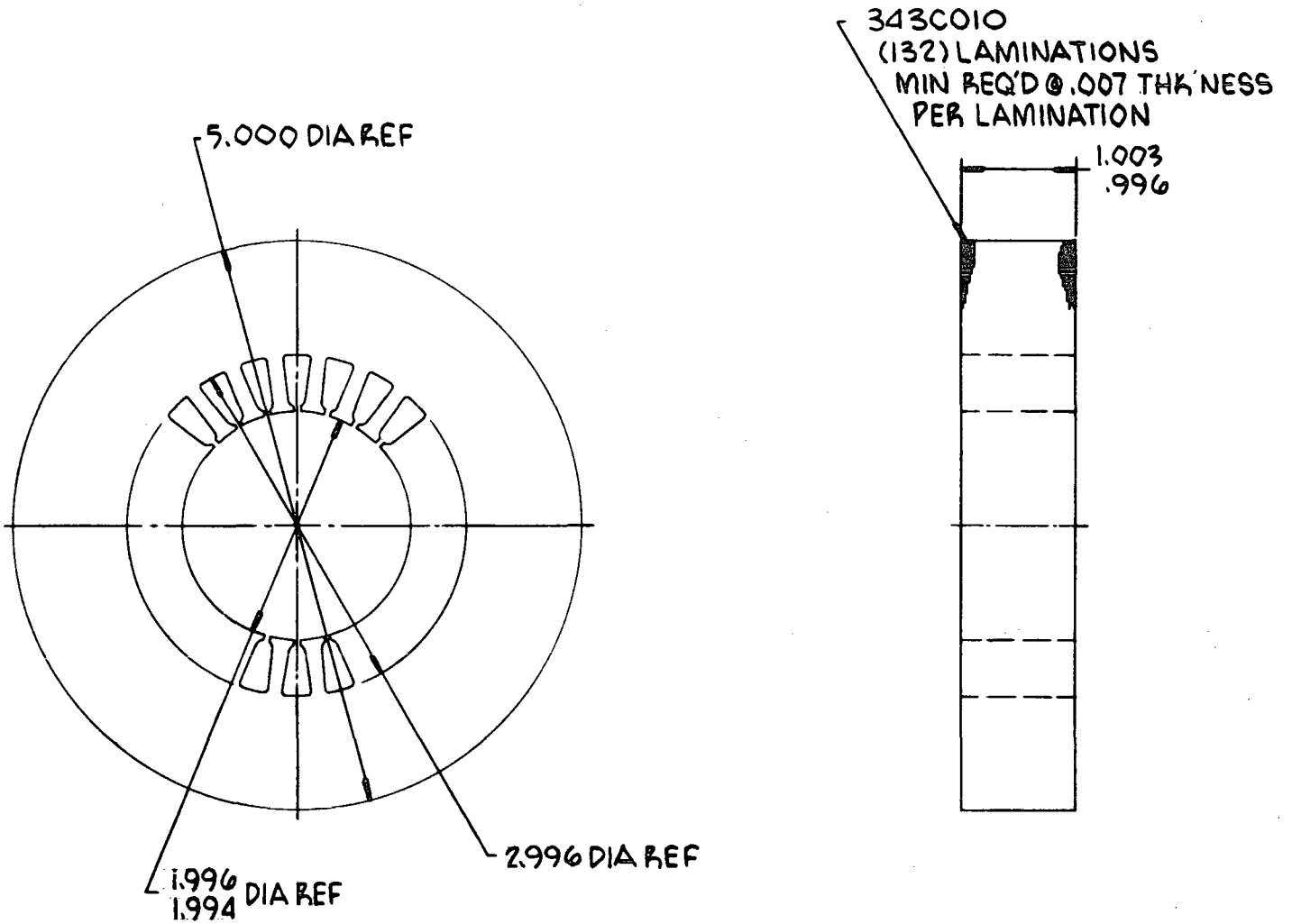

Figure 1-2. Lamination Stack

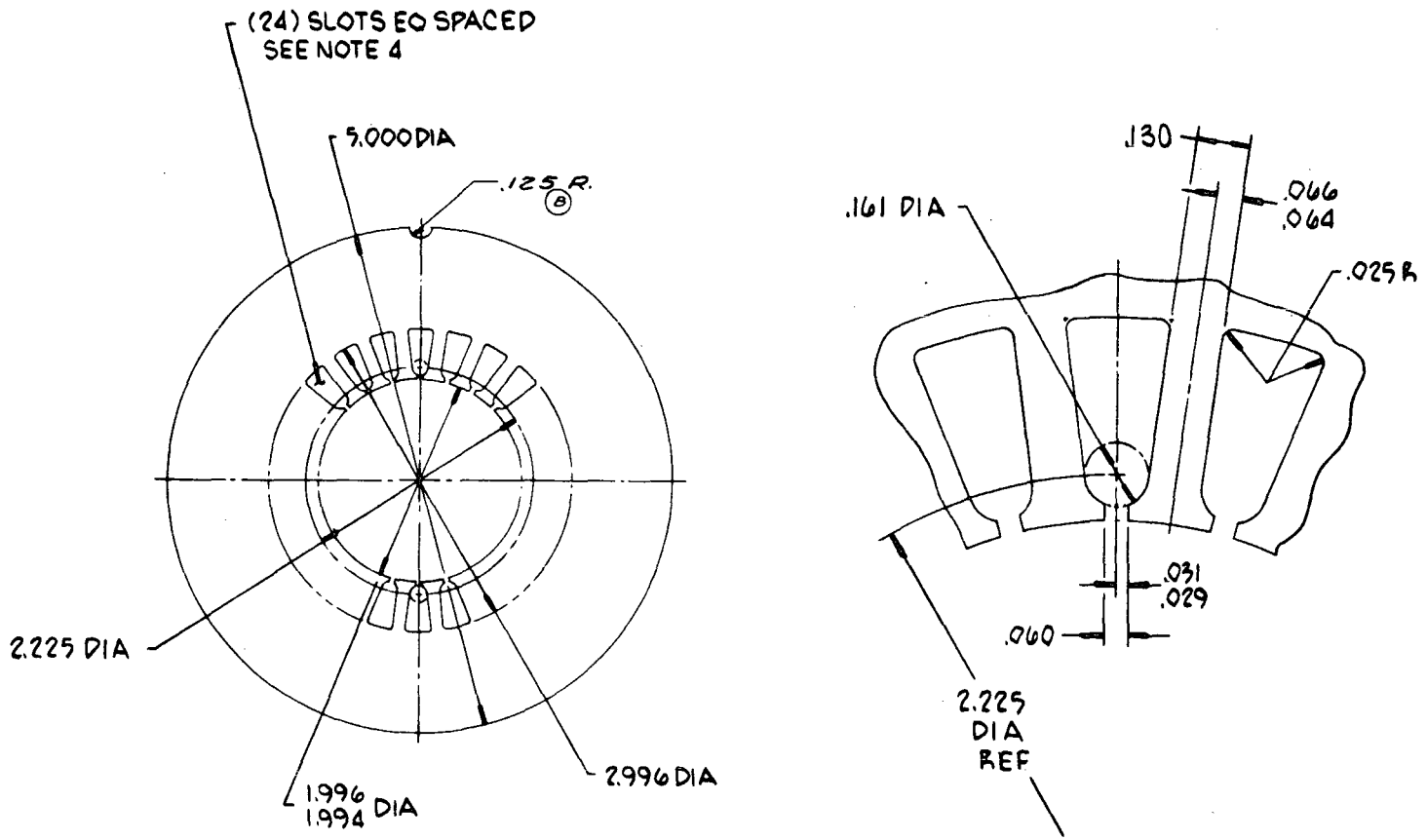

Figure 1-3. Details of the Lamination

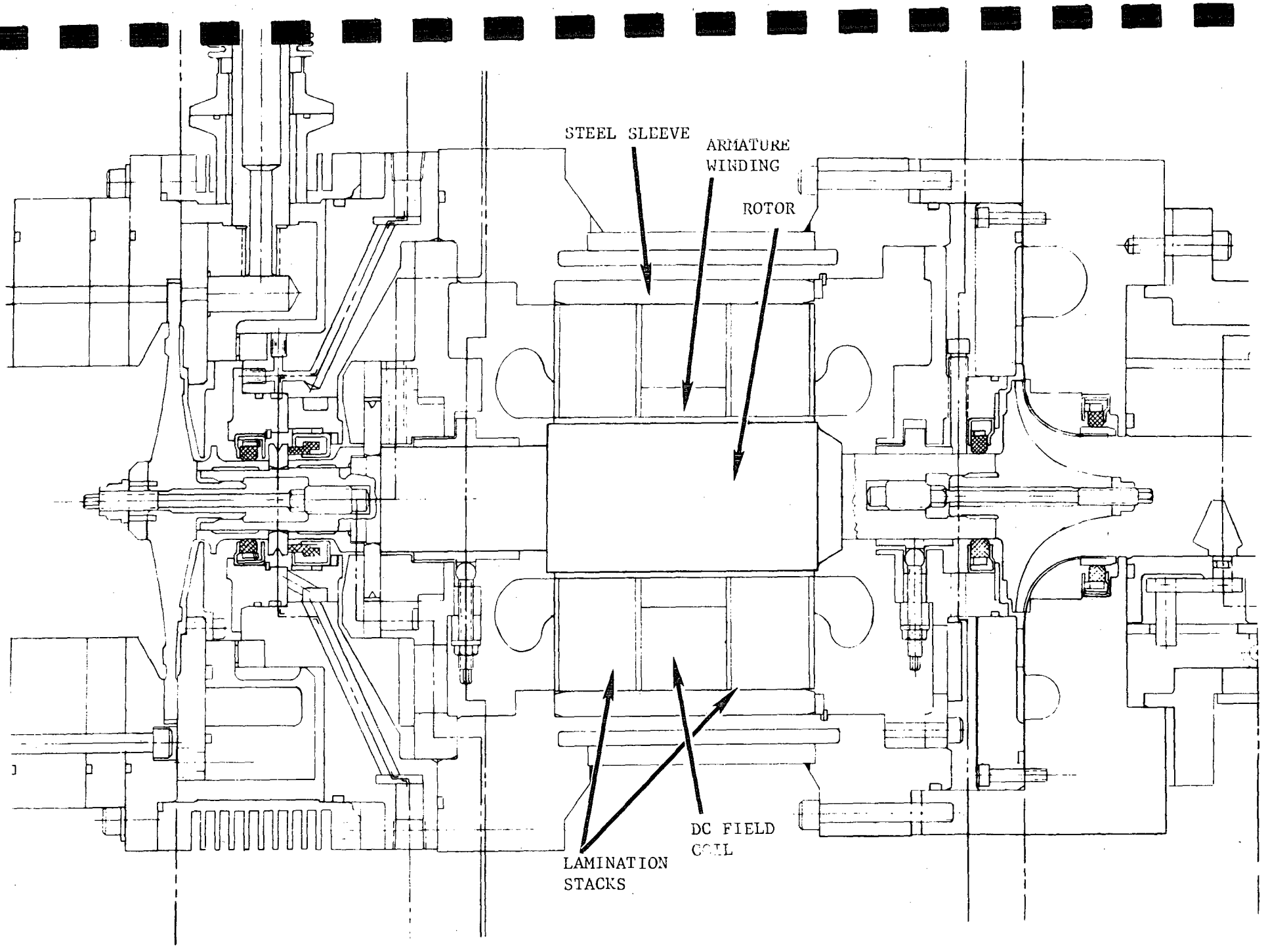

Figure 1-4. Lamination Stacks and Armature Windings

2.0 DESIGN SPECIFICATION

2.1 Output - 240 v d-c 2.0 kw at 50,000 rpm

3.17 kw at 60,000 rpm

2.2 Load - d-c permanent magnet motor, 240 v nominal, driving a fan load; motor load proportional to N^3.

2.3 Efficiency Goal - greater than 90 percent.

3.0 SIZING EQUATION

3.1 Various text books on rotating machinery design have developed sizing equations for providing a starting point in designing a specific machine. These design equations draw on experience over many years with the usual values of airgap flux density, copper current density, and pole flux leakage constants as functions of machine size over a wide range of machine power.

Such a sizing equation is derived for alternating current machines from basic considerations in Design of Electrical Apparatus by John H. Kuhlmann, Chapter 10.

$$\frac{\text{Kva} \times 10^5}{D^2 L N} = C$$

Where: D = Machine airgap diameter, inches

L = Axial airgap length, inches

N = rpm

Kva = Kilovolt amperes

C = Output constant

The constant C depends on the airgap flux density, the number of conductors per inch of circumference of the airgap, and the current density in these conductors. These factors vary with machine size. Rather than considering each of these factors separately, the value of C is determined from a number of successful designs of the same sort of machine when plotted as shown in Figure 3-1.

3.2 Output Constant

It can be seen that for a machine approximately 3.5 kva in size value for $D^2 L$ of 0.8 would be used.

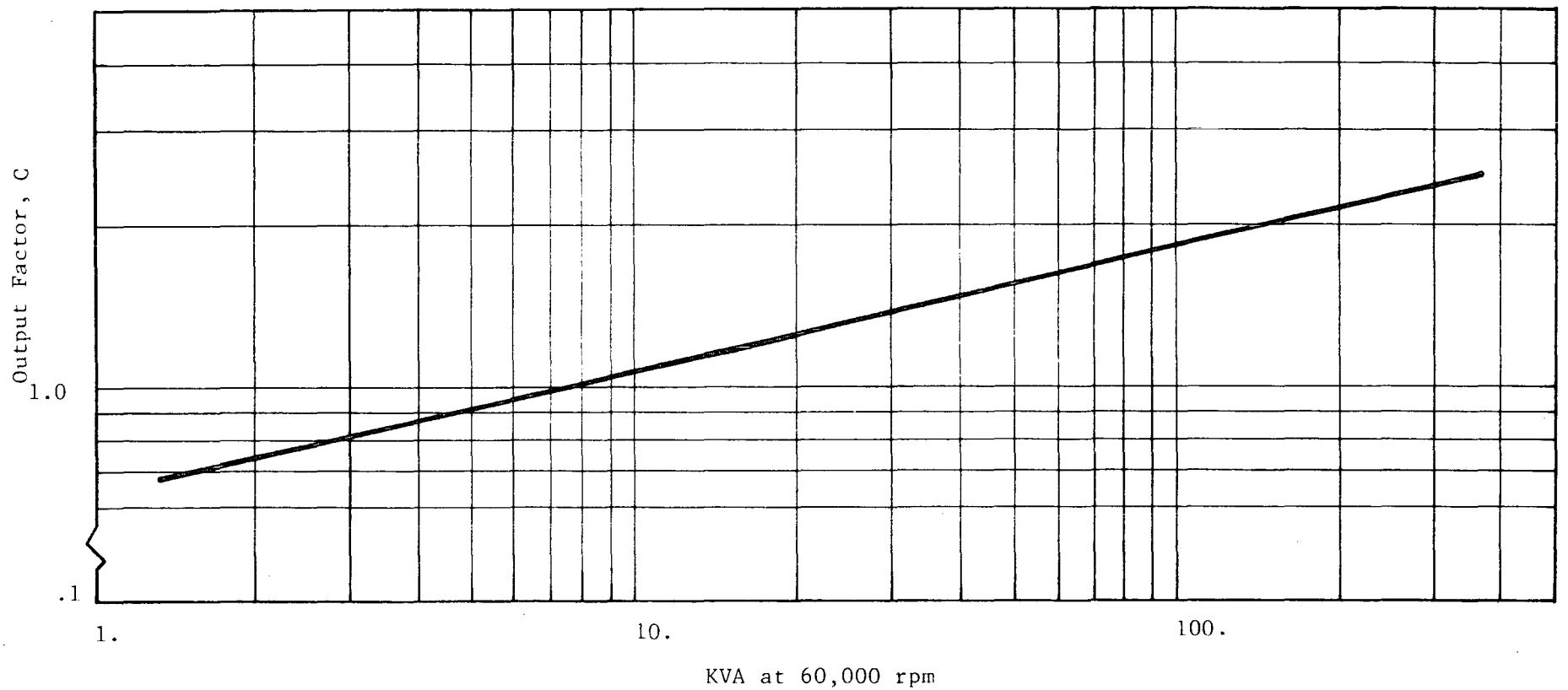

Figure 3-1. Calculated Value of C

3.3 Calculation of $D^2 L$

$$0.8 = \frac{3.17 \times 10^5}{D^2 L \times 6 \times 10^4}$$

$$D^2 L = 6.60$$

3.4 Choice of D and L

3.4.1 The ratio of useful flux (that which links the windings and, hence, generates voltage) to the total flux is controlled by the saliency.

$$\text{Saliency} = \frac{\text{Pole Diameter} - \text{Body Diameter}}{2} \times \frac{1}{\text{Airgap}}$$

A factor of 10 is used resulting in a ratio of useful to total flux of approximately 0.91. With an airgap of 0.04 inches, this pole height is 0.4 inches.

3.4.2 A plot of possible diameter and length combinations is shown in Figure 3-2. The actual choice of diameter depends on the total flux which must be carried in the body of the rotor and the saliency factor used. Centrifugal stresses must also be considered.

3.4.3 Since the stator laminations must have slots to contain the conductors, the stator teeth will have a higher flux density than the airgap. A flux density of 40 kl/in^2 in the airgap is usual for low-speed machines. For high-speed machines such a flux density will give very high iron losses in the surface of the rotor and in the stator tooth tips. An airgap flux density not higher than 30 kl/in^2 will be necessary to achieve 90 percent overall efficiency.

3.4.4 The pole pitch will be 0.9 of $\frac{\pi D}{4}$ where D is the average airgap diameter. The airgap is assumed to be 0.04". The flux passing through the pole areas will be the same as that passing through the body of the rotor times the flux leakage factor.

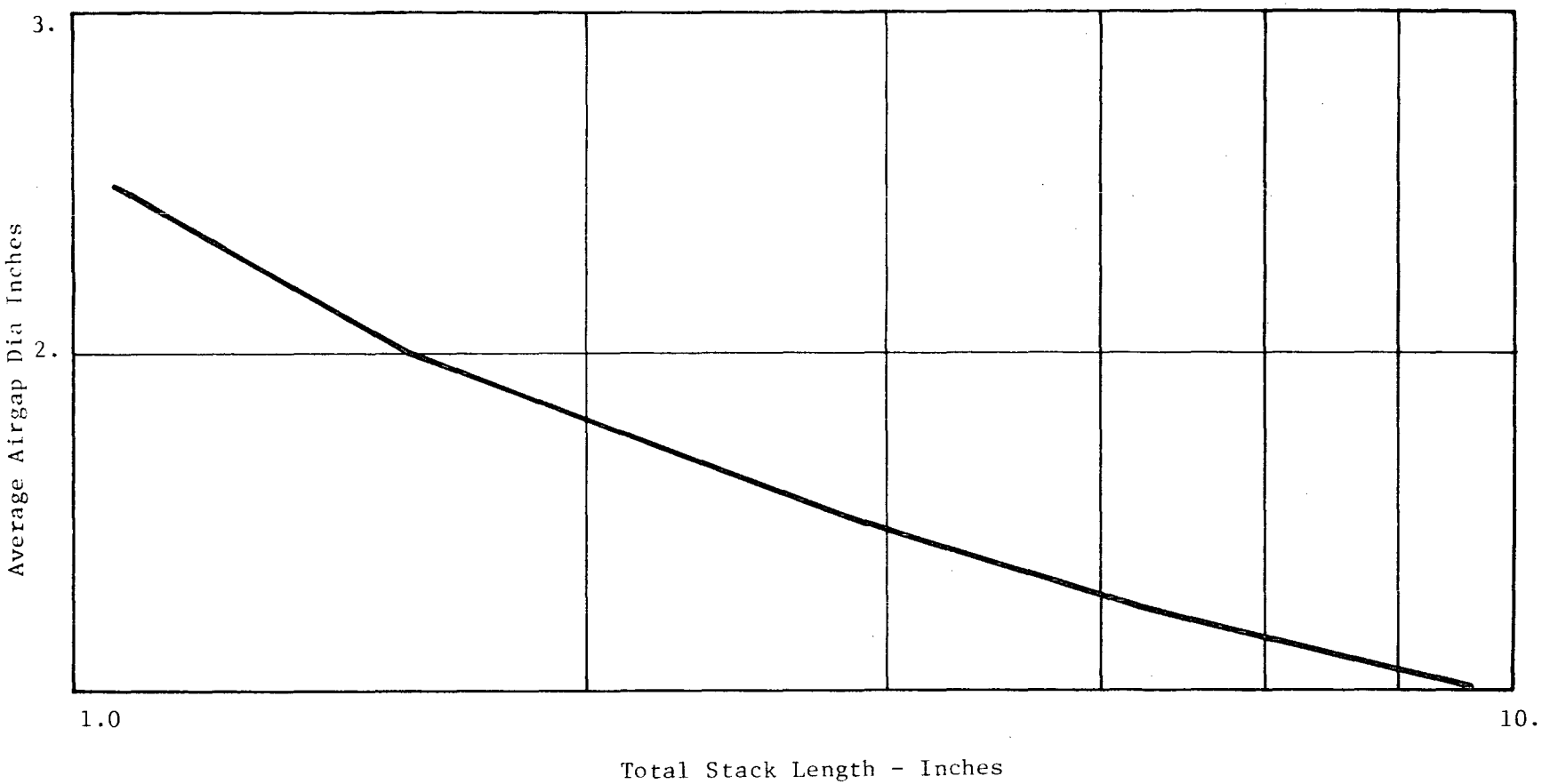

Figure 3-2. Plot of Possible Diameter and Length Combinations

$$(D \times \frac{\pi}{2} \times 0.9 + 2. \times 0.04)\ (L + 0.08)\ B_g = \frac{\pi d^2}{4} B_c \times 0.91 \qquad (2)$$

where d = the diameter of the body of the rotor.

Note that the airgap dimension of 0.04 is added to both the circumferential and axial dimensions of the pole and also that two poles on one end of the rotor are in parallel in the flux path. The average airgap of the rotor is denoted by D. Using the pole height dimension given in Section 3.4.1, d in equation 2 can be replaced by (D - .04 - .8). With B_c = 90 kl/in.^{2} and B_g = 30 kl/in.^{2}, values of L (axial length of both poles) can then be obtained for various values of D.

For a value of D = 1.95, L = 1.702. This is the mechanical dimension. Including the flux fringing factor of 0.04 inches on each end of each pole, the magnetic value is:

$$L = 1.702 + 4 \times 0.04 = 1.862$$

This is somewhat larger than the value of 1.67 obtained from Figure 3-2 but will give a more conservative design and higher efficiency.

The value chosen for the average airgap diameter was 1.955 giving a stator ID of 1.995 and a rotor diameter of 1.875. The length of the two stator stacks was chosen to be 2.00 or 1.00 for each stack.

4.0 MAGNETIC CIRCUIT ANALYSIS

4.1 Waveform of Induced Voltage for One-Turn Coil

Since the alternator is three-phase four-pole, the minimum number of slots in the lamination is one per pole per phase, or a total of 12 slots. The number selected was 2 slots per pole per phase giving a total number of slots of 24. The coils are short pitched with a coil spanning 5 slots (pole pitch 6 slots). This short chording makes the windings easier to fabricate and install and reduces the resistance and reactance of the windings, thus improving the performance. The wave form of the generated voltage is also improved.

With two salient poles on each end of the rotor, two cycles of voltage per revolution are generated. With 24 slots in the stator lamination, each slot spans 720/24 or /30 electrical degrees. The voltage generated in the two sides of a coil spanning 5 slots is then 150° electrical apart, and the voltage generated in a one-turn coil is as shown in Figure 4-1. The harmonic analysis of this wave with a nominal peak value of 1.00 is shown in Table 4-1.

TABLE 4-1

HARMONIC ANALYSIS OF GENERATED WAVEFORM

ONE-TURN COIL - NOMINAL LEAK VOLTAGE = 1.00

HARMONIC	VALUE
1	1.189
3	0.214
5	0.0181
7	0.0114
9	0.0686
11	0.1063
13	0.0914
15	0.0438

With a wye connection of the phases, the third harmonic and multiple thereof will be cancelled. The lowest harmonic not cancelled with an appreciable

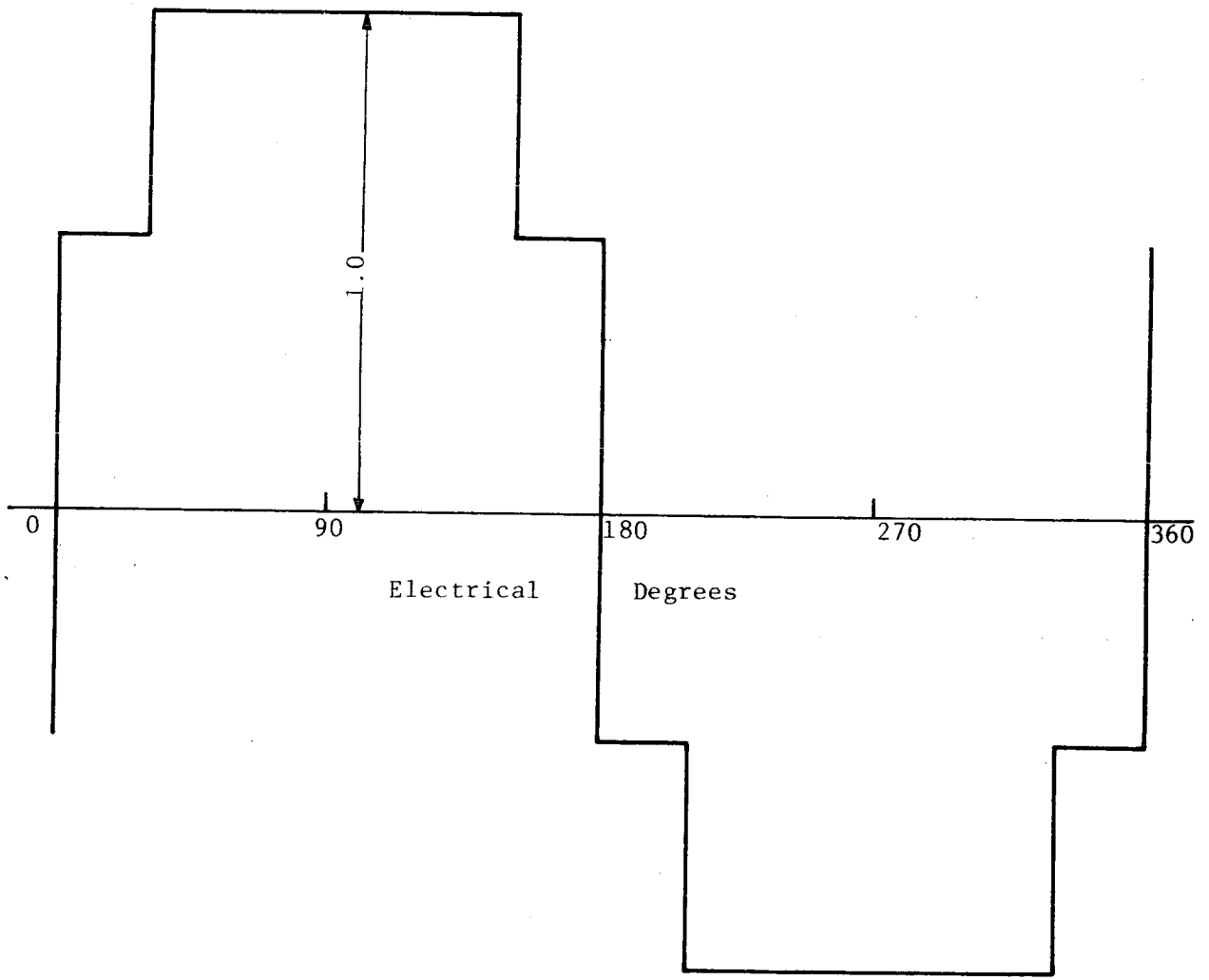

Figure 4-1. Voltage Generated in Two Sides of a Coil and in a One-Turn Coil

amplitude is the 11th. Higher harmonics will be smaller than given in Table 4-1 since the voltage waveform as shown in Figure 4-1 will have rounded instead of square corners.

4.2 Generated Voltage

From Section 3.4.3, the pole diameter is 1.955 and the pole length (at each end of the rotor) = 1.00 inches. Including the flux fringing dimension on 0.04 inches all around each pole tip, the effective area of each pole is:

$$A_p = \left(1.955 \frac{\pi \times .9}{4} + .08\right)(1.00 + .08) = 1.579 \text{ in}^2.$$

The flux through each pole will be:

$$\phi_p = 30 \times 10^3 \times 1.579 = 47.36 \text{ kl}.$$

The flux density distribution around the airgap at the average airgap diameter in mechanical degrees is shown in Figure 4-2.

Assume that the center of a rotor pole is lined up with a slot in lamination stack A. The voltage generated in one conductor in that slot with rotation of the rotor at an angular velocity of $\frac{d\theta}{dt}$ in radians will be:

$$e = \frac{d\phi}{dt} \times 10^{-8} = \frac{d\phi}{d\theta} \times \frac{d\theta}{dt} \times 10^{-8} = \frac{1.955}{2} \times 30 \times 10^3 \times 1.04 \times \frac{60{,}000}{60}$$

$$\times\ 2\pi \times 10^{-8} = 1.916 \text{ volts}$$

The same conductor in a slot in lamination stack B will be opposite the center of the small diameter region of the rotor where the flux density will be 3 kl/in^2. The flux direction will be opposite that in stack A. The voltage generated in this section of the conductor will be:

$$e = \frac{1.955}{2}\left(-3 \times 10^3\right) \times \frac{60{,}000}{60} \times 2\pi \times 10^{-8} = -.184 \text{ volts}$$

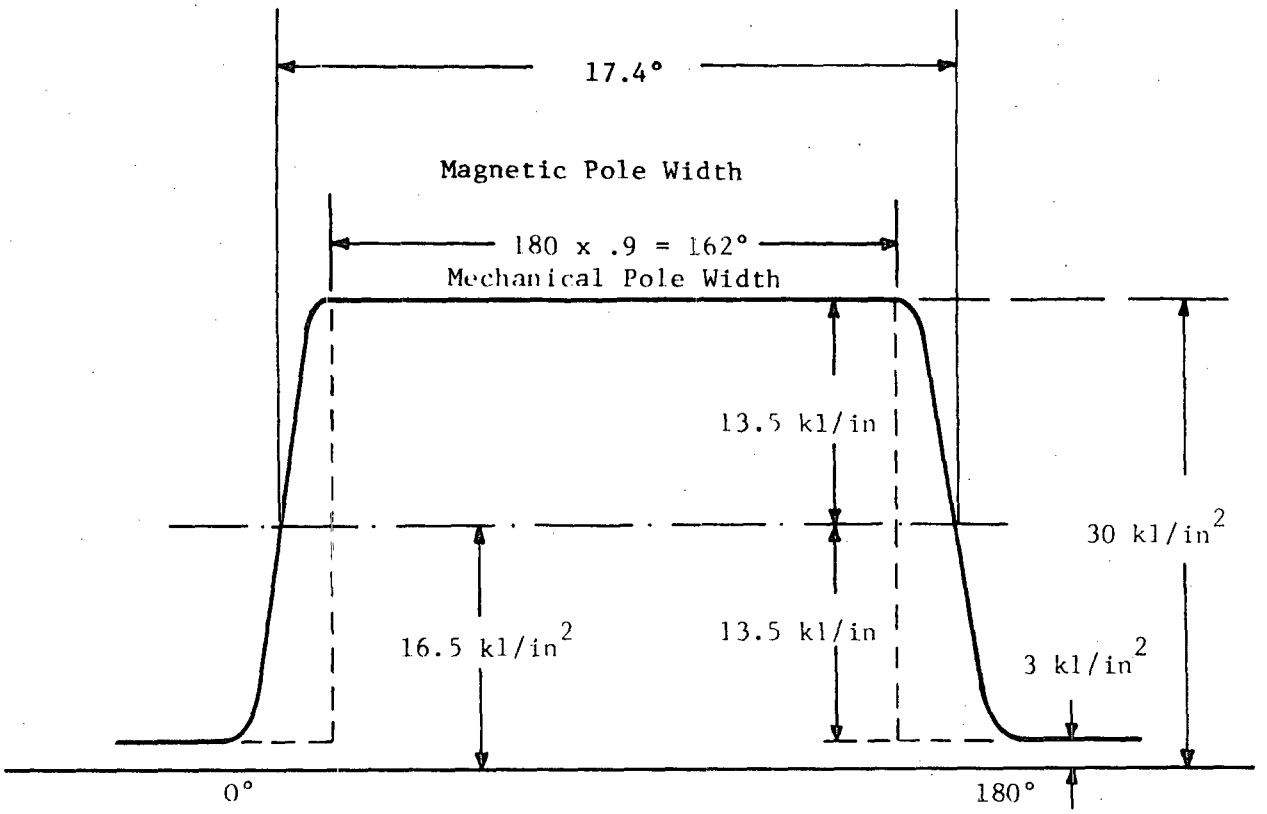

Figure 4-2. Flux Density Distribution Around the Airgap at the Average Airgap Diameter

The net volts per conductor will then be 1.916 - .184 = 1.723 volts (peak) and a coil consisting of two conductors will have a voltage of 3.464 volts (peak).

The fundamental harmonic voltage for a one-turn coil with an airgap flux density of 30 kl/in^2 (see Table 4-1) is, hence

$$e = \frac{3.464 \times 1.189}{\sqrt{2}} = 2.912 \text{ volts rms}$$

Two coils are connected in series per pole. These two coils are 30° electrical apart. The rms volts per phase for one-turn coils are then,

$$e_{ph} = 2.912 \angle 0° + 2.912 \angle 30° = 5.626 \text{ volts}$$

The volts per phase for a four-pole machine are 5.626 x 2 = 11.252.
The volts per phase for likely numbers of turns per coil are:

Turns/Coil	Volts/Phase
9	101.3
10	112.5
11	123.8

4.3 Required Line-to-Line Voltage

The 240-volt d-c motor is to be supplied by a three-phase, two-way rectifier. If the motor were fed directly by the rectifier and if the motor had negligible reactance and resistance, the current supplied by the alternator would consist of short pulses of high amplitude. To insure that sufficient inductance exists in the circuit to obtain a smooth and continuous motor current, an external inductor is used. Any degradation of motor efficiency due to pulsing current is then avoided. With a three-phase, two-way rectifier with constant current output from the rectifier, the average value of the output voltage is 0.866 of the peak value. In this case, the average rectifier output voltage will be 240 volts and the peak value will be 240/.866 = 277.1 volts. The rms value of the alternator terminal voltage will then be $277.1/\sqrt{2}$ = 196.0 volts rms. The required value of induced voltage will be higher by an amount sufficient to include the IR and IX drops in the alternator windings.

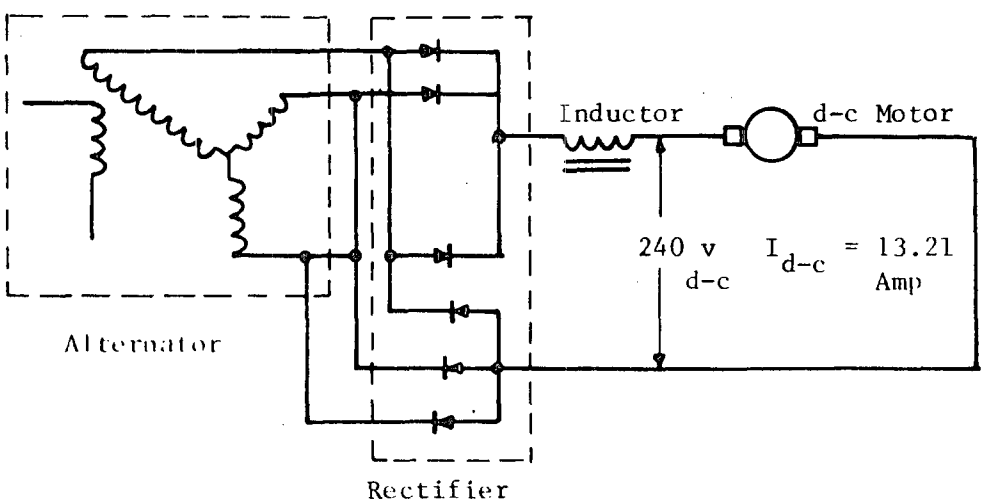

Figure 4-3. Circuit External to the Alternator

4.4 Load Current

The circuit external to the alternator is shown in Figure 4-3 consisting of a three-phase full wave rectifier and inductor such as Stancor #2689 rated at 0.005 Henries at 22.5 amperes. Since the d-c current ripple frequency is six times the input frequency of 2000 Hz, the 0.005 Henry inductor insures constant current in the motor.

The leakage and mutual reactances of the alternator windings are sufficient to cause a gradual commutation of current between the alternator phases rather than an abrupt switch. The current waveforms of the phases will be as shown in Figure 4-4.

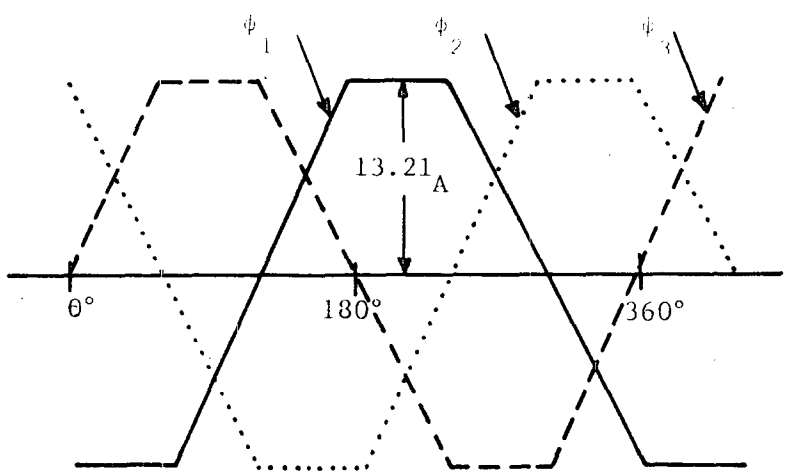

Figure 4-4. Phase Waveforms

The peak of the first harmonic obtained by harmonic analysis will be 13.29 amperes and the rms value is 9.40 amperes.

The line current will be in phase with the alternator terminal voltage due to the presence of the rectifier.

4.5 Lamination Layout

In order to calculate the IR and IX drops, the stator lamination layout is required. The configuration chosen is shown in Figures 1-2 and 1-3. The pertinent slot dimensions are shown in Figure 4-5.

4.6 Leakage Reactance Calculation

The leakage reactance is calculated by a method outlined in Kuhlmann's, Design of Electrical Apparatus, page 219. For a machine with an integral number of slots per pole and without squirrel cage windings in the pole face:

$$X_{\ell(\Omega)} = \frac{2.0 + f\mathcal{L}mn^2}{10^7 S_s} \left\{ \left[k_s \frac{d_3}{w_1} + \frac{2d_2}{w_1 + w_2} + \frac{d_1}{3\frac{(w_2 + w_3)}{2}} \right] + \frac{.3\,(3P - \mathcal{L})\,DS_s}{P^2\mathcal{L}} + \frac{.266\,Df_c^2 f_w^2}{S_s g} + \frac{.319\,Df_c^2 f_w^2 S_s K_p}{P^2 g} \right\}$$

Where:	f - Hz	2000
	$\mathcal{L}$ - length armature core	2.25*
	m - number of phases	3
	n - conductors in series/ph	8
	S_s - number of stator slots	24
	K_s - correction factor for 5/6 pitch chordal windings	.87
	P - pitch	.833
	D - airgap diameter	1.955
	p - number of poles	4

* Length of stator stack increased from 2" to 2.25" to account for flux fringing at end of stator stack.

f_c	- cord factor	.966
f_w	- winding distribution factor	.965
g	- airgap	.04
K_b	- belt leakage constant	.00025

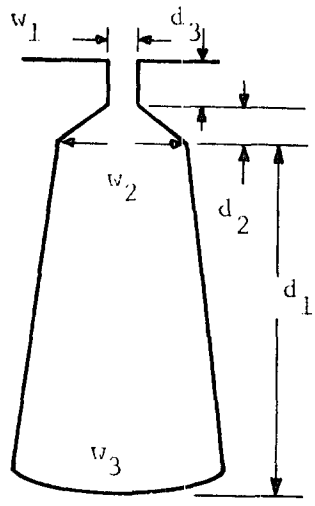

w_1 = .06 inches
w_2 = .14
w_3 = .263
d_1 = .42
d_2 = .04
d_3 = .04

Figure 4-5. Stator Slot Dimensions

For one-turn coils:

$$X_{\ell(\Omega)} = \frac{2.0 \times 2000 \times 2.25 \times 3 \times 8^2}{24 \times 10^7} \left\{ \left[.87 \frac{.04}{.06} + \frac{2 \times .04}{.06 + .14} + \frac{.42}{3\left(\frac{.14 + .263}{2}\right)} \right] \right.$$

$$+ \frac{.3\ (3 \times .833 - 1) 1.955 \times 24}{16 \times 2.25} + \frac{.266 \times 1.955 \times .966^2 \times .965^2}{24 \times .04}$$

$$+ \frac{.319 \times 1.955 \times .966^2 \times .965^2 \times 24 \times .00025}{4^2 \times .04}$$

$$X_\ell(\Omega) = 7.20 10^{-3} \left\{ 1.532 + .586 + .471 + .0048 \right\}$$
$$= 1.868\ 10^{-2}\ \Omega$$

The above calculation is for a machine which does not have two separated armature stacks. The inductance of the length of windings between the two stacks is:

$$L = 10^{-7}\ \angle\ (1 + 4\ \angle n\ \frac{a}{r}\ )\quad \text{Henries}$$

for which two wires of length, l, separated a distance a and with radius r.

$$\angle = 2.54\ 10^{-2} \times 2 = 5.08\ 10^{-2}$$
$$a = 9.0\ 10^{-2}\ M$$
$$r = 5.1\ 10^{-2}\ M$$

For a single one-turn coil the inductance is:

$$L = 5.39\ 10^{-8}\ \text{Henries}$$

There are two coupled coils per pole pair and two pole pairs per phase. The inductance per phase for one-turn coils is, therefore:

$$L = (5.39\ 10^{-8} \times 4)2 = 4.31\ 10^{-7}\ \text{Henries}$$

At 2000 Hz, the reactance is:

$$X_a = 5.42\ 10^{-3}\ \text{ohms}$$

The total reactance is $X_\ell + X_a = 2.41\ 10^{-2}$ ohms

The reactance for various likely numbers of turns per coil is as follows:

Turns/Coil	X_ℓ Ω/Phase
9	1.95
10	2.41
11	2.92

4.7 A-C Winding Resistance Calculation

The slot area is $\frac{.140 + .263}{2} \times .420 = .0846 \text{ in}^2$

Assume a .55 packing factor, bare copper to bare slot. The copper area in a slot = .0846 x .55 = .0465 in^2. The winding will have two coil sides/slot. Area of each coil (with a one-turn coil) = .0233 in^2. The length of the mean turn is (2.25 + 3.14)z = 10.28 inches. Each phase has 4 (one-turn) coils in series (equivalent).

$$R = \frac{10.28 \times 4}{12 \times 1000} \times \frac{1}{.0233} \times .0083 = .122\ 10^{-2} \text{ ohms/phase at } 20°C$$

The resistance per phase for likely numbers of turns/coil is as follows:

Turns/Coil	RΩ/Phase	
	20°C	75°C
9	.0989	.118
10	.122	.146
11	.148	.177

4.8 A-C Coil Turns Calculation

From previous sections, the generated voltage/phase, reactance/phase, and resistance per phase for 9, 10, and 11 turns/coil are listed below.

No Turns/Coil	$V_{gen/ph}$	Reactance/ph	Res/ph (75°C)
9	101.3	1.95	.118
10	112.5	2.41	.146
11	123.8	2.92	.177

The above generated voltage is based on an airgap flux density of 30 kl/in^2. The line current from Section 4.4 is 9.40 amperes. The required value of V_T is 177.5 volts (line-to-line) or 102.48/ph.

For the several number of turns per coil, the required V_{gen} (ph) and θ to give the

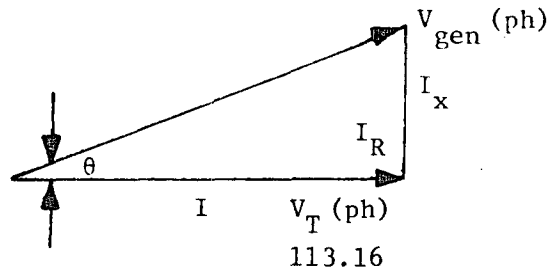

Figure 4-6

V_T (phase) of 102.48 at a current of 9.40 amp rms (three-phase line current) are as follows:

Turns	V_{gen}	θ
9	115.7	9.1°
10	116.7	11.2°
11	118.0	13.4°

The required generated voltage of 116.7 volts can be met with 10 turns with a slight upward adjustment of the airgap flux density from the design value. In addition, the rectifier drop of approximately 1.1 volts and the series inductor drop of 0.4 volts will have to be covered. It is desirable to hold down the number of turns per coil since the stator copper loss and the induced loss in the rotor pole face will vary as the number of turns squared.

The number of turns/coil to be used is 10.

The value of V_{gen} line-to-line for rated load is $116.7 \times \sqrt{3} = 202.1$ volts, neglecting the rectifier and inductor drops.

4.9 D-C Magnetic Circuit

4.9.1 Saturation Curve Calculation

The rotor is constructed of alloy steel SAE 8620. The laminations are 0.007" thickness silicon steel. The sleeve over the outside of the laminations is of low carbon steel but has such low flux density that negligible magnetic drop occurs and is neglected in the magnetic analysis. Figure 4-7 shows saturation curves for the lamination material. Figure

4-8 shows the d-c saturation curve for 4130 alloy steel. The principle difference between the 4130 and 8620 alloy steels is that 8620 has 0.6 percent nickel where 4130 has none. Information published by the American Society for Metals shows negligible effect on the saturation induction level for the addition of several percent of nickel. Any effect on the low induction levels would be a reduction of the magnetomotive force required.

The principle ampere turn drop in the rotor is in the body between the poles plus an estimated 0.1 inch of length. This extra length is required to allow the flux to disperse into the larger area available in the pole area.

The flux per pole from Section 4.2 is 47.36 kl. The ratio of useful flux from Section 3.4.1 is 0.91. The total flux in the body of the rotor will be:

$$\phi_B = 47.36 \times 2 \times \frac{1}{0.91} = 104.1 \text{ kl}$$

The area of the body is $1.2^2\ \pi/4 = 1.131\ \text{in}^2$. The flux density is then:

$$B_b = \frac{104.1}{1.131} = 92\ \text{kl/in}^2$$

The principal drop in the stator is in the teeth of the laminations. The flux which passes through each stator tooth (which is opposite the rotor pole) is:

$$\phi_t = \frac{1.955 \times \pi}{24} \times 1.08 \times 30{,}000 = 8290 \text{ lines}$$

The area of the iron in each tooth with a 0.95 stacking factor for the lamination is:

$$A_t = 1.00 \times .13 \times .95 = .1235\ \text{in}^2$$

The flux density is:

$$B_t = \frac{8290}{.1235} = 67.1\ \text{kl/in}^2 \text{ (d-c flux only)}$$

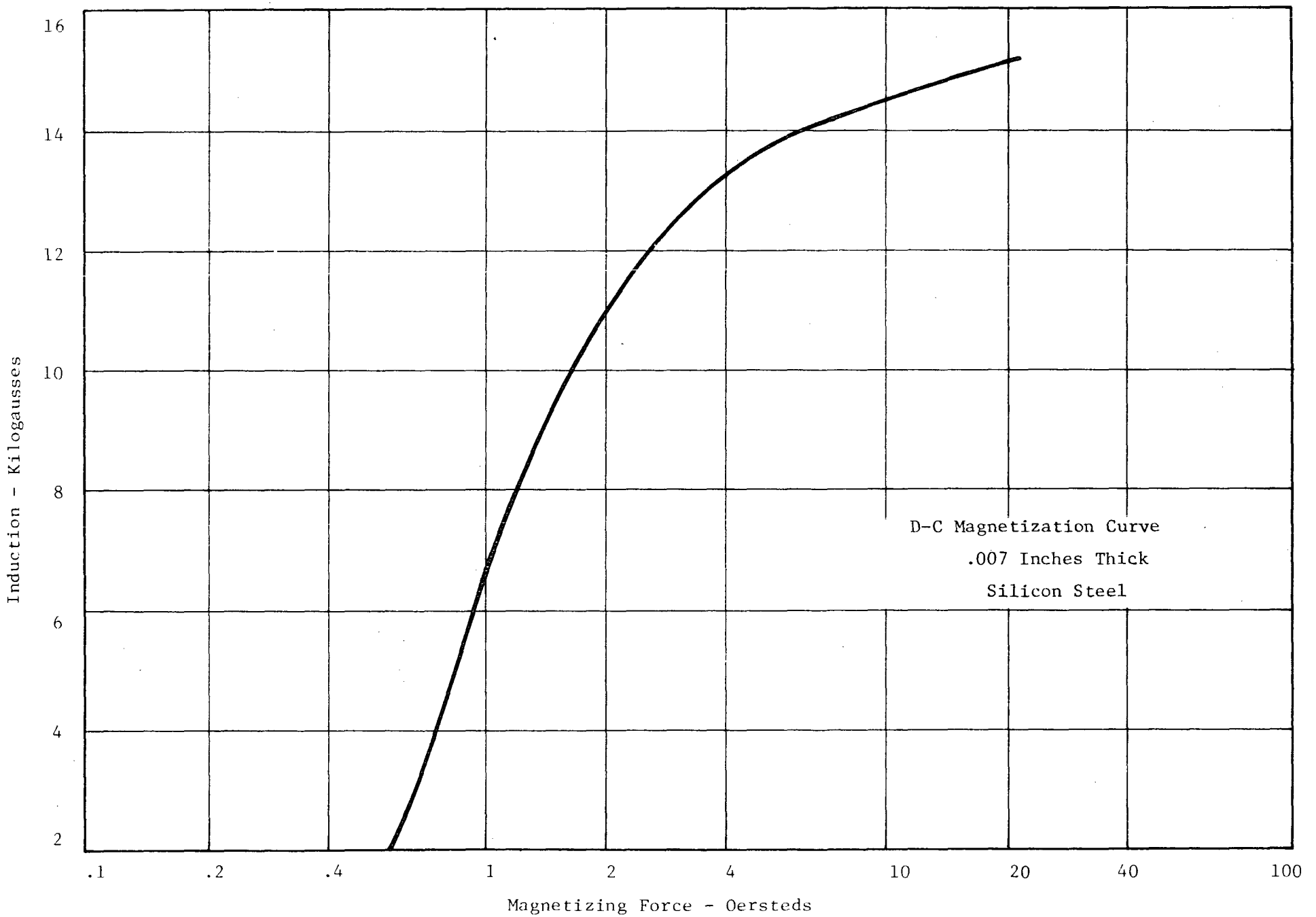

Figure 4-7. D-C Magnetization Curve

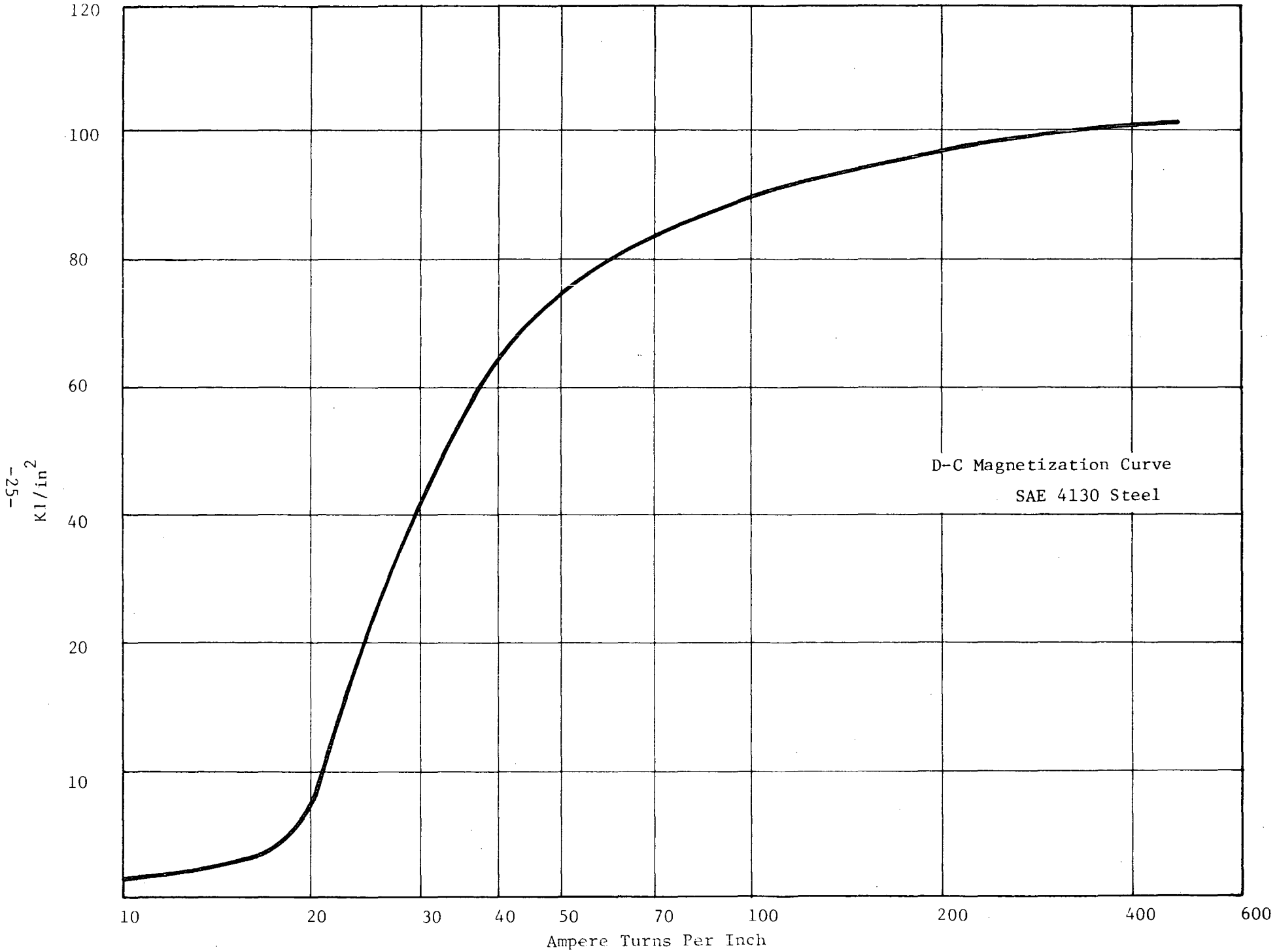
120
100
80
60
40
20
10
Kl/in^2
D-C Magnetization Curve
SAE 4130 Steel
10
20
30
40
50
70
100
200
400
600
Ampere Turns Per Inch

Figure 4-8

Table 4-2 shows the d-c ampere turns required for the magnetic circuit at various flux levels with 100 percent corresponding to 30 kl/in^2 in the airgap.

TABLE 4-2

Percent Flux Density	NI Airgaps	Rotor Iron NI Body	Rotor Iron NI Poletip	Stator Iron NI	Total
50	376	26	12	2	416
70	526	33	12	2	573
90	677	44	12	3	736
100	752	50	13	3	818
110	827	56	13	4	897
120	902	165	14	5	1087
130	978	330	15	8	1331

Figure 4-9 shows the d-c saturation curve plotted from the data in Table 4-2. The 100 percent point on the curve corresponds to 30 kl/in^2 and also corresponds closely to the 100 percent rated open circuit voltage point.

4.9.2 Field Ampere Turns Required

The open circuit generated voltage for 30 kl/in^2 flux density in the airgap is 112.5 (Section 4.8). This is slightly less than that needed to deliver the terminal voltage required underload. The field ampere turns required from Figure 4-9 are 816. In addition, the load current gives demagnetizing ampere turns which must also be supplied.

The armature reaction ampere turns for a three-phase machine are:

$$AT_{crest} = \frac{4\sqrt{2}}{\pi} NI\ f_c\ f_w\ k_a$$

Where: $k_a = \dfrac{\pi\ fd + \sin \pi\ fd}{4 \sin fd \frac{\pi}{2}}$

The flux distribution factor is:

$$fd = \frac{\text{Area Under Flux Distribution Curve}}{\text{Area of Rectangle with Same Base and Max Ordinates}}$$

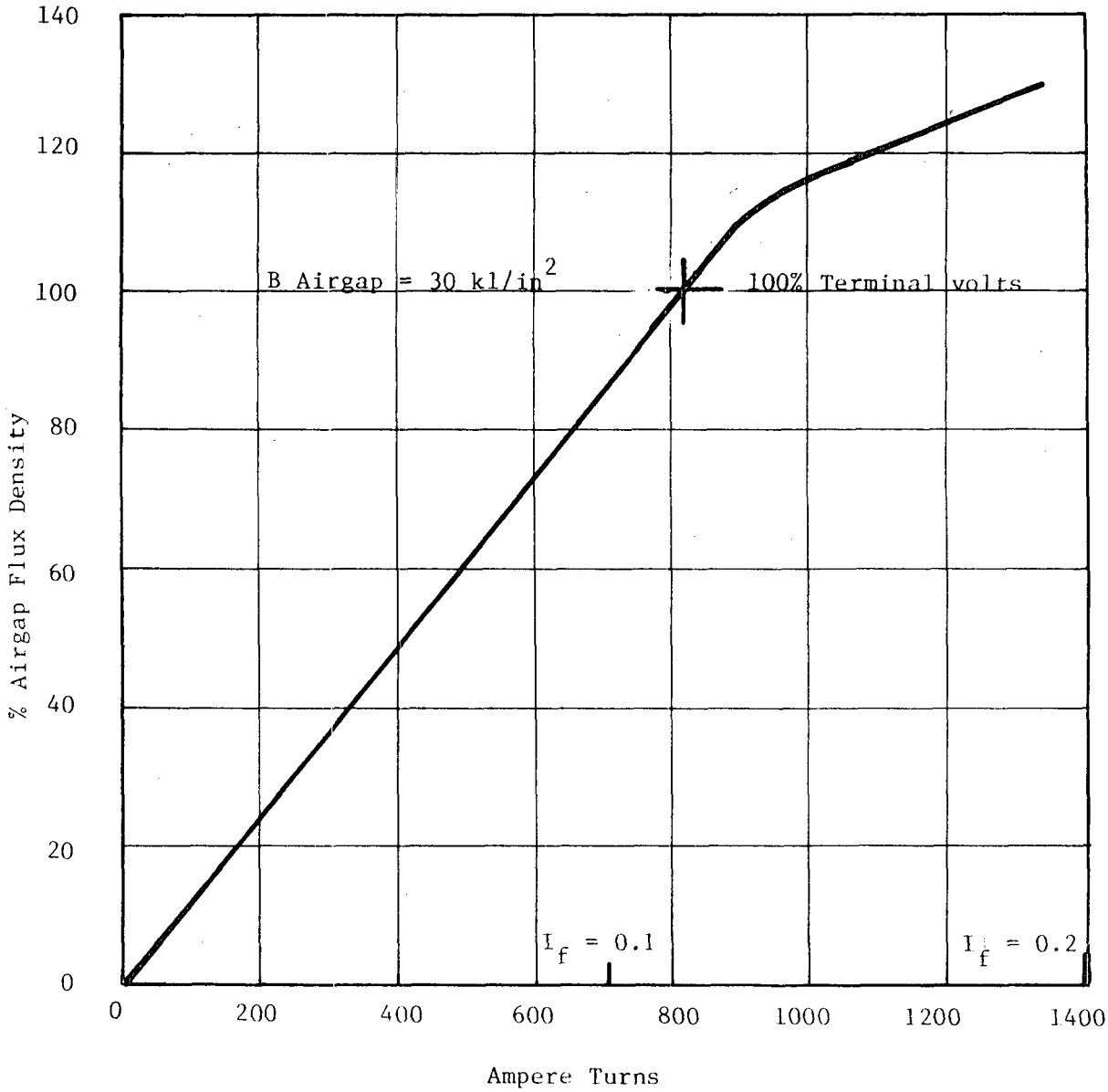

Figure 4-9. D-C Saturation Curve

fd = .95 (from Figure 4-2)

k_a = 0.788 (from equation on page 26)

f_c = chord factor = 5/6

f_w = winding distribution factor = 0.966

N = conductors/phase = 80

I = phase current, rms = 9.40

Then

$$AT_{crest} = \frac{4\sqrt{2}}{\pi} \times 80 \times 9.40 \times 5/6 \times 0.966 \times 0.788 = 859$$

If the angle between the generated voltage and load current is 90° lagging, these ampere turns will be directly subtracted from the field ampere turns. If this angle is zero, only a cross-magnetizing effect will be present which will be negligible as long as the stator iron is operating in the linear region. Due to the low values of flux density used in this design, the cross-magnetization is neglected.

From Section 4.7, the angle between the generated voltage and the line current is 10.66°. The effective value of the armature reaction is then:

$$AT_{eff.} = 859 \sin 10.66° = 159 \text{ ampere turns}$$

The field ampere turns required are, hence:

$$816 + 159 = 975$$

4.9.3 Field Winding Calculation

The voltage used to excite the field winding will be obtained from a separate rectifier from that supplying the load current using a single-phase full wave rectifier. This arrangement as shown in Figure 4-10 gives a lower d-c voltage for the alternator field allowing the use of heavier wire in the field winding.

The rms line-to-line voltage is 177.5 and the average value is 159.7 volts. The required field ampere turns are 975. Approximately 1300 ampere turns should be available to provide for variation in the magnetic circuit

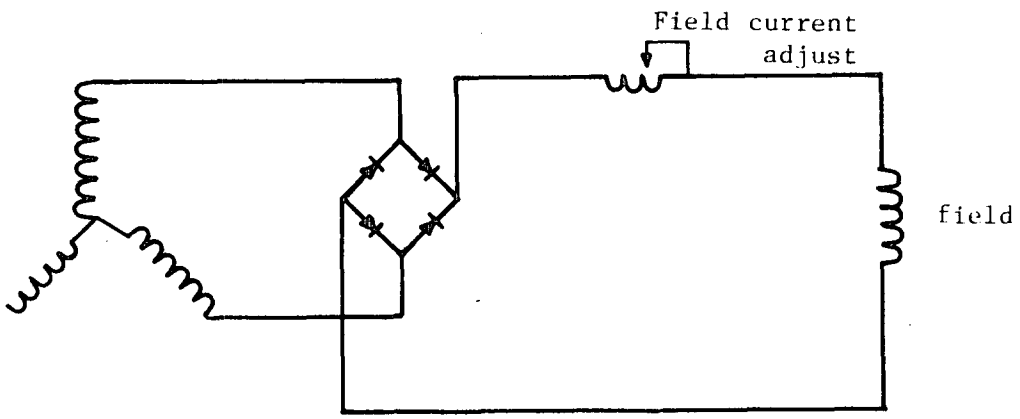

Figure 4-10. Single-Phase Full Wave Rectifier

from the design value and make possible additional output if required. The field current can be reduced by a variable resistor. The space available for the field winding is 1.125" x 1" = 1.125 in^2. Using a packing factor of 0.49, bare copper to bare iron, the area of the copper is 0.550 sq. in. The length of the mean turn is 3.8 π inches. The resistance coil of a one-turn coil is:

$$R = \frac{3.8\,\pi}{12 \times 1000} \times \frac{1}{.55} \times 9.9 \quad 10^{-3} \text{ at } 75^{\circ}C$$

$$= 1.791\ 10^{-5} \text{ ohms}$$

The voltage across the coil is $1.791\ 10^{-5} \times 1300 = 2.328\ 10^{-2}$ volts.

For 159.7 volts, the turns would be:

$$N = \frac{159.7}{2.328\ 10^{-2}} = 6860 \quad \text{(use 7000 turns)}$$

$$\text{Area of wire} = \frac{0.55}{7000} = 7.86\ 10^{-5}\ in.^2 \quad \text{(Use \#30 wire)}$$

The resistance at 75°C is:

$$\frac{3.8\ \pi}{12 \times 1000} \times 7000 \times 126 = 877\ \Omega$$

At 20°C, the resistance would be:

$$877 \times \frac{.0083}{.0099} = 735.\ \text{ohms}$$

5.0 LOSS ANALYSIS

5.0 The losses are divided into the following categories:

- Stator I^2R
- Stator iron loss
- Rotor eddy current loss
- Field loss
- Stray loss

5.1 Stator I^2R Loss

The resistance of each phase was calculated (Section 4.6) to be 0.146 ohms/ph at 75°C. The rms current (Section 4.3) is 9.40 amperes.

$$I^2R_{stator} = 9.40^2 \times 0.146 \times 3 = 38.7 \text{ watts}$$

Since the stator is wound with No. 20 wire, the skin effect at 2000 Hz is negligible.

5.2 Stator Iron Loss

The only portion of the stator iron in which appreciable loss exists is in the stator teeth. The weight of the stator teeth in pounds is:

$$w_{lbs} = 2 \times 24 \times 0.13 \times .5 \times 1 \times 0.278 = 0.867$$

The iron loss is caused by the peak density in the stator teeth caused by the sum of the a-c and d-c fluxes. The d-c flux density had previously been calculated (Section 4.9) as 67.1 kl/in^2. The a-c flux density is 4.2 kl/in^2 as determined from the a-c flux calculated. The total flux density is then 71.3. kl/in^2.

Figure 5-1 shows the core loss per pound versus flux density for the stator lamination material. From Figure 4-9 the core loss per pound is determined as 25 watts per pound. In practice, however, the manufacturer's data is always exceeded by a factor of 1.5 or more due to effects of punching, flux concentration on tooth tips, and eddy currents due to shorts between laminations. Also, some loss exists in the yoke of the stator laminations. The lamination iron loss is:

$$W = 0.867 \times 25 \times 1.5 = 32.9 \text{ watts}$$

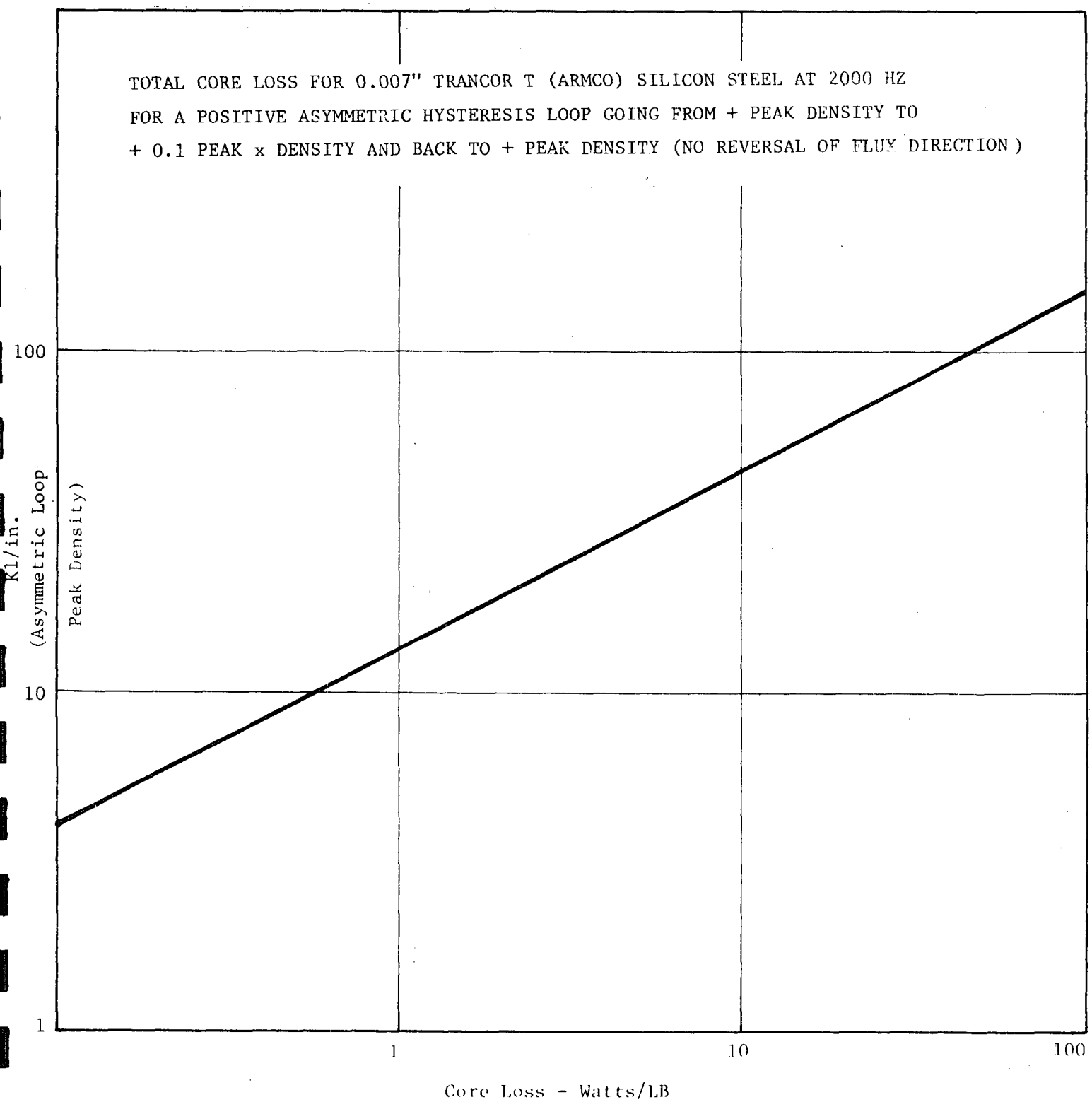
TOTAL CORE LOSS FOR 0.007" TRANCOR T (ARMCO) SILICON STEEL AT 2000 HZ
FOR A POSITIVE ASYMMETRIC HYSTERESIS LOOP GOING FROM + PEAK DENSITY TO
+ 0.1 PEAK x DENSITY AND BACK TO + PEAK DENSITY (NO REVERSAL OF FLUX DIRECTION)
100
10
1
K1/in.
(Asymmetric Loop
Peak Density)
1
10
100
Core Loss - Watts/LB

Figure 5-1.

5.3 Pole Face Loss

The ampere turns in each slot of the stator facing a pole is shown in Figure 5-2 for a particular instant of time. The ampere turns from tooth to tooth are also plotted. The average ampere turn wave travels in synchronism with the pole face, but the increments which are always located at the slot positions are stationary in space although varying in magnitude, and, hence, the surface of the rotor is expcsed through the airgap to a mmf wave with a peak-to-peak amplitude of the peak slot ampere turns and at a frequency of the speed in revolutions/second times the number of stator slots. The frequency of the wave is n/60 x S, where n is the rpm of the rotor and S is the number of slots in the stator. The mmf of the slot ampere turns is divided between the airgap and drop in the rotor across the iron between two slots.

The depth of penetration is that required to carry the flux. The method used to calculate the depth of penetration and the H across the iron is given in "Eddy Current Losses in Solid and Laminated Iron", Paul D. Agarwal, AIEEE Paper 59-12, 1959.

The a-c flux in the airgap, neglecting the iron drop, is:

$$\phi_{ac} = NI \frac{A}{2 \times g} \mu_o \text{ Webers}$$

From the lamination layout, $A = .201'' \times 1'' = 1.297 \text{ E-4 } M^2$

$g = .04'' = \quad = 1.016 \text{ E-3 } M$

$\mu_o = 4\pi \times 10^{-7}$

For the slot having 264 ampere turns peak-to-peak, the a-c flux is:

$$\phi_p = 1.059 \text{ E-5 Webers}$$

This is the limiting value.

The actual value is obtained by iteration by assuming that only part of the potential is dropped across the airgap and comparing the value of a-c flux with that carried by the iron. The depth of penetration in the iron is:

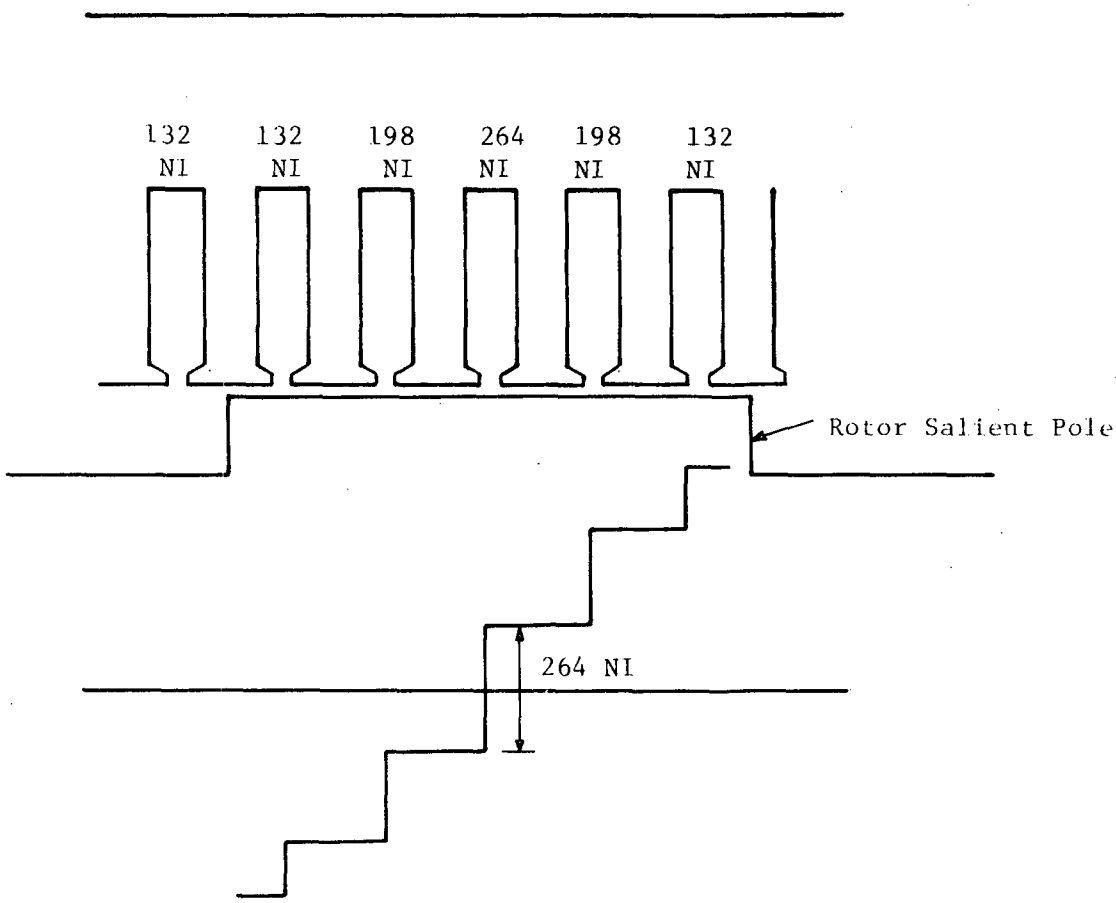

Figure 5-2. Stator Lamination Stack

$$\delta = \left(\frac{2\ P}{\omega\ B_o/H_m} \right)^{\frac{1}{2}}$$

$\omega = n/60 \times \delta x\ 2\pi = 1.508\ 10^{-5}$

$\rho = 20 \times 10^{-8}$ ohm meters

$B_o = .74\ B_m$ Webers/meter^2

From the B/H curve for the rotor iron shown in Figure 4-8, values of B_m and H_m for several values of B_m are calculated and shown in the following table.

TABLE 5-1

H_m NI/in	H_m NI/M	B_m kl/in^2	B_o Webers/M^2
50	1.969 E3	95.0	1.104
100	3.937 E3	110.0	1.279
200	7.874 E3	116.0	1.349
300	1.181 E4	120	1.395
400	1.575 E4	120.8	1.405
500	1.969 E4	121.5	1.413

The depth of penetration and a-c flux for the above values of H_m are as shown in the following table.

TABLE 5-2

H_m NI/M	B_o/H_m	δ Meters	ϕ_{a-c} Webers	NI Required
$1.969\ 10^{-3}$	$5.607\ 10^{-4}$	$6.878\ 10^{-5}$	$1.929\ 10^{-6}$	10.0
$3.937\ 10^{-3}$	$3.249\ 10^{-4}$	$9.036\ 10^{-5}$	$2.935\ 10^{-6}$	20.1
$7.814\ 10^{-3}$	$1.713\ 10^{-4}$	$1.244\ 10^{-4}$	$4.263\ 10^{-6}$	40.2
$1.181\ 10^{-4}$	$1.181\ 10^{-4}$	$1.499\ 10^{-4}$	$5.311\ 10^{-6}$	60.3
$1.575\ 10^{-4}$	$8.921\ 10^{-5}$	$1.724\ 10^{-4}$	$6.152\ 10^{-6}$	80.4
$1.969\ 10^{-4}$	$7.176\ 10^{-5}$	$1.923\ 10^{-4}$	$6.902\ 10^{-6}$	100.5

The values of a-c flux versus NI from Table 5-2 are plotted in Figure 5-3. By trial, a value of ϕ_{ac} of 5.47 E=6 gives a value of 68.2 ampere turns across the airgap and 63.8 ampere turns across the iron length of .201" or $H_m = 2.512\ 10^{-3}$ peak, $1.776\ 10^{-3}$ rms. The corresponding value of $B_o/H_m = 4.587\ 10^{-4}$.

The loss in the solid pole face, watts per square meter, is:

$$N = \frac{8}{3\pi}\left(\frac{\omega B_o/H_m\ \rho}{2}\right)^{\frac{1}{2}} H_m^{\ 2}$$

$$= 8{,}300 \text{ watts/meter}^2$$

The area of the rotor poles is $1.955 \times \pi \times .9 = 5.528$ in.^{2} $= 3.566\ 10^{-3}$ in.^{2}
The loss in the rotor poles is then:

$$N = 8{,}300 \times 3.566\ 10^{-3} = 29.6 \text{ watts}$$

In like manner, there is also loss in the non-magnetic Rene' filler material between the salient poles. This material is conductive, $\rho = 52.\ 10^{-8}$, and non-magnetic; that is, $B_o/H_m = 4\ \pi\ 10^{-7}$.

The watts loss is then:

$$N = \frac{8}{3\pi}\left(\frac{1.508\ 10^{-5} \times 4\ \pi\ 10^{-7} \times 52\ 10^{-8}}{2}\right)^{\frac{1}{2}} (2.628\ 10^{-3})^2$$

$$= 1{,}300 \text{ watts/meter}^2$$

The area of Rene' 41 exposed to the mmf is 6.756 in.^{2} $= 4.359\ 10^{-3}$ m^2.
The loss in the Rene' 41 is then:

$$N = 1{,}300 \times 4.359\ 10^{-3} = 5.6 \text{ watts}$$

The total rotor eddy current loss is then 35.2 watts.

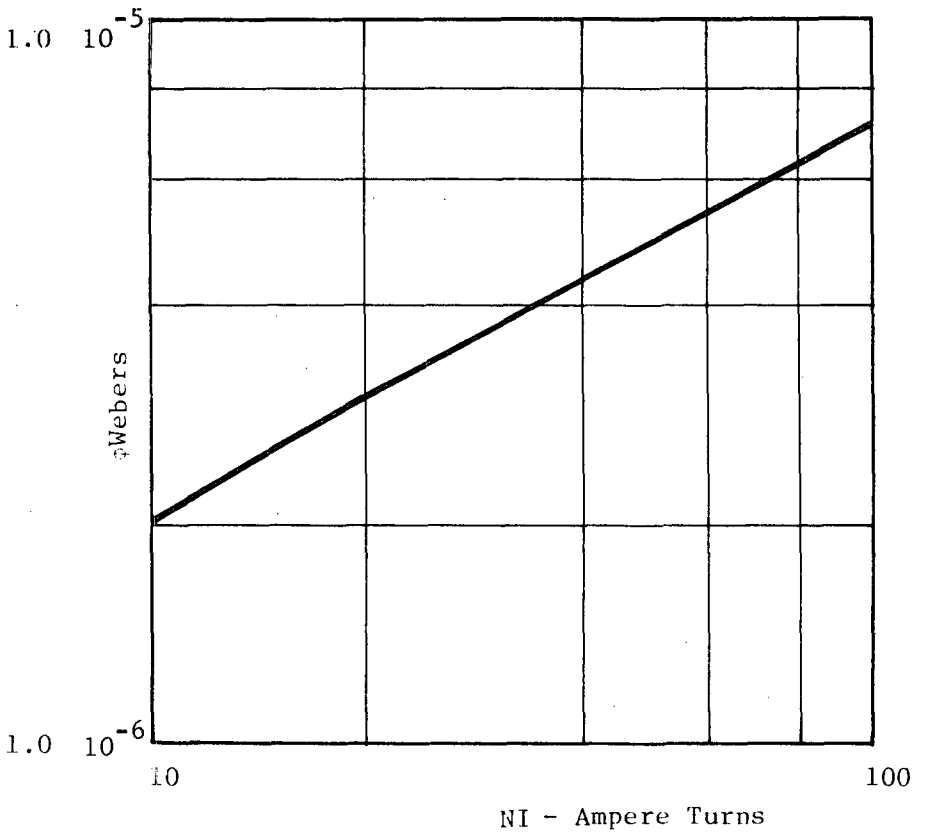

Figure 5-3

5.4 Field Loss

The required field current for the loaded alternator is:

$$I_f = \frac{975}{7000} = 0.139 \text{ amperes}$$

Using the field supply voltage of 159.7, the field power including that dissipated in the series resistor is:

$$W_F = 159.7 \times .139 = 22.2 \text{ Watts}$$

5.5 Stray Loss

The stray loss, primarily in the stator tooth tips, is estimated to be one-third of the stator iron loss.

$$\text{Stray loss} = 1/3 \times 32.9 = 11.0 \text{ watts}$$

6.0 PERFORMANCE SUMMARY

At the design operating point:

RPM = 60,000

V_{out} = 240 Vdc

I_{dc} = 13.40 amp

watts = 3170

The following losses have been calculated in Section 5, exclusive of windage and friction.

I^2R Loss	38.7
Stator Iron Loss	32.9
Rotor Eddy Current Loss	35.2
Field Loss	22.2
Stray Loss	11.0
	140.0

$$\text{Efficiency} = \frac{3170}{3170 + 140} = 95.8\%$$

It is assumed that the alternator terminal voltage varies as n. Since the load watts varies as n^3, the line current will decrease as the speed is reduced by $1/n^2$. The I^2R loss and stray loss vary with I^2, the stator iron loss varies as 1/n, and the field loss remains constant. The rotor eddy current loss varies approximately as $I^{5/2}$. The efficiency as a function of speed is then determined as shown in Table 6-1.

TABLE 6-1

EFFICIENCY AS A FUNCTION OF SPEED

n p.u.	I p.u.	I^2R stray x I	Rotor Eddy x $I^{5/2}$	Iron x 1/n	Field Loss x 1	Total Loss	Output Watts	Eff. %
1.0	1.	49.7	35.2	32.9	22.2	140	3170	95.8
.9	.81	32.6	20.8	29.6	22.2	105.2	2311	95.6
.8	.64	20.4	11.5	21.1	22.2	75.2	1623	95.6
.7	.49	11.9	5.9	16.1	22.2	56.1	1087	95.1
.6	.36	6.4	2.8	11.8	22.2	43.2	685	94.1

7.0 TEST RESULTS

The alternator stator was built as shown in the drawings. The rotor, however, had a body diameter of 1.1" instead of 1.2". Also, when the Rene' 41 pieces were electron-beam-welded to the alloy steel pole pieces, approximately 0.05" on each side of the pole facing the Rene' 41 was alloyed with the Rene' 41, substantially changing the magnetic properties. The rotor pole was then smaller than planned in both the circumferential and axial directions.

Dynamic tests were performed up to 20,000 rpm, making it necessary to extropolate the losses measured at 16,000 and 20,000 rpm up to what would exist at 60,000 rpm.

7.1 D-C Saturation Curve

A one-turn coil placed around the body of the rotor was connected to a flux meter. As the d-c field current was increased, the d-c flux was plotted as shown in Figure 7-1. Comparing the results with Figure 4-3 shows that at 0.071 ampere or 500 ampere turns, the d-c flux was 58 kl instead of 60 kl calculated. With the proper pole area, the calculated flux will be obtained. At 1000 ampere turns (0.143 amperes), the flux is 94 kl instead of 116. This shows the effect of the rotor body being smaller than designed. A new rotor with the proper dimensions has been built but not tested.

7.2 Resistance Measurements Tests

The a-c windings were measured as 0.110 ohms at 20°C as compared to the calculated value of 0.122 ohms.

The field winding was measured as 751.3 ohms at 20°C. The calculated value was 735 ohms.

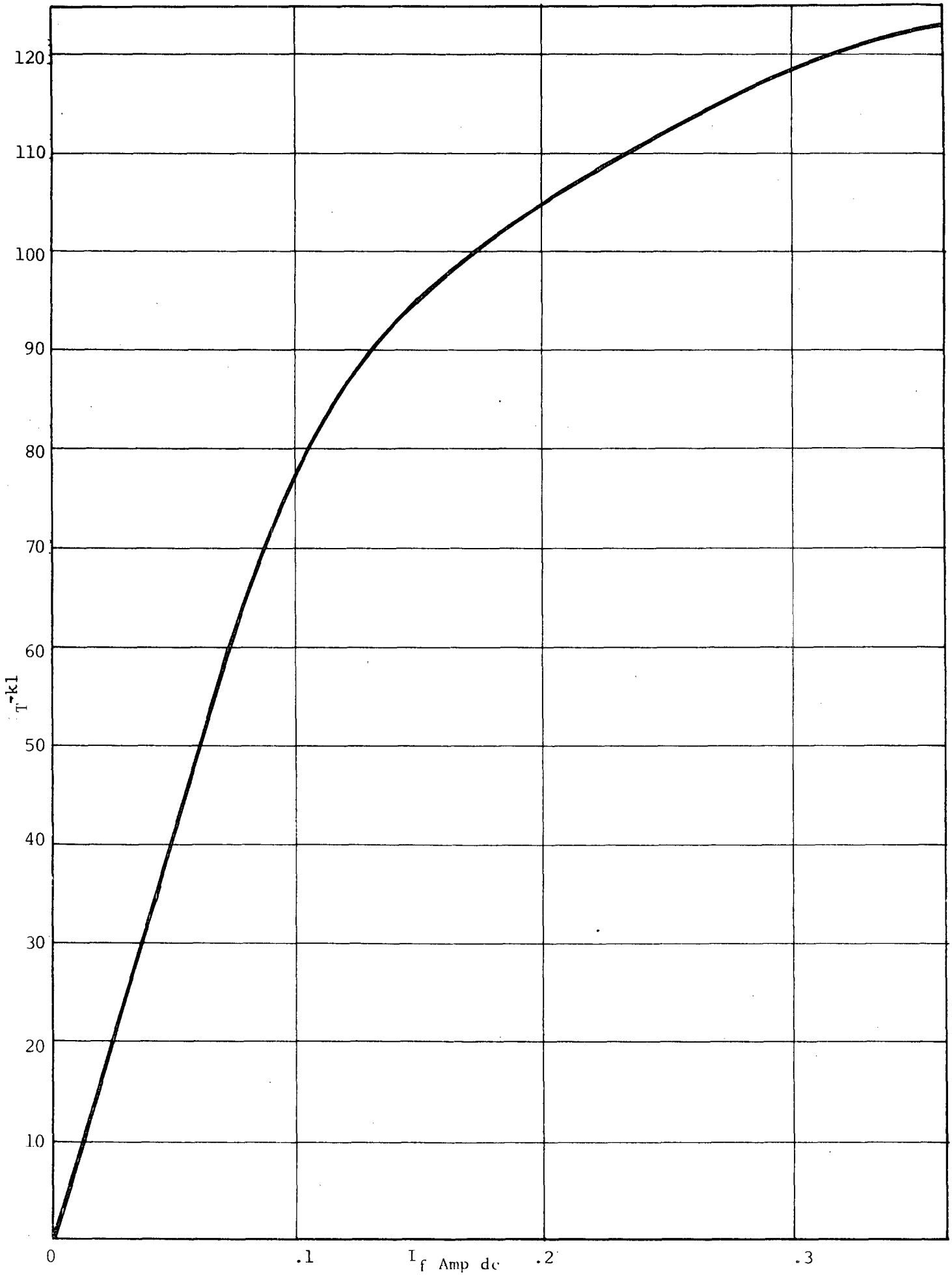

Figure 7-1. CNG Alternator dc Saturation Curve

7.3 Open Circuit Generated Voltage Test

TABLE 7-1

OPEN CIRCUIT TEST

Speed rpm	Torque* lb in.	I_f Amperes	Volts L-L rms
20,000	.0	0	0
20,000	.02	.025	15.82
20,000	.04	.050	30.94
20,000	.05	.075	23.87
20,000	.06	.100	53.60
20,000	.09	.125	59.92
20,000	.09	.150	64.30
20,000	.10	.175	67.50
20,000	.12	.200	70.08

* The tare value of the actual torque reading at $I_f = 0$ is subtracted from the torque value shown.

The open circuit volts versus I_f is plotted in Figure 7-2. The required line-to-line voltage open circuit is 116.7 x 3 = 202.1 volts rms, as determined in Section 4.8. At 20,000 rpm, the voltage generated would be $202.1 \times \frac{20,000}{60,000} = 67.37$ volts. From Figure 4-8 the required field current for this voltage is 0.173 amperes as compared to the calculated value of $\frac{820}{7000} = 0.117$ amperes from Figure 4-3. The discrepancy is largely caused by early saturation caused by the undersized rotor body diameter. The shaft input power at $I_f = .173$ ampere supplies the iron eddy current and hystersis loss. At 20,000 rpm, the power is:

$$W = \frac{.06 \times 20,000}{84.518} = 14.2 \text{ watts}$$

Since the stator iron eddy current loss should be very low, the loss is mainly hystersis and will vary directly with the speed. The loss at 60,000 rpm would then be 42.6 watts. The calculated value in Section 5.2 is 32.9 watts. An oscillogram of the open circuit voltage is shown in Figure 7-3. The waveform is quite sinusoidal with the predominate harmonic being the 11th. This is in agreement with Table 4-1, Section 4.1, keeping in mind that the 3rd and 9th harmonics are cancelled due to the wye connection of the phases.

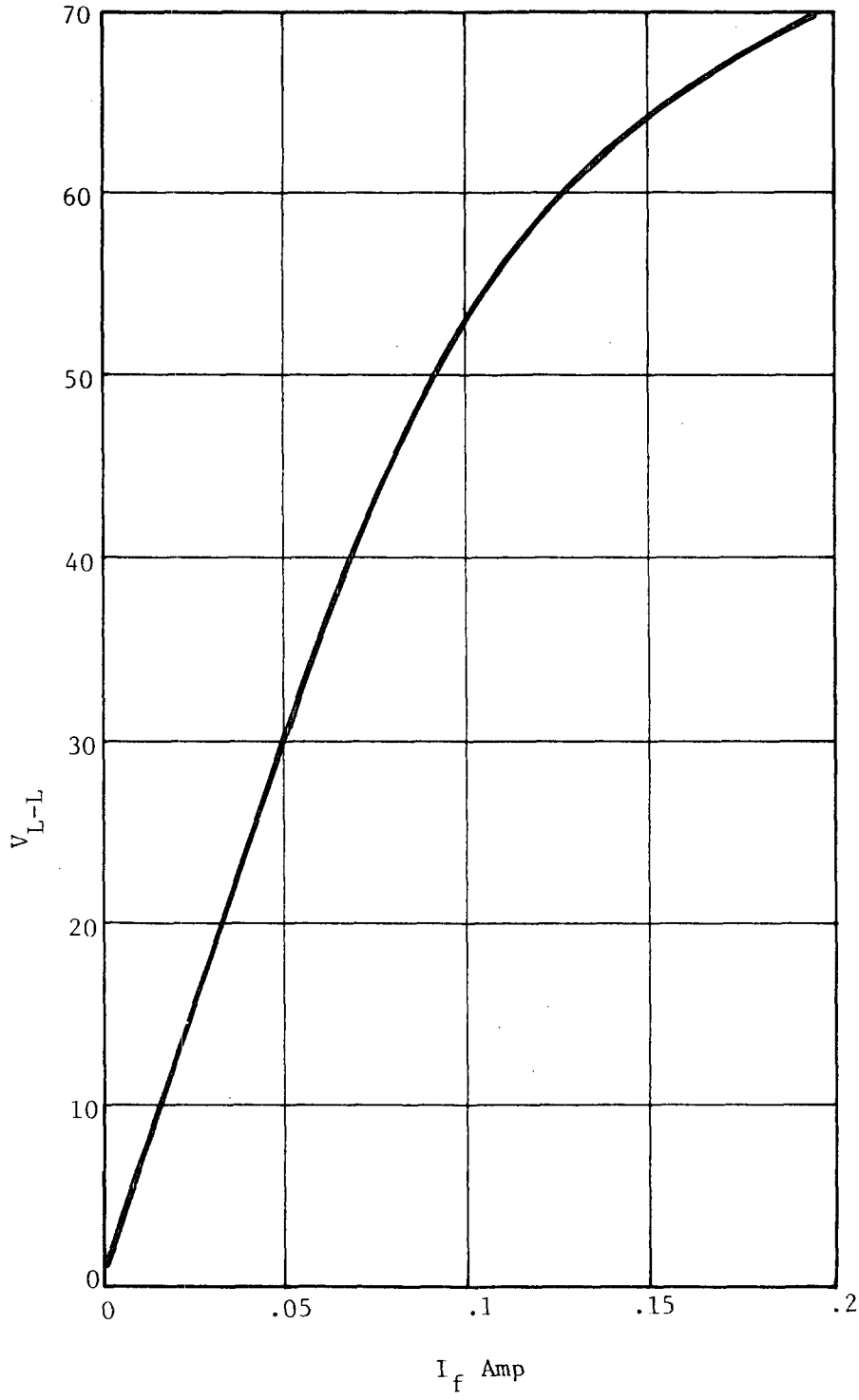

Figure 7-2. Open Circuit Volts - 20,000 RPM

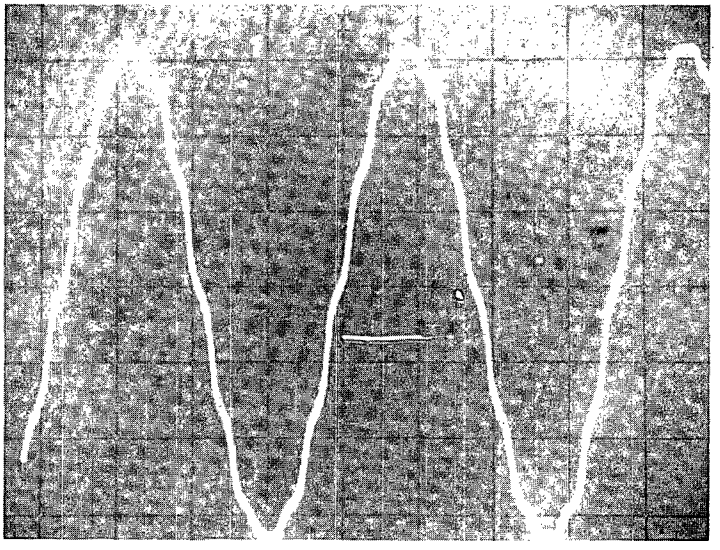

Figure 7-3. Open Circuit Voltage 20,000 RPM

7.4 Short Circuit Test

With the output of the rectifier shorted, the field current was increased in increments until the rated line current of 9.4 amperes a-c is obtained. This corresponds to a d-c current of 13.29 amperes.

Except for the rectifier losses, the entire input power is dissipated in armature I^2R loss and rotor pole face loss. The stator iron loss is assumed to be small. After subtracting the stator I^2R and rectifier losses, the balance is the rotor surface loss. The results of the short circuit test are given in Table 7-2.

If the rotor pole surface loss calculations are repeated for a speed of 20,000 rpm instead of 60,000 rpm, the loss obtained is 23.7 watts. This corresponds to a d-c current of 13.29 amperes d-c in Table 7-2 and a rotor loss of 20 watts. This agreement is excellent.

Since the load on the machine when shorted is almost entirely the reactance of the machine, the phase current and the generated voltage are essentially at right angles, and the generated voltage is that required to overcome the reactance drop. The reactance at 20,000 rpm will be 1/3 of that calculated for 60,000 rpm or 0.80 Ω per phase.

The generated voltage will be:

$$I_z = 9.40\ (0.146 + 0.80) = 7.64 \text{ volts per phase.}$$

The equivalent line-to-line voltage is $7.64\sqrt{3} = 13.23$. From Figure 7-2 this requires .02 amperes or 140 ampere turns.

From Table 7-2 the field current for 13.29 amps d-c is approximately 0.099 amperes or 698 ampere turns. The armature reaction is then 698 - 140 = 558 ampere turns. The value calculated in Section 4.9.2 is 859. This is only fair agreement; however, the degree of d-c saturation encountered and the fact that the armature reaction calculation method is recognized as being pessimistic and conservative accounts for the difference.

7.5 Load Test

A load resistance of approximately 4 ohms was connected to the rectified

TABLE 7-2

SHORT CIRCUIT TEST

Speed rpm	Torque Lb in*	I_f Amp	Output Amps dc	Input Watts	Calc.** I^2R	Calc Rectifier Loss	Calc Rotor Loss
20,000	0	0	0	0		0	
20,000	.03	.025	3.6	8.4	2.4	4.0	2.0
20,000	.09	.050	7.1	25.1	9.3	7.8	8.0
20,000	.15	.075	10.2	41.9	19.1	11.2	11.6
20,000	.25	.100	13.4	69.9	33.0	14.7	22.2
20,000	.39	.125	16.1	108.0	47.6	17.7	43.6
20,000	.48	.150	18.5	134.0	62.8	20.4	50.8
20,000	.60	.175	20.2	167.6	74.9	22.2	70.5
20,000	.69	.200	21.8	192.7	87.3	24.0	81.4

* Tare torque due to windage and friction has been subtracted.

** Stator I^2R losses calculated at 20^oC.

d-c output with the alternator operating at 20,000 rpm. The results are tabulated in Table 6-1. A series inductor as shown in Figure 4-3 was not used.

TABLE 7-3

LOAD TEST

Rpm	Torque* in lbs	I_f Amp	I_L Amp	V_L Volts	Watts Output	Watts Input	Eff.** %
20,000	0	.0	0	0	0	0	-
20,000	.118	.025	2.65	10.15	26.9	27.9	96.4
20,000	.495	.050	5.25	20.22	106.2	117.1	90.7
20,000	.979	.075	7.45	29.65	220.9	231.7	95.3
20,000	1.675	.100	9.65	38.71	373.6	396.4	94.2
20,000	2.336	.125	11.25	45.96	517.1	552.8	93.5
20,000	3.056	.150	12.50	51.26	640.8	723.2	88.6
20,000	3.434	.175	13.20	54.90	724.7	812.6	89.2
20,000	3.811	.200	13.85	57.80	800.5	901.8	88.8
20,000	4.142	.225	14.35	60.00	861.0	980.1	87.8

* Tare torque due to windage and friction has been subtracted.

** Exclusive of field loss.

Since the alternator was running at one-third rated speed, it was necessary to use a load resistance of 4 ohms instead of the rated value of 240/13.21 = 18.2 ohms in order to get rated current. Since rated current gave rated IR and 1/3 rated IX drops, and the generated voltage is 1/3 of normal, the terminal voltage is a smaller fraction of the generated voltage at 20,000 rpm with a 4 ohm load than when running at 60,000 rpm with an 18 ohm load.

Using the data in Table 7-3 where the field current was 0.175 ampere, analysis shows that, at 60,000 rpm and rated load, the output power will be 2800 watts with a field current of 0.094 amperes. At the design field current of 0.139 amperes, the rated output will be exceeded.

At the 0.175 ampere field current point, the output power is 724.7 watts at 20,000 rpm. From Sections 6.3 and 6.4, the iron loss is 14.2 watts and the rotor pole face loss is 20 watts; the stator I^2R loss is 33.0 watts. The field loss is not included in this calculation in order to make a comparison with Table 7-3. The calculated efficiency is then:

$$\text{Eff} = \frac{724.7 \times 100}{724.7 + 14.2 + 20 + 33} = 91.5\%$$

The torquemeter value is 89.2 percent which is very good agreement with the calculated value especially in view of the fact that 3.4 lb in. torque at this point is approximately 13 percent of the rating of the torquemeter.

8.0 CONCLUSIONS

The design meets the specifications given in Section 2. While the testing to date has been performed only to 20,000 rpm, the test results, when extrapolated to 60,000 rpm by calculation, verify the design calculations.

The rotor used in the tests deviated considerably from the design dimensions, both in the body diameter and pole area. This requires more field current to obtain the required flux. The effect on the efficiency is very small.

With the rotor as designed, the performance at 60,000 rpm will be as follows: (See Section 6.0)

Power Output	=	3.17 kw
Output volts DC	=	240
Output IDC	=	13.21 amp
Field I_f	=	.139 amp
Field V_{dc}	=	104.43
Calculated Eff	=	95.8%

The probable error in loss calculations is certainly less than 50 percent which says that the actual efficiency at 60,000 rpm should be not less than 94 percent.

ATTACHMENT D

FINAL SUMMARY REPORT OF CNG HEAT PUMP

ROTOR BEARING DYNAMICS

MEMORANDUM

DATE: December 14, 1976

TO: R. Rose

FROM: S. B. Malanoski

SUBJECT: Final Summary Report of CNG Heat Pump Rotor Bearing Dynamics; MTI P.O. #0270-46033

References:

1. Memo: R. Wingrove to R. Rose, August 24, 1976, CNG Compressor Rotor Dynamic Analysis.

2. Memo: S. B. Malanoski to R. Rose, August 19, 1976, CNG Heat Pump Journal Bearing Specifications.

3. Memo: S. B. Malanoski to R. Rose, November 16, 1976, CNG Heat Pump Journal Bearing Performance Characteristics as Influenced by Bearing Clearance and Diameter.

4. Curwen, P. W., "Research and Development of High-Performance Axial-Flow Turbomachinery, Vol. 2 - Design of Gas Bearings" prepared for Lewis Research Center, NASA,Washington,D.C.,May 1968.

Introduction

Rotor-bearing dynamic studies made on the CNG Heat Pump Rotor included critical speed, unbalance response, and stability analyses and considered many variables as reflected by the mechanical design. Various materials for the compressor and turbine wheels and in addition to this, the effects of methods of attachment of these wheels to the main shaft, and the method of attachment of the alternator rotor to the main shaft were studied. These variables are reflected in the dynamics study as mass distributions and shaft flexibility.

As discussed in Refs. 1 and 2 three factors were of concern in this design: the shaft flexibility in the alternator region, the overhung masses of the compressor and the turbine, and the bearing effective stiffness. These factors are keys to good rotor-bearing dynamic performance. A shaft that is too flexible could give rise to large synchronous response at the maximum operating speed because of the nearness of the third critical speed (free-free mode). Shaft flexibility, and in addition increase in rotor mass and overhung weights, will decrease the first, rotor-bearing natural frequency which is well below operating speed. Typical experience has shown that operating at more than a factor of four above this natural frequency made the rotor-bearing system more prone to subsynchronous vibration problems. The right stiffness and damping combination achieved in the bearing design is very important here. These factors and results of Ref. 1 and 2 were discussed in a design review meeting of October 11, 1976. It was decided at that time to follow-up this review with further calculations in order to assure ourselves that the final rotor-bearing design was optimum and also to raise the confidence level in the design with reference to stability by comparing it with a rotor bearing system of similar design that had successful operating experience.

This memorandum is intended to serve as a summary report of the final CNG rotor-bearing design. The following subjects are discussed:

1) Effects of Bearing Clearance (Preload) and Journal Diameter on Stability
2) Comparison of Theory with Experience of Ref. 4,
and 3) Rotor-Bearing Performance of the Final Design;
    a) Final rotor model
    b) Final bearing model
    c) Undamped lateral critical speeds
    d) Unbalance response analysis
    e) Damped, later critical speed stability analysis

Summary of Results

1. The final rotor having a titanium turbine wheel and either a steel or aluminum compressor wheel will have satisfactory dynamic performance -- good synchronous and subsynchronous response -- provided full shaft stiffness is obtained in the alternator region of the shaft by proper manufacturing procedures. Otherwise large synchronous response will result at 50,000 rpm due to the nearness of the third critical speed.

   A static, shaft ringing test can be used to check the natural frequency.

2. The compressor-end bearing should have a nominal diameter of 1.10 inches. The pads are 1.0 inch in axial length. The turbine-end bearing should have a nominal diameter of 1.35 inches with an axial pad length, also 1.35 inches. The specifications as published in Ref. 2 are essentially unchanged. Thus, the pad radial thicknesses, and the bearing machined and set-up (assembly)clearances are as indicated in this reference.

3. As indicated in Ref. 3, with the results included herein, no significant improvement in stability can be achieved with larger bearing diameters of 1.5 inch (turbine-end) and 1.38 inch (compressor-end).

4. The CNG rotor shows very little sensitivity to preload (bearing assembled clearance) in the range of 0.5 to 0.7. This is good because it allows for larger tolerance variation.

5. Analysis of the rotor-bearing system of Ref. 4 shows very good agreement with experience in that smaller assembled clearances (larger preload) predicted better stability. This rotor-bearing system was more sensitive to clearance change than the present CNG design.

6. The present CNG design is less sensitive to clearance change compared with the rotor-bearing system of Ref. 4 because the CNG bearing pad design is much lighter in weight. Thus the CNG design also provides smaller cross-coupling forces. When these forces are large they contribute to instability.

7. The rotor of Ref. 4 did run stably when the proper bearing assembled clearance was established. The theoretical log decrement value of this stable rotor-bearing system is 0.15. It operated over five times the first damped critical.

8. The present CNG rotor-bearing system has a log decrement of approximately 0.19 and operates at approximately 3.4 times the first damped critical.

9. A high degree of confidence can be drawn from the above results (7, 8) that the CNG rotor-bearing will be stable even though the log decrement value is less than the normal allowable value of 0.3.

Presentation of Results

The dynamic performance of the final heat pump rotor-bearing design is illustrated in the following figures and tables:

Fig. 1 - CNG Heat Pump Rotor Undamped Lateral Critical Speed Map-Typical Bearing Stiffness Indicated.

Fig. 2 - CNG Heat Pump Rotor Undamped Lateral Critical Speed Mode Shapes for First Three Levels (Typical Bearing Stiffness).

Fig. 3 - CNG Heat Pump Rotor Typical Unbalance Response (Major Axis-Half Amplitudes).

Fig. 4 - CNG Heat Pump Rotor Typical Dynamic Bearing Forces Due to Unbalance.

Table I - CNG Heat Pump Rotor Mathematical Model and Engineering Data.

Table II - CNG Heat Pump Bearing Specifications.

Table III - CNG Heat Pump Rotor-Bearing Stability Performance as a Function of Bearing Diameter and Clearance.

Table IV - Comparison of Theoretical Stability Characteristics as a Function of Bearing Clearance per Ref. 4.

The engineering data presented in Table I is consistent with drawing 343D052, with the aluminum compressor wheel and the titanium turbine wheel attached.

The data of Table II is reflected on drawings 343D016 and 343D017.

Fig. 1 illustrates that the rotor will be operating above the first two lateral critical speeds and below the third critical speed. The first two critical speeds are commonly called rigid-rotor, bearing criticals. They are a function of the rotor mass and the bearing properties. The rotor mode shapes for these criticals are shown in Fig. 2. Note that indeed the rotor does appear to be rigid and that the nodes are not at the bearings -- thus the bearing damping will be effective when traversing these criticals. The third critical speed is commonly called the "free-free" critical, or rotor natural frequency. At high speeds a rotor will possess gyroscopic stiffening and shear deformation effects. These are taken into account in the analysis and included in the results.

Thus, the non-rotating rotor natural frequency will be less than 83,000 cpm if this is to be determined on a bench test by "ringing".

As mentioned previously, various rotor modifications were considered in the design stage of this program. The essential conclusions were that:

1) Unless manufacturing processes can provide full shaft stiffness in the alternator region the third critical will drop to near 50,000 cpm from 80,000 cpm and result in large rotor dynamic response and bearing forces.
2) The critical speed levels in cpm vary as follows with compressor wheel material:

Material	N_1	N_2	N_3
Steel	14,500	21,000	73,000
Titanium	14,600	23,000	79,000
Aluminum	14,800	25,000	83,400

No effect on the first, or major effect on the second is realized. The third can be reduced considerably with a steel wheel.

Fig. 3 and 4 illustrate typical unbalance response results. For a given unbalance response, peaks in terms of amplitudes and bearing forces occur at approximately 17,000 cpm, 26,000 cpm and above 60,000 cpm. The peak values are small. However, it is still recommended that a per-plane unbalance of 0.0004 oz-in per plane be met.

Additional calculations were made on the CNG rotor to determine the stability margin of the rotor-bearing system with respect to subsynchronous lateral vibrations. Rotor-bearing systems of this variety are more prone to this instability when the operating speed is well above the first natural frequency (critical speed). Target design values have been a ratio of operating speed to damped critical speed of less than four, and a system log decrement value greater than 0.3.

In this present design the speed ratio criterion is met. However, the log decrement is less than 0.3.

Two studies were made to try to establish an optimum design and gain confidence in this design by reflecting upon past practical experience. The results of these studies are shown in Tables III and IV.

Table III results indicate that the present design with a preload (clearance) value of m = 0.6 is essentially better than a tighter clearance and a larger diameter bearing. The sensitivity to preload in the range 0.5 to 0.7 is small. This is good from a tolerance effect. However, it does not provide a way to go if vibration problems exist.

Confidence in this present design can be gained by reviewing the results of Table IV. This rotor-bearing system was built and tested as discussed in Ref. 4. The pertinent experimental results were that with a preload value of m = 0.56 in bearing No. 2 the rotor could not get to a speed higher than ≈30,000 rpm. Note that the log decrement for Nc_1 is much less than zero at 50,000 rpm operating speed (case 3).

With a value of m = 0.788 (case 1) the rotor was stable to 60,000 rpm. Note that the log decrement for this case 1 is larger than zero, $\delta \approx 0.15$.

In making this theoretical analysis on this experimentally, tested rotor it was found that because of the larger pad masses the natural frequencies of the pads could be in the operating frequency range (at larger clearances) thus changing the dynamic characteristics. This is mentioned on Table IV, remarks. No similar problem to this exists in the present CNG design.

Thus, the CNG rotor-bearing system should be stable operating at 60,000 rpm with a system log decrement of $\delta = 0.19$, and a damped, first natural frequency of 17,700 rpm.

cc - S. Malanoski
P. Lewis
E. Arwas
R. Rose (2)
File

K+E LOGARITHMIC 3 CYCLES
KEUFFEL & ESSER CO. MADE IN U.S.A.
46 7320

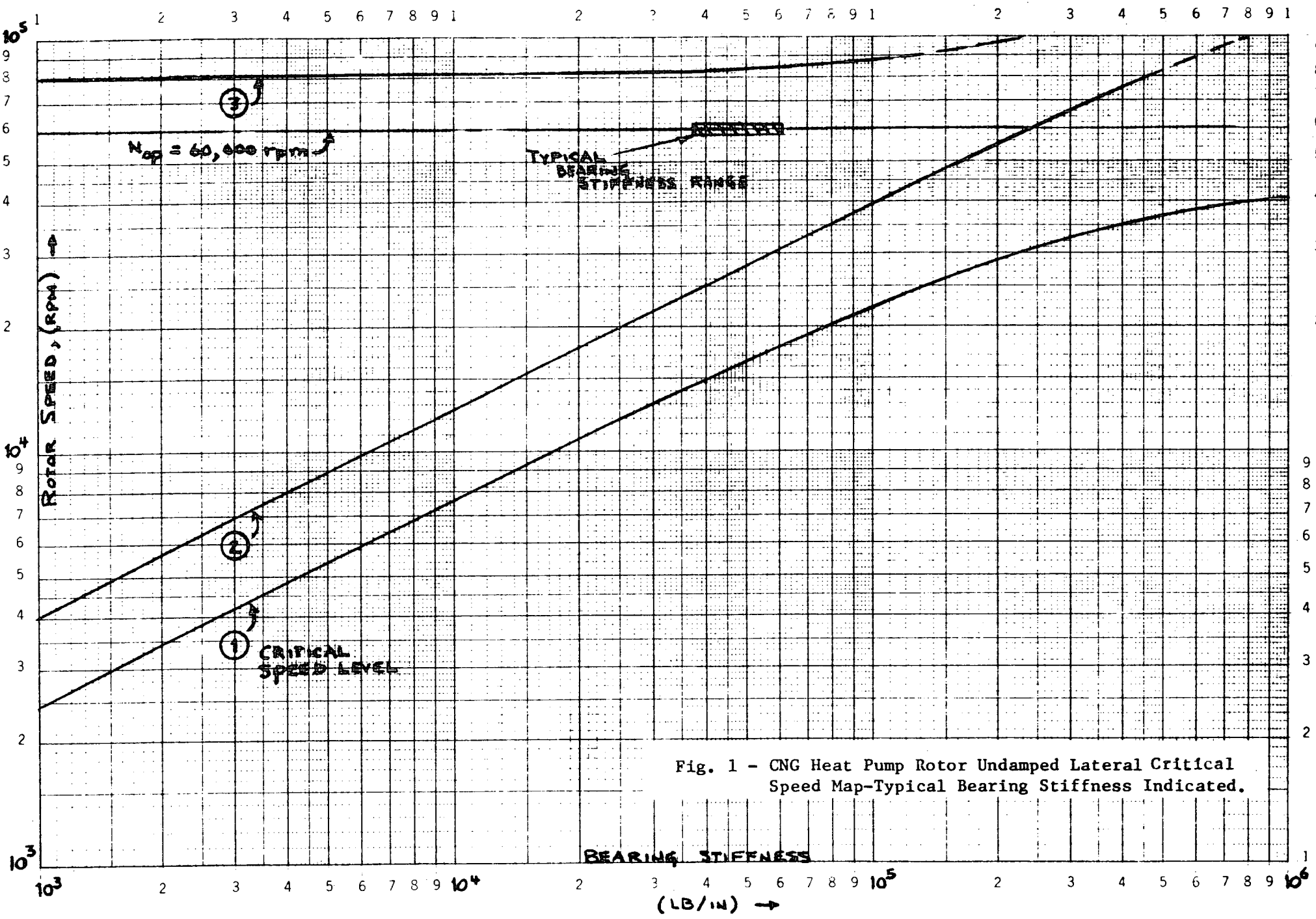

Fig. 1 - CNG Heat Pump Rotor Undamped Lateral Critical Speed Map-Typical Bearing Stiffness Indicated.

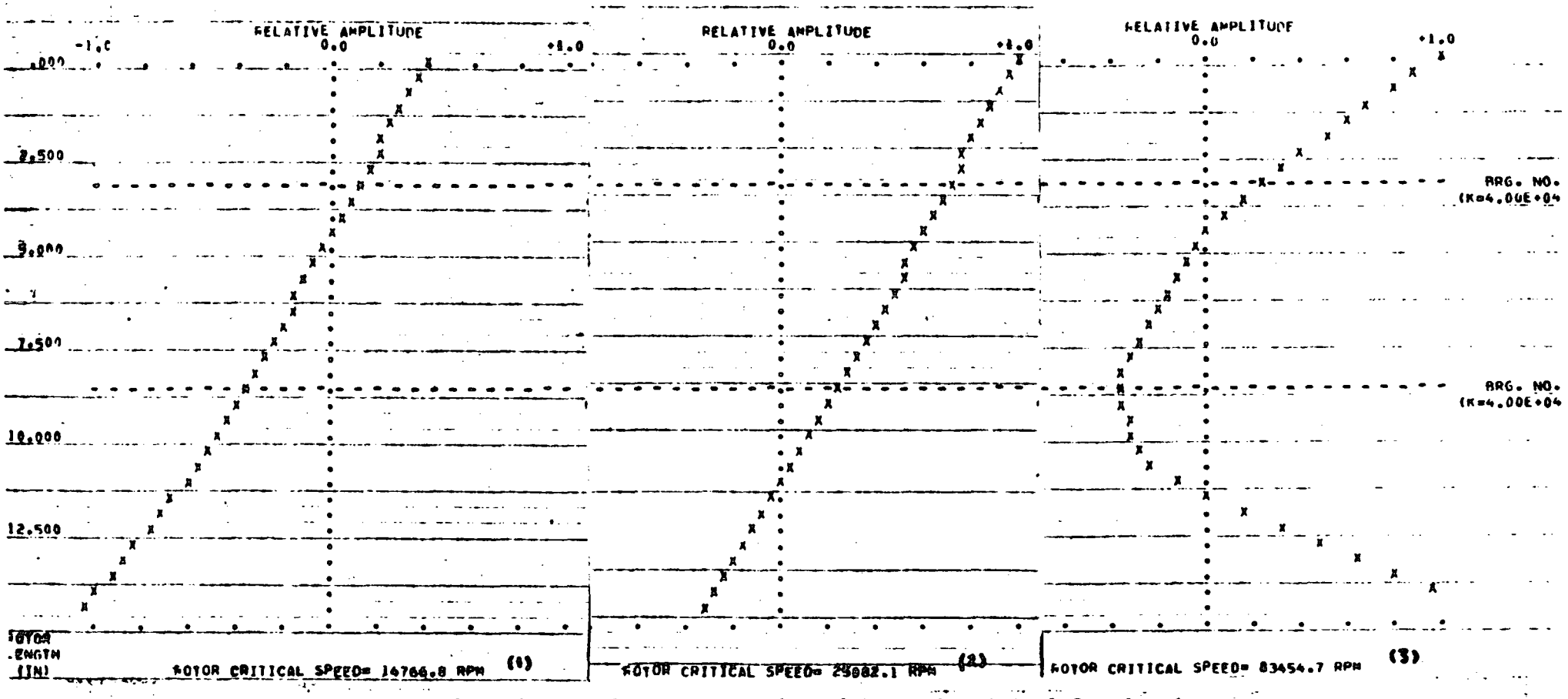

Fig. 2 - CNG Heat Pump Rotor Undamped Lateral Critical Speed Mode Shapes for First Three Levels (Typical Bearing Stiffness)

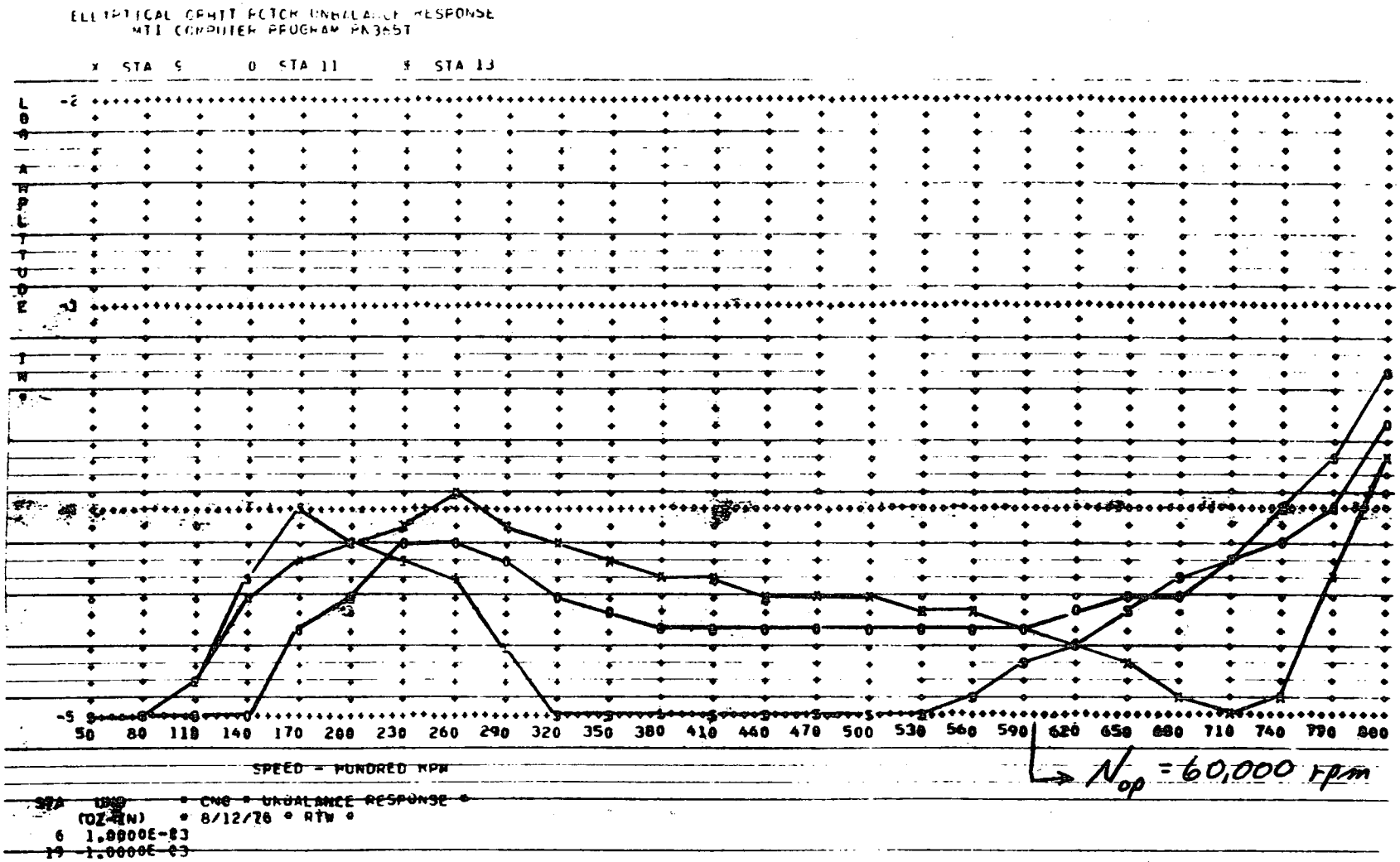

Fig. 3 - CNG Heat Pump Rotor Typical Unbalance Response (Major Axis-Half Amplitudes).

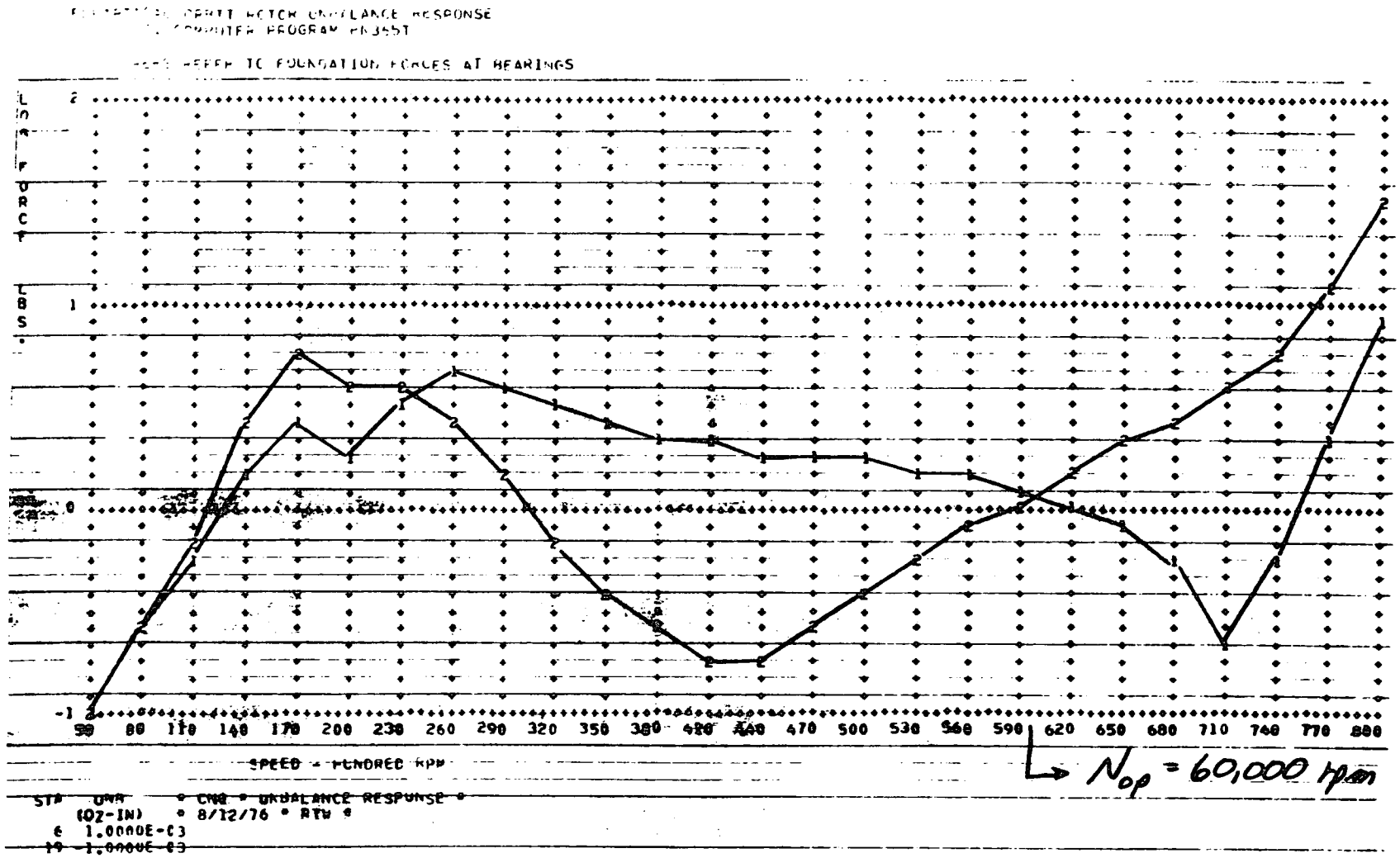

Fig. 4 - CNG Heat Pump Rotor Typical Dynamic Bearing Forces Due to Unbalance.

MAT NO.	YOUNGS MOD. (LB/IN**2)	DENSITY (LB/IN**3)	SHEAR MOD. (LB/IN**2)
1	2.8000E+07	2.830E-01	8.0770E+06

ROTOR DATA

STAT NO.	MASS (LBS)	IP (LB-IN**2)	IT (LB-IN**2)	LENGTH (IN)	STIFF. DIA.	MASS DIA.	INNER DIA.
1	-.0	-.0	-.0	.333	.167	.167	.000
2	-.0	-.0	-.0	.100	.250	.250	.000
3	-.0	-.0	-.0	.167	.333	.333	.000
4	-.0	-.0	-.0	.117	.333	.333	.233
5	-.0	-.0	-.0	1.125	.783	.233	.233
6	3.890E-01	2.5000E-01	1.6000E-01	.183	.783	.300	.300
7	3.214E-02	2.8500E-05	2.7780E-04	.667	1.100	1.100	.540
8	-.0	-.0	-.0	.592	1.100	1.100	.330
9	-.0	-.0	-.0	1.300	1.100	1.100	.330
10	-.0	-.0	-.0	1.570	1.910	1.910	.000
11	-.0	-.0	-.0	1.565	1.910	1.910	.000
12	-.0	-.0	-.0	1.235	1.330	1.330	.000
13	-.0	-.0	-.0	1.110	1.330	1.330	.000
14	-.0	-.0	-.0	.200	1.150	2.440	.000
15	-.0	-.0	-.0	.300	1.100	1.330	.000
16	-.0	-.0	-.0	.158	.800	.967	.000
17	-.0	-.0	-.0	.533	.800	.967	.367
18	-.0	-.0	-.0	.217	.800	1.330	.367
19	-.0	-.0	-.0	.100	.800	1.330	.567
20	-.0	-.0	-.0	.733	.800	.967	.567
21	3.214E-02	2.8500E-05	2.7780E-04	.117	.800	1.330	.567
22	-.0	-.0	-.0	.150	.800	1.330	.467
23	-.0	-.0	-.0	.167	1.060	.467	.467
24	-.0	-.0	-.0	.150	1.060	.300	.300
25	7.800E-01	1.3850E+00	6.9300E-01	.300	1.060	.300	.300
26	-.0	-.0	-.0	.250	.967	.967	.300
27	-.0	-.0	-.0	.225	.550	.550	.300
28	-.0	-.0	-.0	.188	.550	.550	.000
29	-.0	-.0	-.0	.100	.300	.300	.000
30	-.0	-.0	-.0	.333	.233	.233	.000
31	-.0	-.0	-.0	.000	.000	.000	.000

BEARING STATIONS
9 13

ROTOR WT. (LBS)	ROTOR IP (LB-IN**2)	ROTOR IT (LB-IN**2)	BRG.1 -CG (IN)
6.1924E+00	3.412282E+00	7.146251E+01	4.303

LOAD,BRG.1 (LBS)	LOAD,BRG.2 (LBS)	DISTANCE BRG.1- BRG.2 (IN)	ROTOR LENGTH (IN)
1.492E+00	4.700E+00	5.6700	14.2850

Table I - CNG Heat Pump Rotor Mathematical Model and Engineering Data

Dimension	Compressor-End	Turbine-End
Pad Active Length (in)	1.0	1.35
Journal Nominal Diameter (in)	1.10	1.35
Pad Nominal Thickness (in)	0.094	0.094
Pivot Diameter (in)	0.2505	0.2505
Cylindrical Seat Diameter (in)	0.2555	0.2555
Radius to Pivot Point (in)	0.675	0.800
At Set-Up (70°F):		
a) Journal Diameter (in)	1.1001	1.3501
b) Pad Radius of Curvature (in)	0.5509	0.6761
c) C_P/R (mils/in)	1.55	1.56
d) Total Nominal Set-Up Clearance, $2C_B$ (in)	0.0008	0.0008

Table II - CNG Heat Pump Bearing Specifications

CNG - 60,000 rpm, Bearing & Rotor Performance Characteristics

Case No.	Bear. No.	D in.	C_p mils	C_p/R mils/in	C_B mils	m	K_{xx}	K_{xy}	K_{yx}	K_{yy}	B_{xx}	B_{xy}	B_{yx}	B_{yy}	N_{c_1}/δ_1 cpm/-	N_{c_2}/δ_2 cpm/-	N_{c_3}/δ_3 cpm/-
							10^6 lb/in					lb·sec/in					
1	1	1.1	0.83	1.5	0.415	0.5	2.92	0.05	-0.02	3.13	1.44	0.26	-0.26	1.96	15700	23300	77500
	2	1.35	1.01	1.5	0.506	0.5	3.76	0.10	-0.04	4.53	1.81	0.38	-0.39	2.66	0.21	0.39	0.080
2	1	1.1	0.83	1.5	0.332	0.6	3.78	0.04	-0.02	4.30	1.43	0.17	-0.20	2.07	17300	26500	78090
	2	1.35	1.01	1.5	0.405	0.6	4.80	0.08	-0.04	6.06	1.78	0.25	-0.31	2.70	0.19	0.33	0.083
3	1	1.1	0.83	1.5	0.249	0.7	5.11	0.04	-0.02	6.28	1.38	0.10	-0.15	2.12	20300	31540	79200
	2	1.35	1.01	1.5	0.304	0.7	6.43	0.07	-0.04	8.56	1.70	0.15	-0.23	2.67	0.15	0.33	0.081
4	1	1.38	0.83	1.2	0.332	0.6	4.63	0.07	-0.05	5.61	1.34	0.15	-0.21	2.04	15600	27500	75500
	2	1.50	1.01	1.35	0.405	0.6	5.77	0.10	-0.07	7.08	1.65	0.21	-0.31	2.56	0.15	0.31	0.087

Case No.	Remarks
1	Lighter preload
2	As presently designed
3	Heavier preload
4	Larger diameter - preload nominal

Table III - CNG Heat Pump Rotor-Bearing Stability Performance as a Function of Bearing Diameter and Clearance

CNG (P&W Theoretical-Experimental Data Comparison)

Operating Speed = 30,000 rpm
$C_B/R = 8 \times 10^{-3}$ (B-2)
$C_B/R = 1.8 \times 10^{-3}$ (B-1)

Case No.	Bear. No.	C_B mils	m	K_{xx}	K_{xy}	K_{yx}	K_{yy}	B_{xx}	B_{xy}	B_{yx}	B_{yy}	Nc_1/δ_1 cpm/–	Nc_2/δ_2 cpm/–	Nc_3/δ_3 cpm/–
				10^6 lb/in				lb.sec/in						
1	1	1.35	0.5	2.09	0.132	−0.132	2.09	1.38	0.51	−0.51	1.38	9880 / 0.199	14245 / 0.071	101390 / 0.006
	2	0.68	0.788	2.22	0.016	−0.016	2.22	1.60	0.47	−0.47	1.60			
2	1	1.35	0.5	2.09	0.132	−0.132	2.09	1.38	0.51	−0.51	1.38	9215 / 0.162	14240 / 0.072	101370 / 0.007
	2	1.1	0.656	1.75	0.227	−0.227	1.75	3.65	1.63	−1.63	3.65			
3	1	1.35	0.5	2.09	0.132	−0.132	2.09	1.38	0.51	−0.51	1.38	11040 / −.359	14260 / 0.036	101360 / 0.006
	2	1.4	0.562	2.90	1.19	−1.19	2.90	3.04	0.75	−0.75	3.04			

Case No	Remarks
1	Pitch & Roll Nat. Freq. of pads above operating frequency
2	Pitch Nat. Freq. of upper pads for Bear. #2 below operating frequency
3	Pitch & Roll Nat. Freq. of upper pads for Bear. #2 below operating frequency Pitch Nat. Freq. of lower pads for Bear. #2 below operating frequency

Table IV - Comparison of Theoretical Stability Characteristics as a Function of Bearing Clearance per Ref. 4

ATTACHMENT E

THERMAL ANALYSIS OF CNG TURBOCOMPRESSOR

MTI ENGINEERING ANALYSIS REPORT

NO. 76-17

THERMAL ANALYSIS OF CNG TURBO-COMPRESSOR

By:

A. Artiles

Prepared For:

Consolidated Natural Gas

Prepared Under:

0252-46033

October 1976

MECHANICAL TECHNOLOGY INCORPORATED
968 Albany-Shaker Road
Latham, New York 12110

TABLE OF CONTENTS

		Page
I.	INTRODUCTION	1
II.	SUMMARY OF RESULTS	2
III.	THERMAL MODEL OF ROTOR	4
IV.	ALTERNATOR THERMAL ANALYSIS	20
	A. Lamination Model	20
	B. End-Turn Cooling	25
	C. Field Coil Thermal Model	28
V.	STEAM MANIFOLD THERMAL MODEL	29

LIST OF FIGURES

	Page
Figure 1	3
Figure 2(a)	5
Figure 2(b)	6
Figure 2(c)	7
Figure 3	8
Figure 4	9
Figure 5	13
Figure 6	21
Figure 7	22
Figure 8	24
Figure 9	26
Figure 10	27
Figure 11	30
Figure 12	32
Figure 13	33
Figure 14	34

LIST OF TABLES

	Page
TABLE 1	10
TABLE 2	11
TABLE 3	14
TABLE 4(a)	15
TABLE 4(b)	16
TABLE 5(a)	17
TABLE 5(b)	18
TABLE 6	23
TABLE 7	31
TABLE 8	35
TABLE 9(a)	36
TABLE 9(b)	37

I. INTRODUCTION

Mechanical Technology Incorporated is designing a turbo-compressor for commercial heating/cooling applications, for Consolidated Natural Gas.

This report documents the thermal analysis carried out in order to calculate the temperature distribution of this machine at design operating conditions.

Section II of this report summarizes the results. The thermal analysis has been divided into three parts: the rotor, the alternator, and the steam manifold. The thermal model used for each is discussed in Sections III, IV and V, respectively.

II. SUMMARY OF RESULTS

The most significant temperatures are tabulated as follows:

	Temperature (°F)
Freon Gas	
Inlet	118
Rotor-Stator gap, T_{25}	186
Exit, T_{30}	223
Rotor Model	
Seal Hot-Spot	449 to 453
Thrust Bearing	358 to 370
Alternator Centerline, T_{25}	222
Compressor-end journal bearing, T_{32}	218
Turbine-end journal bearing, T_{31}	239
Alternator	
Laminations Hot-Spot at ID	185 to 201
Windings Hot-Spot at Axial Centerline	260 to 350
Field Coil Hot-Spot at ID	350 for $\kappa_e = 0.31$

Figure 1 summarizes the distribution of heat flows between the machine components analyzed.

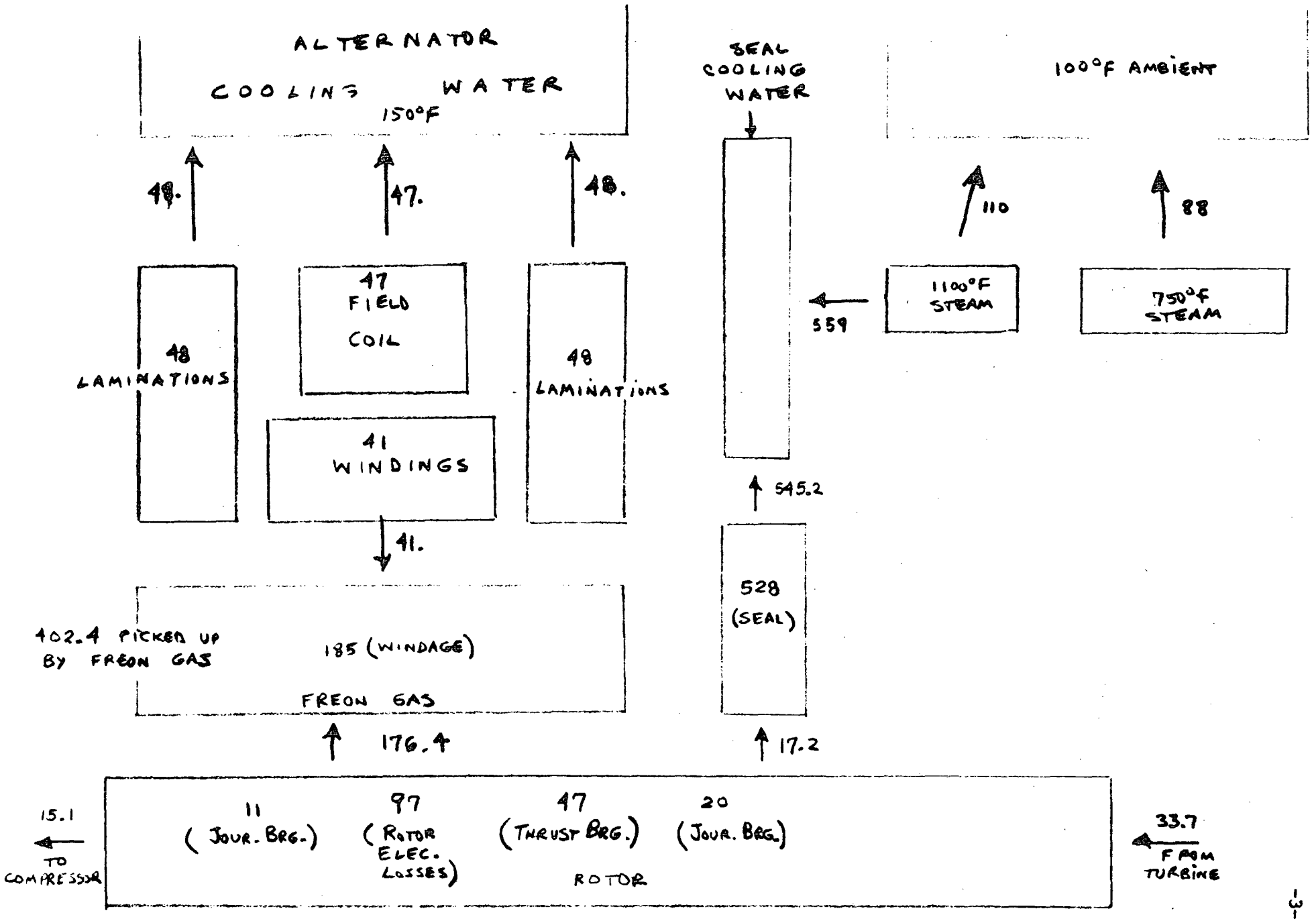

FIGURE 1 HEAT FLOW SCHEMATIC (WATTS)

III. THERMAL MODEL OF ROTOR AND FLUID STREAMS

Figure 2(a) is a sketch of the rotor between the compressor and turbine attachments. The thermal model is a discretized representation of the rotor by nodal temperature stations which are interconnected by thermal resistances, as shown in the network schematic on Figure 2(c). Temperatures T_1 through T_{12} are part of the axial temperature distribution. They are connected in different places to the Freon gas stream flowing axially over the rotor (T_{22} through T_{30}), and to the two journal bearings (T_{31} and T_{32}) which are in turn connected to the stream. The rotor attachment to the compressor has been assumed to be at T_1 = 130°F. The electrical losses in the rotor (q_4) are applied at T_7. The inlet of the Freon gas (at 118°F) is divided into two halves: One half flows over the turbine-end bearing pads (T_{21} and exit temperature T_{38}). The other half flows over the turbine-side end-turns of the alternator, picking up half of the heat generated in the windings (q_{10}). These two halves merge into temperature T_{22} from where it flows axially through the rotor-stator gap (T_{23} through T_{28}), over the compressor-end bearing pads (T_{29}) and exits into the compressor at T_{30}. The heat generation rates q_6 and q_3 that are added to the stream each include 1/2 of the gap windage power loss; in addition, q_3 includes the other half of the heat generated in the windings, which it picks up when flowing over the compressor-side end-turns.

Figure 2(b) shows the details of the turbine end of the rotor. The thrust bearing heat is applied, 1/2 at T_{11} (q_1) and 1/2 at T_{12} (q_7). The rest of the shaft is represented by T_{17} and T_{36}. The tie bolt is represented by T_{18} and T_{20}. The temperature of the wheel at a radius of 0.5 inches has been fixed at 690°F. The two sleeves used for positioning the seal runner are represented by T_{13} and T_{14}, and by T_{16} and T_{19}, respectively. The detail of the runner ID, as well as other dimensions used in modelling this section, are given in Figure 3. The seal runner is represented by T_{15} and T_{33}, at which point the heat generated by the seal faces (q_8) is applied. The outside diameter of the runner is exposed, through a heat transfer coefficient of 7000 BTU/(Hr.Ft^2°F), to the cooling water stream. This water enters at 130°F, has a mean temperature of T_{34}, and exits at T_{35}. Figure 4 shows the heat transfer coefficients which were estimated from the contact pressure at different contact surfaces.

Table 1 contains the material properties that were used in the analysis. Table 2 contains all of the heat generation rates, as were distributed in the model.

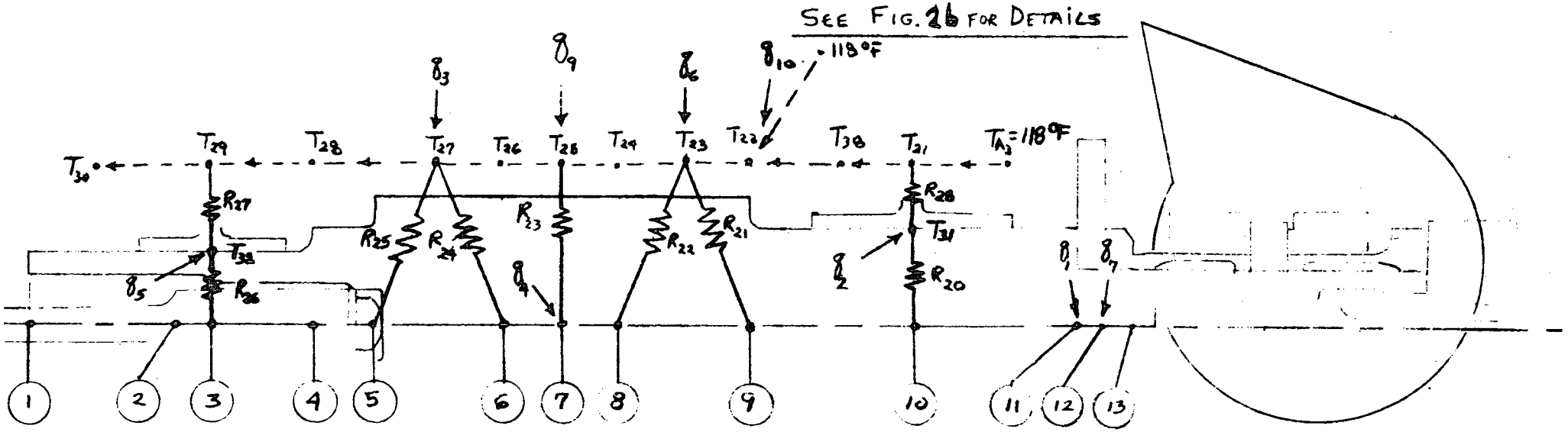

NOTES: 1. TEMPERATURES $T_1, T_2, \ldots, T_{12}$ ARE CONNECTED CONSECUTIVELY BY THERMAL RESISTANCES $R_1, R_2, \ldots, R_{11}$.

2. SEE FIG. 2(b) FOR DETAILS OF TURBINE-WHEEL END.

FIGURE 2(a) SCHEMATIC OF THERMAL MODEL OF ROTOR

FIGURE 2(b)

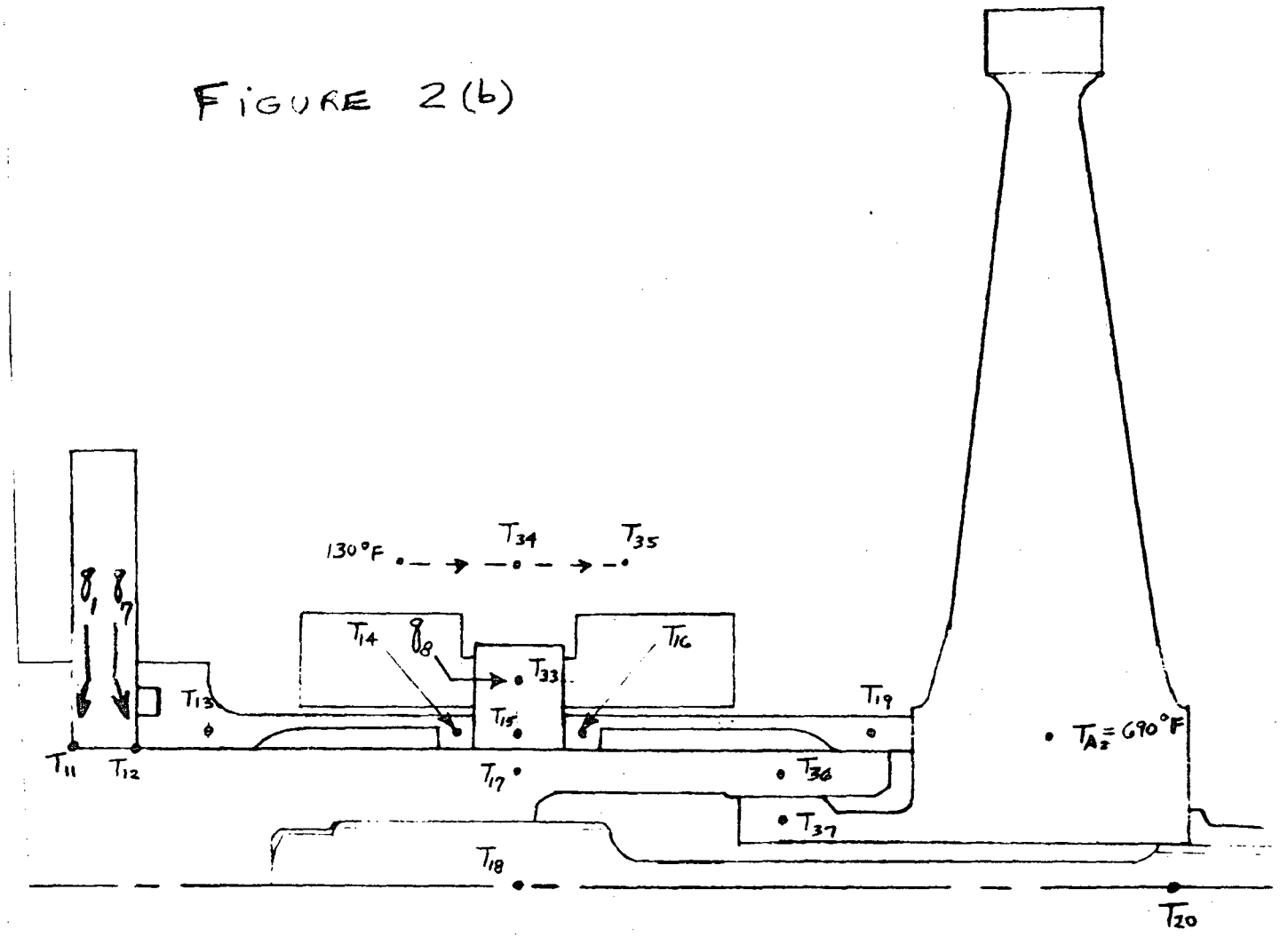
130°F
T_{34}
T_{35}
q_1
q_7
T_{14}
q_8
T_{33}
T_{16}
T_{13}
T_{15}
T_{19}
$T_{A2} = 690°F$
T_{11}
T_{12}
T_{17}
T_{36}
T_{37}
T_{18}
T_{20}

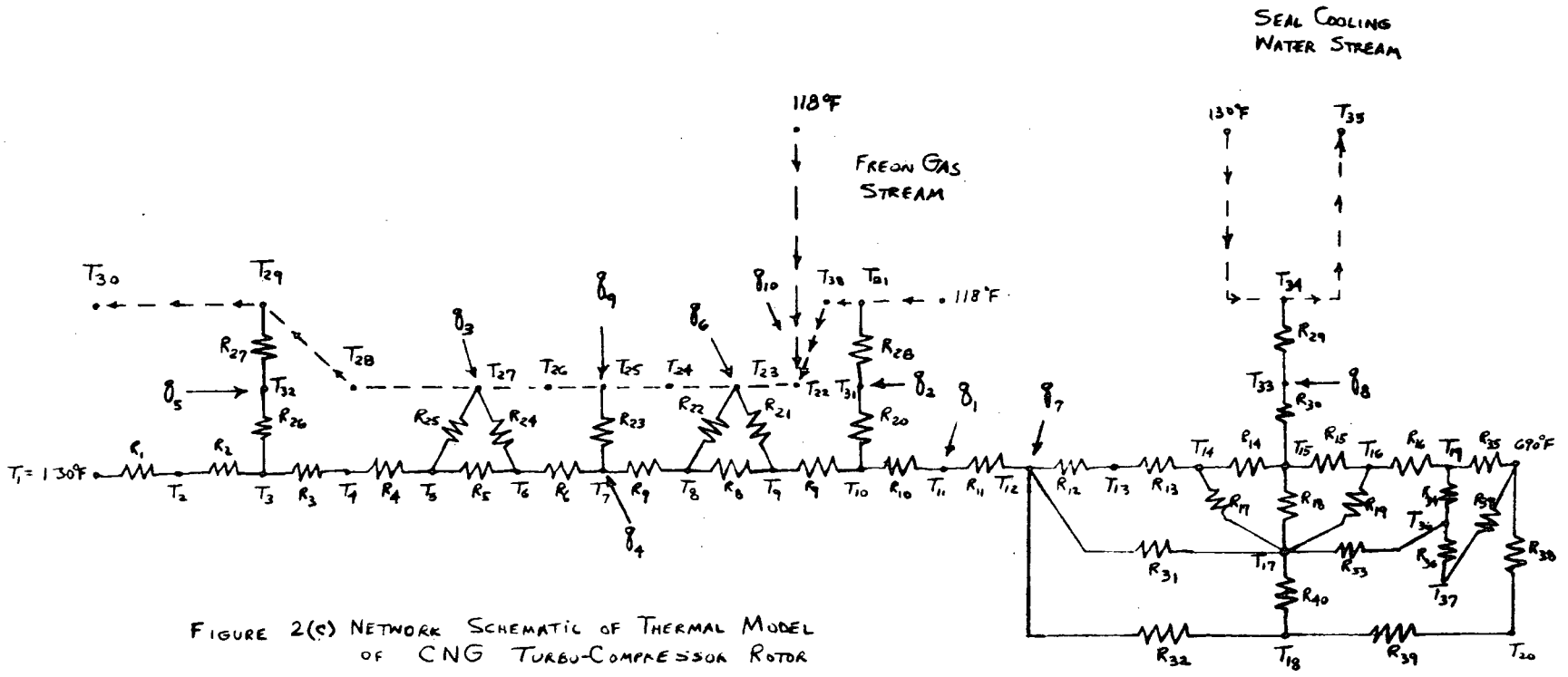

FIGURE 2(c) NETWORK SCHEMATIC OF THERMAL MODEL OF CNG TURBO-COMPRESSOR ROTOR

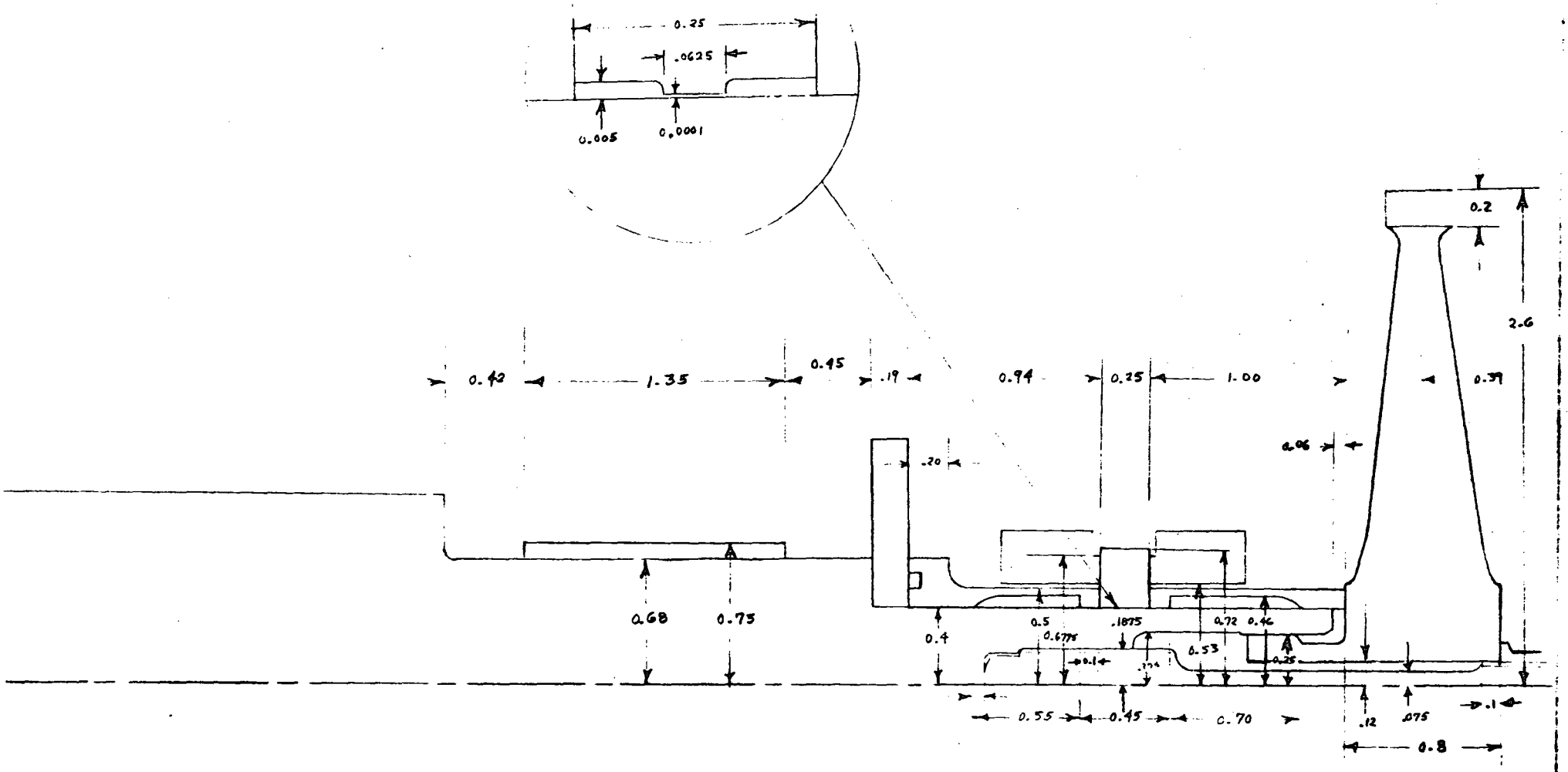

FIGURE 3. DIMENSIONS USED IN MODEL
(ALL DIMENSIONS IN INCHES) SCALE 2:1

FIGURE 4. HEAT TRANSFER COEFFICIENTS AT CONTACT SURFACES

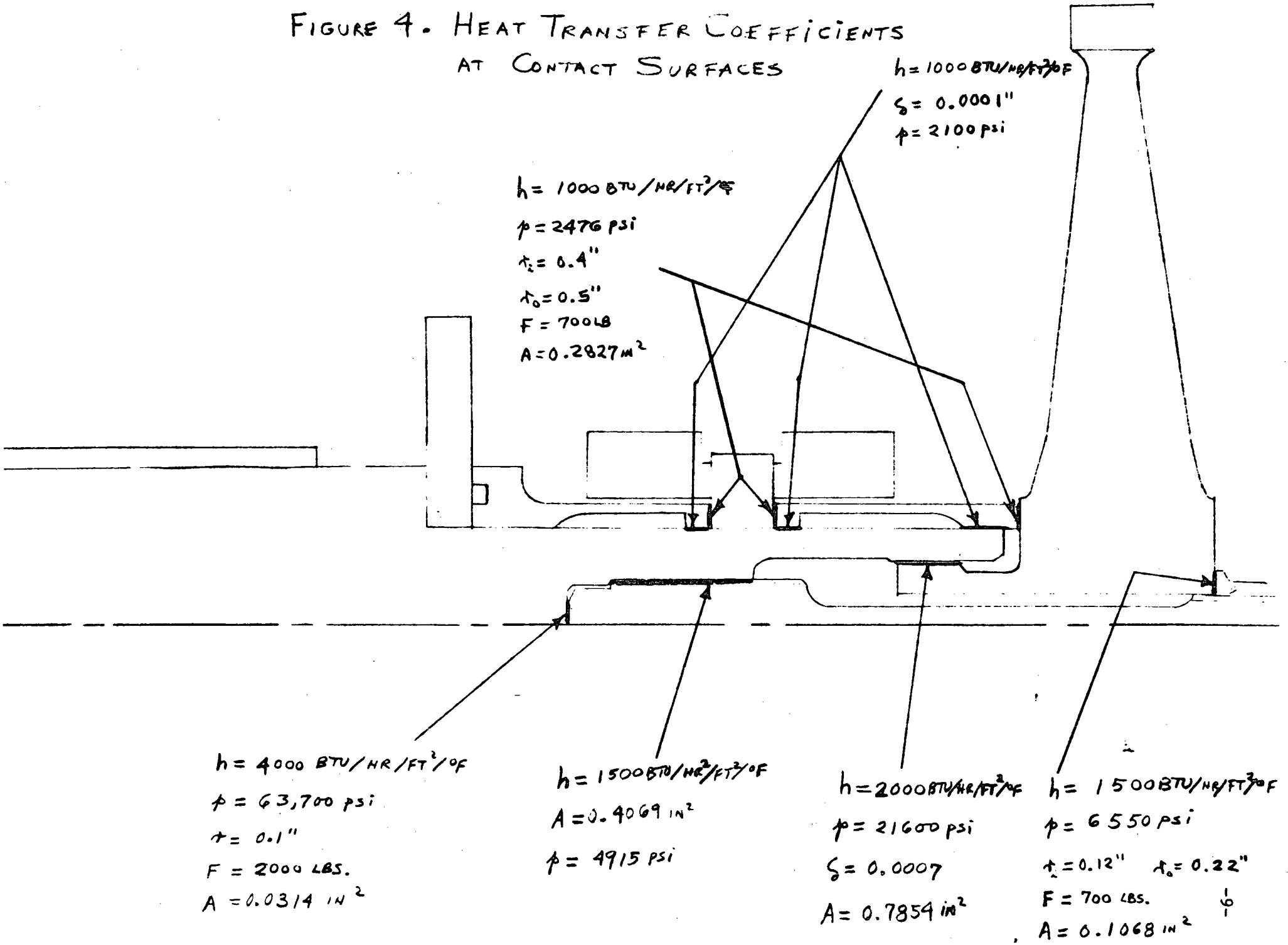

TABLE 1

MATERIAL PROPERTIES

COMPONENT	MATERIAL	κ (BTU/hr/ft/°F)	α (in/in/°F)	C_p BTU/(lb°F)	ρ (lb/in^3)	μ (lb-sec/in^2)
All rotor parts (unless otherwise specified)	4130 Steel	22.0	6.6×10^{-6}	-	-	-
Seal Runner	T_iC_a GRK 162B	12.0	3.7×10^{-6}	-	-	-
Shaft Sleeves	Rene 41	6.3	6.9×10^{-6}	-	-	-
Turbine Wheel	Titanium	8.38	4.7×10^{-6}	-	-	-
Alternator Stator Laminations	3.35% S_i Steel	14.5	-	-	-	-
Refrigerant Gas @ 118°F	Freon R11	0.0045	-	0.1323	2.32×10^{-4}	1.56×10^{-9}
Seal Coolant	Water	0.345	-	0.9988	0.036146	1.46×10^{-7}
	Steam	0.0278	-	-		

TABLE 2

HEAT GENERATION RATES

		(Watts)	(BTU/Sec)
q_1	1/2 of Thrust Bearing	23.5	0.02226
q_2	Turbine-End Bearing	20.0	0.01894
q_3	1/2 of Rotor-Stator Gap Windage (92.5) plus 1/2 of Copper Wire Losses (20.5)	113.0	0.107021
q_4	Rotor Electrical Losses (Poles)	97.0	0.091867
q_5	Compressor-End Bearing	11.0	0.01042
q_6	1/2 of Rotor-Stator Gap Windage	92.5	0.08761
q_7	1/2 of Thrust Bearing	23.5	0.02226
q_8	Seal Losses	528.0	0.50006
q_9	20% of Iron Losses Convected in Rotor-Stator Gap Stream (19.2) For Case 2 (q_9 = 0 for Case 1)	19.2	0.018184
q_{10}	1/2 of Copper Wire Losses	20.5	0.019415
	80% of Iron Losses	76.8	0.072736
	Field Coil Losses	47.0	0.044513
	TOTAL	1072.0	1.015277

Figure 5 tabulates the heat transfer coefficients from the rotor model into the gas, due to rotation. The total Freon flowrate is 100 lb/hr., while that of the water is 100 lb/hr.(=0.0278 lb/sec. = 0.20 GPM). Table 3 contains the resulting thermal resistance representing the network.

Two cases have been studied to see the sensitivity of the results to the exchange of heat between the lamination ID and the gas. The first case assumes that no exchange of heat occurs (i.e., $q_9 = 0$); these results are given in Table 4. The second case assumes that 20% of the lamination iron losses ($q_9 = 19.2$ watts) are convected into the rotor-stator gap gas stream; these results are given in Table 5. As will be shown later from the alternator stator model in Section IV, the first case is very close to the actual design situation, since the resulting temperature at the lamination ID (185°F) is very close to its ambient gas temperature (T_{25}), and very little heat (less than 1 watt) is exchanged due to this temperature difference.

The other results for Case 1 show the following.

Seal Runner

The seal runner shows operating temperature of T_{33} = 389°F at r = 0.60 inches and T_{15} = 400°F at r = 0.45 inches. The axial temperature difference across the seal is only 3.2°F, corresponding to a gradient of 13°F/in. The seal OD convects into the water the heat generated by the seal plus 17 watts that are picked up from the rotor. The model shows that the water temperature rises from 130°F to a mean value of T_{34} = 139°F and exits at T_{35} = 149°F.

Axial Temperature Gradient

The maximum axial gradient of 188°F/in. occurs in the turbine-side sleeve (from T_{16} to T_{19}). The sleeve on the other side of the seal runner has a gradient of 72°F/in. The shaft gradient (between T_{17} and T_{36}) is 170°F/in., and the gradient in the turbine bolt (between T_{18} and T_{20}) is 128°F/in.

Miscellaneous Temperatures and Heat Flows

The resulting bearing temperatures at the compressor and turbine ends are T_{32} = 217°F and T_{31} = 233°F, respectively. The rotor temperature at the alternator centerline has a local hot-spot of T_7 = 220°F. The freon gas

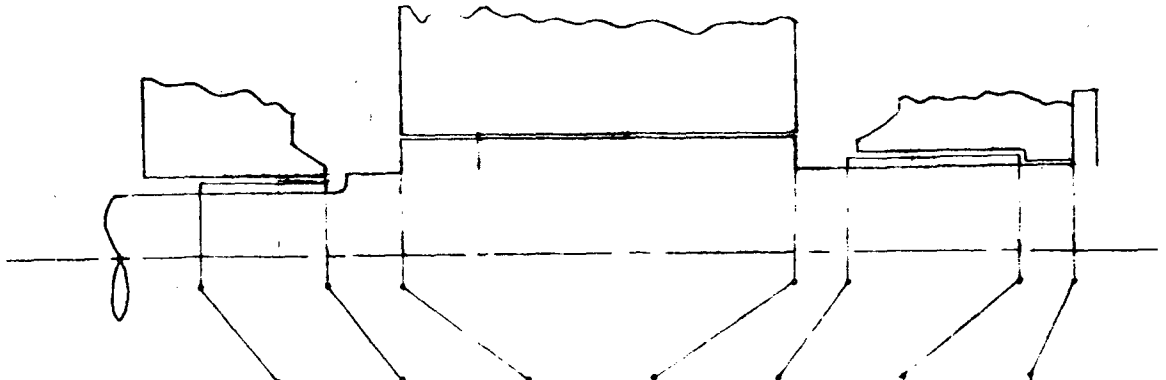

SECT.		1	2	3	4	5	6
r_i	(IN)	0.60	0.65	0.958	0.68	0.78	0.68
r_o	(IN)	0.65		0.998		0.83	0.73
c	(IN)	0.05		0.040		0.05	0.05
Q	(LB/SEC)	0.02778				0.01389	
A	(IN^2)	0.1964				0.2529	
D_h	(IN)	0.05				0.05	
$\bar{V}$	(IN/SEC)	689.6				236.7	
Re		11,745	1.743×10^6	185,523	2.239×10^6	4,560.1	164,608
Ta				37,909			44,636
Nu_c				1.021			1.036
Nu		37.93	1707	69.56	2034	17.80	76.63
h	BTU/(SEC IN^2 °F)	7.890×10^{-3}	1.479×10^{-4}	1.808×10^{-3}	1.555×10^{-4}	3.702×10^{-3}	1.594×10^{-4}
	BTU/(HR FT^2 °F)	40.9	76.7	93.78	80.6	19.2	82.6

FIGURE 5 COMPUTATION OF HEAT TRANSFER COEFFICIENTS DUE TO ROTATION

FREON R11

$\mu = 1.56\times10^{-9}$ LB SEC/IN^2

$\eta = 1.04\times10^{-7}$ BTU/(SEC IN °F)

$\rho = 2.32\times10^{-4}$ LB/IN^3

$C_p = 0.1323$ BTU/(LB °F)

$P_r = 0.76602$

N = 60,000 RPM

$\omega = 6283$ RAD/SEC

FLOW THROUGH A CHANNEL (SECT. 1 & 5)

$$A = \pi(r_o^2 - r_i^2)\ ; \qquad \bar{V} = Q/(\rho A)$$

$$Re = \frac{\bar{V} D \rho}{\mu g}$$

$$\frac{D h}{\eta} = Nu = 0.023\, Re^{.8}\, P_r^{1/3}$$

HORIZ. CYL. WITHOUT CLOSE OBSTRUCTIONS (SECT. 2 & 4)

$$\frac{2 r_i h}{\eta} = Nu = 0.073\, Re^{.7} = 0.073\left(\frac{2\omega r_i^2 \rho}{\mu g}\right)^{.7}$$

ROTATING CYL. WITHIN CONCENTRIC TUBE (SECT. 3 & 6)

$$Re = \frac{r_i^2 \omega c \rho}{\mu g}\ ; \qquad Ta = Re\left(\frac{c}{r_i}\right)^{1/2}$$

$$Nu_c = \frac{c/r_i}{\ln(1 + c/r_i)}$$

$$\frac{c h}{\eta} = Nu = 0.35\, Nu_c\, (Ta)^{1/2}$$

A.A.
7/15/76

TABLE 3

ARRAY OF THERMAL RESISTANCES, R (DEG F/(BTU /SEC))

1	4441.6	2	888.35
5	612.55	6	272.42
9	1536.5	10	1509.0
13	37743	14	4637.7
17	2938.7	18	1309.0
21	1111.9	22	1875.8
25	1111.9	26	884.63
29	483.23	30	659.31
33	4936.2	34	1906.3
37	17784	38	19998

3	1750.1	4	558.43
7	272.42	8	612.55
11	256.83	12	1443.6
15	4637.7	16	45057
19	2938.7	20	598.04
23	833.68	24	1875.8
27	4176.8	28	2072.2
31	5507.3	32	23745
35	4474.9	36	2605.2
39	1.86576E+05	40	1021.0

TABLE 4 (a)

CNG * THERMAL MODEL OF RCTOR * 9/22/76 *AFA* CASE 1 LAM. ID INSULATED
TEMPERATURE DISTRIBUTION (DEG F)

T(1)	130.00	T(2)	193.55	T(3)	206.26	T(4)	210.85
T(5)	212.32	T(6)	216.76	T(7)	220.13	T(8)	210.00
T(9)	203.88	T(10)	290.53	T(11)	341.25	T(12)	350.97
T(13)	353.01	T(14)	406.32	T(15)	399.71	T(16)	415.61
T(17)	414.67	T(18)	413.35	T(19)	584.68	T(20)	663.22
T(21)	131.83	T(22)	136.53	T(23)	159.01	T(24)	178.75
T(25)	184.82	T(26)	190.27	T(27)	207.18	T(28)	222.04
T(29)	221.87	T(30)	221.70	T(31)	232.74	T(32)	216.59
T(33)	388.97	T(34)	139.40	T(35)	148.57	T(36)	546.96
T(37)	565.24	T(38)	144.50				

TABLE 4(b)

COMPUTATION OF HEAT FLOWS

FROM TEMP	TO TEMP	THROUGH RESISTANCE	HEAT FLOW (BTU /SEC)
T(2)	T(1)	R(1)	1.43073E-02
T(3)	T(2)	R(2)	1.43073E-02
T(4)	T(3)	R(3)	2.62637E-03
T(5)	T(4)	R(4)	2.62637E-03
T(6)	T(5)	R(5)	7.24512E-03
T(7)	T(6)	R(6)	1.23506E-02
T(7)	T(8)	R(7)	3.71711E-02
T(8)	T(9)	R(8)	9.98733E-03
T(10)	T(9)	R(9)	3.03645E-02
T(11)	T(10)	R(10)	6.01177E-02
T(12)	T(11)	R(11)	3.78612E-02
T(13)	T(12)	R(12)	1.41243E-03
T(14)	T(13)	R(13)	1.41243E-03
T(14)	T(15)	R(14)	1.42700E-03
T(16)	T(15)	R(15)	3.43022E-03
T(19)	T(16)	R(16)	3.75217E-03
T(17)	T(14)	R(17)	2.83943E-03
T(17)	T(15)	R(18)	1.14297E-02
T(16)	T(17)	R(19)	3.21949E-04
T(10)	T(31)	R(20)	2.97533E-02
T(9)	T(23)	R(21)	4.03518E-02
T(8)	T(23)	R(22)	2.71838E-02
T(7)	T(25)	R(23)	4.23457E-02
T(6)	T(27)	R(24)	5.10545E-03
T(5)	T(27)	R(25)	4.61875E-03
T(32)	T(3)	R(26)	1.16809E-02
T(29)	T(32)	R(27)	1.26288E-03
T(31)	T(21)	R(28)	4.86953E-02
T(33)	T(34)	R(29)	.51635
T(15)	T(33)	R(30)	1.62869E-02
T(17)	T(12)	R(31)	1.15653E-02
T(18)	T(12)	R(32)	2.62704E-03
T(36)	T(17)	R(33)	2.68003E-02
T(19)	T(36)	R(34)	1.97849E-02
650.000	T(19)	R(35)	2.35370E-02
T(37)	T(36)	R(36)	7.01545E-03
650.000	T(37)	R(37)	7.01545E-03
650.000	T(20)	R(38)	1.33922E-03
T(20)	T(18)	R(39)	1.33922E-03
T(17)	T(18)	R(40)	1.28782E-03

TABLE 5(a)

CNG * THERMAL MODEL OF RCTOR * 9/22/76 *AFA* CASE 2 .2 OF IRON LOSSES TO GAS
TEMPERATURE DISTRIBUTION (DEG F)

T(1)	130.00	T(2)	196.20	T(3)	209.44	T(4)	214.53
T(5)	216.15	T(6)	220.05	T(7)	222.91	T(8)	212.17
T(9)	205.25	T(10)	251.33	T(11)	341.89	T(12)	351.58
T(13)	353.61	T(14)	406.49	T(15)	399.81	T(16)	415.76
T(17)	414.85	T(18)	413.55	T(19)	584.74	T(20)	663.24
T(21)	131.91	T(22)	136.61	T(23)	159.36	T(24)	179.34
T(25)	187.56	T(26)	195.69	T(27)	212.30	T(28)	226.88
T(29)	226.66	T(30)	226.45	T(31)	233.37	T(32)	220.06
T(33)	389.01	T(34)	139.40	T(35)	148.58	T(36)	547.05
T(37)	565.32	T(38)	144.65				

TABLE 5(b)

COMPUTATION OF HEAT FLOWS

FROM TEMP	TO TEMP	THROUGH RESISTANCE	HEAT FLOW (BTU /SEC)
T(2)	T(1)	R(1)	1.49049E-02
T(3)	T(2)	R(2)	1.49049E-02
T(4)	T(3)	R(3)	2.90505E-03
T(5)	T(4)	R(4)	2.90505E-03
T(6)	T(5)	R(5)	6.36771E-03
T(7)	T(6)	R(6)	1.05011E-02
T(7)	T(8)	R(7)	3.94401E-02
T(8)	T(9)	R(8)	1.12854E-02
T(10)	T(9)	R(9)	2.99887E-02
T(11)	T(10)	R(10)	6.00114E-02
T(12)	T(11)	R(11)	3.77549E-02
T(13)	T(12)	R(12)	1.40122E-03
T(14)	T(13)	R(13)	1.40122E-03
T(14)	T(15)	R(14)	1.44191E-03
T(16)	T(15)	R(15)	3.44010E-03
T(19)	T(16)	R(16)	3.75043E-03
T(17)	T(14)	R(17)	2.84313E-03
T(17)	T(15)	R(18)	1.14908E-02
T(16)	T(17)	R(19)	3.10322E-04
T(10)	T(31)	R(20)	3.00227E-02
T(9)	T(23)	R(21)	4.12741E-02
T(8)	T(23)	R(22)	2.81547E-02
T(7)	T(25)	R(23)	4.19262E-02
T(6)	T(27)	R(24)	4.13341E-03
T(5)	T(27)	R(25)	3.46266E-03
T(32)	T(3)	R(26)	1.19998E-02
T(29)	T(32)	R(27)	1.58181E-03
T(31)	T(21)	R(28)	4.89647E-02
T(33)	T(34)	R(29)	.51643
T(15)	T(33)	R(30)	1.63728E-02
T(17)	T(12)	R(31)	1.14875E-02
T(18)	T(12)	R(32)	2.60970E-03
T(36)	T(17)	R(33)	2.67826E-02
T(19)	T(36)	R(34)	1.97716E-02
650.000	T(19)	R(35)	2.35221E-02
T(37)	T(36)	R(36)	7.01093E-03
650.000	T(37)	R(37)	7.01093E-03
650.000	T(20)	R(38)	1.33827E-03
T(20)	T(18)	R(39)	1.33827E-03
T(17)	T(18)	R(40)	1.27143E-03

rises from 118°F to T_{30} = 222°F before it is discharged into the compressor, picking up 402 watts; this is 38% of the total heat load (see Table 2) on the system. About 33.7 watts flow from the turbine into the rotor, and about 15.1 watts flow from the rotor into the compressor, through the respective attachments.

IV. ALTERNATOR MODEL

Figure 6 is a schematic of the alternator showing pertinent dimensions. Figure 7 shows a section of a lamination side-view and the inner ring of the water cooling jacket. In order to simplify the analysis, the cooling of the lamination iron losses, the copper winding losses, and the field coil losses have been treated separately.

A. Lamination Model

The parameters and dimensions of the lamination-sector model are given in Table 6. The iron losses are distributed as follows: 36 watts within the first 1/8" from the ID, 30 watts in the iron bars, and 30 watts in the rest of the lamination. At the inner surface of the water cooling jacket, a heat transfer coefficient of h = 100 BTU/(Hr Ft^2 °F) and a water mean temperature of 150°F were used. Four cases have been run, the results of which are shown plotted in Figure 8. The lower two curves correspond to using only the iron losses in the model; the upper two curves include both the iron and the copper winding losses in the model. The solid line curves correspond to the cases where the lamination ID was assumed insulated; for the dotted lines, convection to the Freon gas at T_{25} = 186°F was used.

From these results, it can be concluded that if the heat in the windings is insulated from the iron in such a way that it must escape through the end-turns (lower two curves), very little heat exchange (about 0.85 watts) occurs between the lamination ID and the Freon gas. However, if all of the heat in the windings must escape by way of the lamination iron (upper two curves), as much as 14 watts could be transfered from the lamination ID to the Freon gas. In any case, the hot-spot occurs at the lamination ID; it may range from 185°F for the former case to 201°F for the latter.

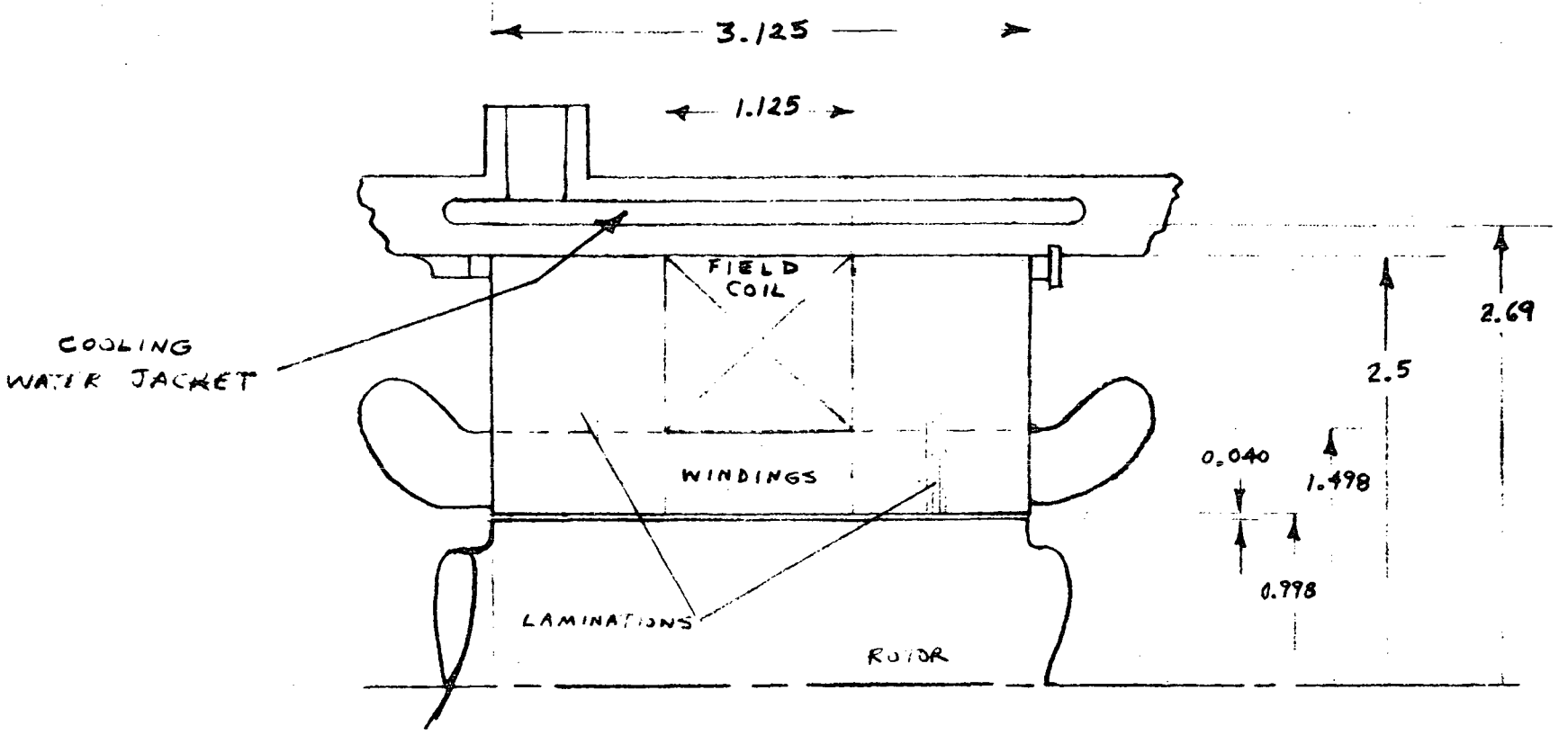

FIGURE 6 ALTERNATOR SCHEMATIC

SCALE 1:1 A. A. 7/20/76 UNITS IN INCHES

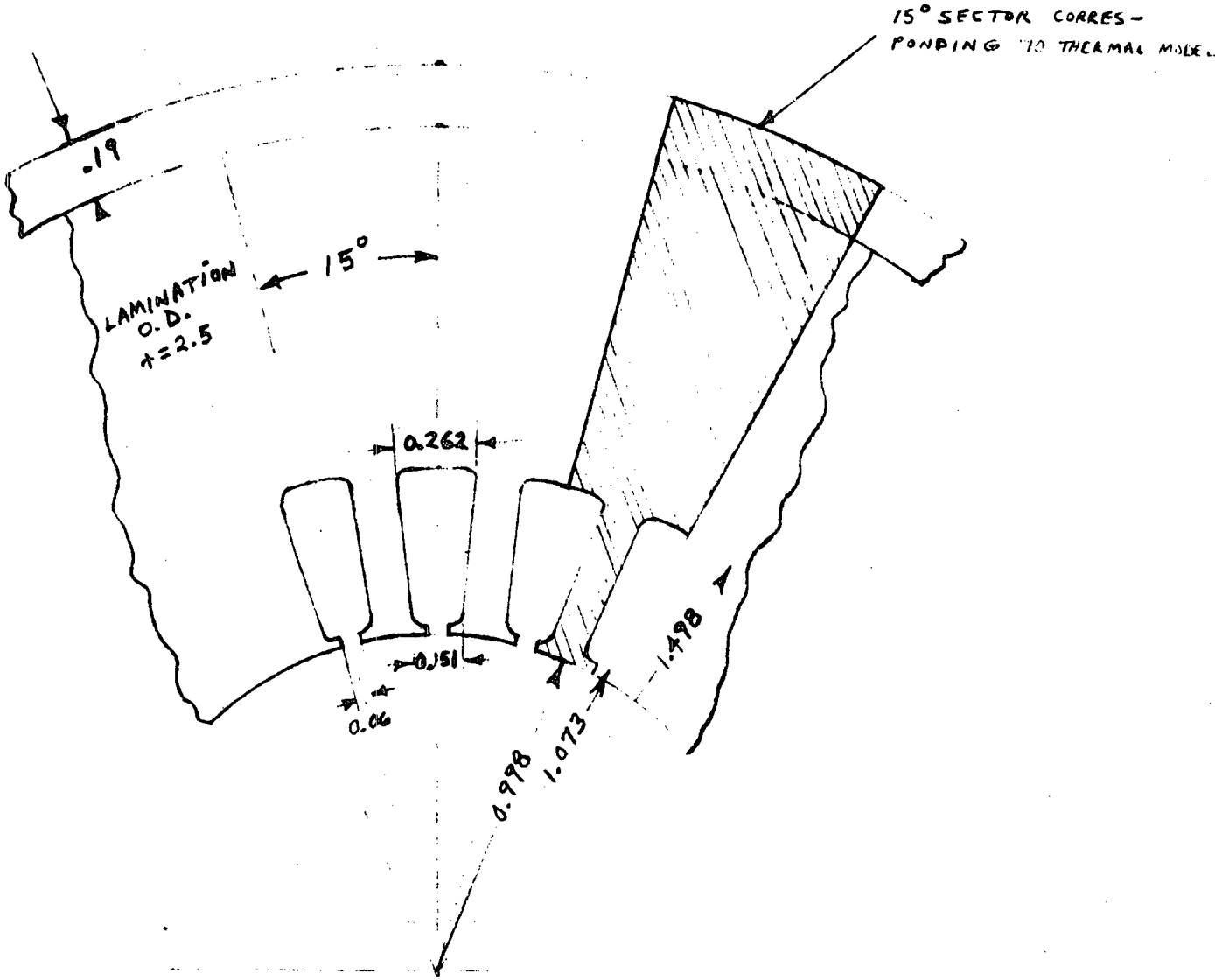

24 SLOTS

$$\text{Approx. Slot Area} = \frac{.262 + .151}{2}\, 0.425 = 0.0878 \text{ in}^2$$

FIGURE 7 LAMINATION SCHEMATIC

SCALE 2:1

A. A. 7/20/76

DIMENSIONS IN INCHES

TABLE 6

PARAMETERS OF LAMINATION SECTOR MODEL

q = Heat Gen./Unit Vol.
L = Radial Extent
A = Cross-sec. area
b = Axial Extent
r = Radius

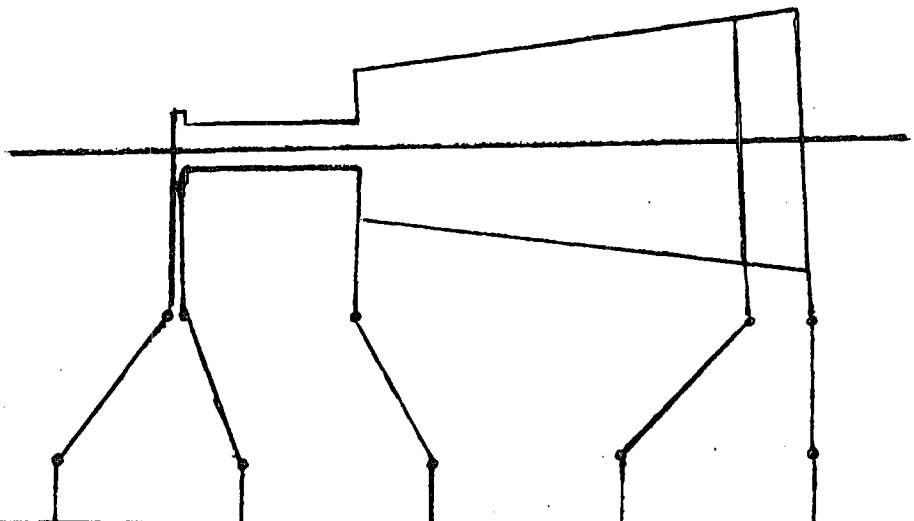

	Q	(BTU/sec)	.0014206	.0028018 (1)	.0011839	0.		
r		(in)	0.998	1.073	1.498	2.500	2.690	
	L	(in)	0.075	0.425	1.002	0.19		
A		(in^2)	0.40255	0.26	0.26/.78435	1.3090	2.20075	
	q	(BTU/(sec. in^3)	1.372036	0.608535	0.001129	0.		
h		(BTU/(sec. in^2°F)	1.81×10^{-4} (2)	∞	∞	3.86×10^{-3}	1.93×10^{-4}	
	V	(in^3)	0.02485	0.1105	1.04877			
T_a		(°F)	186.	-	-	-	150.	
	κ	(BTU/(sec. in°F)	3.3565×10^{-4}	3.3565×10^{-4}	3.3565×10^{-4}	5.0926×10^{-4}		
b		(in)	2.0	2.0	2.0	2.0	3.125	

Notes: 1. The above value of Q is for cases where losses in windings are added to iron bar. For the other cases, Q = 0.0011839.

2. For cases when ID is insulated h = 0.

FIGURE 8 RADIAL TEMPERATURE DISTRIBUTION IN ALTERNATOR LAMINATION

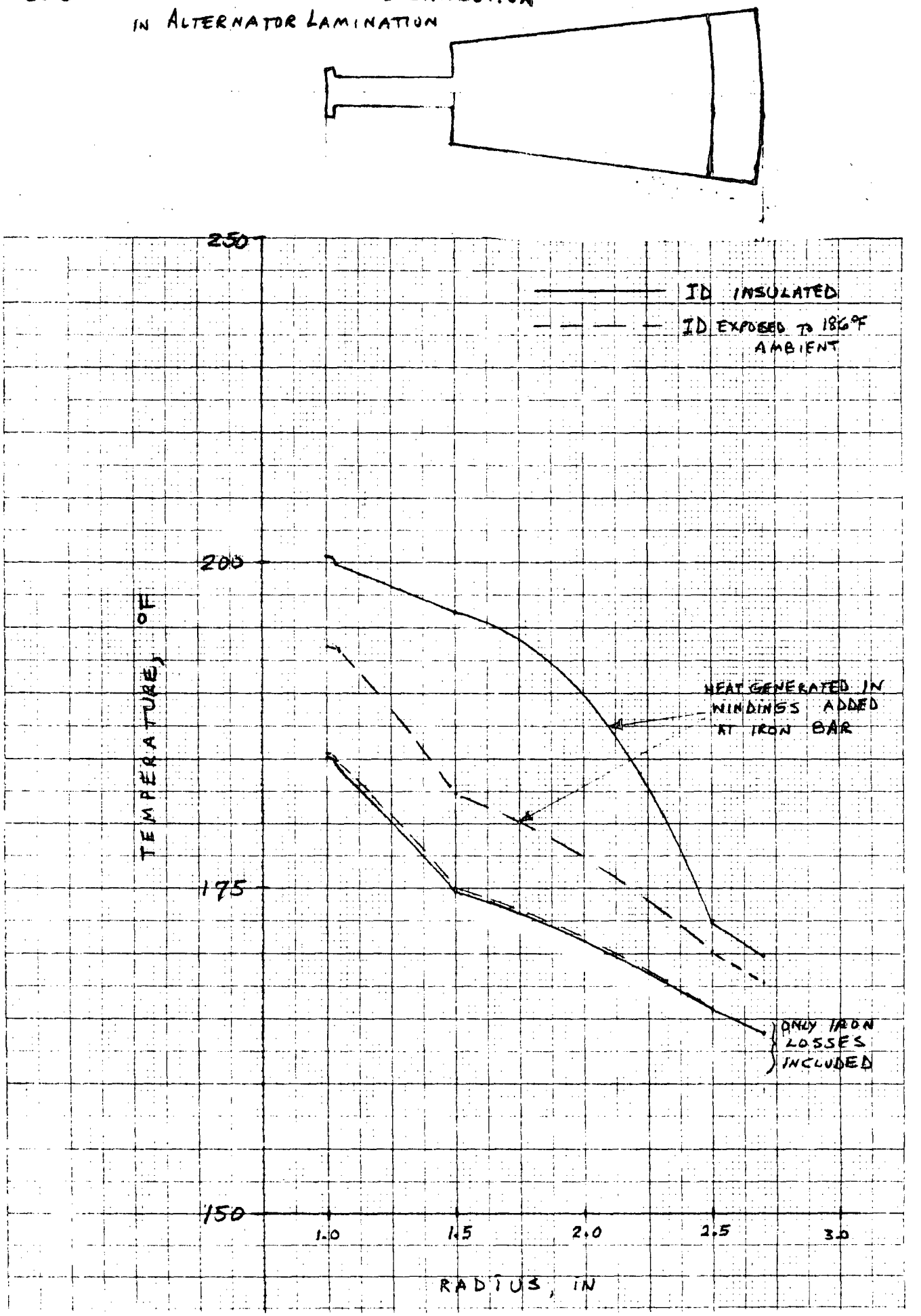

46 1320

B. End-Turn Cooling

Figure 9 is a schematic of a development cross-section of the windings. Each lamination slot has four bundles of wire, with 10 wires per bundle. Since the length of each wire is about 5.625 inches and the diameter (not including insulation) is 0.032 inches, the heat per unit volume can be computed as follows:

$$q = \frac{41 \text{ watts}}{24 \text{ slots } (40 \text{ wires/slot}) \ (5.625 \text{ in}) \ \pi \ (0.032 \text{ in}/2)^2/\text{wire}}$$

$$= 9.4406 \text{ watts/in}^3 = 0.00894 \text{ BTU/Sec/in}^3$$

In the thermal model of the rotor it was assumed that the copper windings dissipated one half of the heat generated within them through each end-turn. The result showed that the end-turn ambients were T_{22} = 137°F and T_{28} = 224°F, at the turbine and compressor sides respectively. With a thermal conductivity of 0.00417 BTU/hr/ft/°F for the wire insulation, the maximum temperature in the windings can be calculated using the formula given in the schematic of Figure 10.

h (BTU/hr/ft^2/°F)	T_A (°F)	T_{max} (°F)
1	137.3 223.6	284.7 371.1
2	137.3 223.6	226.3 312.6
10	137.3 223.6	177.6 264.0

Since more heat will be dissipated through the cold side end-turns (and less through the hot side), the actual maximum temperature will be somewhere in between the two values given above for the given value of h. In conclusion, the hot-spot in the windings is not expected to be higher than about 350°F. However, if a heat transfer coefficient of 10 BTU/hr/ft^2/°F can be achieved by the end-turn cooling arrangement, this hot-spot could be lowered below 260°F.

FIGURE 9

DESIGN MEMORANDUM

Subject: END TURN COOLING SCHEMATIC — Date: 8/76

Project Name: CNG ALTERNATOR — Sheet ..... of ..... Sheets

DEVELOPED CROSS-SECTIONAL VIEW OF SLOTS AT A 2.5" DIAMETER

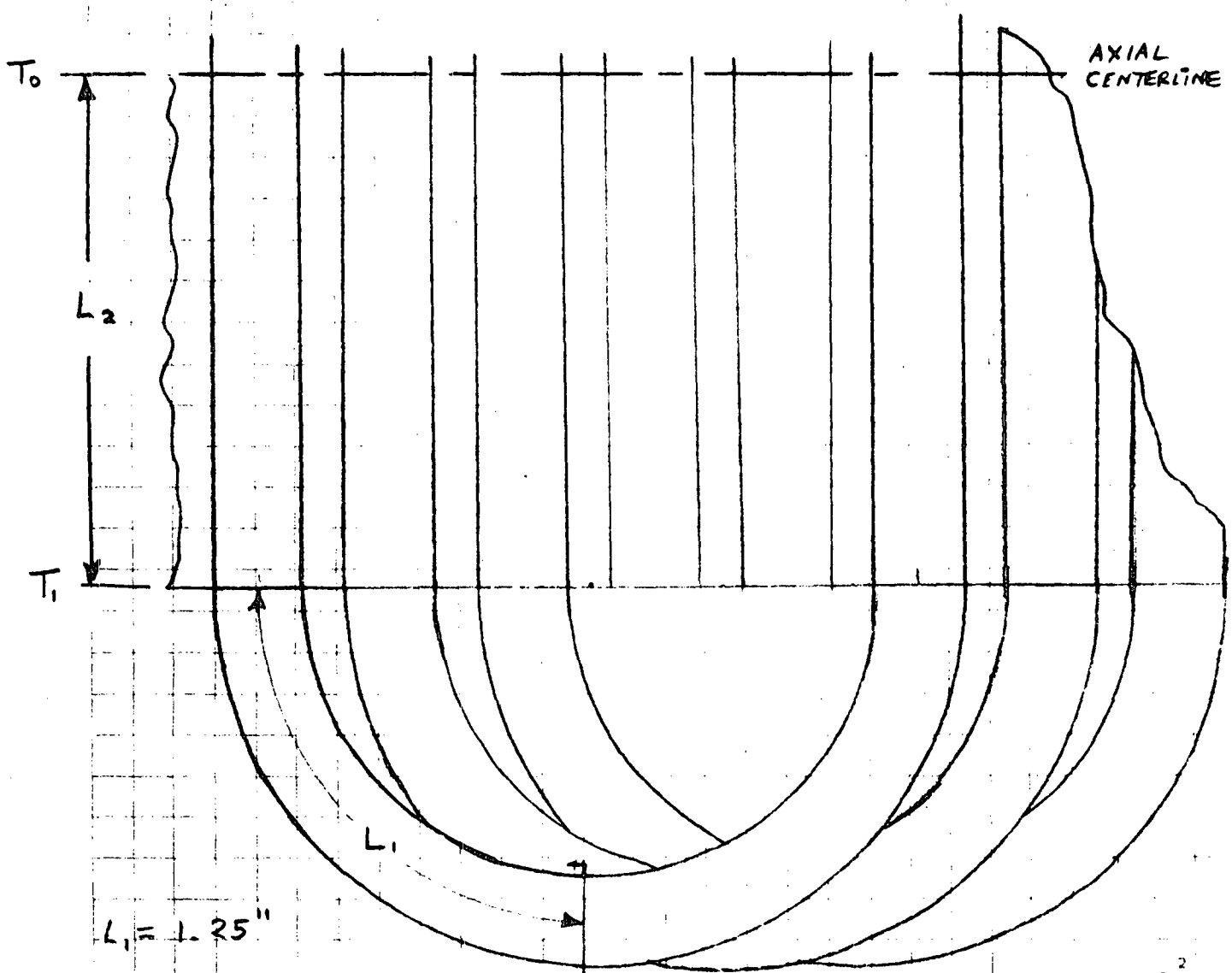

$L_1 = 1.25''$

$L_2 = 1.5625''$

COPPER CROSS-SECTIONAL AREA, $A_c = 10\pi \frac{.032^2}{4}$
$= .008042 \text{ IN}^2$

BUNDLE CROSS-SECTION:

4 BUNDLES/SLOT
24 SLOTS

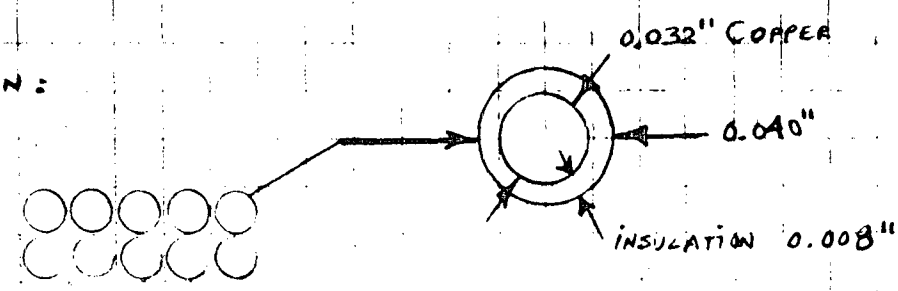

WETTED PERIMETER, $p \sim 7\pi(.032'')/2 = 0.3519$ IN

MT1-2 (7-63)

By: A. ARTICES

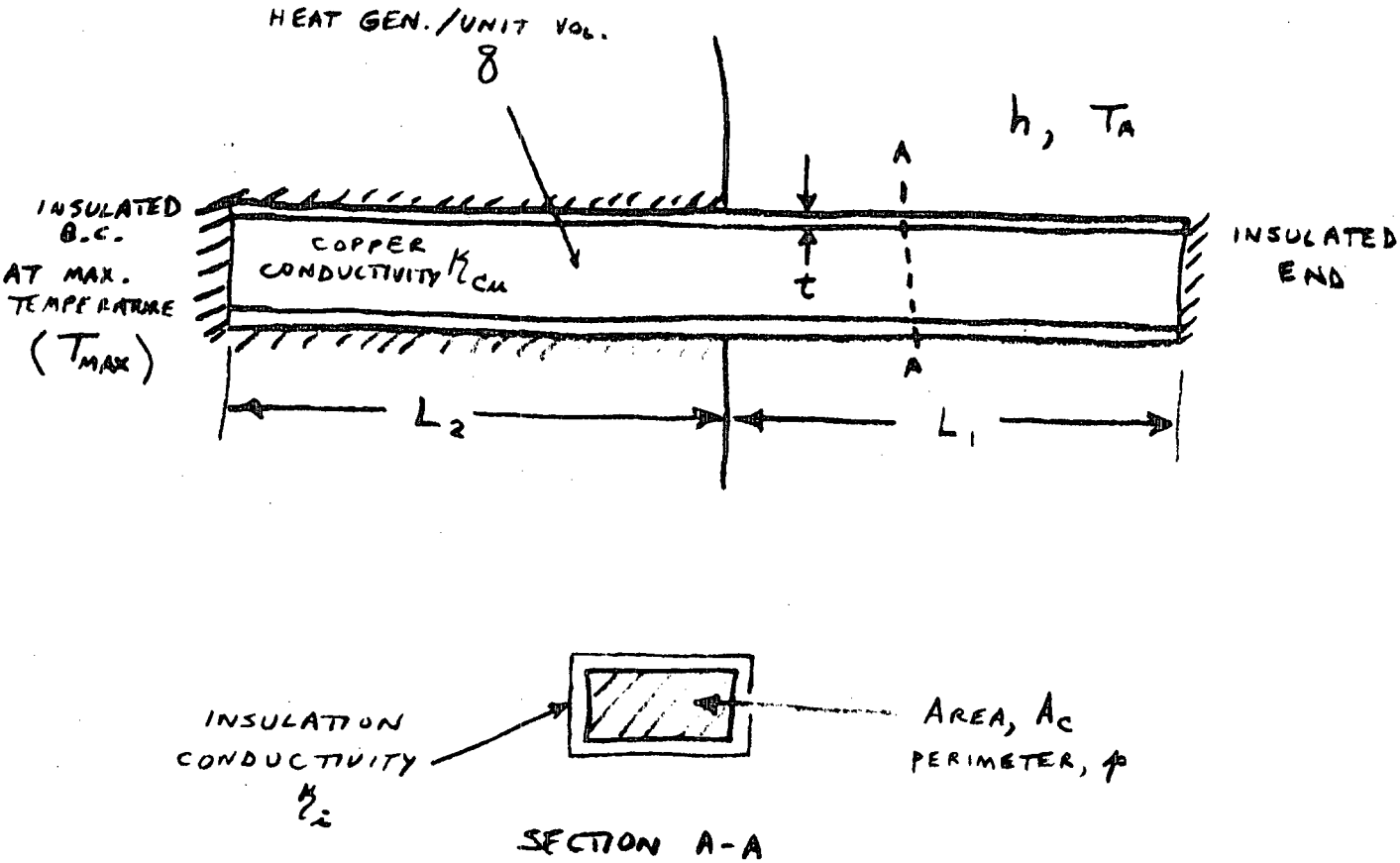

$$T_{MAX} = T_A + q L_2 \left[\frac{A_c}{k_{cu}\, p\, h'} \right]^{1/2} + q \frac{A_c}{p\, h'} + q \frac{L_2^2}{2 k_{cu}}$$

WHERE $h' = \dfrac{1}{\dfrac{1}{h} + \dfrac{p}{k_i}}$

FIGURE 10. END TURN COOLING SCHEMATIC

C. Field Coil Thermal Model

The field coil was shown previously in Figure 6. The model used is internal heat generation per unit volume within an annular cylinder (R_i = 1.498", R_o = 2.5", L = 1.125", Q = 47 watts). All sides are insulated except the O.D. From R = 2.5 to 2.69 in., there is conduction through a carbon steel ring (κ = 22), the outside of which there is convection (h = 100 BTU/hr.ft°F) to 150°F water. The resulting hot spot temperature at the ID of the coil is given by:

$$T(r_i) = T_a + Q\left[\frac{1}{2\pi R\ L\ h} + \frac{\ln\ (R/R_o)}{2\pi\ L\ \kappa}\right] +$$

$$+ \frac{Q}{4\pi L\ \kappa_e}\left[1 + \frac{2\ R_i^2}{R_o^2 - R_i^2}\ \ln\ (R_i/R_o)\right]$$

$$= 163.0 + \frac{57.97}{\kappa_e}\ ,\ °F$$

Where κ_e is the effective thermal conductivity of the field coil in the radial direction in BTU/hr/ft/°F. Therefore, in order not to exceed a maximum temperature of 350°F, an effective conductivity of 0.31 is required.

V. STEAM MANIFOLD THERMAL MODEL

Figure 11 shows the steam manifold, its insulation and housing. Table 7 indicates the material and thermal conductivity of each component. Figure 12 shows the contact areas between the components, and the heat transfer coefficient assumed at each interface. For calculating the heat loss from the steam manifold, high values for these conductance coefficients are conservative.

The steam manifold temperature distribution has been discretized by the model temperatures as shown in Figure 13. T_2 through T_7 represent the inlet water stream to cool the seal. The heat from the seal (q_1 = 0.51635 BTU/sec, as obtained from the results in Section III of this report) is applied to the water from T_7 to T_8. The temperatures of the existing water stream are represented by T_8 through T_{16}. The remaining temperatures (T_{17} through T_{34}) represent points in the solid componnets. The interconnectivity between the nodal temperatures is shown by the network schematic on Figure 14. The box connecting T_1 to T_{27} in this figure represents a thermal resistance with distributed convection to the 100°F ambient, along its length. The values of the thermal resistances are given on Table 8.

The temperature and heat flow results are given in Tables 9(a) and 9(b), respectively. The steam losses 764 watts; 721 watts from the 1100°F steam and 43 watts from the 750°F steam. Most of this heat, 559 watts, flows into the cooling water stream. The rest flows into the 100°F ambient, about 110 watts through the fins and about 88 watts through the diffuser O.D.

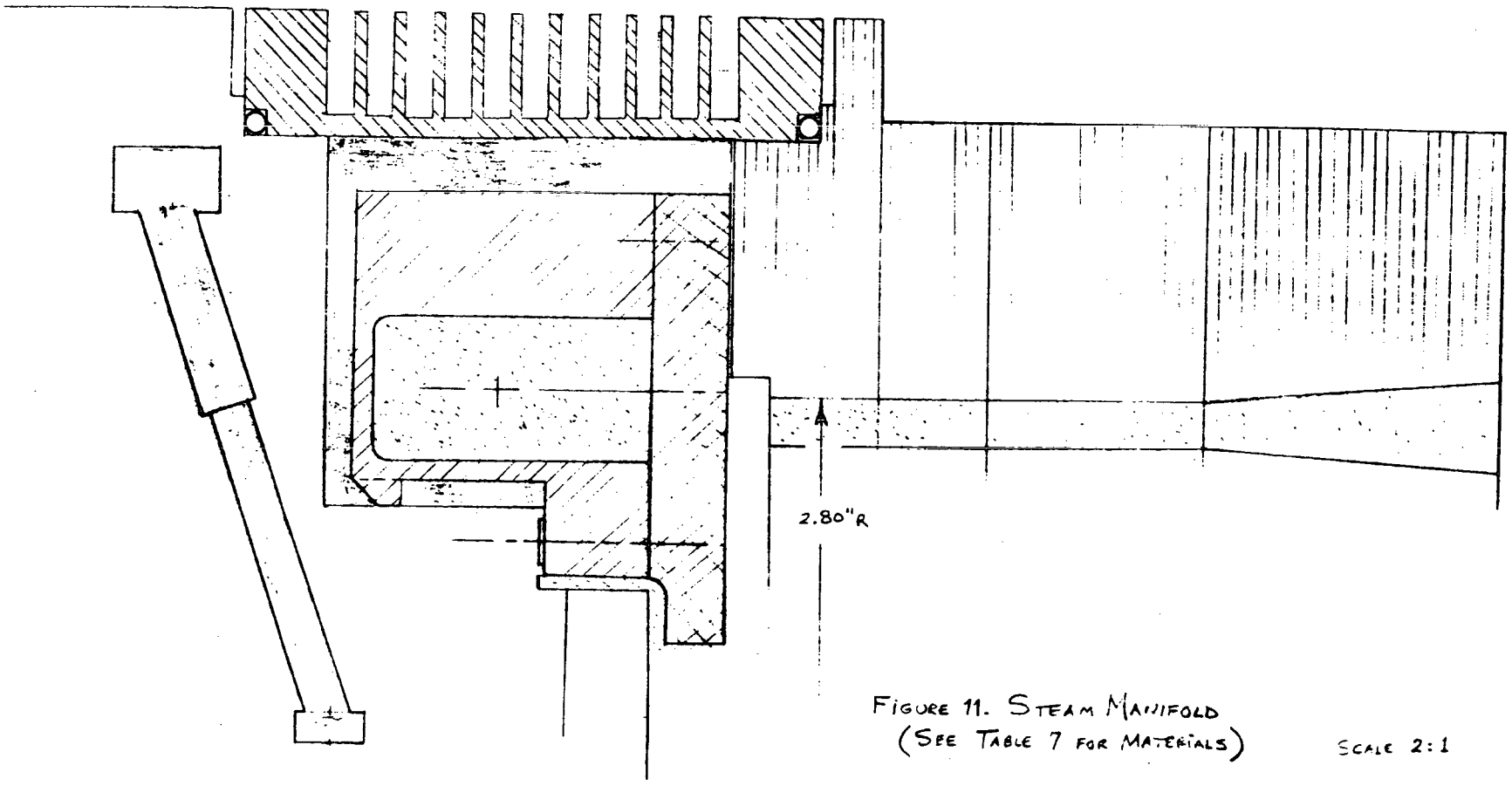

FIGURE 11. STEAM MANIFOLD
(SEE TABLE 7 FOR MATERIALS)

SCALE 2:1

TABLE 7. THERMAL CONDUCTIVITY OF MANIFOLD MATERIALS

MATERIAL CODE (From Fig.11)	MATERIAL	TEMPERATURE (F°)	THERMAL CONDUCTIVITY	
			$\frac{\text{BTU}}{\text{Hr Ft °F}}$	$\frac{\text{BTU}}{\text{Sec In °F}}$
	Inconel 600	800	12.0833	2.79707×10^{-4}
	Refrasil B-100	1100	0.1083	2.50772×10^{-6}
	Stainless Steel 303	400	9.00	2.0833×10^{-4}
	Stainless Steel 416	300	14.5	3.3565×10^{-4}
	Steam at 25 psia	1100	0.0374	8.6653×10^{-7}
	Inconel 718	800	10.333	2.3920×10^{-4}
	Stainless Steel 416	700	16.5	3.8194×10^{-4}

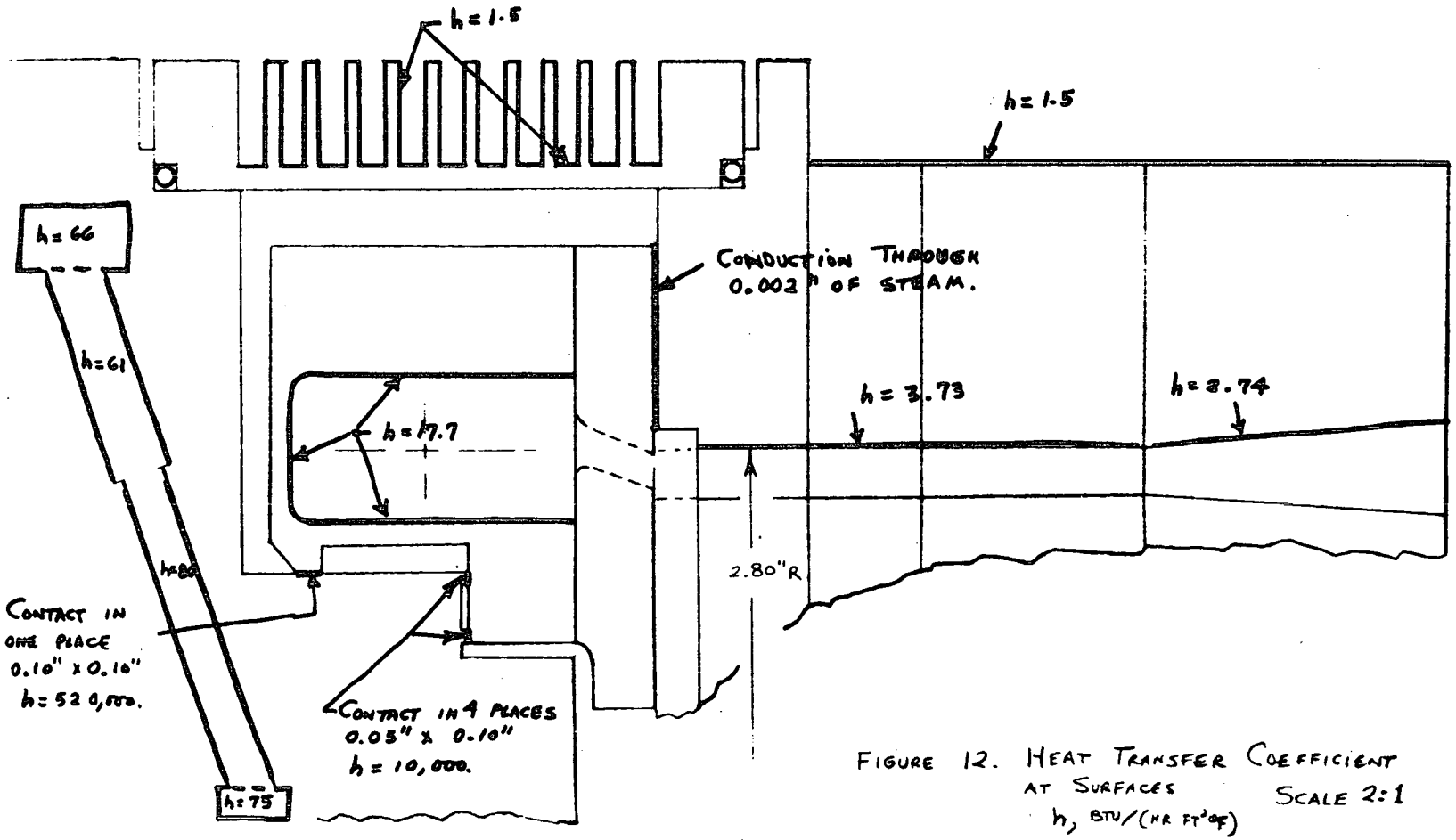

FIGURE 12. HEAT TRANSFER COEFFICIENT AT SURFACES SCALE 2:1
h, BTU/(HR FT²°F)

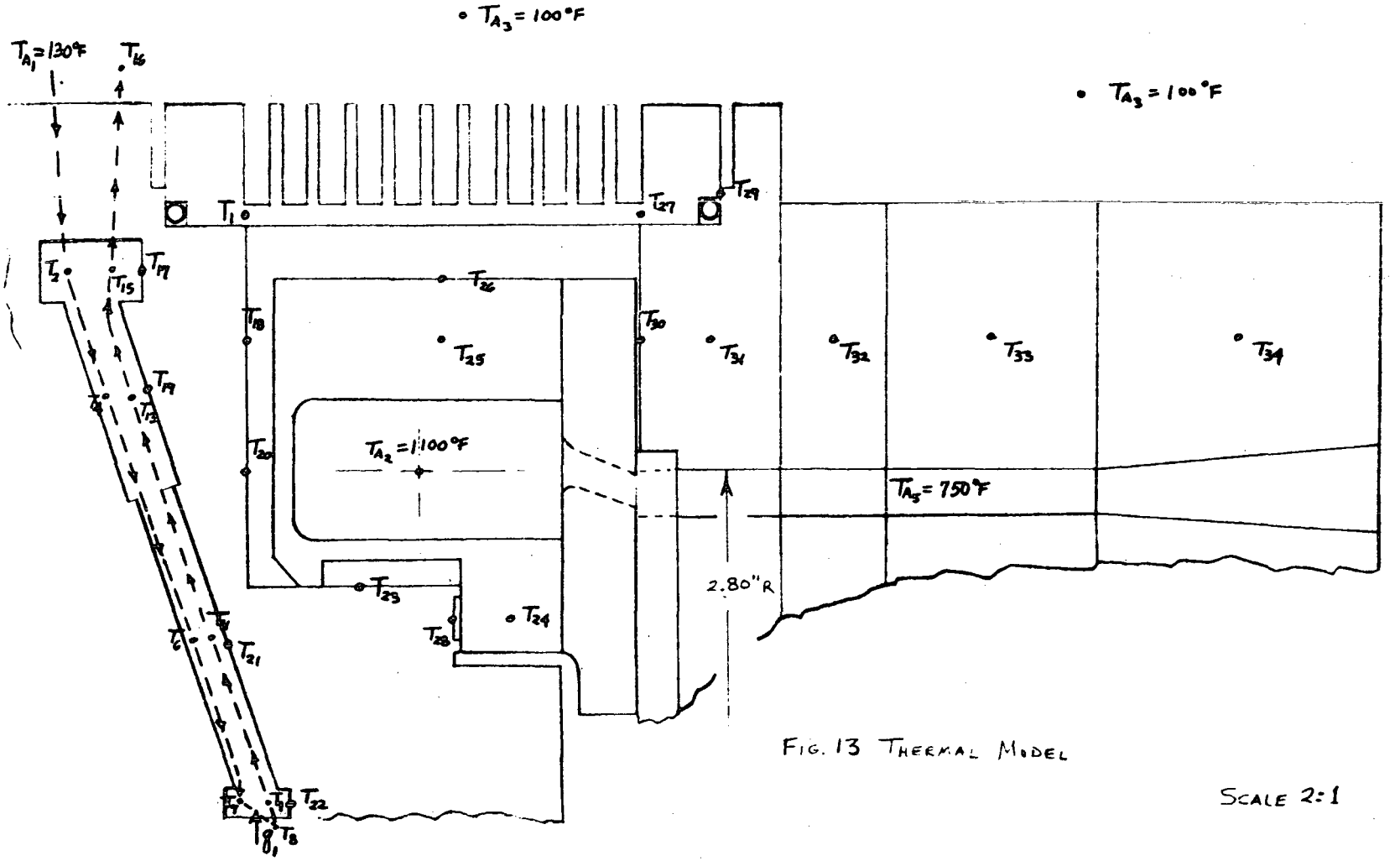

FIG. 13 THERMAL MODEL

SCALE 2:1

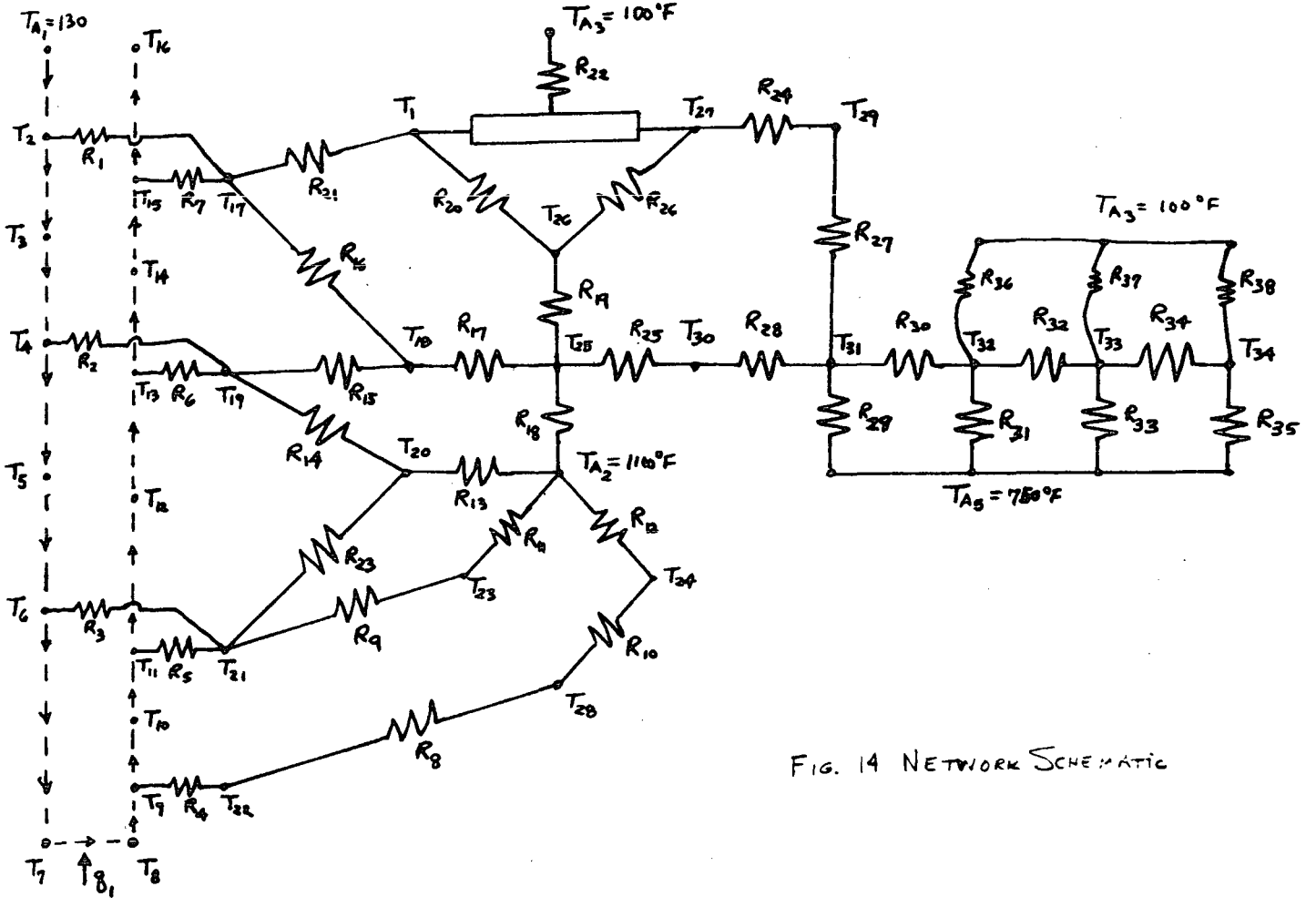

FIG. 14 NETWORK SCHEMATIC

TABLE 8

THERMAL RESISTANCES, R (DEG F/(BTU /SEC))

1	683.55	2	2869.0	3	1817.0	4	1872.4
5	1817.0	6	2869.0	7	683.55	8	991.42
9	347.84	10	7180.6	11	5657.6	12	4153.8
13	6646.0	14	252.36	15	333.27	16	147.28
17	4322.6	18	1205.6	19	34.532	20	4477.1
21	143.15	22	2185.1	23	248.22	24	705.81
25	495.16	26	4477.1	27	972.36	28	43.452
29	24527	30	245.69	31	31885	32	188.36
33	15942	34	120.23	35	113.47	36	32821
37	16411	38	12156				

THERMAL MODEL OF STEAM MANIFOLD *CNG* A.ARTILES* 9/27/76 TABLE 9(a)

TEMPERATURE DISTRIBUTION (DEG F)

T(1)	245.92	T(2)	132.60	T(3)	135.15	T(4)	135.93
T(5)	136.71	T(6)	138.16	T(7)	139.61	T(8)	158.19
T(9)	159.38	T(10)	160.57	T(11)	161.79	T(12)	163.00
T(13)	163.61	T(14)	164.22	T(15)	165.93	T(16)	167.61
T(17)	230.43	T(18)	249.46	T(19)	260.29	T(20)	287.94
T(21)	284.79	T(22)	283.42	T(23)	332.01	T(24)	824.81
T(25)	667.74	T(26)	663.05	T(27)	472.17	T(28)	349.10
T(29)	525.89	T(30)	605.37	T(31)	599.89	T(32)	586.14
T(33)	577.42	T(34)	574.04				

TABLE 9 (6)

COMPUTATION OF HEAT FLOWS

FROM TEMP	TO TEMP	THROUGH RESISTANCE	HEAT FLOW (BTU /SEC)
T(17)	T(2)	R(1)	.14312
T(19)	T(4)	R(2)	4.33474E-02
T(21)	T(6)	R(3)	8.06988E-02
T(22)	T(9)	R(4)	6.62491E-02
T(21)	T(11)	R(5)	6.76960E-02
T(19)	T(13)	R(6)	3.36988E-02
T(17)	T(15)	R(7)	9.43583E-02
T(28)	T(22)	R(8)	6.62491E-02
T(23)	T(21)	R(9)	.13574
T(24)	T(28)	R(10)	6.62491E-02
1100.000	T(23)	R(11)	.13574
1100.000	T(24)	R(12)	6.62491E-02
1100.000	T(20)	R(13)	.12219
T(20)	T(19)	R(14)	.10954
T(19)	T(18)	R(15)	3.24914E-02
T(18)	T(17)	R(16)	.12926
T(25)	T(18)	R(17)	9.67650E-02
1100.000	T(25)	R(18)	.35854
T(25)	T(26)	R(19)	.13580
T(26)	T(1)	R(20)	9.31696E-02
T(1)	T(17)	R(21)	.10822
T(20)	T(21)	R(23)	1.26514E-02
T(29)	T(27)	R(24)	7.61095E-02
T(25)	T(30)	R(25)	.12597
T(26)	T(27)	R(26)	4.26352E-02
T(31)	T(29)	R(27)	7.61095E-02
T(30)	T(31)	R(28)	.12597
750.000	T(31)	R(29)	6.12018E-03
T(31)	T(32)	R(30)	5.59812E-02
750.000	T(32)	R(31)	5.13919E-03
T(32)	T(33)	R(32)	4.63087E-02
750.000	T(33)	R(33)	1.08255E-02
T(33)	T(34)	R(34)	2.80422E-02
750.000	T(34)	R(35)	1.09547E-02
T(32)	100.000	R(36)	1.48118E-02
T(33)	100.000	R(37)	2.90920E-02
T(34)	100.000	R(38)	3.89968E-02

ATTACHMENT F

7 1/2-TON DEMONSTRATOR HSPF GAS HEAT PUMP SYSTEM TEST

MTI 79TR4

FINAL REPORT

7½ TON DEMONSTRATOR HSPF GAS HEAT PUMP SYSTEM TEST

Prepared for:
Consolidated Natural Gas Company Incorporated

Prepared by:
David Ruscitto

October 1978

MECHANICAL TECHNOLOGY INCORPORATED
968 Albany-Shaker Road
Latham, New York 12110

FINAL REPORT

7½ TON DEMONSTRATOR HSPF GAS HEAT PUMP SYSTEM TEST

Prepared for:

Consolidated Natural Gas Company Incorporated
Cleveland, Ohio

Prepared by:

David Ruscitto

October 1978

MECHANICAL TECHNOLOGY INCORPORATED
968 Albany-Shaker Road
Latham, New York 12110

TABLE OF CONTENTS

Section		Page
1.0	INTRODUCTION	1-1
2.0	SUMMARY	2-1
3.0	SYSTEM TEST PROGRAM	3-1
	3.1 Description of Test System	3-1
	3.2 Description of Major Components	3-5
	3.3 Test Program	3-16
	3.4 Post Test Inspection	3-17
4.0	ANALYSIS OF TEST RESULTS	4-1
	4.1 Data Reduction	4-1
	4.2 Component Performance Curves	4-1
	4.3 Parasitic Losses	4-5
5.0	SYSTEM PERFORMANCE	5-1

1.0 INTRODUCTION

This report describes the system test program conducted by MTI for CNG on a 7½ Ton Gas Fired Heat Pump. The test system was designed and constructed to simulate an actual heat pump installation and included all the basic components associated with such an installation. An air handling system was constructed to allow simulation of inside return air and outside ambient air conditions. The conditioned air was obtained by passing air through either the condensers or evaporator, depending on whether the system was operating in the heating or cooling mode.

The system utilized a high speed turbo-compressor. High pressure (300 psi) superheated steam (1100°F) generated in a package boiler was used to drive a re-entry axial flow turbine. The turbine powered a centrifugal compressor and a Homopolar alternator. The turbine, compressor and alternator rotor were arranged on a single shaft. Electrical power generated by the alternator was designed to supply the air handling fans and circulating pumps. The turbo-compressor utilized process fluid (Freon vapor) lubricated bearings; two rigid tilting pad bearings provided the radial support, and a double acting spiral groove thrust bearing provided the axial restraint.

The cooling effect produced by the system was obtained by vaporizing Freon-11 in an air-to-Freon evaporator. The test building return air was used as the heat source to vaporize the Freon as it was forced circulated through the evaporator. Heat from the system was obtained by condensing the Freon and steam with the return air.

2.0 SUMMARY

A gas fired heat pump system was designed, constructed and tested. The test data obtained has been reduced and is presented as a series of curves showing both the individual component performance and the system performance.

The test system was configured to operate in the cooling mode. A number of piping changes can be made to the test rig to simulate the heating mode.

Three separate cases have been presented on the system COP curve. Case 1 shows as a reference, the system performance predicted during the initial design study conducted at the program start. Case 2 is the system COP observed during the test program, and is based directly on test data obtained from the test system. Case 3 represents the present system, modified to incorporate slight hardware modifications that would result in an increase in system performance. These changes include reduction in the turbine wheel clearance to the design value and improvements to both the compressor wheel design and fabrication methods.

The seasonal heating COP's obtained for Cleveland (a representative geographical area from the weather standpoint) for the three cases which are representative of the system heating performance, were:

Case 1:	Original Prediction	-	1.21
Case 2:	Observed in Test	-	1.08
Case 3:	Upgraded System	-	1.18

The cooling COP values obtained for the three cases, for a 95°F outside ambient temperature day were:

Case 1:	Original Prediction	-	0.62
Case 2:	Observed in Test	-	0.47
Case 3:	Upgraded System	-	0.60

The turbo-compressor, which incorporated state-of-the-art technology in several areas, operated satisfactorily throughout the system test program. The maximum speed obtained was 43,000 rpm. The design maximum speed of 60,000 rpm

could not be obtained due to the large nozzle to turbine wheel and turbine wheel to diffuser clearance set during the initial assembly of the turbo-compressor. The large clearance was set as a precaution to avoid possible wheel rubs due to unexpected thermal growth.

3.0 SYSTEM TEST PROGRAM

The system test program was designed to incorporate all the components required to represent a functional gas fired heat pump system. The test system was so constructed to allow simulation of both inside and outside heat exchangers and to produce the conditioned air that would be supplied to a dwelling employing the heat pump.

Freon-11, which has a 75°F boiling point at atmospheric pressure, was used as the refrigerant for this system.

3.1 Description of Test System

A schematic of the test system is shown in Figure 3-1. Figures 3-2 and 3-3 show the actual test facility.

The mechanical portion of the system consisted of a high speed turbo-compressor, incorporating on a single shaft an axial flow re-entry steam drive turbine, a centrifugal compressor, and the rotor for a Homopolar alternator. The steam was generated in a Scientific Energy Systems, Inc. (SES) package boiler. The first stage discharge steam was returned to the boiler and reheated prior to an axial re-entry to the turbine through the second stage nozzles. Second stage steam discharge passed through a regenerator used to preheat the boiler feed water, then entered the steam condenser; the overall turbine pressure ratio was approximately 100/1. The steam condensate drained into a hot well where makeup water was added as required. The feed water was then pressurized by the boiler feed pumps and preheated in the regenerator.

Liquid Freon was pumped from a low pressure separator/reciever into the evaporator by a circulating pump. The circulation rate through the evaporator was higher than the net system flow resulting in a liquid/vapor mixture exiting from the evaporator to a vortex type separator where the liquid/vapor mixture was separated. The liquid dropped out to the receiver portion to be recirculated, and the vapor was supplied to the compressor inlet. The Freon vapor leaving the compressor was condensed, and the liquid drained to a receiver tank which was at the condenser pressure. The Liquid Freon was throttled through an expansion valve and entered the low pressure separator/receiver.

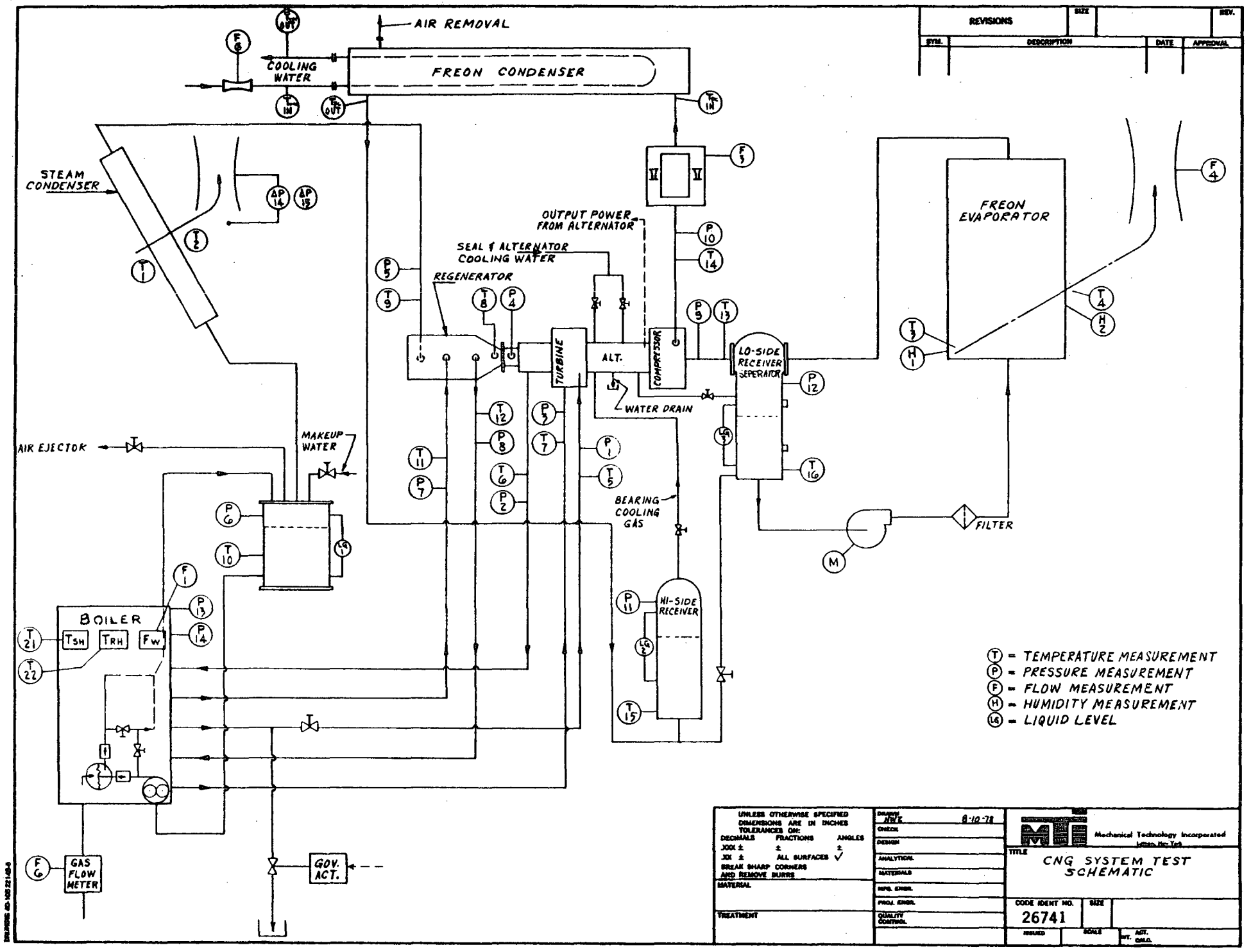

Fig. 3-1 Test System Schematic

MTI-18452

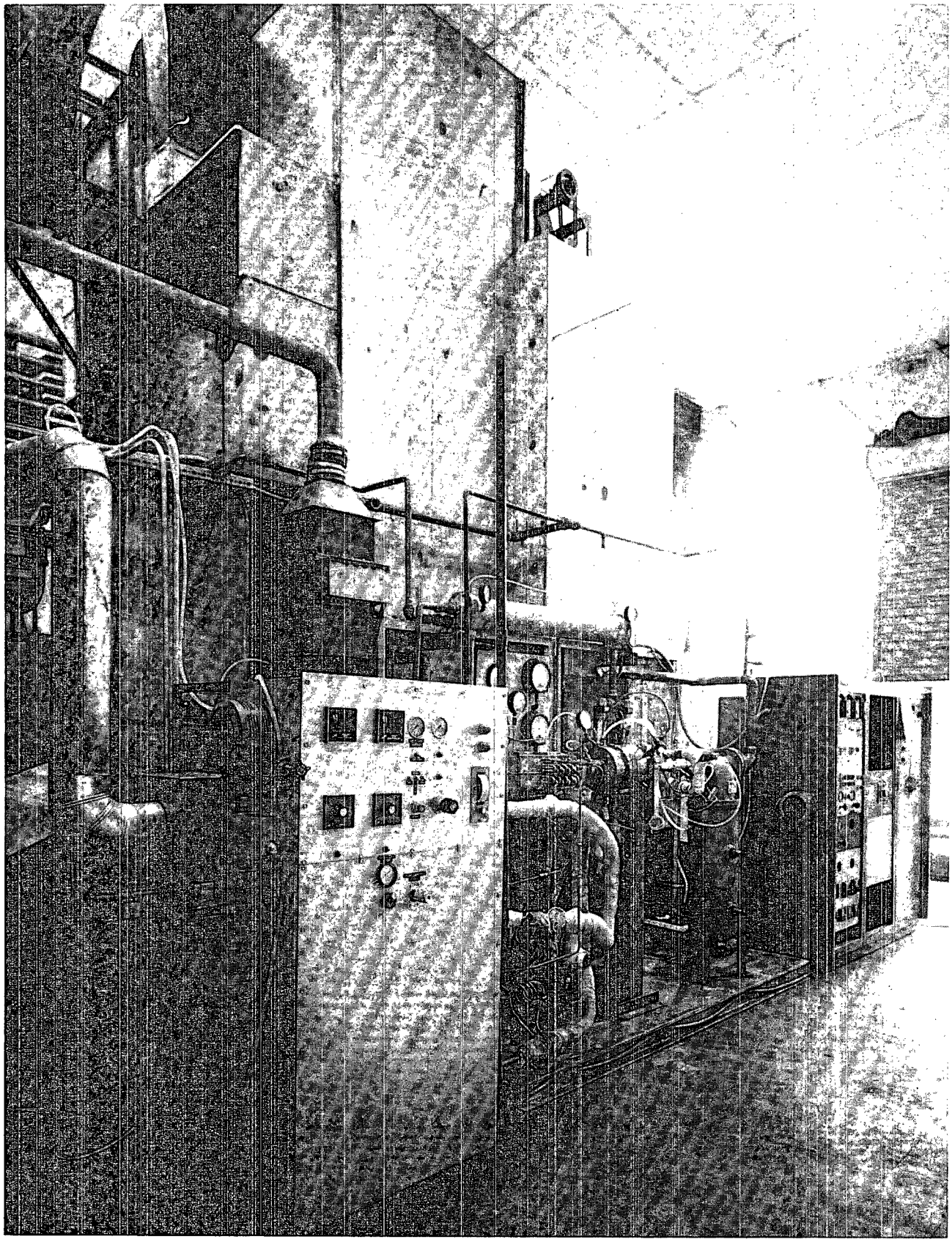

Fig. 3-2 CNG System Test Facility

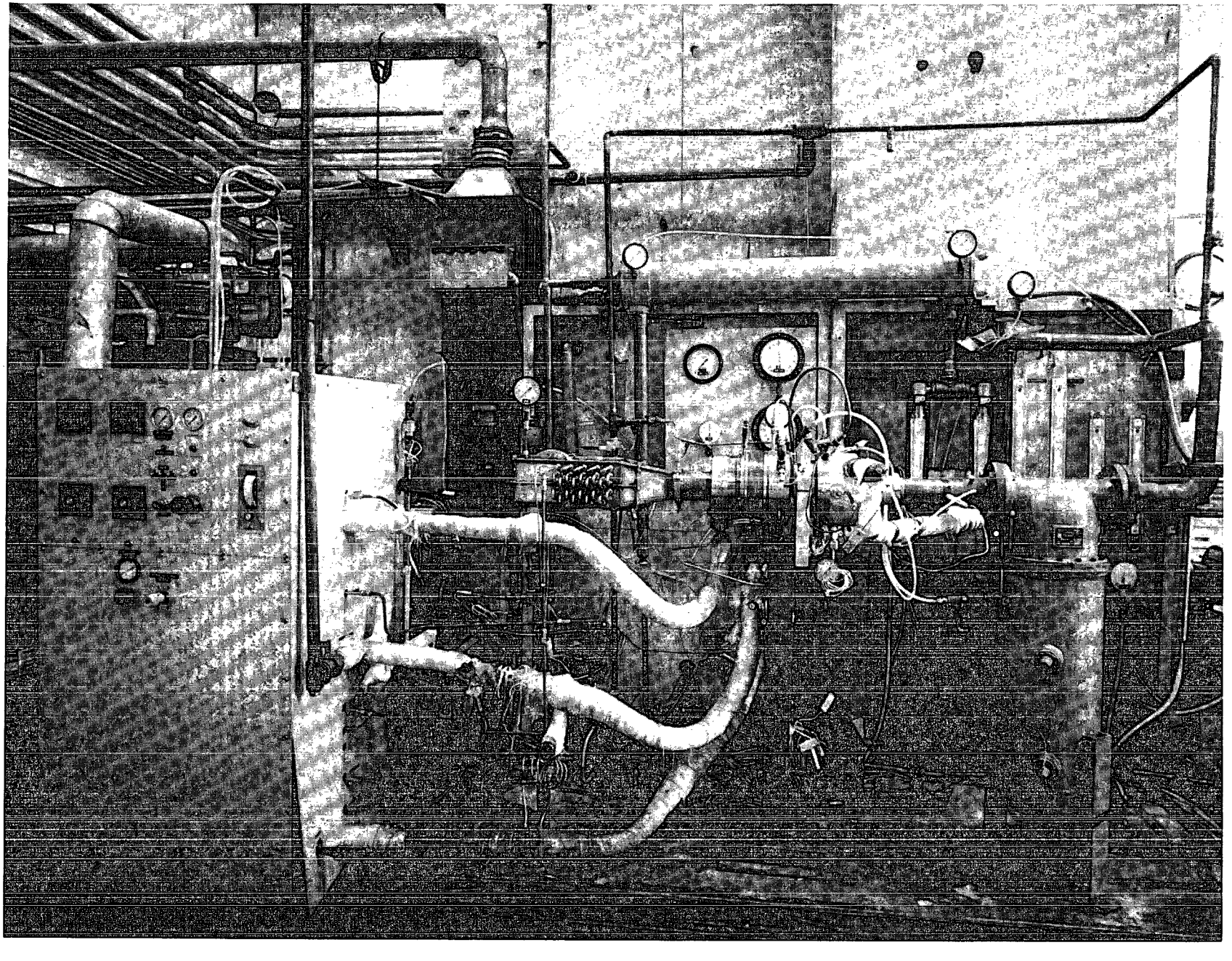

Fig. 3-3 CNG System Test Facility

MTI-18446

The air handling system shown in Figure 3-4 was constructed to allow conditioned air to be obtained utilizing the heat pump, and to simulate various inside and outside ambient air conditions. The air handling fans were driven by DC motors which were designed to receive power generated by the alternator portion of the turbo-compressor unit. The air volume handled varied with the fan motor speed which was dependent on the electrical output voltage level from the alternator. The output voltage from the alternator varied with turbo-compressor speed which, in turn, depended on system demand.

3.2 Description of Major Components

3.2.1 Boiler. The package boiler used in this program was designed and fabricated by Scientific Energy Systems Corporation (SES). The boiler had the following rated load conditions:

Flow:	200 lb/hr
1st Stage:	
Temperature	1100°F
Pressure	300 psia
2nd Stage:	
Temperature	1100°F
Pressure	28.5 psia
Feedwater:	
Temperature	120°F
Suction Pressure	5 psia
Pump Discharge Pressure	360 psia

3.2.2 Turbo-Compressor. A cross section layout of the turbo-compressor is shown in Figure 3-5 and Figure 3-6 shows the turbo-compressor installed for system tests. The turbo-compressor incorporated on a single shaft, an axial flow re-entry steam turbine, the rotor for a Homopolar alternator, and a shrouded Freon compressor. The shaft was supported radially on two rigid tilting pad journal bearings and axially by a double acting spiral groove thrust bearing. These bearings were hydrodynamic gas bearings designed for operation on Freon-11 vapor. The use of process fluid (Freon vapor) lubrication

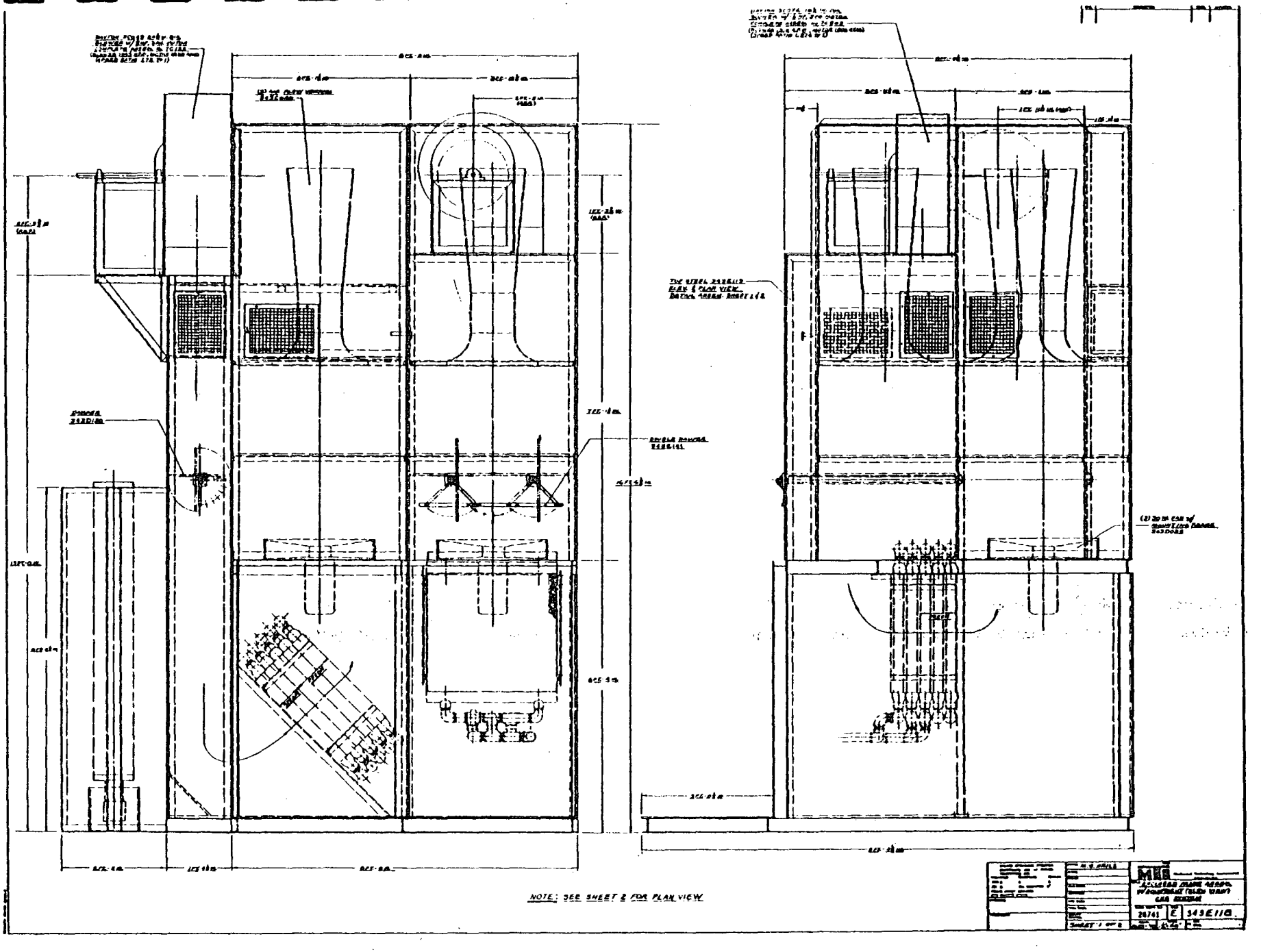

Fig. 3-4 Air Handling System

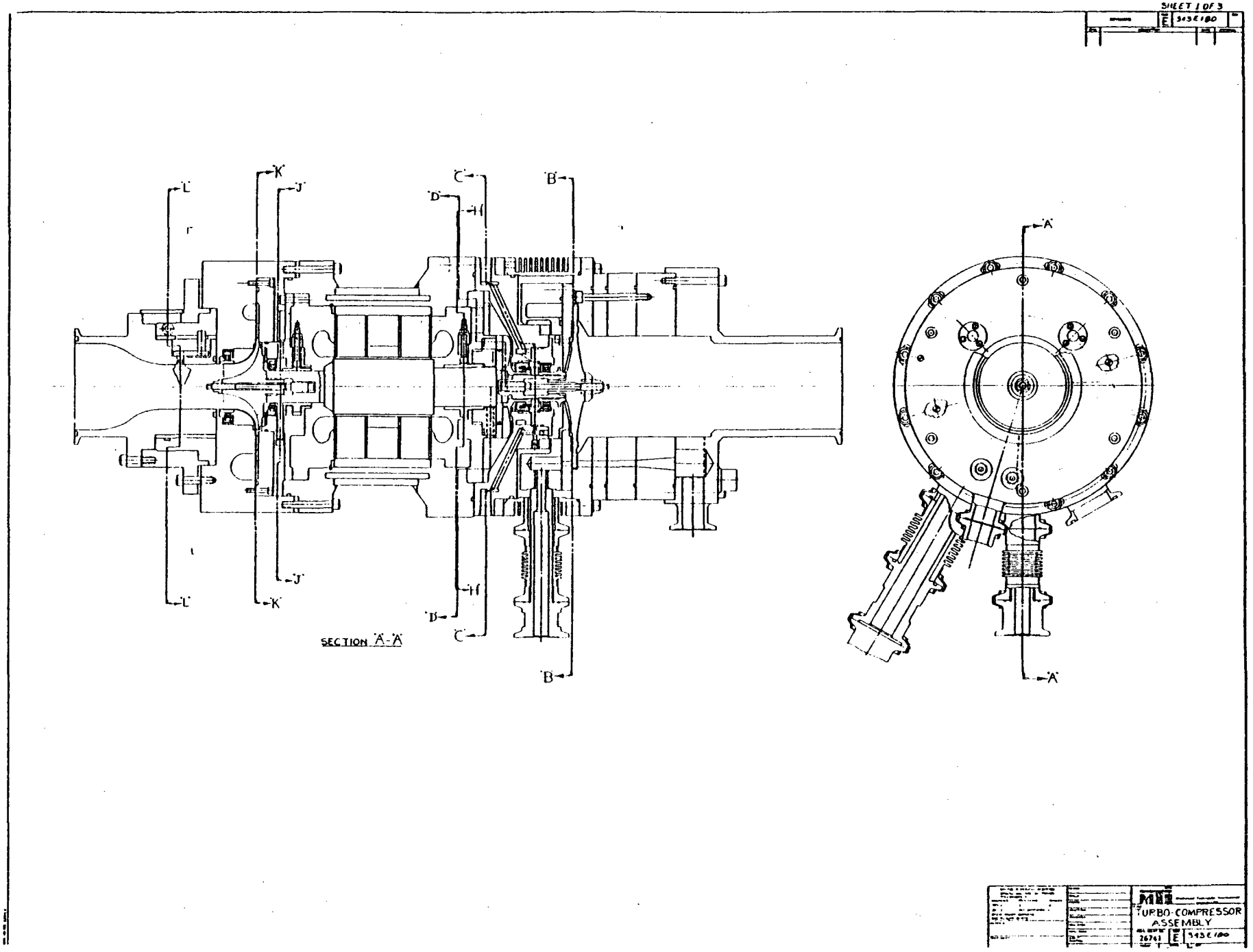

Fig. 3-5 Turbocompressor Layout

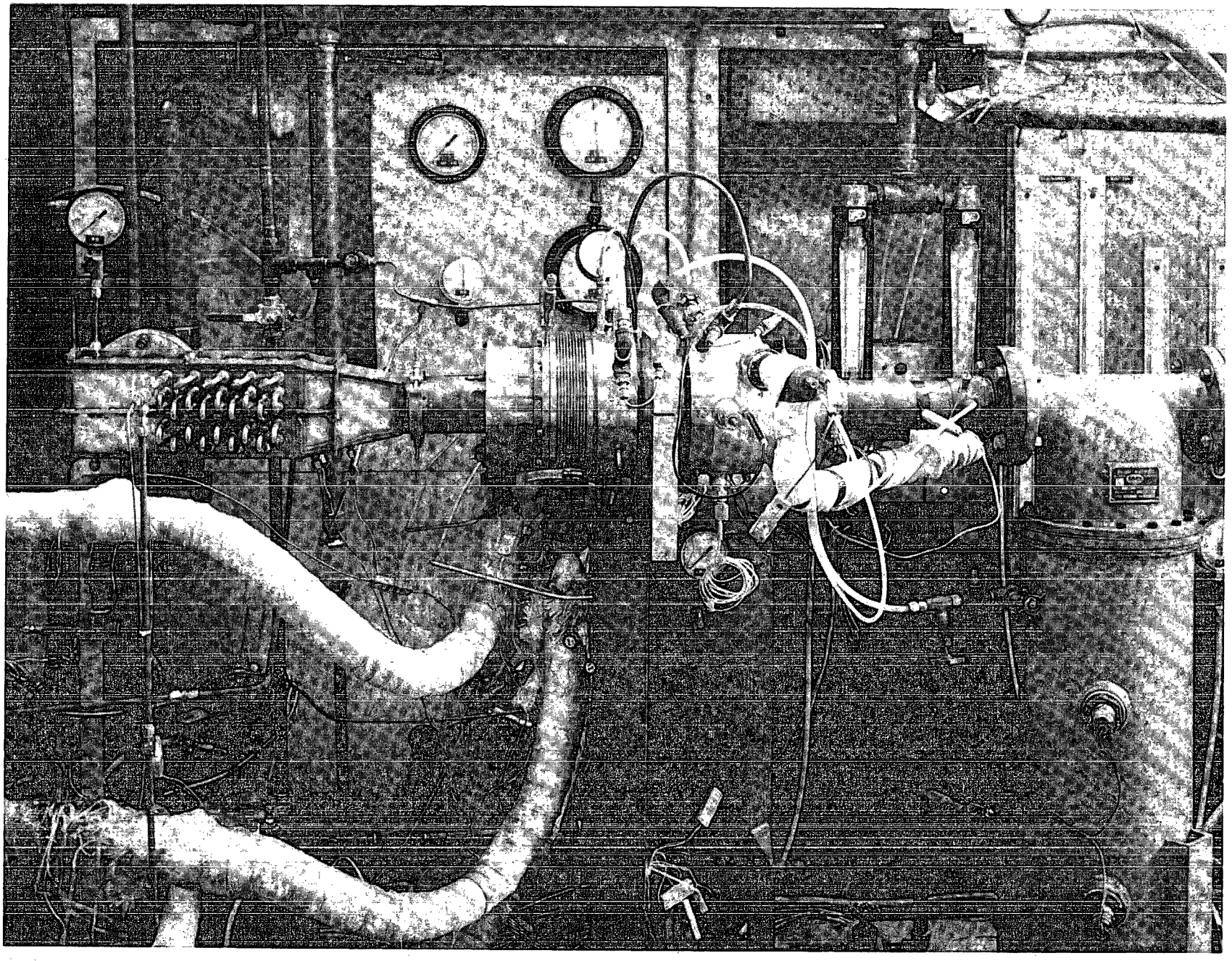

Fig. 3-6 Turbo-Compressor Installed in System Test Facility

MT'-18444

for the bearings, instead of oil lubricated bearings, eliminated an additional complicated sealing requirement and resulted in lower bearing losses charged to the system.

Several design iterations were required to obtain a system of seals that would seal the Freon from the steam and be within a space limitation dictated by the shaft rotor dynamics. The system utilized employed a water pocket between the Freon and steam. A contacting face seal provided the positive seal to contain the Freon. Lubrication and cooling of this seal was accomplished by the water. A non-contacting carbon ring seal was placed between the steam and water. Due to a pressure differential between the steam and water, there was limited control leakage of water through the seal into the second stage turbine steam discharge.

The use of 1100°F steam and cool Freon in the same machine, coupled with the requirements for close tolerances and a compact package, resulted in a complex thermal design for the turbo-compressor. The final configuration was the result of a detail thermal analysis and incorporated a system of heat dams and cooling passages which restricted the flow of heat from the turbine end of the machine, and prevented thermal distortions which would effect the performance of the machine.

Figures 3-7 through 3-9 show the components which make up the shaft assembly. Figure 3-10 shows the compressor end bearing pedestal with the bearing pads installed and two of the three bearing pads from the turbine end bearing. Figure 3-11 shows the double acting thrust bearing and thrust runner.

3.2.3 Regenerator. The regenerator, shown in Figure 3-12, was designed to preheat the boiler feed water with discharge steam from the turbine. The unit consisted of stainless steel finned tubes in a welded stainless steel body.

3.2.4 Condensers and Evaporator. Both the steam and Freon condensers and the Freon evaporator consisted of a series of Modine oil coolers, without

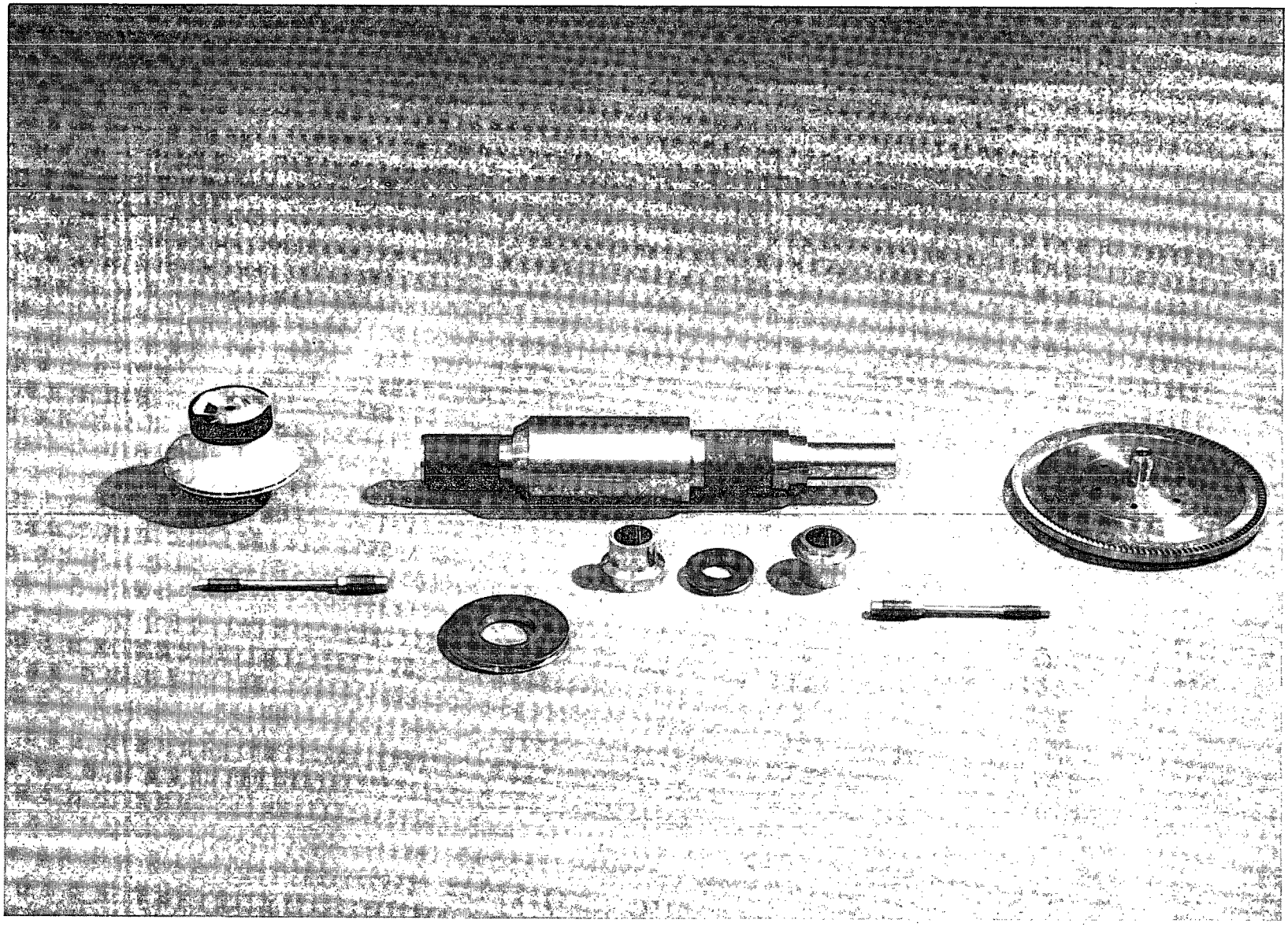

Fig. 3-7 Turbo Compressor Rotative Assembly

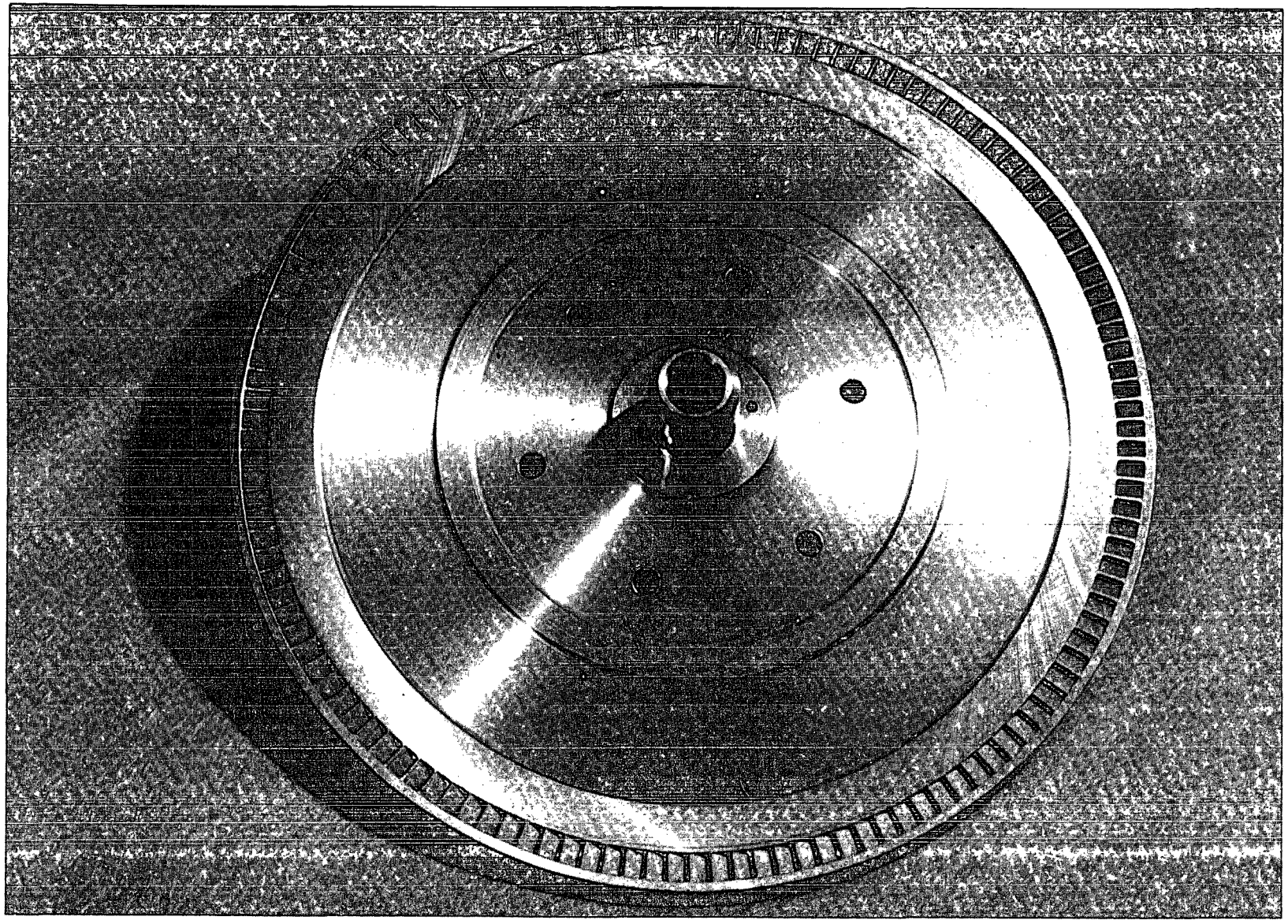

Fig. 3-8 Steam Turbine Wheel

MTI-17863

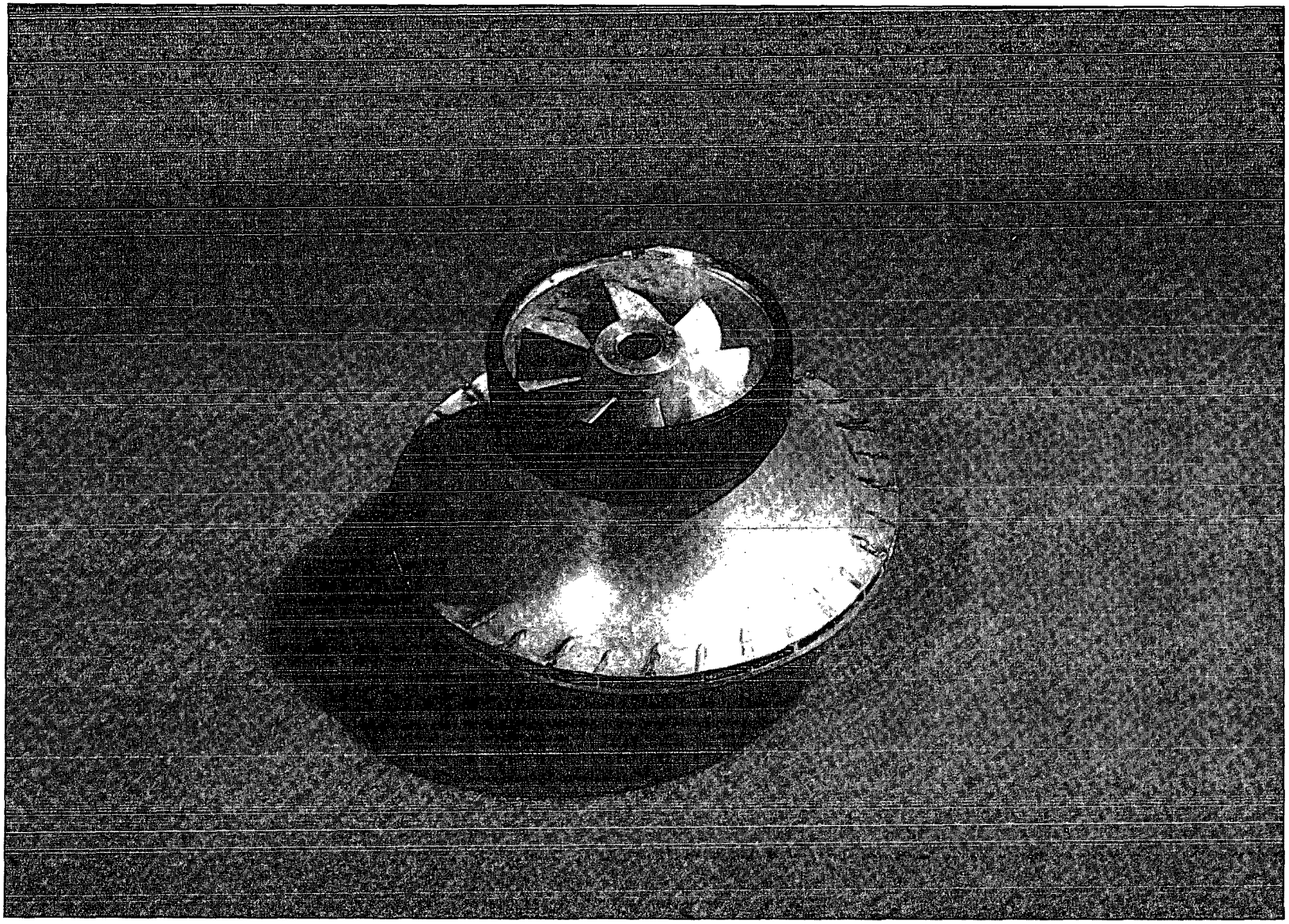

Fig. 3-8 Freon Compressor Wheel

MTI-17864

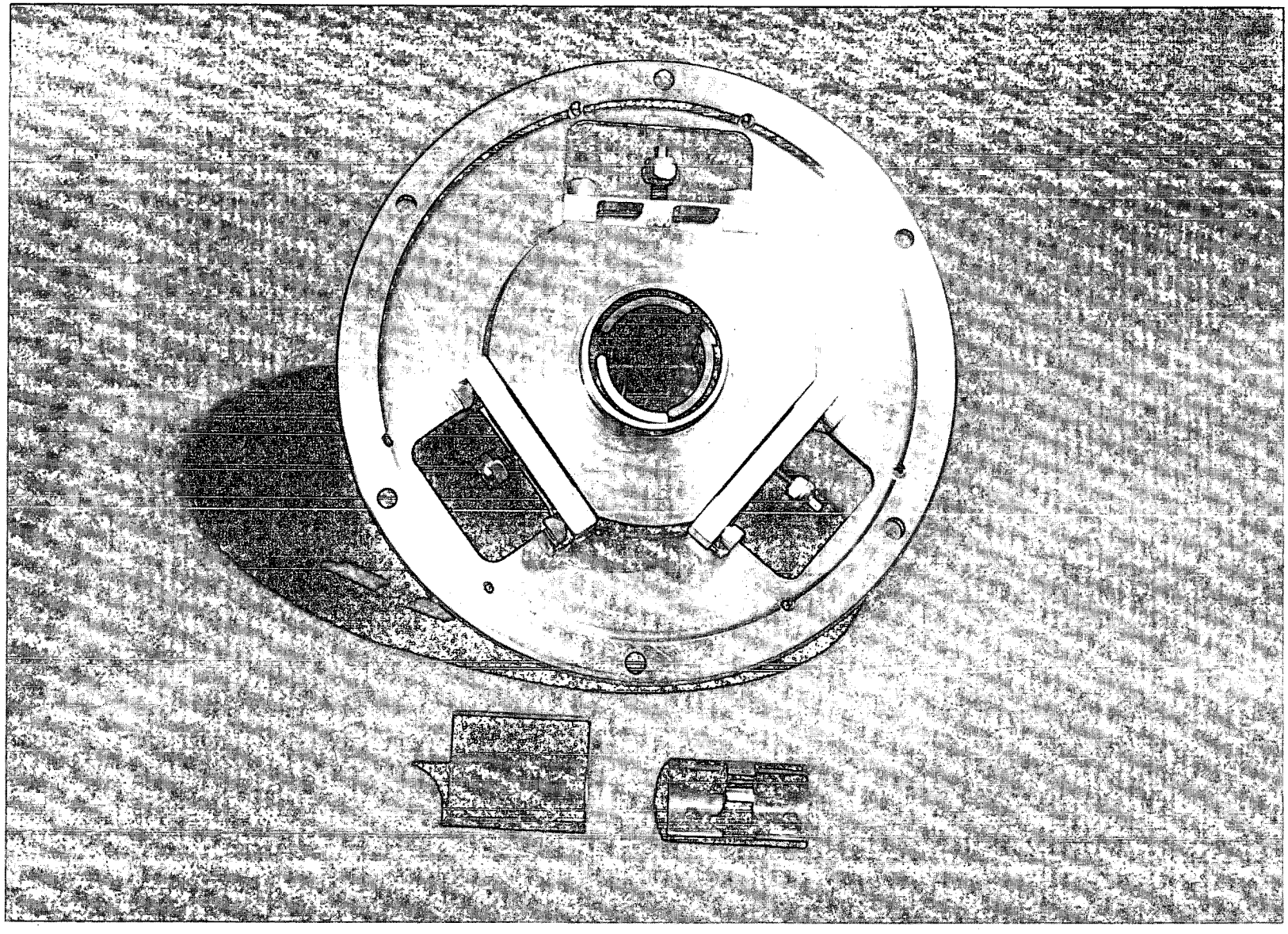

Fig. 3-10 Turbo Compressor Journal Bearings

MTI-18448

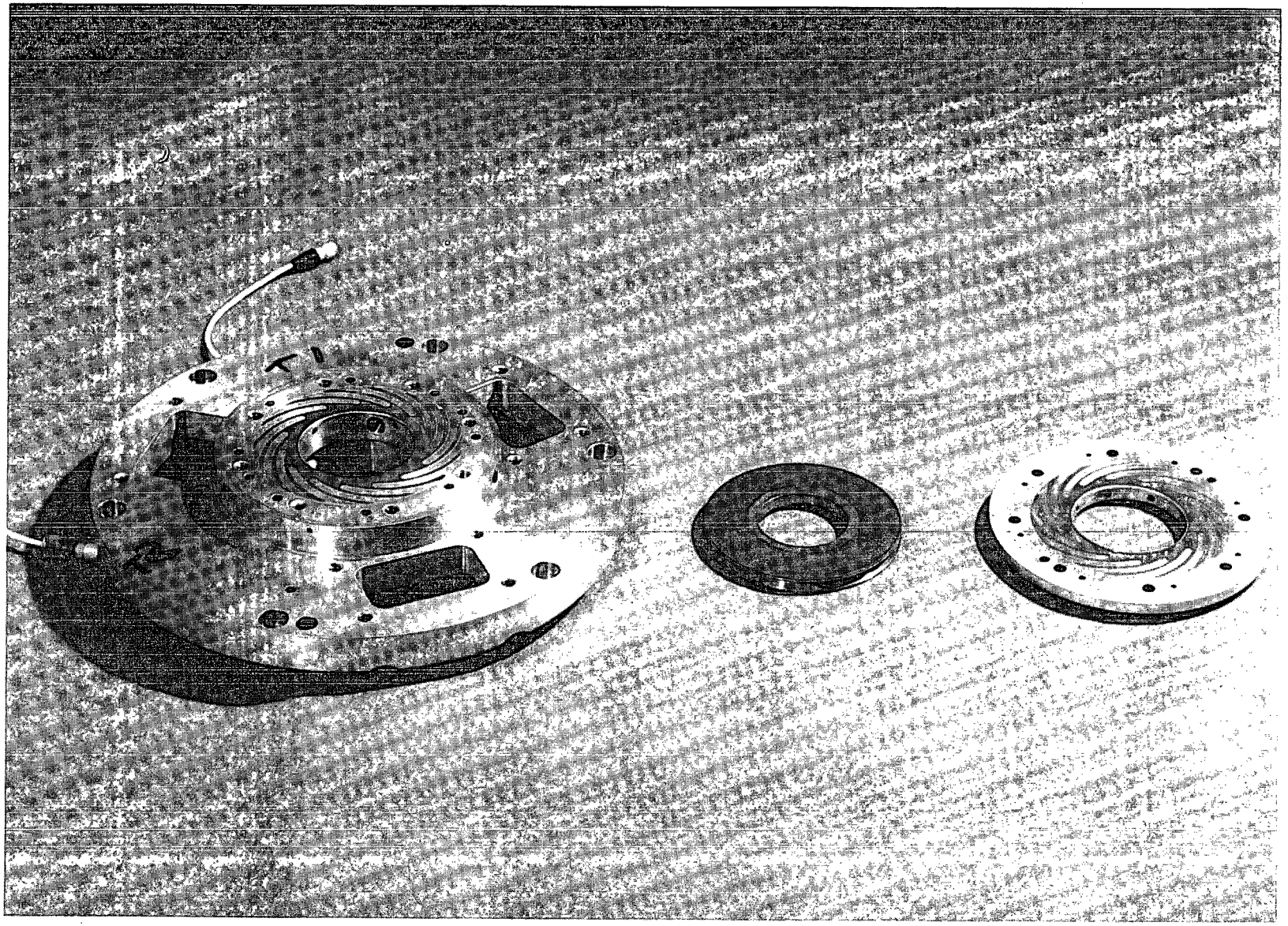

Fig. 3-11 Turbo Compressor Thrust Bearing

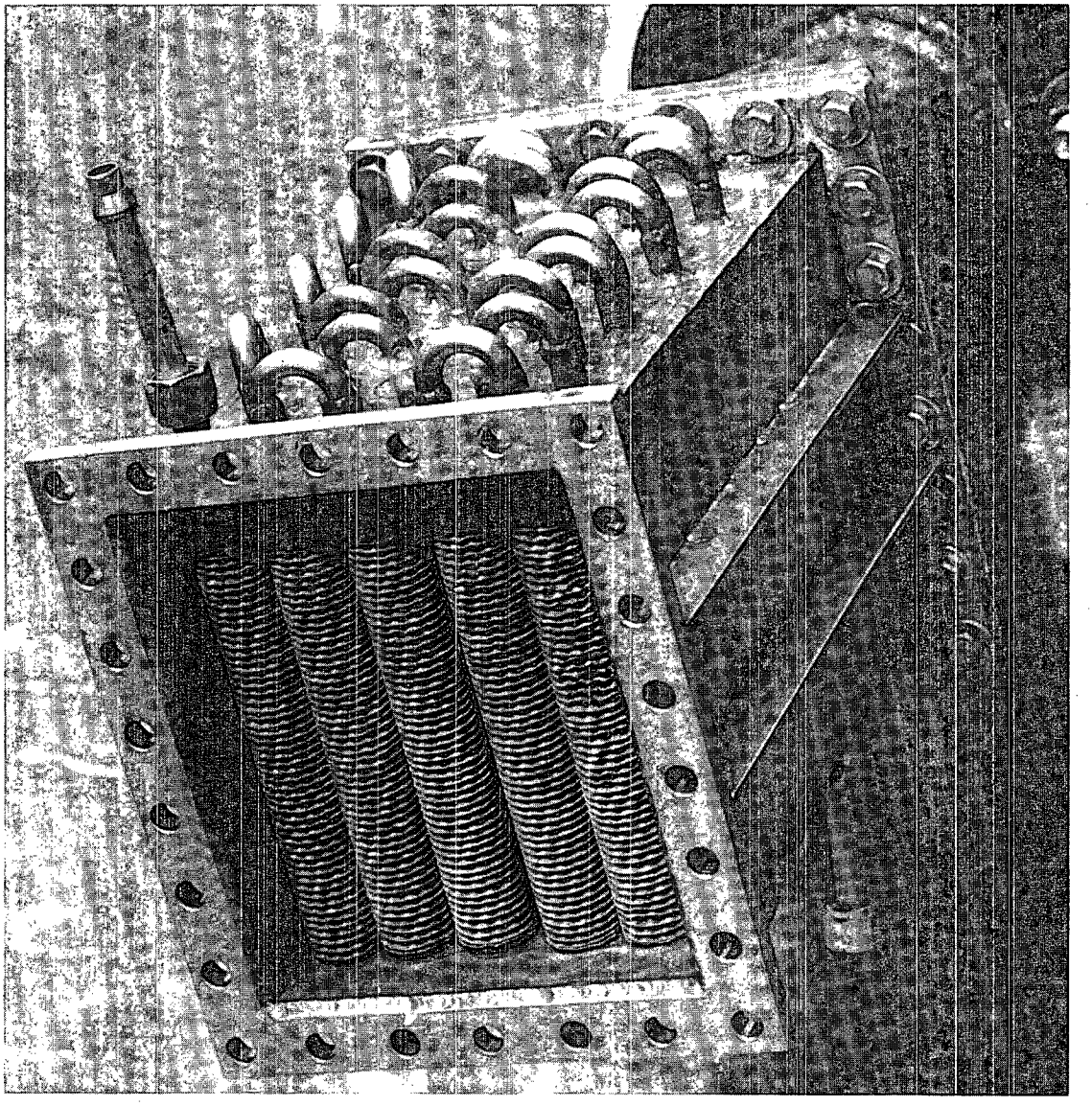

Fig. 3-12 Boiler Feedwater Regenerator

the turbulator section, manifolded together to obtain the required surface area for each application. Each cooler had 317 square feet of heat transfer area. Three (3) units were required for the Freon evaporator, six (6) for the Freon condenser and four (4) for the steam condenser.

3.3 Test Program

3.3.1 System Modifications

At the start of the system test program, the Freon condenser which was originally a series of Modine oil coolers, was changed to a shell and tube heat exchange. This change was necessary to eliminate condensate trap problems in the manifold arrangement of the six (6) coolers. In addition, the manifold arrangement was causing uneven and uncontrollable condensate loading in the parallel exchangers.

3.3.2 Operation of the Turbo-Compressor. The performance and operation of the turbo-compressor throughout the test program was excellent. It should be noted that although individual components were tested separately, the turbo-compressor was not first tested as a simulator but was operated for the first time as a complete assembly.

The maximum speed obtained during the test program was 43,000 rpm. To obtain this speed, the maximum steam conditions available from the boiler were required. The turbine did not have sufficient power to drive the machine faster due to high interstage leakage caused by the large nozzle to turbine wheel and turbine wheel to diffuser clearance. At times, up to 40% of the first stage flow was being exhausted without passing through the second stage nozzle. The large clearance was a precaution taken during initial assembly to avoid possible damage to the turbine wheel due to unexpected thermal growth occurring. The program intent was to reduce the clearance to the design values once the thermal effects were experimentally determined. The test program was terminated prior to tests being conducted with the reduced clearances. The turbo-compressor was fully operational when the program ended.

3.3.3 Data Acquisition. The system schematic shown in Figure 3-1 identifies the location of the instrumentation used to obtain the test data. Thermocouples were used to obtain the temperature measurements. Gages were used for all pressure measurements except the compressor suction and discharge pressure which utilized mercury manometers. Flow tubes were used to measure the Freon flow through the compressor and the cooling water through the Freon condenser. Venturi tubes in the air handling system enclosure were used to measure air flow across the evaporator and condensers. A turbine type flow meter in the SES boiler was used to measure boiler feed water flow. The steam flow could also be checked based on temperature and pressure measurements at the turbine inlet as the nozzles had previously been calibrated. Wet and dry bulb thermometers were used to obtain humidity readings.

Prior to each set of test data being recorded, the system was allowed to run in a steady-state condition to allow all temperatures to stabilize.

In addition, the turbo-compressor contained instrumentation which allowed its operation to be monitored. This instrumentation included temperature measurements of the bearings, and the use of special noncontacting capacitance proximity probes for monitoring axial and radial dynamic rotor motion. Rotor motion was continuously displayed on cathode ray oscilloscopes.

3.4 Post Test Inspection

At the completion of the test program, a post test teardown inspection was performed on the SES package boiler and high speed turbo-compressor.

The package boiler was disassembled to allow the internal heat transfer components to be examined. The steam generator tube bundle is shown in Figure 3-13. The general condition of the tube bundle was found to be good. The aluminum fins on the preheat section were found badly deteriorated. The steel fins on the preheat section were still in good condition as was the exterior of the remaining tubes. Portions of the tube bundle were removed from the preheater, vaporizor and superheater sections to allow the interior walls of the tubes to be examined. No build up of scale was found on any of the sections checked. This lack of build up is attributed to the use of only deionized water in the boiler.

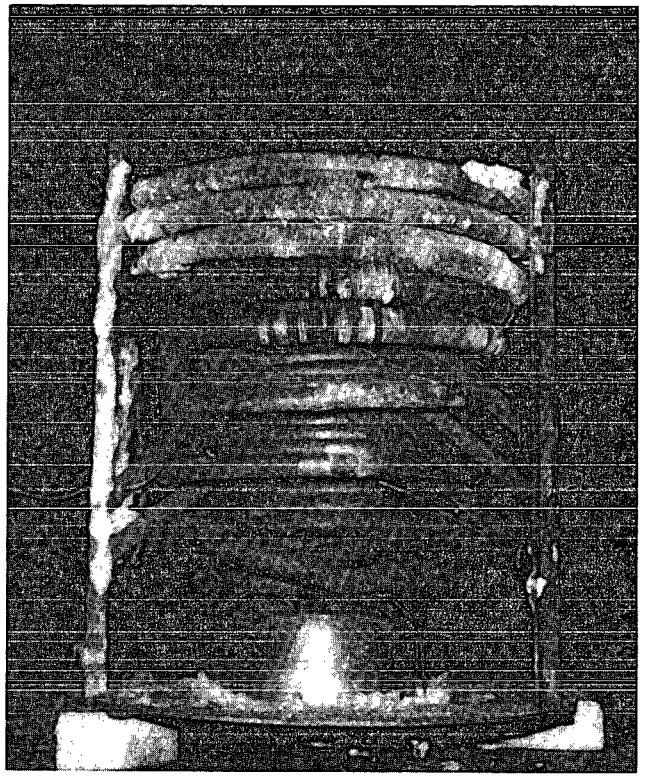

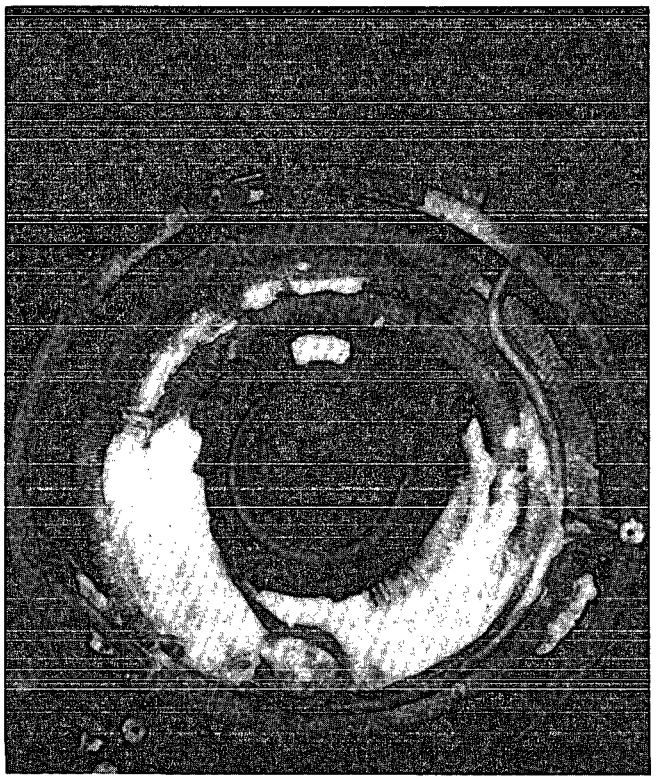

Fig. 3-13 Steam Generator Tube Bundle

MTI-18496

As previously mentioned, the turbo-compressor was operational at the completion of the test program. During the teardown inspection, there were no unusual items noted that would have limited future operation of the turbo-compressor. The condition of the gas bearings and mating journals were good. The components that were exposed to either the steam or seal cooling water exhibited a significant amount of corrosion. Figure 3-14 shows the turbine wheel still installed after the system test.

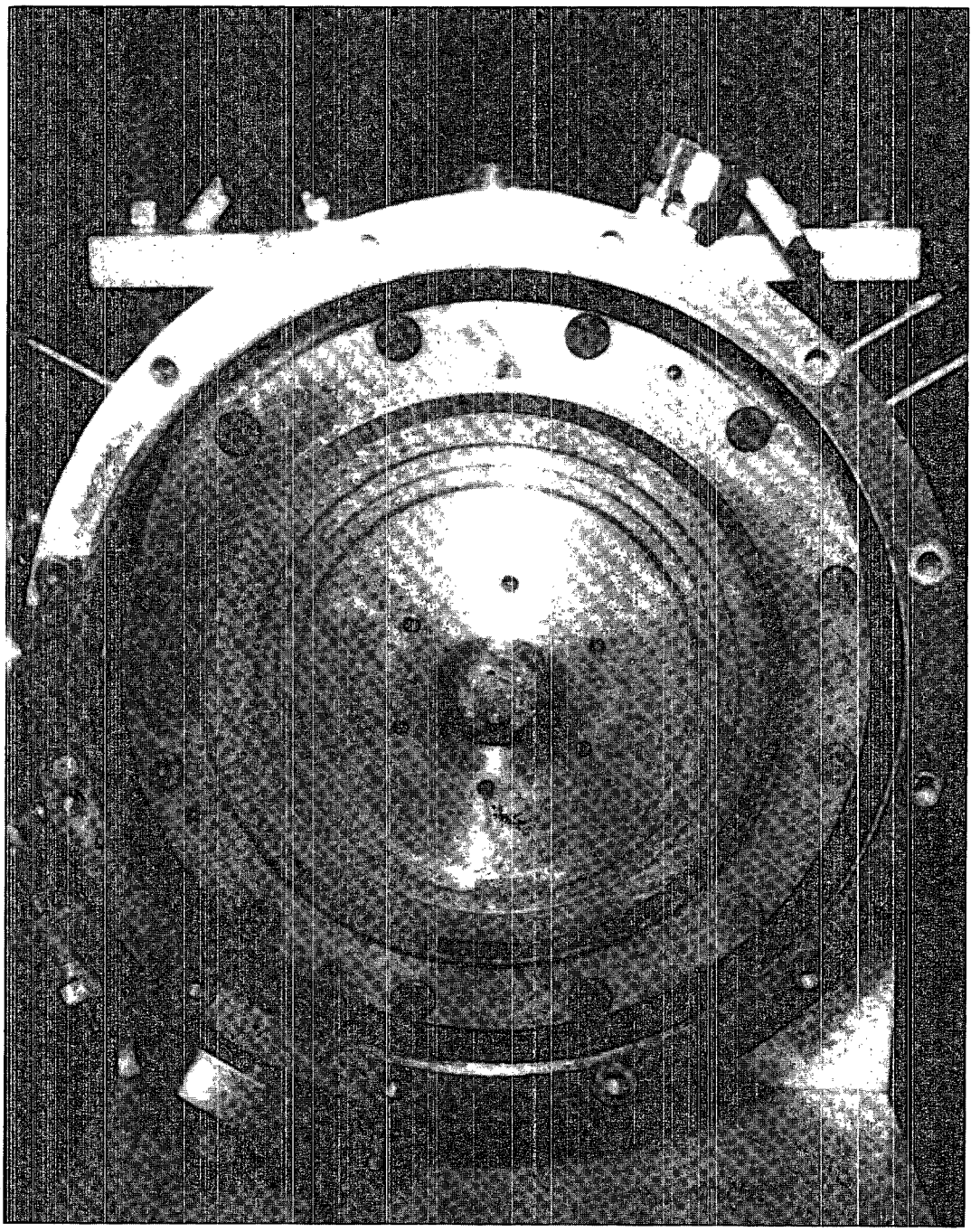

Fig. 3-14 Turbine Wheel After System Test

4.0 ANALYSIS OF TEST RESULTS

4.1 Data Reduction

Seven complete sets of test data were obtained during the test program. The desired form of the test data was a plot of system COP as a function of outside ambient temperature, for both heating and cooling. Since the turbocompressor was not operated to full design speed and the system operated only in the cooling mode, the system COP covering the desired range of outside ambient temperatures could not be obtained directly by performing a system heat balance. To obtain the desired results, the raw test data was first reduced to allow component performance to be plotted as a function of speed, enabling calculations to be made to determine system COP for an entire range of outside ambient temperatures.

Three cases are discussed in the subsequent sections:

- Case 1 — "Predicted Performance" - Performance predicted for the system in Fall 1976.
- Case 2 — "Observed Performance" - Performance based on the actual operation of the system during the test phase.
- Case 3 — "Expected Performance" - Performance that can be expected based on correcting present hardware related problems, i.e., reducing turbine clearance and modest increase in compressor efficiency.

4.2 Component Performance Curves

4.2.1 Compressor. Curves of compressor pressure ratio, corrected flow, and efficiency as a function of corrected speed are shown in Figures 4-1, 4-2, and 4-3 respectively. Each curve has three plots: Case 1 - "Predicted"; Case 2 - "Measured or Observed"; and Case 3 - "Expected". The actual test points are indicated on the curve by an -X-. The pressure ratio and corrected flow curves are plotted directly from test data, correcting for temperature and pressure. The efficiency data is based on temperature rise measurements through the compressor.

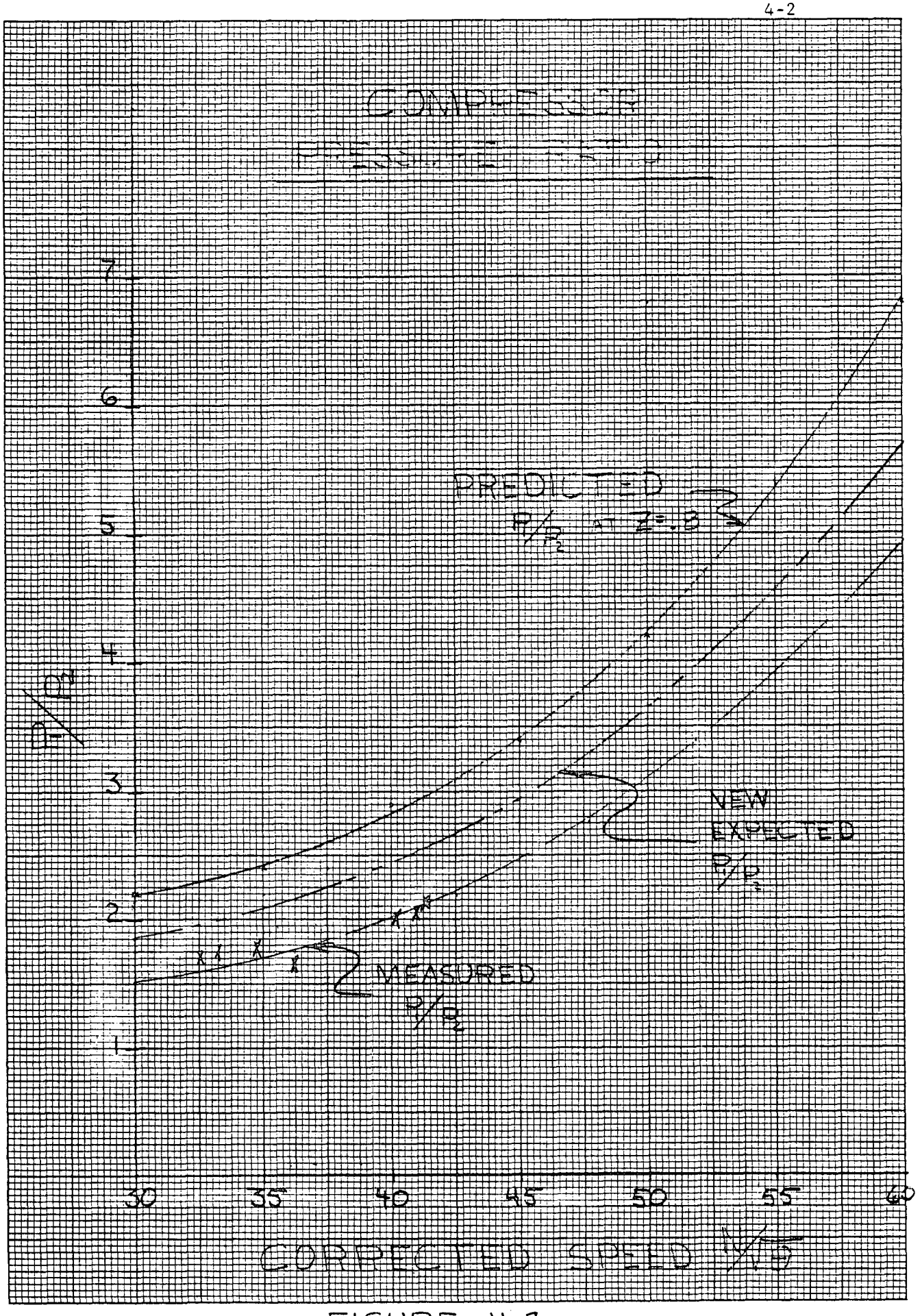

FIGURE 4-1
COMPRESSOR PRESSURE RATIO

46 1322
K+E 10 X 10 TO ½ INCH 7 X 10 INCHES
KEUFFEL & ESSER CO. MADE IN U.S.A.

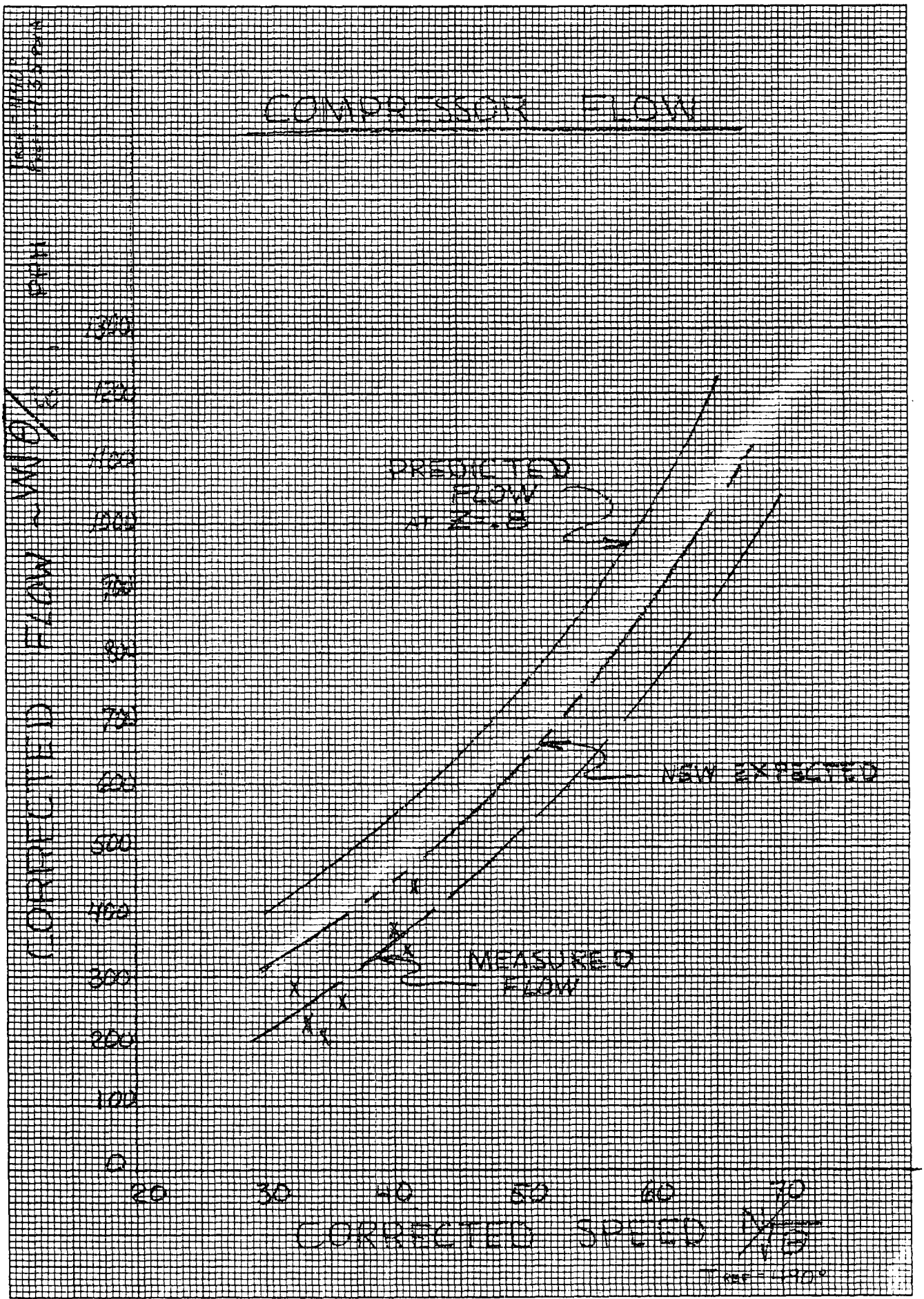

FIGURE 4-2
COMPRESSOR FLOW

46 1322
K+E 10 X 10 TO ½ INCH 7 X 10 INCHES
KEUFFEL & ESSER CO. MADE IN U.S.A.

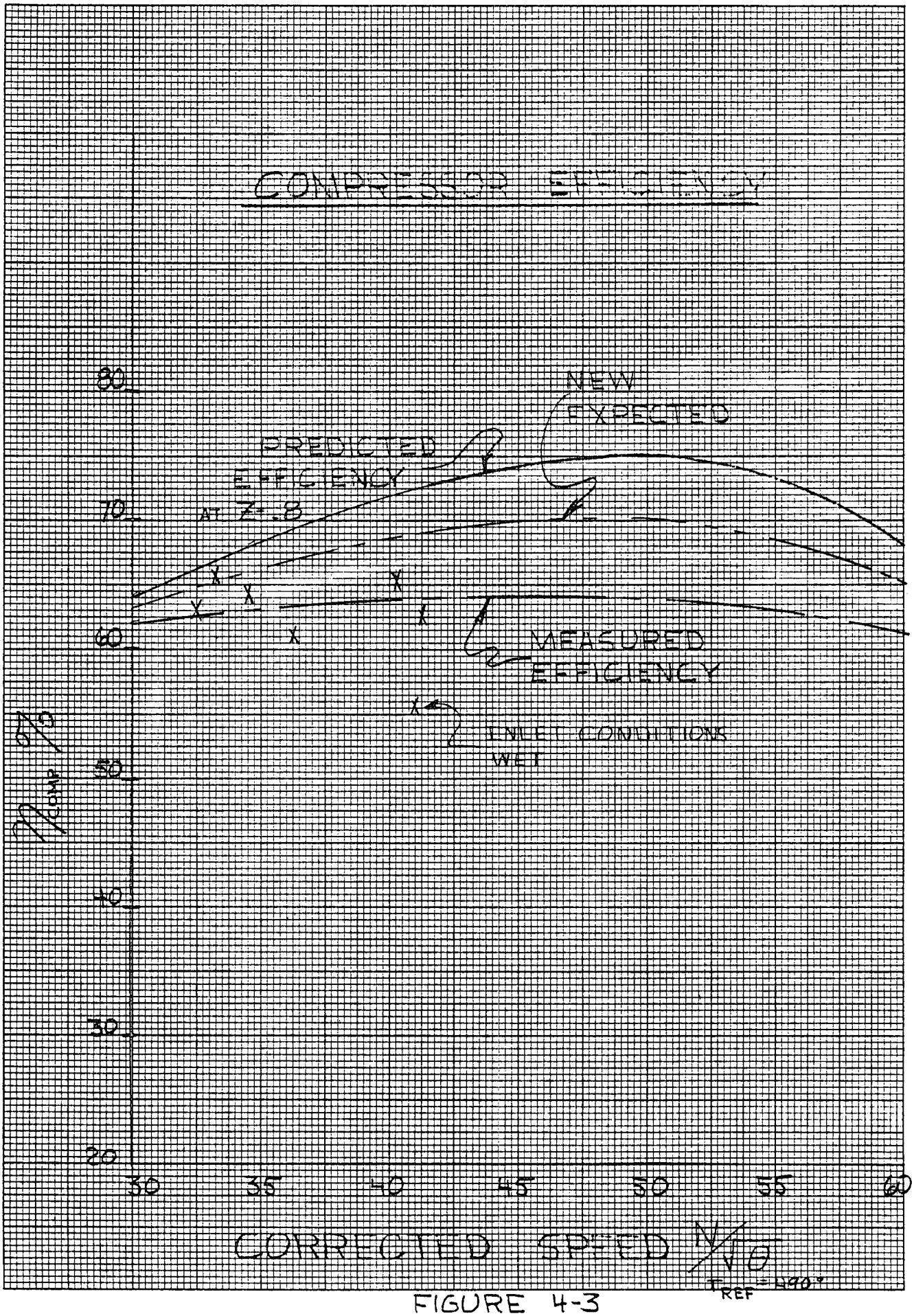

FIGURE 4-3
COMPRESSOR EFFICIENCY

46 1322
K+E 10 X 10 TO ½ INCH 7 X 10 INCHES KEUFFEL & ESSER CO. MADE IN U.S.A.

4.2.2 Turbine. The curve of turbine performance for each stage is shown in Figure 4.4. This curve was generated during component testing performed on the component test rig prior to the start of system testing. Figure 4-5 shows measured first stage flow and measured interstage leakage plotted as a function of corrected speed. Also included is a plot of the ratio of leakage to total flow. A curve indicating the expected leakage based on reducing the turbine wheel clearance is included, as is the ratio of the total flow to reduced leakage.

4.2.3 Boiler. The boiler efficiency calculated at MTI was .826, without the air preheater. The efficiency with the preheater was estimated to be .860. These efficiencies were used in calculating system performance and agree very closely with the values supplied by SES. These values are based on the lower heating value of propane (2282.6 Btu/cu ft).

4.2.4 Regenerator. The regenerator effectiveness as a function of inlet steam temperature is shown in Figure 4-6.

4.3 Parasitic Losses

The source of the parasitic losses in the system are shown in Figure 4-7. The magnitude of each loss is indicated for a rotor speed of 50K rpm and is compared with the original predicted values. A plot of the parasitic losses vs. speed for both the original and present predicted values is shown in Figure 4-8. The present predicted values were used in computing system performance.

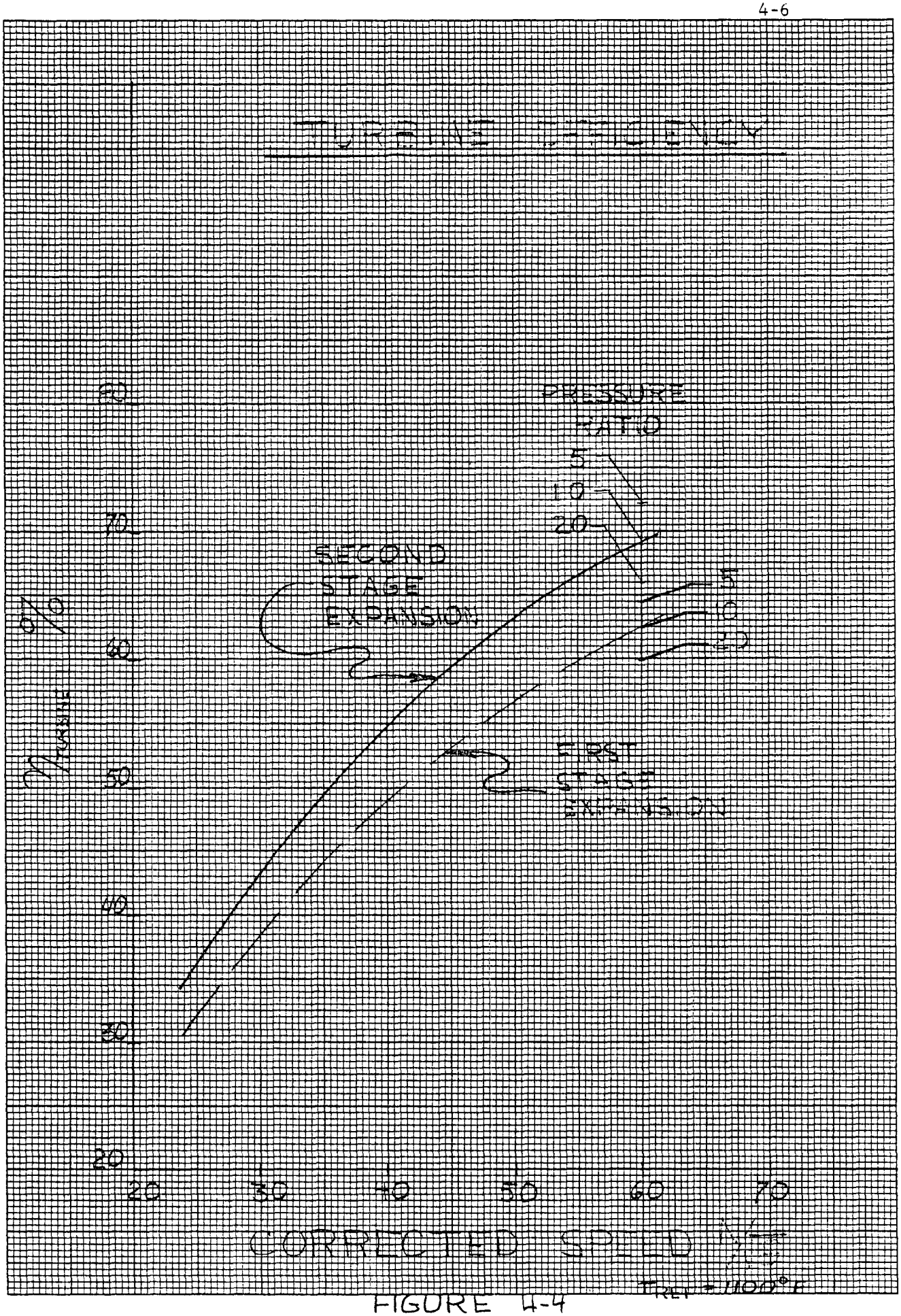

FIGURE 4-4
TURBINE EFFICIENCY

46 1322
K+E 10 X 10 TO ½ INCH 7 X 10 INCHES
KEUFFEL & ESSER CO. MADE IN U.S.A.

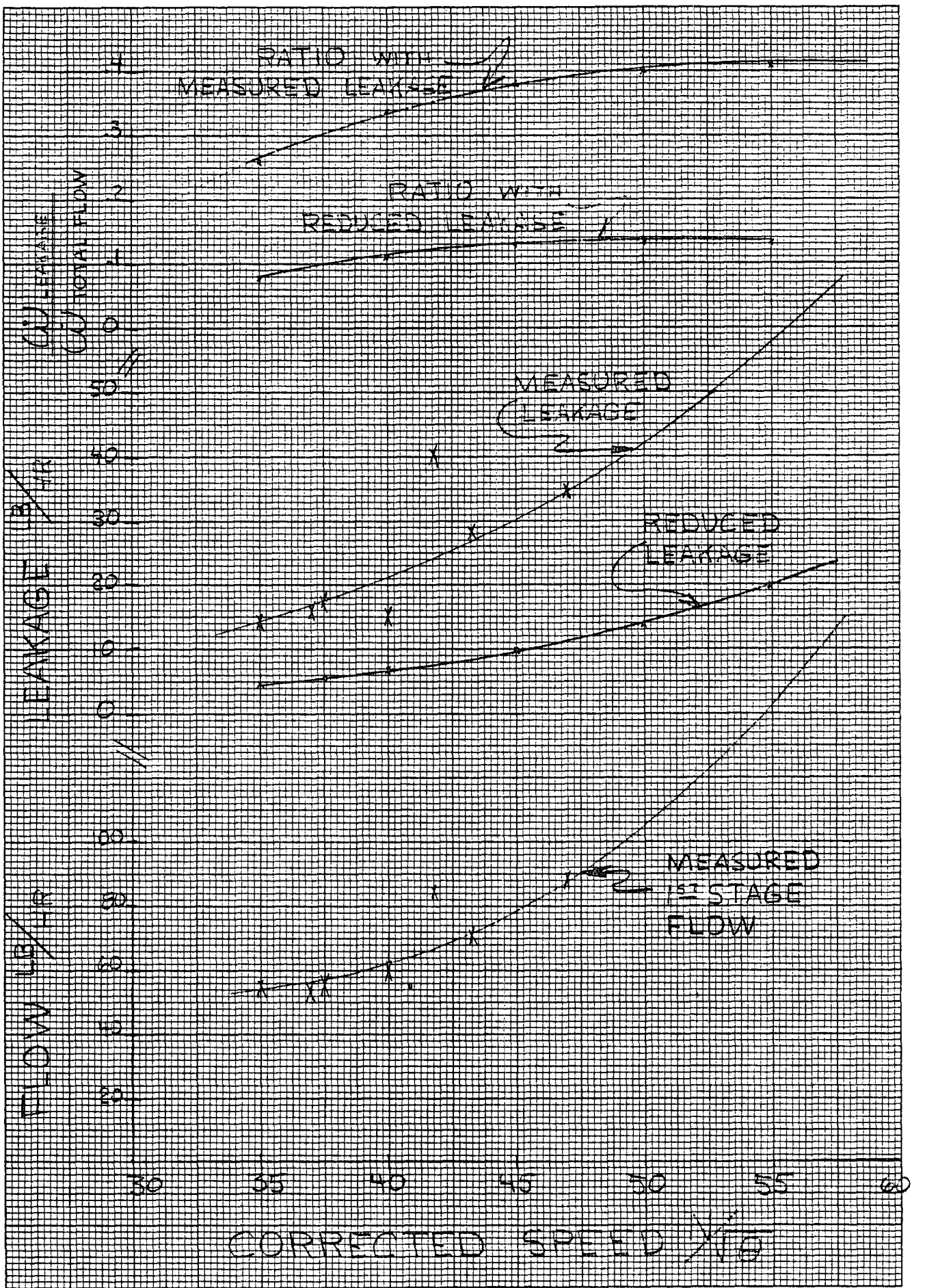

FIGURE 4-5

STEAM FLOW & LEAKAGE

46 1322
K+E 10 X 10 TO ½ INCH 7 X 10 INCHES KEUFFEL & ESSER CO. MADE IN U.S.A.

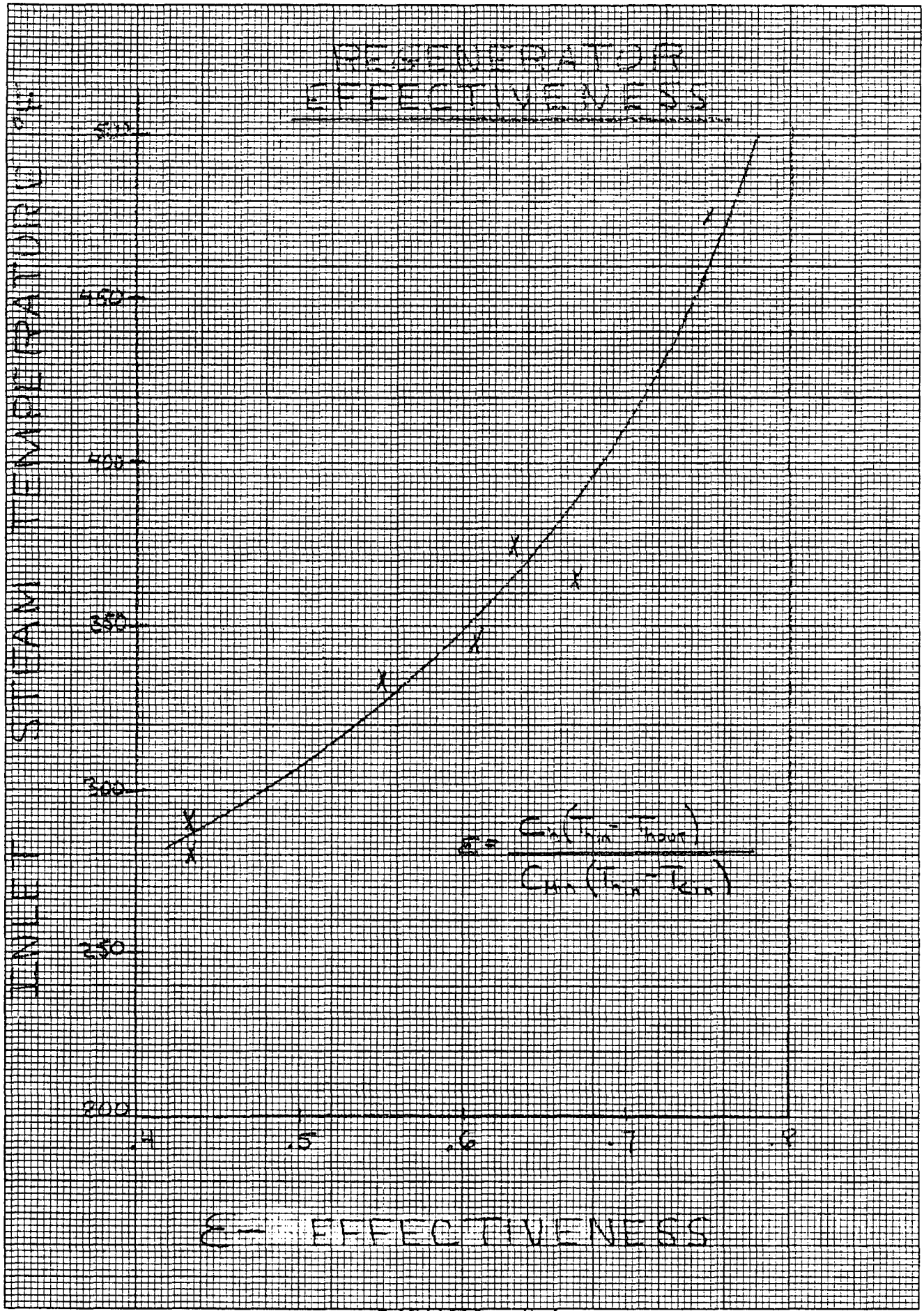

FIGURE 4-6
REGENERATOR EFFECTIVENESS

46 1322
K+E 10 X 10 TO ½ INCH 7 X 10 INCHES
KEUFFEL & ESSER CO. MADE IN U.S.A.

CNG TURBO-COMP SHAFT LOSSES

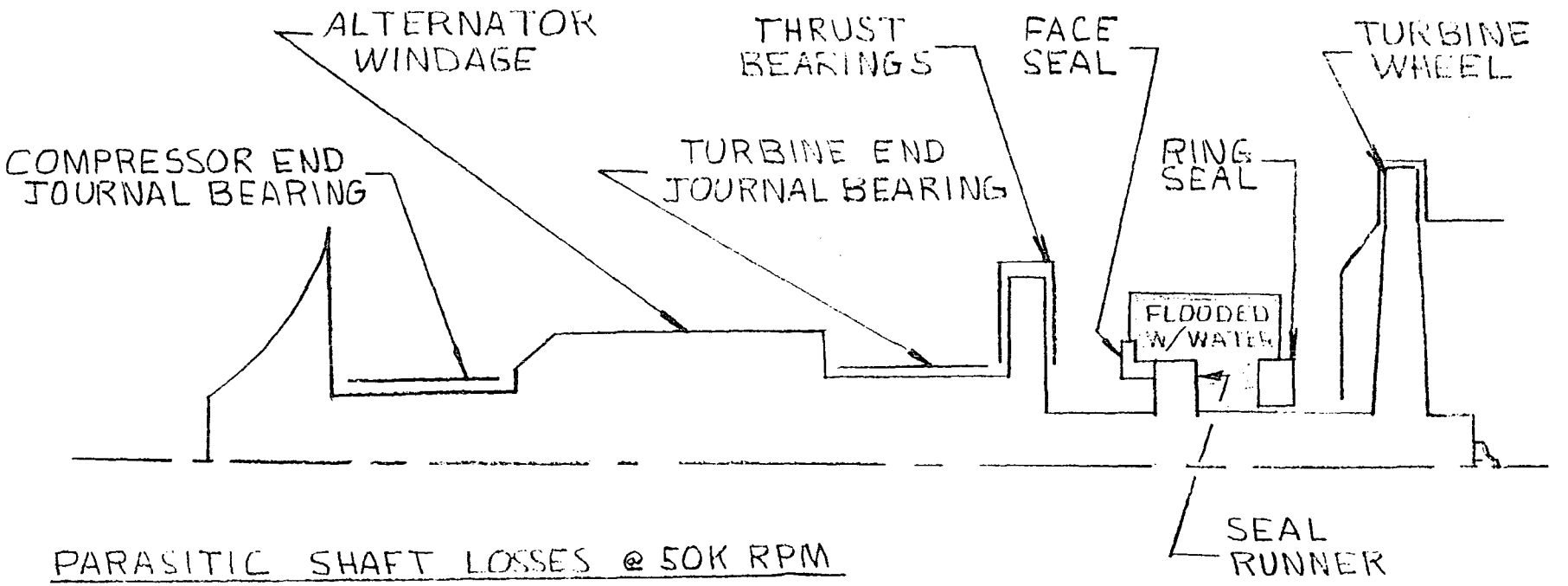

PARASITIC SHAFT LOSSES @ 50K RPM

SOURCE	ORIGINAL PREDICTED	PRESENT PREDICTED
JOURNAL BEARINGS	22 WATTS	61 WATTS
THRUST BEARINGS	39	119
FACE SEAL	419 (BASED ON 2)	129
ALTERNATOR WINDAGE	168	235
RING SEAL	—	94
SEAL RUNNER	—	633
Δ DUE TO HIGH TURBINE BACK PRESSURE	—	328
TOTAL	648 WATTS 0.869 HP	1589 WATTS 2.13 HP

FIGURE 4-7
SHAFT LOSSES

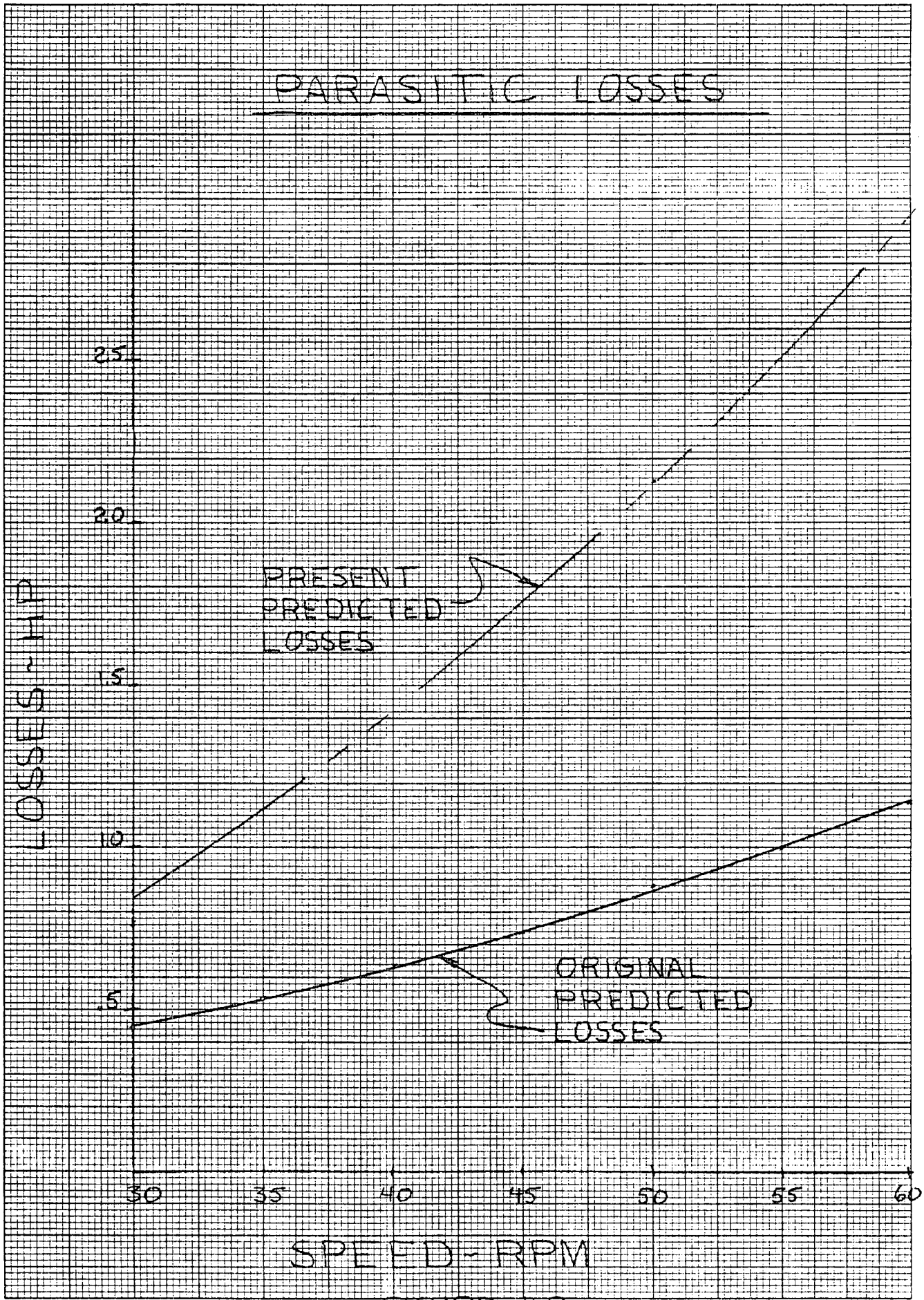

FIGURE 4-8
SHAFT LOSSES

K+E 10 X 10 TO ½ INCH 7 X 10 INCHES KEUFFEL & ESSER CO. MADE IN U.S.A.
46 1322

5.0 SYSTEM PERFORMANCE

The heating mode system COP as a function of outside ambient temperature is shown in Figure 5-1. Curves for the three cases, Original Predicted, Observed, and New Predicted are shown. Also shown in Figure 5-1 is the cooling COP at 95° outside ambient for the three cases and the seasonal heating COP for Cleveland. The seasonal COP was calculated using the curves of Figure 5-1 and the heat distribution curve shown in Figure 5-2.

The Case #1 curve, Original Predicted, was taken from the preliminary design work performed in Fall 1976. Case #2, Observed Performance, was obtained directly from test data recorded during the system test. The actual test points fall within the range indicated on the curve. The "New Predicted" curve was calculated using the Case #3 component performance curves described in Section 4.

In obtaining the system COP for Cases 2 and 3, some assumptions were made since the system could not operate at the design point due to the limitation of the turbo-compressor speed, and since the system was only tested in the cooling mode. A summary of the assumptions follow.

The steam discharge temperature from the boiler for both the first and second stage was assumed to be at the design temperature of $1100^{o}F$. Steam flow rate was as measured for the data points and as required for all other points. There was assumed to be no heat loss from the boiler discharge to the turbine inlets or in any other steam or refrigerant piping in the system.

Both the steam and Freon condensers and Freon evaporator were assumed to operate at their design points and to be of sufficient size for the heat transfer duty requirement.

K+E X 10 INCH 10 INC
KEUFFEL & ESSER CO. MADE IN U.S.A. 46-1322

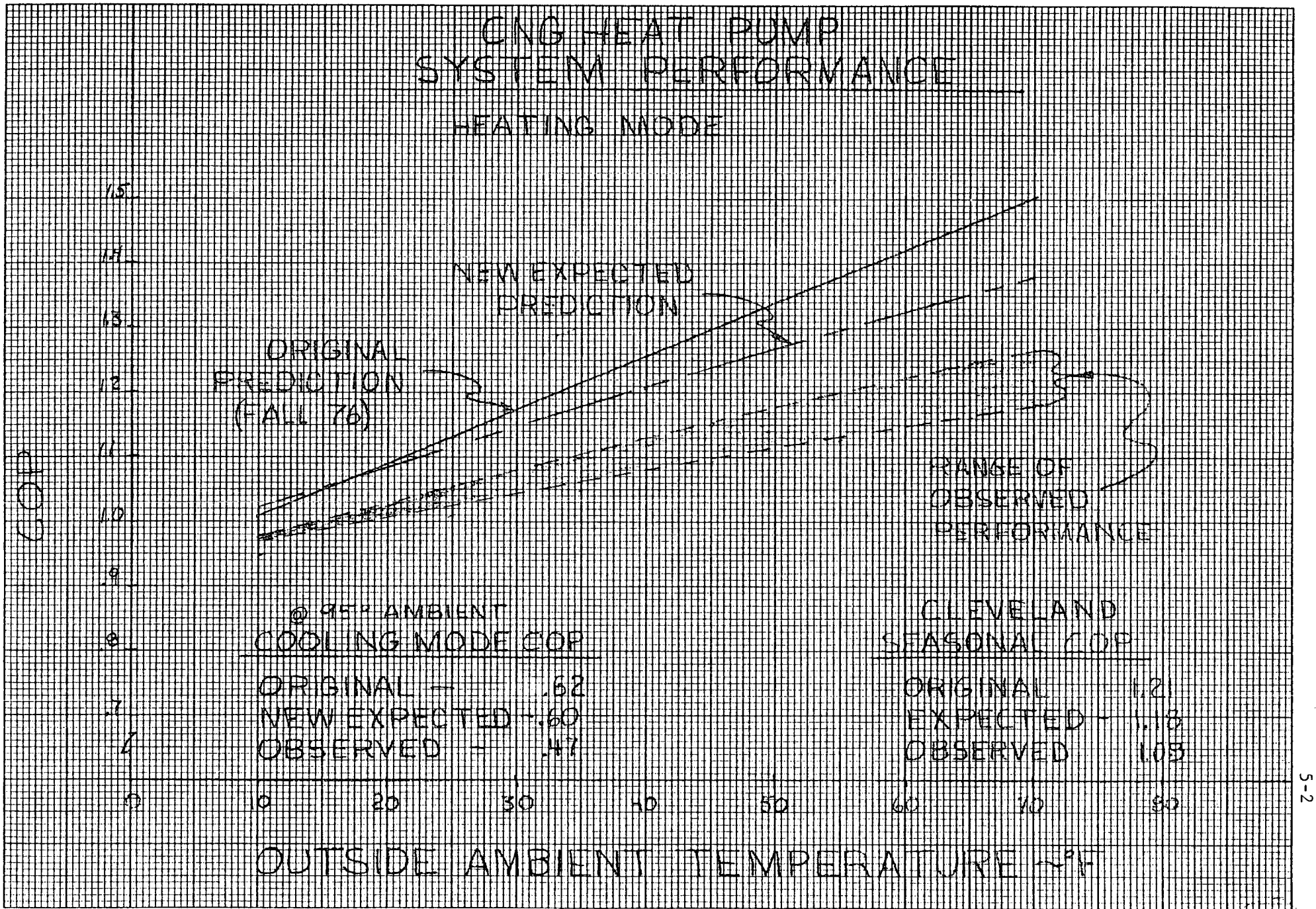

FIGURE 5-1
SYSTEM PERFORMANCE

9/7/78
MIT

K+E 10 TO 1/2 INCH 7 X 10 INCHES
KEUFFEL & ESSER CO. MADE IN U.S.A.
46 1322

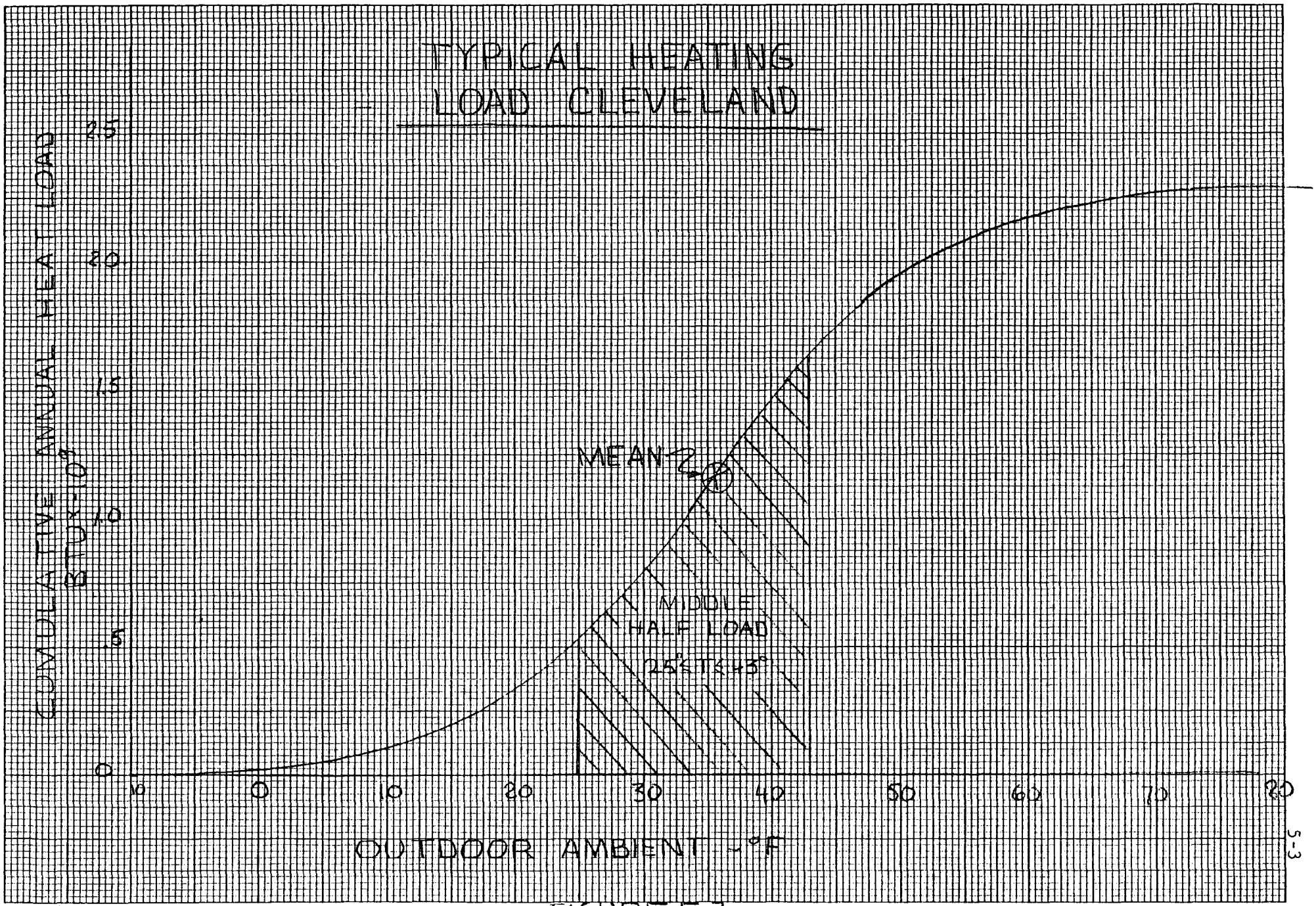

FIGURE 5-2
TYPICAL HEATING LOAD

In calculating the system COP, the expressions shown below were used:

Heating Mode

$$COP = \frac{\text{Heat Rejected by Steam + Heat Rejected by Freon}}{\text{Total Shaft Work}/\eta_{TC}\ \eta_B}$$

Cooling Mode

$$COP = \frac{\text{Heat Absorbed by Freon}}{\text{Total Shaft Work}/\eta_{TC}\ \eta_B}$$

Where:

Heat Rejected by Steam -

$$Q_s = \dot{W}_s\ (H_{in} - H_{out})\ \text{Steam Condenser}$$

Heat Rejected by Freon -

$$Q_{f_c} = \dot{W}_F\ (H_{in} - H_{out})\ \text{Freon Condenser}$$

Heat Absorbed by Freon

$$Q_{f_e} = \dot{W}_F\ (H_{out} - H_{in})\ \text{Freon Evaporator}$$

Total Shaft Work/η_{TC} x η_B

$$\frac{\text{Compressor Work + Alternator Work + Parasitic Losses}}{\eta_{TC} \times \eta_B}$$

η_{TC} - Thermal Cycle Efficiency

η_B - Boiler Efficiency